

ISSN 0233-7584

---

**Vol. 41, Iss. 3**

**May – June**

**2025**

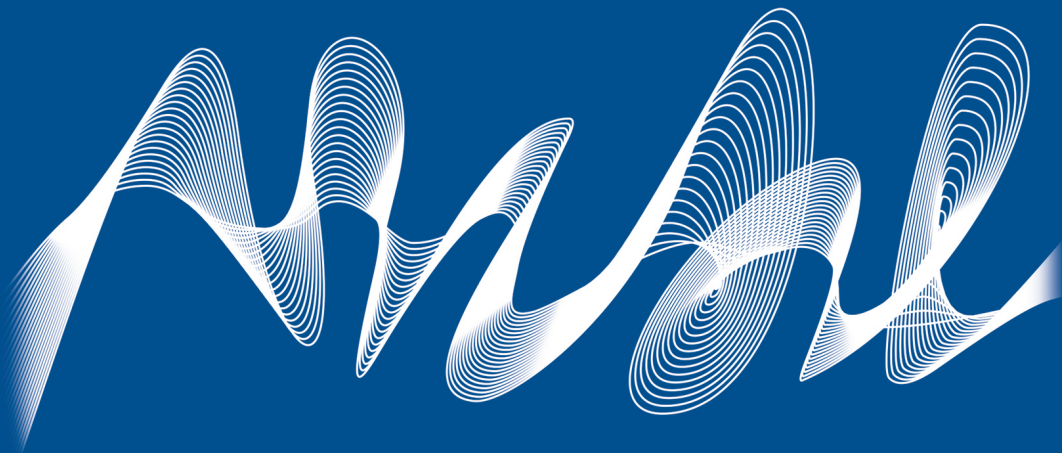
---



# Physical Oceanography

---

<http://physical-oceanography.ru/>



ISSN 1573-160X

Vol. 32, no. 3. 2025

May – June

Founded in January 1987

Publication frequency:

6 issues per year

# Physical Oceanography

Scientific and theoretical journal

FOUNDER AND PUBLISHER:

Federal State Budget Scientific Institution

Federal Research Centre

“Marine Hydrophysical Institute of RAS”

---

Peer reviewed scientific journal.

The Journal publishes original research results, review articles (at the editorial board's request) and brief reports on the following sections of hydrophysics:

- thermohydrodynamics of the ocean and atmosphere;
- analysis of observational results and methods of calculation of ocean hydrophysical fields;
- experimental and expeditionary studies;
- satellite hydrophysics;
- mathematical modelling of marine systems;
- automation of scientific research of the seas and oceans.

Objectives

- familiarisation of the world and Russian scientific community with the results of theoretical, experimental and expeditionary studies of the World Ocean;
- exchange of scientific information, experience, research and observation data with specialists from different regions of the country and abroad;
- increase of publication activity of national authors, rating of scientific organisations of Russia and level of national publications in the world scientific community according to their citation data;
- theoretical and practical assistance to scientists in preparing articles for printing that meet modern requirements of publication and scientific ethics;
- strengthening the popularity and authority of the publication, increasing the number of regular subscribers

The Journal is indexed in:

Google Scholar  
Web of Science (ESCI)  
Scopus

[journal@mhi-ras.ru](mailto:journal@mhi-ras.ru)

<http://physical-oceanography.ru/>

**Founder, Publisher and Editorial Office address:**

2, Kapitanskaya St., Sevastopol, 299011

Russia

Phone, fax: + 7 (8692) 54-02-23

---

## EDITORIAL BOARD

- Sergey K. Konovalov** – Editor-in-Chief, Director of FSBSI FRC MHI, corresponding member of RAS, Dr.Sci. (Geogr.), ORCID ID: 0000-0002-5200-8448, secretary@mhi-ras.ru (Sevastopol, Russia)
- Vladimir N. Belokopytov** – Deputy Editor-in-Chief, Head of Department of FSBSI FRC MHI, Dr.Sci. (Geogr.), ORCID ID: 0000-0003-4699-9588 (Sevastopol, Russia)
- Aleksandr I. Kubryakov** – Deputy Editor-in-Chief, Chief Scientist Researcher of FSBSI FRC MHI, Dr.Sci. (Phys.-Math.), ORCID ID: 0000-0003-1899-9230, ResearcherID: F-8959-2014 (Sevastopol, Russia)
- Anton A. Bukatov** – Executive Editor, Leading Research Associate of FSBSI FRC MHI, Ph.D. (Phys.-Math.), ORCID ID: 0000-0002-1165-8428, journal@mhi-ras.ru (Sevastopol, Russia)
- Yuri V. Artamonov** – Head Scientist Researcher of FSBSI FRC MHI, Dr.Sci. (Geogr.), ResearcherID: AAC-6651-2020 (Sevastopol, Russia)
- Sergey V. Berdnikov** – Director of FRC SSC of RAS, Dr.Sci. (Geogr.), ORCID ID: 0000-0002-3095-5532 (Rostov-on-Don, Russia)
- Valery G. Bondur** – Scientific Supervisor of ISR “AEROCOSMOS”, academician of RAS, Dr.Sci. (Techn.), ORCID ID: 0000-0002-2049-6176 (Moscow, Russia)
- Demuri I. Demetrashvili** – Head of the sector of mathematical modeling of geophysical processes of sea and atmosphere, the Nodia Institute of Geophysics of the Javakishvili Tbilisi State University, Dr.Sci. (Phys.-Math.), ORCID ID: 0000-0002-4789-4852 (Tbilisi, Georgia)
- Sergey A. Dobrolyubov** – Dean of Faculty of Geography of MSU, academician of RAS, Dr.Sci. (Geogr.), prof., ResearcherID: A-9688-2012 (Moscow, Russia)
- Grigory I. Dolgikh** – Head Scientific Researcher of POI FEB of RAS, Dr.Sci. (Phys.-Math.), academician of RAS, prof., ORCID ID: 0000-0002-2806-3834 (Vladivostok, Russia)
- Stanislav G. Dolgikh** – Head of Laboratory of Nonlinear Hydrophysics and Natural Disasters, POI FEB of RAS, corresponding member of RAS, Dr.Sci. (Techn.), ORCID ID: 0000-0001-9828-5929 (Vladivostok, Russia)
- Vladimir A. Dulov** – Head of Laboratory of FSBSI FRC MHI, Dr.Sci. (Phys.-Math.), prof., ORCID ID: 0000-0002-0038-7255 (Sevastopol, Russia)
- Vladimir V. Efimov** – Head of Department of FSBSI FRC MHI, Dr.Sci. (Phys.-Math.), prof., ResearcherID: P-2063-2017 (Sevastopol, Russia)
- Vladimir V. Fomin** – Head of Department of FSBSI FRC MHI, Dr.Sci. (Phys.-Math.), ORCID ID: 0000-0002-9070-4460 (Sevastopol, Russia)
- Isaac Gertman** – Head of the Physical Oceanography Department of Israel Oceanographic & Limnological Research, Head of IOLR data center ISRAMAR, Ph.D. (Geogr.), ORCID ID: 0000-0002-6953-6722 (Haifa, Israel)
- Dmitry G. Gryazin** – Head of Department, Chief Metrologist of SRC of the “Concern CSRI Elektropribor” JSC, Dr.Sci. (Techn.), prof. of Mechatronics of ITMO University, Scopus Author ID: 25638150600 (Saint Petersburg, Russia)
- Rashit A. Ibraev** – Chief Scientist Researcher of INM of RAS, corresponding member of RAS, Dr.Sci. (Phys.-Math.), ORCID ID: 0000-0002-9099-4541 (Moscow, Russia)
- Igor K. Ivashchenko** – Senior Scientist of FSBSI FRC MHI, Ph.D. (Econ.) (Sevastopol, Russia)
- Vasily V. Knysch** – Head Scientist Researcher of FSBSI FRC MHI, Dr.Sci. (Phys.-Math.), prof., ResearcherID: B-3603-2018 (Sevastopol, Russia)
- Gennady K. Korotaev** – Scientific Supervisor of FSBSI FRC MHI, corresponding member of RAS, Dr.Sci. (Phys.-Math.), prof., ResearcherID: K-3408-2017 (Sevastopol, Russia)
- Vladimir N. Kudryavtsev** – Executive Director of Satellite Oceanography Laboratory of RSHU, Dr.Sci. (Phys.-Math.), prof., ResearcherID: G-1502-2014 (Saint Petersburg)
- Michael E. G. Lee** – Head of Department of FSBSI FRC MHI, Dr.Sci. (Phys.-Math.), prof., ORCID ID: 0000-0002-2292-1877 (Sevastopol, Russia)
- Gennady G. Matishov** – Deputy President of RAS, Deputy academician-Secretary of the Department of Earth Sciences of Supervisor of RAS – Head of the Oceanology, Atmospheric Physics and Geography Section, Scientific Supervisor of SSC of RAS, academician of RAS, Dr.Sci. (Geogr.), prof., ORCID ID: 0000-0003-4430-5220 (Rostov-on-Don, Russia)
- Nickolay A. Rimski-Korsakov** – Deputy Director (Marine Engineering) of FSBSI P.P. Shirshov IO of RAS, Dr.Sci. (Techn.), ResearcherID: K-8378-2017 (Moscow, Russia)
- Angelo Rubino** – Professor of Ca’ Foscari University, Ph.D. (Phys. Oceanogr.), ORCID ID: 0000-0003-3857-4811 (Venice, Italy)
- Anatoly S. Samodurov** – Head of Department of FSBSI FRC MHI, Dr.Sci. (Phys.-Math.), ResearcherID: V-8642-2017 (Sevastopol, Russia)
- Georgy I. Shapiro** – Head of Plymouth Ocean Forecasting Centre of the University of Plymouth, Dr.Sci. (Phys.-Math.), prof. in Phys. Oceanogr. (Plymouth, Great Britain)
- Naum B. Shapiro** – Head Scientist Researcher of FSBSI FRC MHI, Dr.Sci. (Phys.-Math.), ResearcherID: A-8585-2017 (Sevastopol, Russia)
- Mikhail V. Shokurov** – Head Scientist Researcher of FSBSI FRC MHI, Dr.Sci. (Phys.-Math.), ORCID ID: 0000-0003-1595-8281 (Sevastopol, Russia)
- Elena F. Vasechkina** – Deputy Director of FSBSI FRC MHI, Chief Research Associate of FSBSI FRC MHI, Dr.Sci. (Geogr.), ORCID ID: 0000-0001-7007-9496 (Sevastopol, Russia)
- Elizaveta V. Zabolotskikh** – Head Scientist Researcher of RSHU, Dr.Sci. (Phys.-Math.), Scopus Author ID: 6506482460 (Saint Petersburg, Russian)
- Vladimir B. Zalesny** – Head Scientific Researcher of INM of RAS, Dr.Sci. (Phys.-Math.), prof., ORCID ID: 0000-0003-3829-3374 (Moscow, Russia)
- Andrey G. Zatsepin** – Chief of Laboratory of FSBSI P.P. Shirshov IO of RAS, Chief Research Associate of FSBSI P.P. Shirshov IO of RAS, Dr.Sci. (Phys.-Math.), ORCID ID: 0000-0002-5527-5234 (Moscow, Russia)
- George Zodiatis** – Senior Researcher of Laboratory of Coastal and Marine Research of the Institute of Applied and Computational Mathematics, for Research and Technology Foundation – Hellas, Ph.D. (Oceanol.), ResearcherID: J-3032-2013 (Heraklion, Crete, Greece)

## CONTENTS

Vol. 32, no 3. 2025

May – June, 2025

### ANALYSIS OF OBSERVATIONS AND METHODS OF CALCULATING HYDROPHYSICAL FIELDS IN THE OCEAN

- Morozov A. N.** Vertical mixing in the main pycnocline of the Black Sea in summer ..... 271
- Korotaev G. K., Belokopytov V. N., Dorofeev V. L., Mizyuk A. I., Puzina O. S., Kholod A. L.** Trends in Acceleration of Climate Changes in the Thermohaline Structure of the Black Sea upper layer ..... 283
- Saprykina Ya. V., Divinsky B. V., Shtremel M. N., Likutova O. A.** Estimation of the stationarity interval of wind wave field ..... 297
- Shokurova I. G., Plastun T. V., Simonova Yu. V., Kasianenko V. Yu.** Upwelling index at the Southern coast of Crimea in the Black Sea ..... 312

### EXPERIMENTAL AND FIELD RESEARCH

- Gurov K. I., Kotelyanets E. A., Gurova Yu. S.** Accumulation of heavy metals and distribution of the areas of technogenic loads in Balaklava Bay: Results of long-term research ..... 326

### MATHEMATICAL MODELING OF MARINE SYSTEMS

- Kovalyova I. V.** Parameterization of the dependence of integral phytoplankton biomass on chlorophyll concentration at the Black Sea surface based on expeditionary research data ..... 347
- Demyshev S. G.** Arakawa–Lamb scheme in application to stratified incompressible fluid in the absence of friction ..... 361
- Semin S. V., Kalnitskii L. Yu., Ushakov K. V., Ibraev R. A.** Model of the Lagrangian particle transport in a quasi-two-phase ocean – ice medium in a parallel ocean dynamics model ..... 372

### AUTOMATION OF RESEARCH OF SEAS AND OCEANS

- Svergun E. I., Zimin A. V., Motyzhev S. V., Lunev E. G., Tolstosheev A. P., Volikov M. S.** Measuring the characteristics of short-period internal waves using an array of drifting thermoprofiling buoys ..... 392

### SATELLITE HYDROPHYSICS

- Pivaev P. D., Kudryavtsev V. N.** On Tropical Cyclone Footprints in Sea Surface Height Anomalies ..... 408



All the materials of the journal are available under Creative Commons Attribution-NonCommercial 4.0 International (CC BY-NC 4.0)

Original article

## Vertical Mixing in the Main Pycnocline of the Black Sea in Summer

**A. N. Morozov***Marine Hydrophysical Institute of RAS, Sevastopol, Russian Federation*✉ [anmorozov@mhi-ras.ru](mailto:anmorozov@mhi-ras.ru)

### Abstract

**Purpose.** The study is aimed at assessing the parameters of vertical turbulent mixing in the main pycnocline of the Black Sea based on the data on current velocity and density measured by standard hydrological instruments.

**Methods and Results.** The data collected during six summer cruises of R/V *Professor Vodyanitsky* in the central sector of the northern sea area in 2016–2021 were used in the research. Temperature, salinity and current velocity profiles were measured by the CTD/LADCP probes. The vertical turbulent diffusion coefficient was calculated with the G03 parameterization. The applied relations are given. The values of the required parameters on the isopycnal surface with the conditional density value  $15 \text{ kg/m}^3$  are used as the initial data. Their filtered dependencies on its depth are substituted into the calculated relations. It is found that a well-pronounced maximum of specific kinetic energy is observed on average when the isopycnal depth is 77 m. The values of the shear/strain ratio and the canonical internal wave spectrum are close. The average value of the measured shear constitutes about one third of the value of the canonical internal wave spectrum. The average value of the vertical turbulent diffusion coefficient is  $10^{-6} \text{ m}^2/\text{s}$ . Its value in the central sea area is comparable to the heat molecular diffusion coefficient. At the isopycnal depth 90 m the maximum value reaching  $1.6 \cdot 10^{-6} \text{ m}^2/\text{s}$ , is shifted to the right relatively the Rim Current at a horizontal distance of about 26 km. The average value of the turbulent kinetic energy dissipation rate is  $2 \cdot 10^{-9} \text{ W/kg}$ .

**Conclusions.** The value of the vertical turbulent diffusion coefficient calculated based on the data collected with a depth resolution of about 10 m agrees well with the estimates obtained from the data of microstructure probes. However, the results of the study should be considered preliminary; in order to obtain a more convincing confirmation of their correctness, it is advisable to conduct synchronous measurements using the microstructure probes and standard hydrological instruments.

**Keywords:** Black Sea, main pycnocline, vertical turbulent mixing, Rim Current, current velocity shear, strain

**Acknowledgements:** The study was carried out as part of the state assignment theme FSBSI FRC MHI FNNN-2024-0012, titled “Operational Oceanology”.

**For citation:** Morozov, A.N., 2025. Vertical Mixing in the Main Pycnocline of the Black Sea in Summer. *Physical Oceanography*, 32(3), pp. 271-282.

© 2025, A. N. Morozov

© 2025, Physical Oceanography

### Introduction

In a stratified marine environment, vertical turbulent mixing is the primary mechanism of diapycnal exchange of heat, salt, and other substances [1]. It plays a crucial role in water mass transformation, maintaining stratification and modulating large-scale circulation [2]. Currently, numerical modeling is one of the most important tools for studying the marine environment. However, the vertical resolution of modern models is insufficient to directly account for vertical mixing



directly and requires parameterization [3]. The need for a deeper understanding of the impact of vertical mixing on biogeochemical processes, and for improving its parameterization in numerical models, highlights the importance of *in situ* studies.

For the experimental assessment of vertical mixing parameters, measurements with centimeter-scale vertical resolution are required [4]. However, the current use of microstructure profilers, which can achieve this level of resolution, is limited due to the high cost of the equipment and the significant time investment required for the measurements [5]. Microstructure measurements have only been conducted three times in the deep-water part of the Black Sea [1, 6, 7]. Measurements taken in March 2003 in the center of the western gyre [6] revealed that, in the oxycline, the values of the vertical turbulent diffusion coefficient ( $K_v$ ) were as low as  $(1-4) \cdot 10^{-6} \text{ m}^2/\text{s}$ . A single profile obtained in July 2005 in the northeastern part of the sea [1] showed  $K_v$  value of approximately  $4 \cdot 10^{-6} \text{ m}^2/\text{s}$  in the main pycnocline. Measurements conducted in August 2022 in the northern part of the central sector of the sea showed a minimum  $K_v$  value in the main pycnocline [7]. Unfortunately, the presentation format of the results does not allow for precise determination.

An alternative approach to estimating vertical mixing parameters uses density and current velocity profiles with a vertical resolution of about 10 meters. Such data are abundant for the Black Sea. In particular, these include measurements from the *Aqualog* probe [8], which was deployed at a depth of approximately 300 meters near Gelendzhik. The temporal variability of  $K_v$  vertical structure was studied using these data by applying a parameterization based on Richardson number values [9, 10]. Additionally, velocity profiles obtained using a lowered acoustic Doppler current profiler (LADCP) from a drifting vessel enabled the mean vertical structure  $K_v$  to be derived in the Sevastopol anticyclone region [11] and the northern part of the sea [12].

In this study, we analyze data collected during summer expeditions of the Marine Hydrophysical Institute [13] to examine the horizontal distribution of vertical turbulent mixing parameters within the main pycnocline. This issue remains unexplored to date, although there is a need to address it, particularly to improve our understanding of how large-scale dynamics affect vertical mixing processes. The G03 parameterization [14] was applied to estimate the vertical turbulent mixing parameters. This approach originated from theoretical work [15], followed by the practical application of its results [16, 17]. It was further developed in [18] and presented in its final form in [19]. The widespread use of the G03 parameterization today stems from its strong agreement with estimates derived from microstructure measurements [4, 5, 20, 21, 22].

This study aims to assess the parameters of vertical turbulent mixing in the main pycnocline of the Black Sea using current velocity and density data obtained from standard hydrological instruments.

### **Instruments and data**

This study utilizes temperature, salinity, and current velocity profiles obtained during six summer research cruises of R/V *Professor Vodyanitsky* in the northern Black Sea (31.5–36.5°E, 43.5–45.0°N), between: 1–18 July 2016; 14 June – 3 July 2017; 9–30 June 2018; 12 July – 3 August 2019; 5–24 June 2020 and

29 June – 7 July 2021. The area covered by the sampling stations was non-uniform and varied from expedition to expedition (Fig. 1). The average inter-station distance was  $\sim 20$  km. Temperature and salinity profiles were collected using a SBE911+ probe until 2019 and an Idronaut Ocean Seven 320 PlusM probe from 2019 onwards. Current velocity profiles were acquired using a lowered acoustic Doppler current profiler (LADCP) based on the WHM300 model. Setup parameters of the instrument were as follows: depth segment size – 4 m; broadband operating mode; descent/ascent speed:  $\sim 0.5$  m/s.

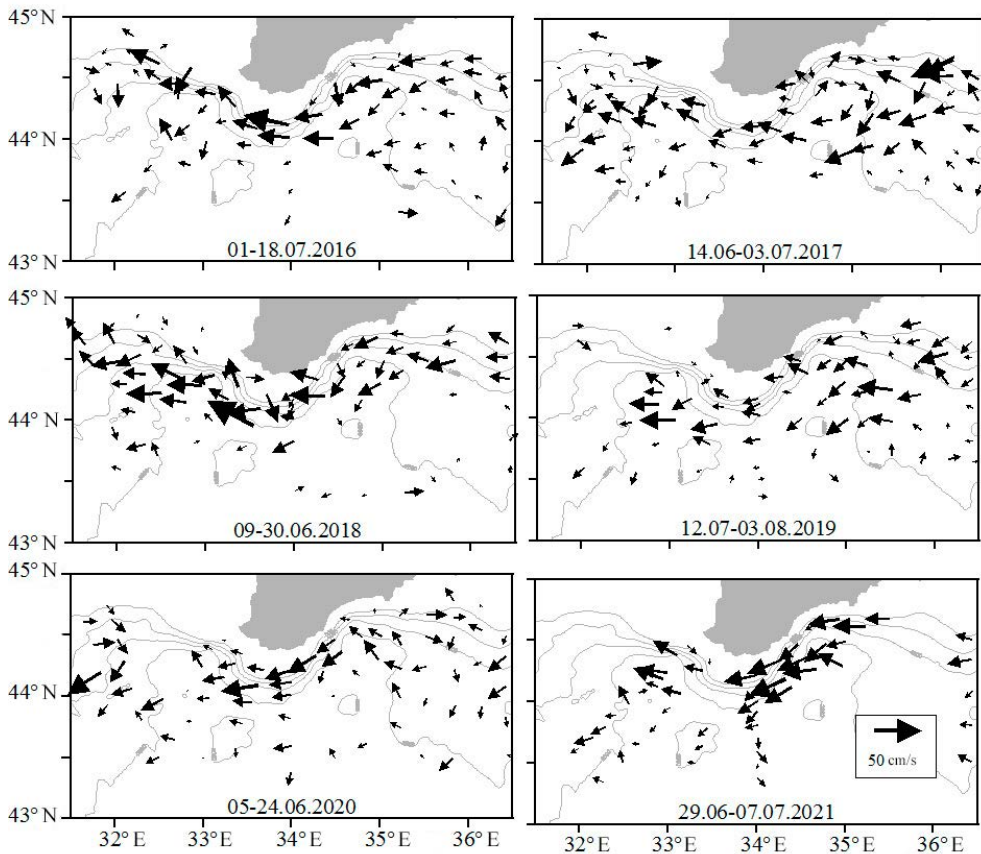


**Fig. 1.** Current velocity measured at the 20 m depth during six summer cruises of R/V *Professor Vodyanitsky*. The arrow beginning corresponds to the station position (353 stations in total)

Large-scale cyclonic circulation is manifested by a predominance of westward currents (Fig. 1), with maximum values observed over the continental slope near the Southern Coast of Crimea. The Black Sea Rim Current (RC) is not clearly expressed, which can be explained by two factors. Firstly, it usually weakens during the summer months. Secondly, its jet width is approximately 30 km. With a spacing of approximately 20 km between sampling stations, it may not always be evident in the measurements. Mesoscale eddies were detected in two of the six expeditions. During the 2017 expedition, the Crimean anticyclone, centered at  $34.78^{\circ}\text{E}$ ,  $44.35^{\circ}\text{N}$  with a diameter of approximately 60 km, was observed. During the 2020 expedition,

a fragment of the Sevastopol anticyclone, centered at 31.6°E, 44.34°N with a similar diameter, was identified.

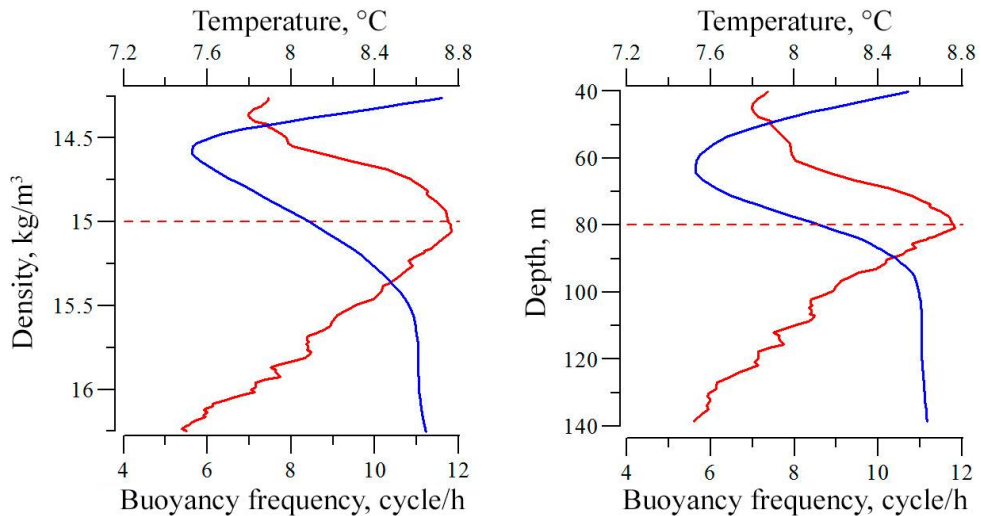


**Fig. 2.** Along-isopycnal averaged dependencies of water temperature (blue lines) and buoyancy frequency (red lines) upon density (*left*) and depth (*right*) during the cruise in 2017

Due to the cyclonic nature of a large-scale circulation in the Black Sea, its isopycnal surfaces are dome-shaped. Their depth increases from the center of the sea towards the continental slope. The depth difference between the center of the sea and the continental slope can reach 70 m or more. Therefore, to correctly understand the characteristic features of the mean vertical distribution of hydrological parameters and other environmental factors in the marine environment, isopycnal averaging should be performed. In the present study, special attention is given to determining the parameters of vertical turbulent mixing at a specific isopycnal surface. To select the conditional density value ( $\sigma_t$ ), isopycnal averaging of buoyancy frequency profiles was performed for a set of stations from each expedition. The isopycnal relationships between buoyancy frequency and density averaged over the 2017 expedition (Fig. 2, left) reveal a pronounced maximum at  $\sigma_t = 15 \text{ kg/m}^3$ . Data from other expeditions confirm the presence of this maximum [13]. The isopycna with a conditional density value of  $15 \text{ kg/m}^3$  was selected for assessing diapycnal mixing parameters. One might intuitively expect enhanced density stratification at this isopycnal surface to lead to weakened vertical turbulent mixing. The isopycnal averaged temperature profiles shown in Fig. 2 demonstrate the relative position of the Cold Intermediate Layer, the best-known feature of the Black Sea's vertical thermal structure [13].

### Results and discussion

The values of hydrological parameters on the  $\sigma_t = 15 \text{ kg/m}^3$  isopycnal surface were calculated for all 353 stations using linear interpolation. Low-frequency filtering of the raw data was performed using a cosine filter with a window width of

30 meters. The horizontal-to-vertical gradient ratio for the  $\sigma_t = 15 \text{ kg/m}^3$  isopycnal surface depth was approximately 2 km per 1 m [23]. The following discussion focuses on the dependence of parameters on the isopycnal surface  $\sigma_t = 15 \text{ kg/m}^3$  upon its depth ( $z_{15}$ ).

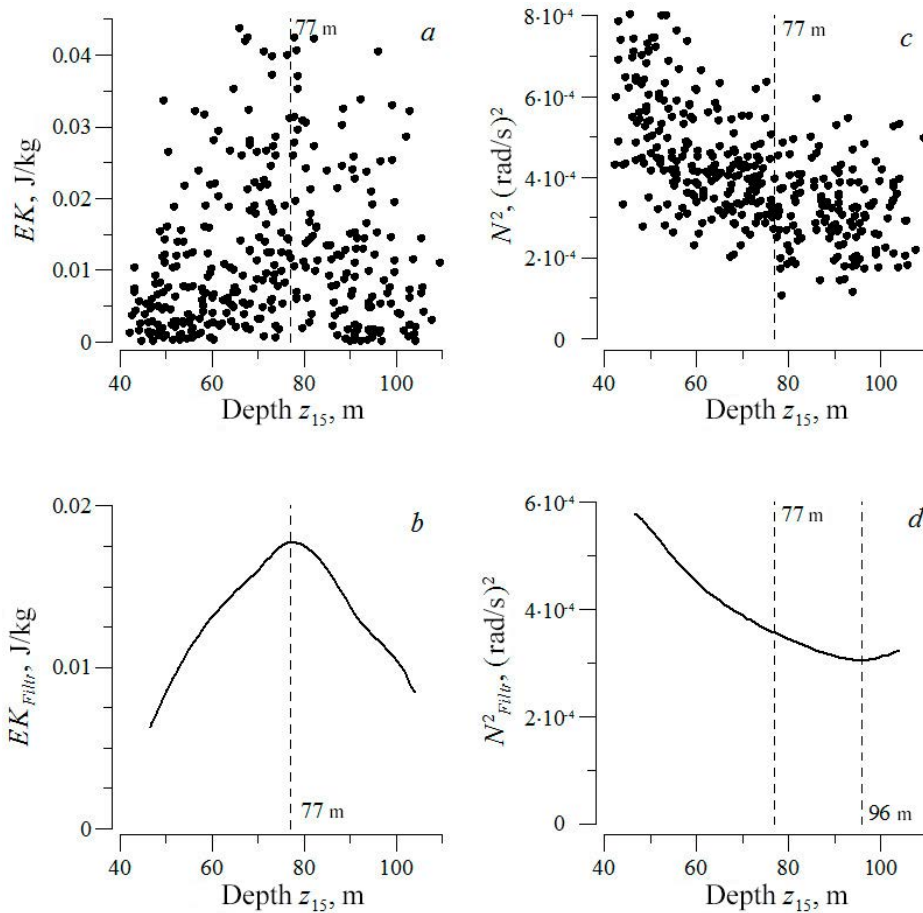


**Fig. 3.** Dependencies of kinetic energy and square of buoyancy frequency (*a, c* – initial data; *b, d* – after filtration) on isopycnal surface  $\sigma_t = 15 \text{ kg/m}^3$  upon depth

Fig. 3, a shows the relationship between the measured values of specific kinetic energy ( $EK$ ) and the depth of the isopycnal surface with a conditional density of  $\sigma = 15 \text{ kg/m}^3$ . The considerable scatter in the raw data (Fig. 3, *a*) may be partially attributed to the temporal variability of the current velocity field since the measurements were conducted in different years, as well as to internal waves with frequencies close to the local inertial frequency since each expedition lasted at least 30 inertial periods. Following filtering (Fig. 3, *b*), the dependence  $EK_{Filtr}(z_{15})$  reveals a well-defined maximum at  $z_{15} = 77$  m, with a current velocity magnitude of 19 cm/s at this maximum. This velocity maximum is associated with the Black Sea Rim Current (RC); its center is typically observed at  $z_{15} = 77$  m (dashed line with 77 m marker in Figs. 3–6).

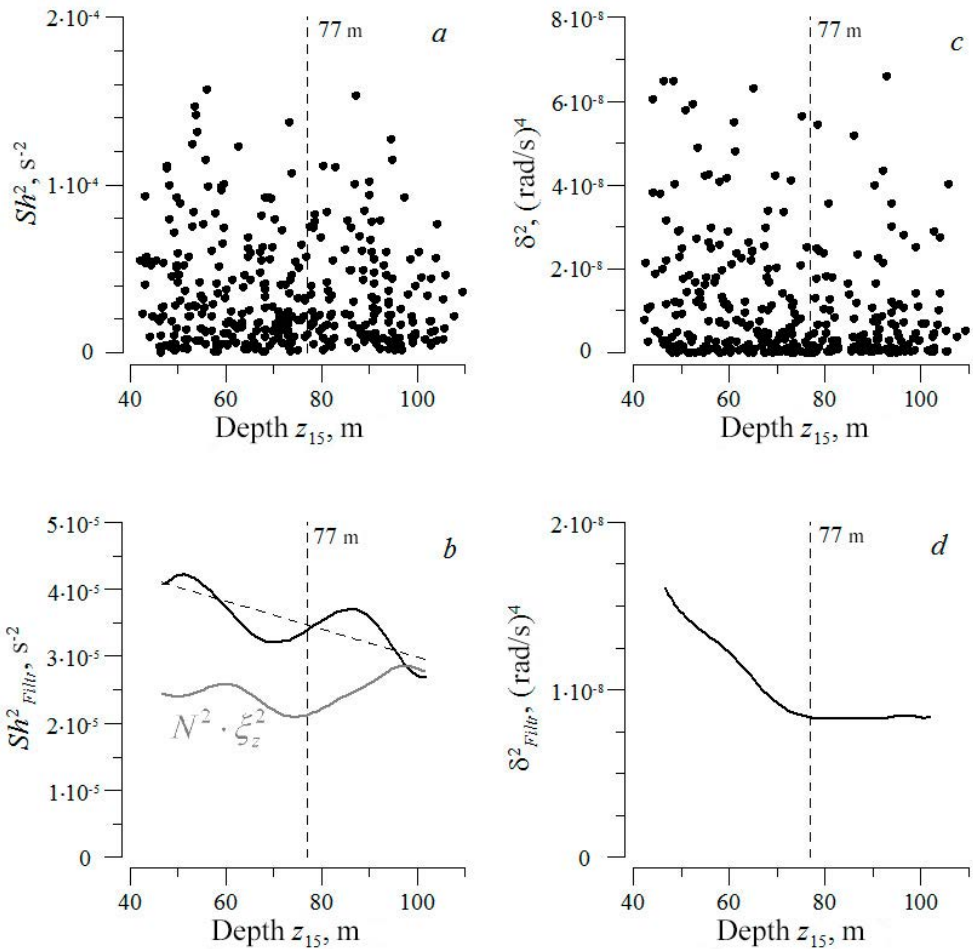


**Fig. 4.** Dependencies of shear square and buoyancy frequency anomaly square (*a, c* – initial data; *b, d* – after filtration) on isopycnal surface  $\sigma_t = 15 \text{ kg/m}^3$  upon depth. The grey line on fragment *b* is the ratio of square of buoyancy frequency anomaly to its square

Fig. 3, *c* shows the dependence of the measured square of buoyancy frequency values ( $N^2 = \frac{g}{\rho} \rho_z$ , where  $g$  is the gravitational acceleration;  $\rho$  is the density and  $\rho_z$  is its depth derivative) on depth  $z_{15}$ . The same filtered dependence is presented in Fig. 3, *d*. The buoyancy frequency decreases nearly monotonically from  $\sim 14$  cycles/hour in the center of the sea to  $\sim 10$  cycles/hour near the continental slope. A weakly pronounced minimum is observed at  $z_{15} = 96 \text{ m}$ .

The dependence of the measured squared velocity shear ( $Sh^2 = U_z^2 + V_z^2$ , where  $U_z$  and  $V_z$  are the depth derivatives of the eastward and northward current velocity components, respectively) on depth  $z_{15}$  (Fig. 4, *a*) exhibits the characteristics of a random process. This is understandable, given that velocity shear is primarily determined by internal waves, whose spatiotemporal scales are

significantly smaller than the dimensions of the survey area and the measurement intervals. After filtering (Fig. 4, *b*), the dependence shows decreasing shear values from the center of the sea towards the continental slope. The nearly harmonic component of the dependence, with a horizontal wavelength of approximately 70 km (35 m by depth  $z_{15}$ ), may result from specific data sampling. Alternatively, this harmonic component may be generated by dynamic processes induced by the RC in its transverse direction. Further discussion of this issue based on the available data would be speculative.

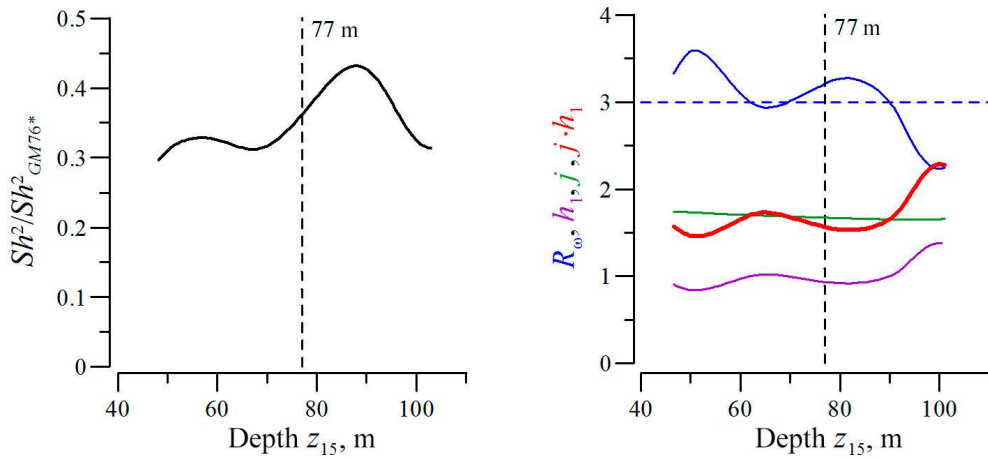


**Fig. 5.** Dependency of the ratio of measured shear square to *GM76\** shear square on isopycnal surface  $\sigma_t = 15 \text{ kg/m}^3$  upon its depth (left), and dependencies of *G03* parameterization multipliers on isopycnal surface  $\sigma_t = 15 \text{ kg/m}^3$  upon its depth (right)

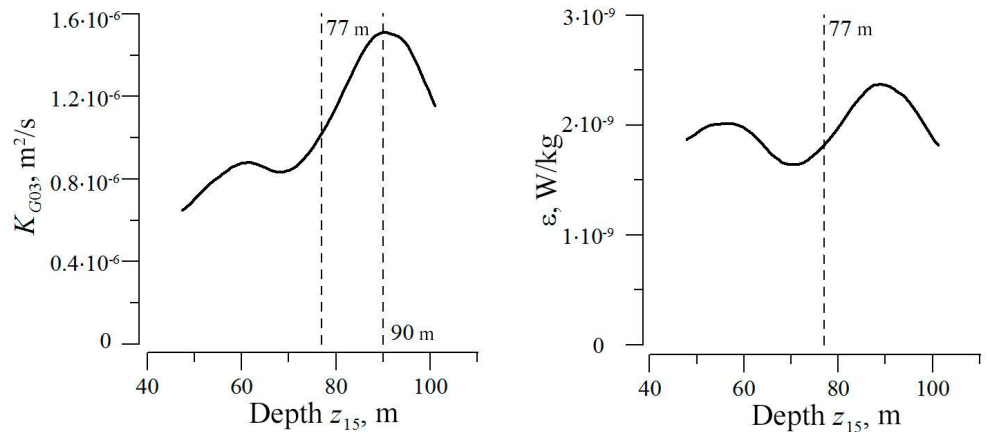


**Fig. 6.** Dependencies of vertical turbulent diffusion coefficient (left) and dissipation rate of turbulent kinetic energy (right) on isopycnal surface  $\sigma_t = 15 \text{ kg/m}^3$  upon its depth

The square of deformation is determined from the relationship given in [18]:

$$\xi_z^2 = \frac{(N^2 - N_{Pol}^2)^2}{N_{Pol}^4} = \frac{\delta^2}{N_{Pol}^4},$$

where  $N_{Pol}^2$  is the third-degree polynomial approximation of dependence  $N^2(z_{15})$ , calculated separately for station groups from each expedition, and a combined dataset was formed for all expeditions;  $\delta^2 = (N^2 - N_{Pol}^2)^2$  is the squared buoyancy frequency anomalies (Fig. 4, c). Similar to velocity shear, the  $\delta^2(z_{15})$  dependence exhibits characteristics of a random process. After filtering, the  $\delta_{Filtr}^2(z_{15})$  dependence shows decreasing values from the center of the sea to the RC core, with nearly constant values between the RC and continental slope. The product  $N^2 \xi_z^2 = \delta_{Filtr}^2 / N_{Filtr}^2$  characterizes the potential energy of small-scale processes and, like velocity shear, contains a harmonic component with a wavelength of about 70 km (Fig. 4, b, grey line).

The empirical formulas from the work [19] are given below:

$$K_{G03} = K_0 \cdot \left( \frac{Sh_{Filtr}^2}{Sh_{GM76*}^2} \right)^2 \cdot h_1(R_\omega) \cdot j \left( \frac{f}{N_{Filtr}} \right),$$

$$h_1(R_\omega) = \frac{3(R_\omega + 1)}{2\sqrt{2}R_\omega\sqrt{R_\omega - 1}},$$

$$j(f/N_{Filtr}) = \frac{f \operatorname{arctanh}(N_{Fit}/f)}{f_{30} \operatorname{arctanh}(N_0/f_{30})},$$

where  $K_0 = 5 \cdot 10^6 \text{ m}^2/\text{s}$ ;  $f$  is the local inertial frequency at 44°N;  $f_{30}$  is the inertial frequency at 30°N;  $N_0 = 5.24 \cdot 10^{-3} \text{ rad/s}$ ;  $Sh_{GM6}^2$  value was calculated for the canonical GM76 internal wave spectrum, taking into account the vertical resolution of LADCP current velocity measurements, as described in [24]:

$$Sh_{GM76*}^2 = \int_0^{100} \Phi_{Sh\_GM76}(k) \cdot H_{ADCP}(k) \cdot H_{Dif\_ADCP}(k) \cdot H_{DP\_ADCP}(k) \cdot dk,$$

where  $\Phi_{Sh\_GM76}(k)$  is the velocity shear spectrum for the GM76 spectrum in the vertical wavenumber space ( $k$ );  $H_{ADCP}(k) = (\sin(\pi 4k)/(\pi 4k))^4$  is the spatial averaging transfer function characteristic of ADCP measurements;  $H_{Dif\_ADCP}(k) = (\sin(\pi 4k)/(\pi 4k))^2$  is the differentiation transfer function for a depth increment of 4 m;  $H_{DP\_ADCP}(k) = (\sin(\pi 4k)/(\pi 4k))^4$  is the window-type filtering transfer function used during data processing. The shear-to-strain ratio  $R_\omega = \frac{Sh^2}{N^2 \cdot \xi_z^2}$  is interpreted as the ratio of the kinetic to the potential energy of internal waves and equals 3 for the GM76 spectrum. This value was calculated by accounting for the differences in the depth-averaging transfer functions when processing density and current velocity data, according to the following relationship:

$$R_\omega \approx \frac{Sh_{GM76}^2}{N_{Filtr}^2 \cdot \xi_{zGM76}^2} \cdot \frac{Sh_{Filtr}^2 / Sh_{GM76*}^2}{\xi_z^2 / \xi_{zGM76*}^2} = 3 \cdot \frac{Sh_{Filtr}^2 \cdot N_{Filtr}^2}{\delta_{Filtr}^2} \cdot \frac{N_{Filtr}^2 \cdot \xi_{zGM76*}^2}{Sh_{GM76*}^2},$$

where  $\xi_{z_{GM76}^*}^2 = \int_0^{100} \Phi_{\xi_{z_{GM76}^*}}(k) \cdot H_{Dif\_CTD}(k) \cdot H_{DP\_CTD}(k) \cdot dk$ ;  $\Phi_{\xi_{z_{GM76}^*}}(k)$  is the deformation spectrum of GM76;  $H_{Dif\_CTD}(k) = (\text{Sin}(\pi 4k)/(\pi 4k))^2$  is the differentiation transfer function at a depth increment of 4 m;  $H_{DP\_CTD}(k) = (\text{Sin}(\pi 1k)/(\pi 1k))^4$  is the transfer function of CTD data processing. After appropriate integration, we obtain the ratio used in the calculations:  $R_\omega \approx 2.1 \cdot \frac{Sh_{Filtr}^2 \cdot N_{Filtr}^2}{\delta_{Filtr}^2}$ .

The average ratio of the square of the measured velocity shear to  $Sh_{GM76}^2$  shear (Fig. 5, left) is 0.35, showing no distinct features in the RC region (the maximum is located 20 km to the right of this region). This mean value appears realistic, given that wind serves as the sole source of internal waves in the non-tidal Black Sea and the study specifically examines summer conditions. The dependence  $R_\omega(z_{15})$  (the blue line in Fig. 5, right) closely matches the values of the canonical internal wave spectrum (the blue dashed line in Fig. 5, right). Near the continental slope, the shear-to-strain ratio decreases to 2.2. The coefficient  $h_1$ , which is a function of the shear-to-strain ratio, shows a sharp increase as it approaches the continental slope. The latitude- and buoyancy-frequency-dependent coefficient  $j$  exhibits a slight decrease from the center of the sea towards its periphery (the green line in Fig. 5, right).

The parameter  $K_{G03}(z_{15})$  varies from  $6.5 \cdot 10^{-7}$  m<sup>2</sup>/s at  $z_{15} = 50$  m to a maximum of  $1.5 \cdot 10^{-3}$  m<sup>2</sup>/s at  $z_{15} = 90$  m (Fig. 6, left). In the central part of the sea, the values of the vertical turbulent diffusion coefficient are comparable to the molecular heat diffusion coefficient ( $1.4 \cdot 10^{-7}$  m<sup>2</sup>/s). The maximum value is offset 26 km horizontally (23 m vertically) to the right of the Black Sea Rim Current (RC) and is presumably associated with anticyclonic eddies, which exhibit intensified vertical mixing in their cores. The relatively low values obtained for the vertical turbulent mixing coefficients (on average  $10^{-6}$  m<sup>2</sup>/s) may be questionable, yet they show good agreement with microstructure profiler data [1, 6]. A more accurate comparison of vertical mixing parameters between fine-scale and microstructure measurements requires additional synchronous observations. The turbulent kinetic energy dissipation rate, calculated from the Osborn relation  $\varepsilon = K_{G03} \cdot N_{Filtr}^2 / 0.2$ , averages  $2 \cdot 10^{-9}$  W/kg and contains a harmonic component with a wavelength of approximately 70 km (Fig. 6, right). The obtained  $\varepsilon$  value is typical for many regions of the World Ocean.

## Conclusion

This study utilized density and current velocity profiles obtained during six summer research cruises of R/V *Professor Vodyanitsky* in the northern Black Sea between 2016 and 2021. Vertical turbulent mixing parameters were determined using the G03 parameterization. The filtered dependencies of the required parameters on the isopycnal surface with a conditional density value of 15 kg/m<sup>3</sup> were used as input data for the depth. The resolution capabilities of the density and

current velocity sensors were considered during the integration of the canonical internal wave spectrum.

The presence of a buoyancy frequency maximum was confirmed on the isopycnal surface, which had a conditional density value of  $15 \text{ kg/m}^3$ . Analysis revealed a well-defined maximum in specific kinetic energy occurring at the mean depth of this isopycnal surface (77 m).

It was found that the values of the squares of the current velocity shear and buoyancy frequency anomaly values on the specified isopycnal surface decreased from the center of the sea to the continental slope. The shear and deformation dependencies reveal a distinct harmonic component with a horizontal wavelength of approximately 70 km, oriented perpendicular to the RC. The square of the measured shear is approximately one third of that of the internal wave canonical spectrum. The shear-to-strain ratio in the center of the sea is approximately equal to the ratio of the canonical spectrum of internal waves, decreasing to 2.3 near the continental slope.

The mean value of the vertical diffusion coefficient on the isopycnal surface at  $\sigma_t = 15 \text{ kg/m}^3$  during the summer period is  $10^{-6} \text{ m}^2/\text{s}$ , which shows good agreement with estimates from a microstructure profiler. In the central part of the sea, the coefficient values are comparable to those of molecular thermal diffusivity. The maximum coefficient value is observed at a depth of 90 m on the isopycnal surface and reaches  $1.6 \cdot 10^{-6}$ . This maximum is offset approximately 26 km to the right of the RC, corresponding roughly to the radius of a mesoscale anticyclonic eddy. The mean turbulent kinetic energy dissipation rate is  $2 \cdot 10^{-9} \text{ W/kg}$ .

#### REFERENCES

1. Zatsepin, A.G., Golenko, N.N., Korzh, A.O., Kremenetskii, V.V., Paka, V.T., Poyarkov, S.G. and Stunzhas, P.A., 2007. Influence of the Dynamics of Currents on the Hydrophysical Structure of the Waters and the Vertical Exchange in the Active Layer of the Black Sea. *Oceanology*, 47(3), pp. 301–312. <https://doi.org/10.1134/S0001437007030022>
2. Munk, W.H., 1966. Abyssal Recipes. *Deep Sea Research and Oceanographic Abstracts*, 13(4), pp. 707-730. [https://doi.org/10.1016/0011-7471\(66\)90602-4](https://doi.org/10.1016/0011-7471(66)90602-4)
3. Nan, F., Xue, H., Yu, F., Ren, Q. and Wang, J., 2022. Diapycnal Mixing Variations Induced by Subthermocline Eddies Observed in the North Pacific Western Boundary Region. *Frontiers in Marine Science*, 9, 997599. <https://doi.org/10.3389/fmars.2022.997599>
4. Takahashi, A. and Hibiya, T., 2019. Assessment of Finescale Parametrizations of Deep Ocean Mixing in the Presence of Geostrophic Current Shear: Results of Microstructure Measurements in the Antarctic Circumpolar Current Region. *Journal of Geophysical Research: Oceans*, 124(1), pp. 135-153. <https://doi.org/10.1029/2018JC014030>
5. Gregg, M.C. and Yakushev, E., 2005. Surface Ventilation of the Black Sea's Cold Intermediate Layer in the Middle of the Western Gyre. *Geophysical Research Letters*, 32(3), L021580. <https://doi.org/10.1029/2004GL021580>
6. Samodurov, A.S., Chukharev, A.M., Kazakov, D.A., Pavlov, M.I. and Korzhuev, V.A., 2023. Vertical Turbulent Exchange in the Black Sea: Experimental Studies and Modeling. *Physical Oceanography*, 30(6), pp. 689-713.
7. Zatsepin, A.G., Ostrovskii, A.G., Kremenetskiy, V.V., Nizov, S.S., Piotukh, V.B., Soloviev, V.A., Shvov, D.A., Tsubul'sky, A.L., Kuklev, S.B. [et al.], 2014. Subsatellite Polygon for Studying

- Hydrophysical Processes in the Black Sea Shelf-Slope Zone. *Izvestiya, Atmospheric and Oceanic Physics*, 50(1), pp. 13-25. <https://doi.org/10.1134/S0001433813060157>
8. Podymov, O.I., Zatsepin, A.G. and Ostrovsky, A.G., 2017. Vertical Turbulent Exchange in the Black Sea Pycnocline and Its Relation to Water Dynamics. *Oceanology*, 57(4), pp. 492-504. <https://doi.org/10.1134/S0001437017040142>
  9. Podymov, O.I., Zatsepin, A.G. and Ostrovskii, A.G., 2023. Fine Structure of Vertical Density Distribution in the Black Sea and Its Relationship with Vertical Turbulent Exchange. *Journal of Marine Science and Engineering*, 11(1), 170. <https://doi.org/10.3390/jmse11010170>
  10. Morozov, A.N. and Lemeshko, E.M., 2014. Estimation of Vertical Turbulent Diffusion Coefficient by CTD/LADCP-measurements in the Northwestern Part of the Black Sea in May, 2004. *Morskoy Gidrofizicheskiy Zhurnal*, (1), pp. 58-67 (in Russian).
  11. Ivanov, V.A. and Morozov, A.N., 2018. Vertical Mixing in the Active Layer of the Black Sea. *Doklady Earth Sciences*, 482(2), pp. 1328-1330. <https://doi.org/10.1134/S1028334X18100069>
  12. Morozov, A.N. and Mankovskaya, E.V., 2020. Cold Intermediate Layer of the Black Sea According to the Data of Field Research in 2016-2019. *Ecological Safety of Coastal and Shelf Zones of Sea*, (2), pp. 5-16. <https://doi.org/10.22449/2413-5577-2020-2-5-16> (in Russian).
  13. Gregg, M.C., Sanford, T.B. and Winkel, D.P., 2003. Reduced Mixing from the Breaking of Internal Waves in Equatorial Waters. *Nature*, 422(6931), pp. 513-515. <https://doi.org/10.1038/nature01507>
  14. Henyey, F.S., Wright, J. and Flatté, S.M., 1986. Energy and Action Flow through the Internal Wave Field: An Eikonal Approach. *Journal of Geophysical Research: Oceans*, 91(C7), pp. 8487-8495. <https://doi.org/10.1029/JC091iC07p08487>
  15. Gregg, M.C., 1989. Scaling Turbulent Dissipation in the Thermocline. *Journal of Geophysical Research: Oceans*, 94(C7), pp. 9686-9698. <https://doi.org/10.1029/JC094iC07p09686>
  16. Wijesekera, H., Padman, L., Dillon, T., Levine, M., Paulson, C. and Pinkel, R., 1993. The Application of Internal-Wave Dissipation Models to a Region of Strong Mixing. *Journal of Physical Oceanography*, 23(2), pp. 269-286. [https://doi.org/10.1175/1520-0485\(1993\)023<0269:TAOIWD>2.0.CO;2](https://doi.org/10.1175/1520-0485(1993)023<0269:TAOIWD>2.0.CO;2)
  17. Polzin, K.L., Toole, J.M. and Schmitt, R.W., 1995. Finescale Parameterizations of Turbulent Dissipation. *Journal of Physical Oceanography*, 25(3), pp. 306-328. [https://doi.org/10.1175/1520-0485\(1995\)025<0306:FPOTD>2.0.CO;2](https://doi.org/10.1175/1520-0485(1995)025<0306:FPOTD>2.0.CO;2)
  18. Kunze, E., Firing, E., Hummon, J.M., Chereskin, T.K. and Thurnherr, A.M., 2006. Global Abyssal Mixing Inferred from Lowered ADCP Shear and CTD Strain Profiles. *Journal of Physical Oceanography*, 36(8), pp. 1553-1576. <https://doi.org/10.1175/JPO2926.1>
  19. Ferron, B., Kokoszka, F., Mercier, H. and Lherminier, P., 2014. Dissipation Rate Estimates from Microstructure and Finescale Internal Wave Observations along the A25 Greenland–Portugal OVIDE Line. *Journal of Atmospheric and Oceanic Technology*, 31(11), pp. 2530-2543. <https://doi.org/10.1175/JTECH-D-14-00036.1>
  20. Fine, E.C., Alford, M.H., MacKinnon, J.A. and Mickett, J.B., 2021. Microstructure Mixing Observations and Finescale Parameterizations in the Beaufort Sea. *Journal of Physical Oceanography*, 51(1), pp. 19-35. <https://doi.org/10.1175/JPO-D-19-0233.1>
  21. Baumann, T.M., Fer, I., Schulz, K. and Mohrholz, V., 2023. Validating Finescale Parameterizations for the Eastern Arctic Ocean Internal Wave Field. *Journal of Geophysical Research: Oceans*, 128(11), e2022JC018668. <https://doi.org/10.1029/2022JC018668>
  22. Sasaki, Y., Yasuda, I., Katsumata, K., Kouketsu, S. and Uchida, H., 2024. Turbulence across the Antarctic Circumpolar Current in the Indian Southern Ocean: Micro-Temperature Measurements and Finescale Parameterizations. *Journal of Geophysical Research: Oceans*, 129(2), e2023JC019847. <https://doi.org/10.1029/2023JC019847>

23. Morozov, A.N. and Mankovskaya, E.V., 2021. Spatial Characteristics of the Black Sea Cold Intermediate Layer in Summer, 2017. *Physical Oceanography*, 28(4), pp. 404-413. <https://doi.org/10.22449/1573-160X-2021-4-404-413>
24. Morozov, A.N. and Mankovskaya, E.V., 2022. Vertical Mixing in the Black Sea Active Layer from Small-Scale Measurement Data. *Ecological Safety of Coastal and Shelf Zones of Sea*, (4), pp. 25-38. <https://doi.org/10.22449/2413-5577-2022-4-25-38>

Submitted 14.10.2024; approved after review 29.10.2024;  
accepted for publication 13.03.2025.

*About the author:*

**Alexey N. Morozov**, Senior Research Associate, Marine Hydrophysical Institute of RAS (2 Kapitanskaya Str., Sevastopol, 299011, Russian Federation), CSc. (Tech.), **ORCID ID: 0000-0001-9022-3379**, **Scopus Author ID: 7202104940**, **ResearcherID: ABB-4365-2020**, [anmorozov@mhi-ras.ru](mailto:anmorozov@mhi-ras.ru)

*The author has read and approved the final manuscript.*

*The author declares that he has no conflict of interest.*

Original article

## Trends in Acceleration of Climate Changes in the Thermohaline Structure of the Black Sea Upper Layer

G. K. Korotaev, V. N. Belokopytov, V. L. Dorofeev , A. I. Mizyuk, O. S. Puzina, A. L. Kholod

*Marine Hydrophysical Institute of RAS, Sevastopol, Russian Federation*

 *dorofeyev\_viktor@mail.ru*

### Abstract

**Purpose.** The purpose of the study is to assess the trends in a change of the Black Sea thermohaline structure on the interannual time scales in 2000–2020 based on three reanalyses performed using different methods, as well as direct observations.

**Methods and Results.** Four datasets are applied to perform the research. The first one is an array of temperature and salinity profiles on a regular grid with a 10-day time resolution and a  $10' \times 15'$  spatial resolution for 2000–2021, which is based on the data of 13952 oceanographic stations. The second set is formed according to the results of reanalysis carried out using the MHI Black Sea circulation model. The ERA-5 atmospheric reanalysis results are used as an atmospheric forcing. The satellite data on sea surface temperature and altimetry are assimilated in the model. The third dataset represents the reanalysis results obtained based on the NEMO model regional configuration. The atmospheric forcing is also preset using the ERA-5 reanalysis results. The following data are engaged in assimilation: the arrays of temperature and salinity profiles, and the satellite altimetry and sea surface temperature measurements. The BLKSEA\_MULTYEAR\_PHY\_007\_004 product of the Copernicus Marine Service containing the reanalysis of daily average fields for the Black Sea basin from 01.01.1993 to 30.06.2021 constitutes the fourth set. The described four data sets have made it possible to analyze the trends in temperature and salinity changes in the upper layer of the Black Sea.

**Conclusions.** It is shown that since 2005, an increase in the average sea surface temperature in the Black Sea area has resulted in a tendency towards disappearance of the cold intermediate layer in its traditional understanding as a subsurface layer with a water temperature  $\leq 8^\circ\text{C}$ . Besides, the accelerated sea water warming within the main pycnocline is observed. The sea haline regime in 2012–2015 is characterized by a transition from freshening to salinization of the sea surface layer that is related to a change in the external budget of fresh water, and a long-term increase in water salinity in the main pycnocline.

**Keywords:** retrospective analysis, Black Sea, seawater temperature, salinity, climatic changes, thermohaline structure

**Acknowledgments:** The observational data (array 1) and climate profiles were prepared within the framework of state assignment of FSBSI FRC MHI FNNN-2024-0014, the numerical models intended for simulations were prepared within the framework of state assignment of FSBSI FRC MHI FNNN-2024-0012, reanalysis calculations based on the MHI model (array 2) and the NEMO model (array 3) were prepared within the framework of state assignments of FSBSI FRC MHI FNNN-2023-0001) and the Ministry of Education and Science FMWE-2023-0002 of the Federal programs “Climate” and “Ecology”.

**For citation:** Korotaev, G.K., Belokopytov, V.N., Dorofeev, V.L., Mizyuk, A.I., Puzina, O.S. and Kholod, A.L., 2025. Trends in Acceleration of Climate Changes in the Thermohaline Structure of the Black Sea Upper Layer. *Physical Oceanography*, 32(3), pp. 283-296.

© 2025, G. K. Korotaev, V. N. Belokopytov, V. L. Dorofeev, A. I. Mizyuk, O. S. Puzina, A. L. Kholod

© 2025, Physical Oceanography



## Introduction

The Black Sea is a semi-enclosed body of water, completely surrounded by land and connected to the World Ocean via the Mediterranean and Marmara Seas, as well as a network of straits. The Black Sea basin has a positive water balance and a distinctive thermohaline structure with a sharp halocline and a cold intermediate layer (CIL). In addition, the Black Sea exhibits unique interannual and long-term variability in its thermohaline structure, differing significantly from other seas. In the main pycnocline layer, the influx of Mediterranean waters results in a gradual and continuous increase in temperature and salinity. In the upper layer of the sea, this trend changes to well-defined interdecadal fluctuations [1]. Various combinations of positive and negative anomalies in the heat and salt content of the top 100 meters of the Black Sea form a sequence of 10–20-year periods in its hydrological regime – cold and salty in the 1950s, warm and salty in the 1970s and 1980s, and so on. At the turn of 2010–2015, there was a transition from the freshened, warm period of the 2000s to the current state, which is characterized by higher temperatures and salinity [1–3].

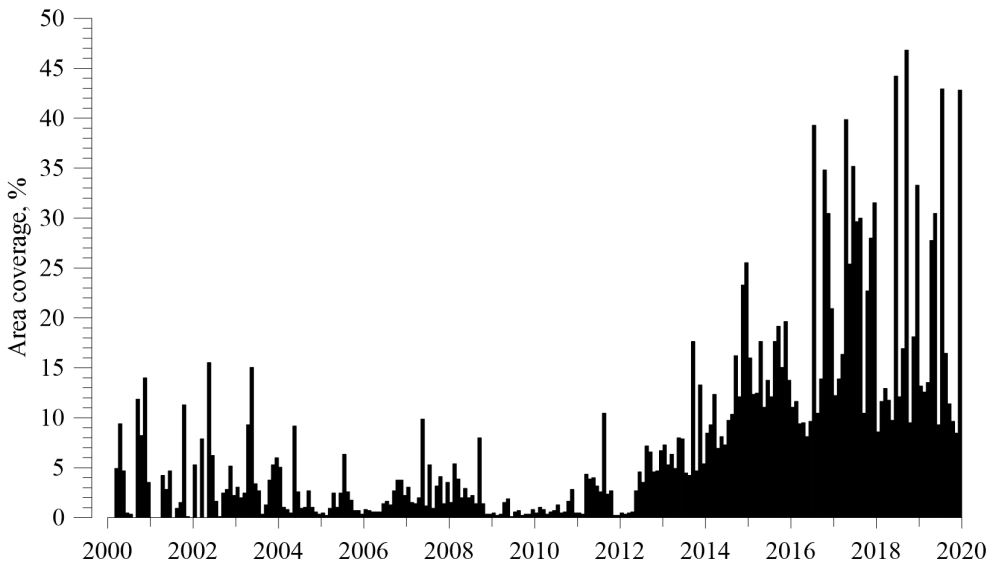


**Fig. 1.** Relative portion of coverage of the Black Sea deep part (%) with oceanographic observation data in 2000–2020

A more detailed study of the transition to modern climatic conditions is complicated by the sharp reduction in the Black Sea instrumental measurements between 1996 and 2013 (Fig. 1). The coverage of its deep-water region fell from 70–100% in the 1980s to 0–10%, and only increased to 20–40% from 2014 due to the resumption of oceanographic surveys in the Russian Federation economic zone and the operation of profiling floats. The existing gap in observational data can only be filled using reanalysis arrays created based on numerical thermohydrodynamic models. Work [4] presents the results of an assessment of trends in the state of

the marine environment on interannual timescales between 2000 and 2020, based on three reanalyses performed using different methods, as well as direct observations during periods when the Black Sea area was covered fairly uniformly. Comparing the results of calculations performed using different methods made it possible to determine general climatic trends and identify how they differ in reconstructing natural processes during certain periods. This work demonstrates, in particular, that the previously observed trend of sea water warming, which led to the episodic disappearance of the CIL within its traditional boundaries, with a water temperature in the core below 8 °C, accelerated significantly after 2012. Consequently, CIL renewal ceased completely in winter by 2020.

This work is purposed at providing a detailed analysis of thermal changes in the upper layer of the Black Sea in 2000–2020 and discussing trends in seawater salinity.

### **Methods for assessing trends in changes of the Black Sea thermohaline characteristics**

In this study, trend assessments of changes in the Black Sea thermohaline characteristics were conducted, as in [4], according to direct observations and the results of three reanalyses based on different methods.

Direct analysis of observational data. A temperature and salinity data array was prepared on a regular grid (array 1) with a spatial resolution of 10' × 15' and a discreteness of 10 days. Gandin's optimal interpolation method was applied to create this array<sup>1</sup>. The interpolation equation system was solved using the Gauss method and the observation error was estimated as the sum of the instrumental error and the standard deviation of the mesoscale variability. The average monthly climatic fields of temperature and salinity were used as the norm for the anomalies. Assuming isotropy of the spatial correlation functions in the Black Sea [5, 6], we applied the approximation from [5] as the autocorrelation function to approximate the structure of the Gaussian fields depending on depth. A total of 16,845 profiles were prepared for the period 2000–2021 at regular grid nodes, based on 13,952 oceanographic stations. In this case, we set a condition whereby the number of extrapolation cases used to fill the free space was kept to a minimum.

Reanalysis based on the Black Sea circulation model of Marine Hydrophysical Institute (MHI). The reanalysis was based on the MHI Black Sea circulation model, which relies on an approximation of a system of primitive ocean dynamics equations [7]. We applied a version of the model with a spatial step of 4.8 km, which provided an adequate description of both large-scale circulation and synoptic processes. The model contains 35 computational z-levels vertically, which converge towards the sea surface. Climatic discharge values were specified at the mouths of major rivers. To take into account water exchange through the Bosphorus Strait at horizons corresponding to the lower Bosphorus current, velocities were preset based on the climatic discharge rate and a salinity value of 36. At the horizons corresponding

---

<sup>1</sup> Gandin, L.S., 1963. *Objective Analysis of Meteorological Fields*. Leningrad: Gidrometeoizdat, 287 p. (in Russian).

to the upper Bosphorus current, where water flows out of the Black Sea, a constant velocity value was preset to ensure water balance for the time period under consideration.

The circulation model equations were solved using the parameters from the ERA-5 atmospheric reanalysis (ECMWF) [8] for the boundary conditions on the free sea surface: surface wind, heat and fresh water fluxes, and solar radiation. We applied the atmospheric fields with the spatial resolution of  $0.25^\circ \times 0.25^\circ$  and a time frequency of 1 h.

The Black Sea circulation model used satellite sea surface temperature (SST) and altimetry data. The surface temperature data were prepared by CMEMS as a daily gridded dataset with a spatial resolution of  $0.05^\circ \times 0.05^\circ$ . The altimetry data (also from CMEMS) were prepared as L4 gridded sea level anomalies (SLA) with a spatial resolution of  $0.15^\circ \times 0.15^\circ$ , calculated with respect to the 20-year mean (1993–2012). To be assimilated into the circulation model, the sea level anomalies were transformed into free surface elevation using the mean dynamic topography, which was calculated from the reanalysis results (1993–2012) [9]. The annual mean temperature and salinity profiles were prepared based on all available hydrographic surveys and Argo float data for the period under consideration.

SST assimilation was performed using the relaxation method. Satellite SST values were compared with model surface temperature values once a day. Sources on the right-hand side of the heat transport – diffusion equation proportional to the temperature value discrepancy were included at measurement points on model horizons which were part of the upper mixed layer.

We used the algorithm described in [10] to assimilate satellite altimetry data. The temperature and salinity profiles were adjusted proportionally at each point according to the difference between the measured and modelled free sea surface elevation values. In this case, depth-dependent weighting factors were calculated using cross-covariance functions of errors in level, salinity and/or temperature.

In accordance with the annual average profiles obtained from all available contact measurement data, temperature and salinity values were corrected at depths below 500 m. This dataset is further identified as array 2.

Reanalysis based on the NEMO model. The reanalysis (hereinafter referred to as array 3) was carried out using the regional configuration of the NEMO<sup>2</sup> ocean dynamics numerical modeling complex. This allows the dynamics and trends of hydrophysical parameters in the Euxine Cascade seas (the Black Sea, the Sea of Azov and the Marmara Sea (BAMS24)) to be reconstructed [11]. The computational grid is geographic and covers the marked basins with spatial steps of  $\approx 4.6 \times 4.6$  km.

The atmospheric impact was specified based on ERA-5 (ECMWF) reanalysis fields [8]. The air temperature and humidity fields were considered at a height of 2 m, while the horizontal wind velocity components were considered at a height of 10 m. The downward long-wave and short-wave radiation flows, total precipitation and precipitation in the solid phase were also taken into account. The meteorological

---

<sup>2</sup> Madec, G. and the NEMO Team, 2008. *NEMO Ocean Engine*. Note du Pôle de Modélisation de Institut Pierre-Simon Laplace (IPSL). 412 p.

parameters noted with initial discreteness in time were applied to calculate the total heat, mass and wind friction stress flows according to the CORE<sup>3</sup> protocol's bulk formulas.

The regional configuration takes into account the climatic discharge of the 16 rivers in the Black Sea basin. For the Sea of Azov and the Kerch Strait, where water exchange occurs, real changes in the water balance over time are considered. For this purpose, data on the volumetric runoff of the Don and Kuban rivers are used<sup>4</sup>. At the exit from the Dardanelles Strait to the west of Marmara Island, boundary conditions are set on an open liquid boundary. Quasi-real changes in sea level, barotropic and baroclinic current velocities, temperature and salinity obtained from the CMEMS global reanalysis system products are used for this purpose<sup>5</sup>.

To carry out a retrospective analysis for the period 2000–2021, we utilized the following observational database:

- a combined array of temperature and salinity profiles in the Black Sea from the EasyCORA arrays of the CMEMS service (1999–2021) and the SeaDataNet oceanographic database (<https://www.seadatanet.org/>) (1999–2008);

- gridded satellite altimetry data of the sea surface level at the L4 processing level, provided by the CMEMS marine forecast service (<https://doi.org/10.48670/moi-00141>);

- gridded satellite data of the Black Sea SST at the L4 processing level, provided by the CMEMS marine forecast service (<https://doi.org/10.48670/moi-00160>).

Three-dimensional sea temperature and salinity fields are reconstructed for assimilation into the model based on the joint analysis procedure for altimetry level anomalies and temperature and salinity profiles presented in [12]. As in the aforementioned study, the basic thermohaline stratification of the basin was determined within a given time range, but the averaging window reached a maximum value of 180 days based on a limited number of observations. Due to insufficient observations in certain years in the early 2000s, the basic stratification was calculated by interpolation using neighboring values.

Next, the depth-dependent coefficients of the direct regression between altimetric sea level values (processing level L4) within a given time window and the deviations of temperature and salinity observations from basic stratification were determined. These coefficients were then used to reconstruct three-dimensional arrays of pseudo-measurements of seawater temperature (Tobs) and salinity (Sobs).

Data assimilation was performed using the following hybrid procedure. In the main pycnocline layer, the temperature and salinity fields were relaxed to three-

---

<sup>3</sup> Large, W.G. and Yeager, S.G., 2004. *Diurnal to Decadal Global Forcing for Ocean and Sea-Ice Models: The Data Sets and Flux Climatologies*. USA, Colorado: National Center for Atmospheric Research, 105 p. <https://doi.org/10.5065/D6KK98Q6>

<sup>4</sup> Polonskii, V.F. and Ostroumova, L.P., 2012. [*Basic Hydrological Characteristics of the Marine Estuaries of European Russia Rivers: A Database*]. State Certificate 2012620681 of Database Registration. Moscow: FSBI SOIN. (in Russian).

<sup>5</sup> Copernicus Marine Monitoring Service, 2016. *Global Ocean Physics Analysis and Forecast*. Mercator Ocean International. <https://doi.org/10.48670/moi-00016>

dimensional arrays of pseudo-measurements Tobs and Sobs over the entire depth for salinity and in the layer below 60 m for temperature. In the upper sea layer, satellite altimetry observations were assimilated using the procedure described in [9]. SST data assimilation was performed by correcting the heat flux in the upper layer <sup>2</sup>.

CMEMS reanalysis (array 4). This Copernicus Marine Service product (*BLKSEA\_MULTIYEAR\_PHY\_007\_004*) represents the daily mean hydrodynamic fields in the Black Sea from 01.01.1993 to 30.06.2021, obtained through reanalysis. These fields were analyzed earlier in [3] for the time period up to the end of 2018. The hydrodynamic core of the reanalysis is based on the NEMO v4 ocean general circulation model configured for the Black Sea basin, with a horizontal resolution of  $1/27^\circ \times 1/36^\circ$  at 31 vertical levels. The atmospheric fields of the ERA-5 ECMWF system, which have a spatial resolution of  $1/4^\circ$  and a temporal resolution of 1 h, are applied as atmospheric forcing. In the current configuration, the Bosphorus Strait boundary is closed when calculating the reanalysis. Data assimilation was carried out on the basis of the 3DVAR variation scheme, for which the authors used the OceanVar program [13, 14]. During the reanalysis, they assimilated *in situ* temperature and salinity measurements from the SeaDataNet and CMEMS datasets, as well as satellite data tracking sea surface level anomalies (CMEMS).

Firstly, it should be noted that the main difference between arrays 3 and 4 lies in the data assimilation procedure. For array 3 reconstruction, we applied an original MHI-developed procedure, the essence of which is presented above. The versions of the models used and the parameters of the computational grids also differ. In addition, the MHI reanalysis (array 3) takes the Marmara Sea basin into account in the calculations, which should affect the characteristics of water exchange through the Bosphorus Strait. Due to the difference in size of the computational grid cells, it can be expected that the turbulent exchange coefficients and time step for the two reanalyses will also differ. However, the authors do not provide more detailed information when describing array 4.

### **Main trends in temperature and salinity field changes in the Black Sea in 2000–2020**

The prepared arrays of results from three reanalyses and observational data for individual months, when hydrological soundings more or less uniformly covered the area of the Black Sea, are used to analyze trends in temperature and salinity changes in seawater over the past 20 years. If significant discrepancies are observed in the reanalysis data under consideration, those close in at least two of the analyses are considered reliable. This approach is due to the fact that reanalyses performed on the basis of different models can produce noticeably different results <sup>6</sup> [15].

Trends in temperature field variation and the CIL structure. In [4], trends in upper layer heating in the Black Sea are examined through an analysis of changes in average temperature values at 60 m horizons near the CIL's minimum temperature

---

<sup>6</sup> IPCC, 2023. *Climate Change 2021 – The Physical Science Basis: Working Group I Contribution to the Sixth Assessment Report of the Intergovernmental Panel on Climate Change*. Cambridge University Press, 2392 p. <https://doi.org/10.1017/9781009157896>

and at 150 m, which is the main pycnocline's lower boundary, according to three reanalyses. This paper will mainly illustrate the warming process of the upper 200-meter layer of the Black Sea by examining the behavior of the CIL.

Fig. 2 shows the time evolution of the averaged temperature over the Black Sea basin at a 5 m horizon. The graph clearly shows the seasonal variation in surface temperature and interannual variability of its maximum and minimum values. At the same time, all reanalyses provide similar temperature change values.

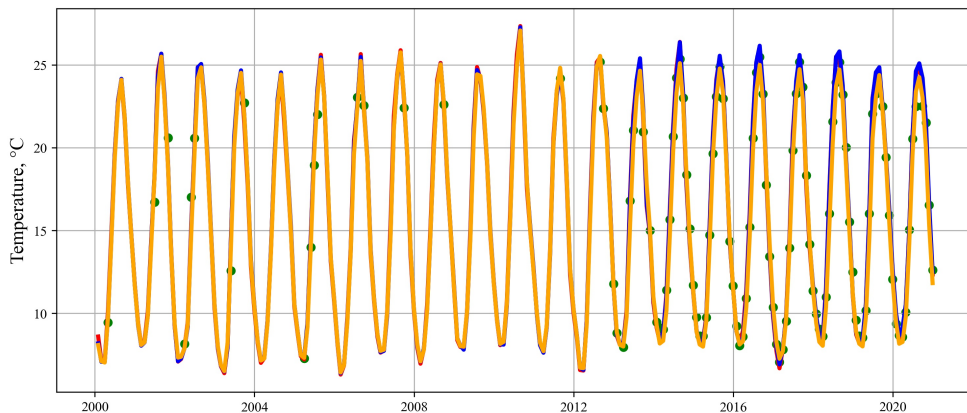


**Fig. 2.** Time evolution of the area-averaged temperature at the 5 m horizon obtained from three reanalyses. The red line corresponds to array 3, the blue line – to array 4, and the yellow line – to array 2. Green circles denote measurements

The similarity in the temperature time evolution at the 5 m horizon in different reanalyses is largely due to the fact that they all assimilate SST satellite observations. Therefore, the temperature evolution over time in the near-surface sea layer in the reanalyses is close to satellite SST (see Fig. 1 from [4]) and, consequently, to each other. Until 2012, there are quite a large number of minima of the average Black Sea near-surface temperature below 8 °C, after which there is a noticeable decrease. In [4], time diagrams showing changes in the average values of seawater temperature over horizontal sections are presented for all three reanalyses. Moreover, all reanalyses demonstrate areas of water limited by the 8°C isotherm, up until 2012, with brief interruptions. In addition, the renewal of CIL waters by cold surface waters in winter is clearly visible. After that, traditional CIL, which is limited by the 8 °C isotherm and ventilated during winter convection, is observed less frequently.

This paper considers the CIL behavior since 2012 in more detail, i.e. during the period of greatest heating of the upper layer of the Black Sea. According to Fig. 5 from [4], a linear regression constructed using observational data and all reanalyses demonstrates an increase in the temperature growth rate after 2012 for the time intervals 2000–2011 and 2012–2020. For the second time period, an almost twofold increase in the rate of seawater temperature growth is evident. Fig. 3 shows the diagrams of changes in the area-averaged horizon temperatures in the upper

300-meter layer over time for data arrays 3 and 4. As shown in [4], array 2 provides slightly overestimated values of seawater temperature at the 60 m horizon, which approximately corresponds to the CIL core depth. It also fails to reconstruct the winter convection of 2017 (Fig. 3 from [4]). Meanwhile, arrays 3 and 4 demonstrate similar temperature changes during the time period under study.

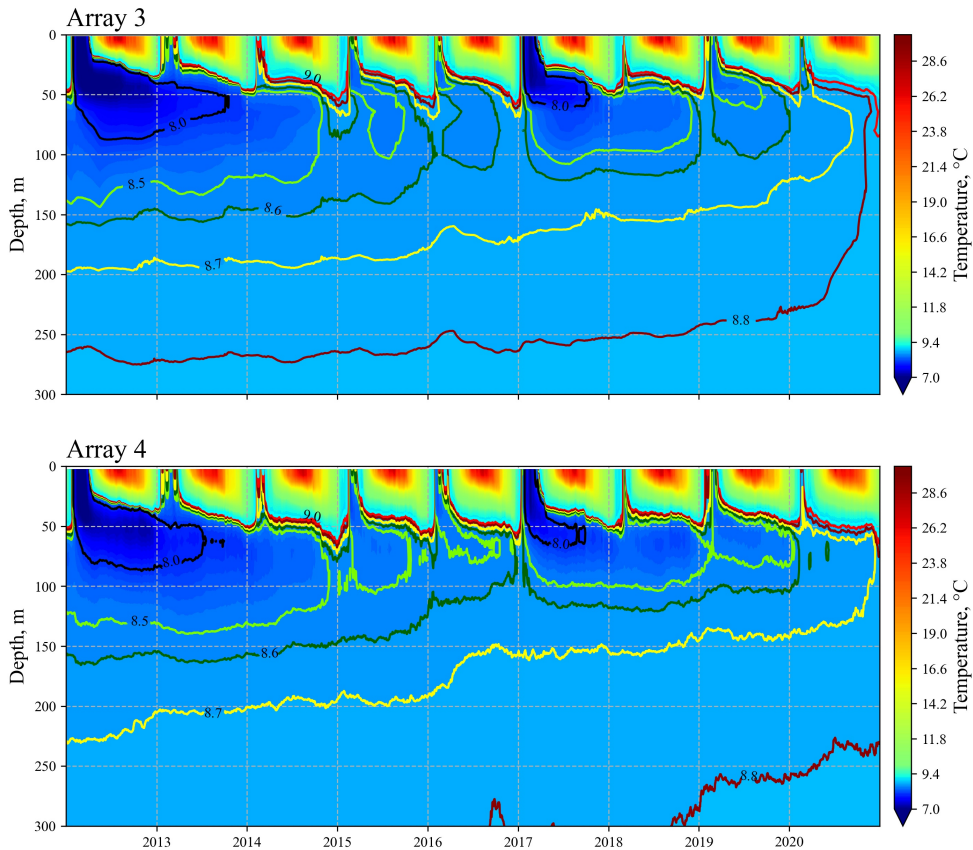


**Fig. 3.** Time diagram of changes in sea water temperature average over the horizontal cross-sections in the Black Sea deep part for two reanalyses

A cold winter was observed in 2012. As a result of winter convection, the CIL was restored, reaching a core temperature below 8 °C. This temperature was maintained until around mid-2013. In contrast, the CIL core temperature had exceeded 8 °C for the previous three years (Fig. 4).

The traditional ventilated CIL remained after 2013, but the temperature values in its core increased to 8.5–8.6 °C. In 2017, a rather cold winter was observed in the Black Sea, with minimum near-surface temperature values below 8 °C (Fig. 2), similar to the conditions in winter 2004. The traditional ventilated CIL formed due to winter convection had a significantly smaller cold content than in 2004. The mass of cold water entering the CIL in 2017 further supported this layer, with temperature values in the core increasing to 8.6–8.7 °C by the end of 2018. The following year,

2019, saw a slight drop in the near-surface winter temperature below 8°C, while the CIL formed due to winter thermal convection had a seawater temperature of 8.5 °C in its core. This increased to 8.6 °C by the end of the year.

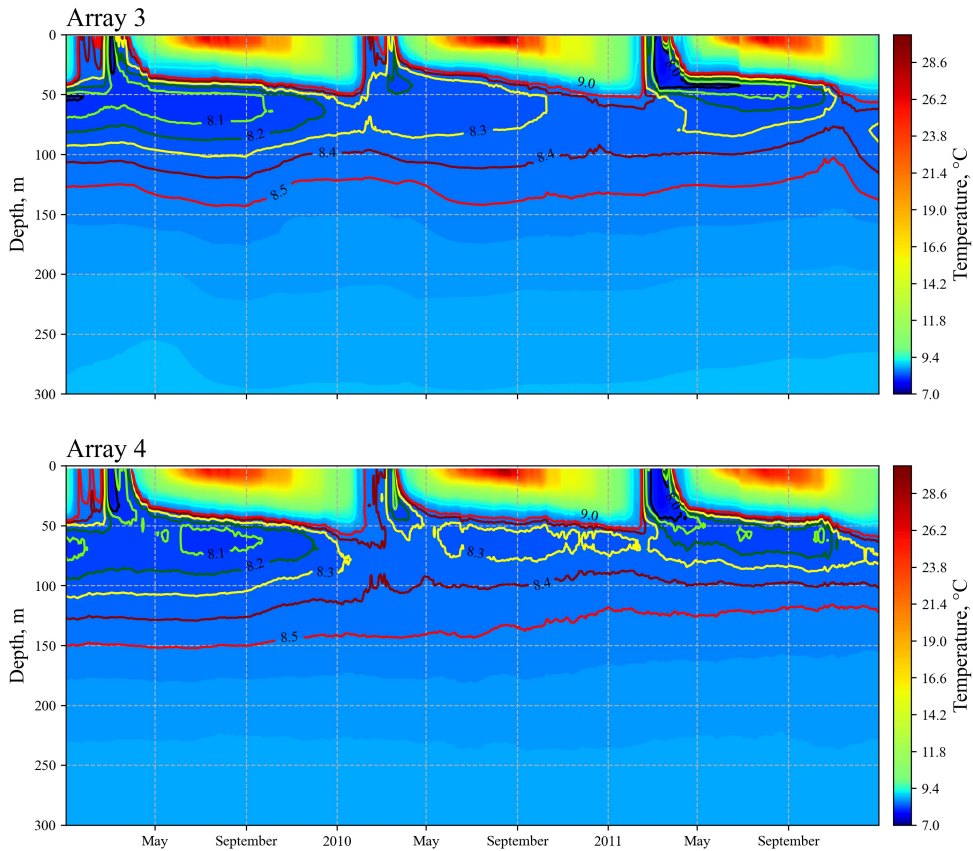


**Fig. 4.** The same as in Fig. 3, for 2009–2011

In 2020, winter thermal convection did not reach 50 m, meaning the traditional CIL, which is formed by the inflow of cold surface waters, was not renewed (Fig. 5). This phenomenon has never been observed throughout the history of oceanographic research in the Black Sea. However, according to data from arrays 3 and 4, a temperature minimum of ~ 8.7 °C is observed at a depth of ~ 75 m, and this layer is fundamentally different in nature to the traditional CIL, which is ventilated in winter. Its existence is solely due to the presence of warm waters with temperatures above 9 °C near the basin bottom.

Trends in salinity field changes. Let us examine the trends in seawater salinity over the study period. Fig. 6 shows the temporal evolution plots of the spatially averaged salinity at a depth of 5 m in the deep-water part of the Black Sea. The figure clearly reveals an increasing salinity trend in the sea surface layer. Notably, the salinity of surface waters in the deep-water part of the basin was relatively low between 2000 and 2008, reaching an annual mean of ~ 17.6

in 2006–2007. The maximum freshening of the surface waters of the Black Sea, which was observed between 2005 and 2006, had previously been noted in observational data. However, the limited number of measurements made it difficult to provide reliable quantitative estimates of this state. Nevertheless, the water balance assessments in atmospheric reanalyses indirectly confirmed it. From 2008 onwards, surface salinity increased in both reanalysis arrays 3 and 4, as well as in the observational data, reaching 18.1–18.15 in 2019–2020. These changes in the Black Sea surface salinity align with an approximately 20-year cycle associated with fluctuations in the freshwater budget entering the Black Sea.

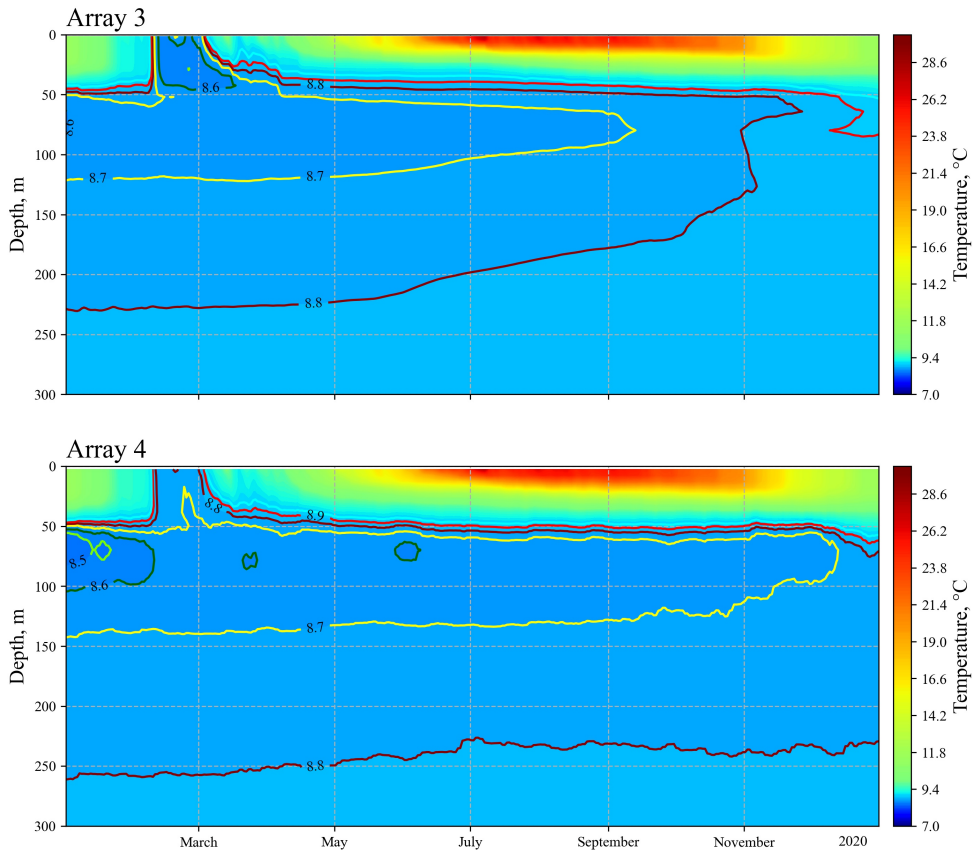


**Fig. 5.** The same as in Fig. 3, for 2020

Across all the reanalysis datasets presented in this study, an increase in seawater salinity of approximately 0.2 over 20 years has been observed at a depth of 150 m, which roughly corresponds to the lower boundary of the pycnocline (Fig. 7). Since the beginning of regular hydrological observations in the Black Sea [16], a continuous upward trend in both temperature and salinity has been recorded in the deeper layers of the main pycnocline. This trend emphasises the non-stationary nature of the basin’s haline regime, which is linked to the inflow of warm, saline Mediterranean waters through the Bosphorus Strait.

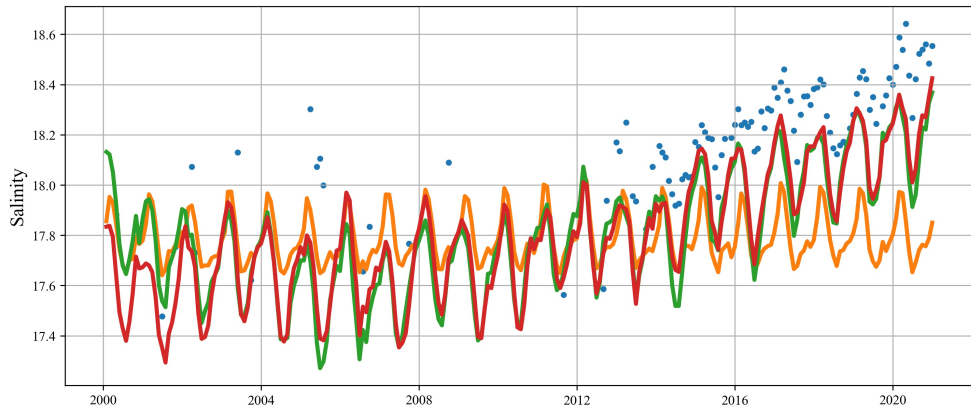


**Fig. 6.** Temporal evolution of monthly average values of seawater salinity at the 5 m horizon for each reanalysis and based on available observations. The red line corresponds to array 4, the green line – to array 3, and the yellow line – to array 2. Blue points denote measurement results

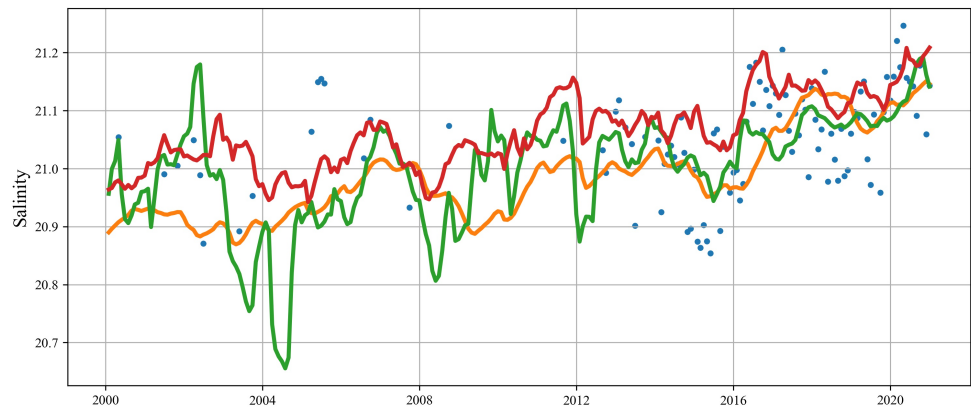


**Fig. 7.** The same as in Fig. 6, for the 150 m horizon

### Conclusion

This study examines trends in changes to the hydrological regime of the Black Sea. The study is based on reanalysis data obtained through three different methods and, where possible, supplemented by direct observational data. Analysis revealed that, due to the increasing mean SST of the Black Sea waters (since 2005), the Black Sea Cold Intermediate Layer (CIL) is disappearing from its traditionally defined state as a subsurface water layer with temperatures  $\leq 8$  °C. Furthermore, accelerated warming of the sea within the main pycnocline has been observed. If these trends persist for 8–10 years, it could lead to significant changes in the vertical stratification of Black Sea waters, which would likely affect the basin's biological resources. Simultaneously, the haline regime of the sea is characterized by a transition from freshening to salinization of the surface layer in 2012–2015, associated with changes in the external freshwater budget and a long-term increase in salinity in the main

pycnocline. Ultimately, we can expect an intensification of density stratification in the basin, as well as slowing of deep-water ventilation processes, due to the gradual, constant uplift of the main pycnocline and the warming of the surface layer.

#### REFERENCES

1. Polonskii, A.B. and Novikova, A.M., 2020. Interdecadal Variability of the Black Sea Cold Intermediate Layer and Its Causes. *Russian Meteorology and Hydrology*, 45(10), pp. 694-700. <https://doi.org/10.3103/S1068373920100039>
2. Belokopytov, V.N., 2011. Interannual Variations of the Renewal of Waters of the Cold Intermediate Layer in the Black Sea for the Last Decades. *Physical Oceanography*, 20(5), pp. 347-355. <https://doi.org/10.1007/s11110-011-9090-x>
3. Stanev, E.V., Peneva, E. and Chtirkova, B., 2019. Climate Change and Regional Ocean Water Mass Disappearance: Case of the Black Sea. *Journal of Geophysical Research: Oceans*, 124(7), pp. 4803-4819. <https://doi.org/10.1029/2019JC015076>
4. Korotaev, G.K., Belokopytov, V.N., Dorofeev, V.L., Mizyuk, A.I. and Kholod, A.L., 2024. Acceleration of Climate Change in the Upper Layer of the Black Sea. *Doklady Earth Sciences*, 518(1), pp. 1550-1555. <https://doi.org/10.1134/S1028334X24602797>
5. Grigor'ev, A.V., Ivanov, V.A. and Kapustina, N.A., 1996. Correlation Structure of the Black Sea Thermohaline Fields in the Summer Season. *Oceanology*, 36(3), pp. 334-339.
6. Polonskii, A.B. and Shokurova, I.G., 2008. Statistical Structure of the Large-Scale Fields of Temperature and Salinity in the Black Sea. *Physical Oceanography*, 18(1), pp. 38-51. <https://doi.org/10.1007/s11110-008-9008-4>
7. Demyshev, S.G. and Korotaev, G.K., 1992. [Numerical Energy-Balanced Model of the Baroclinic Currents in Ocean with Uneven Bottom on a C-Grid]. In: INM RAS, 1992. *Numerical Models and Results of Calibration Calculations of Currents in the Atlantic Ocean*. Moscow: Institute of Numerical Mathematics RAS, pp. 163-231 (in Russian).
8. Hersbach, H., Bell, B., Berrisford, P., Hirahara, S., Horányi, A., Muñoz-Sabater, J., Nicolas, J., Peubey, C., Radu, R. [et al.], 2020. The ERA5 Global Reanalysis. *Quarterly Journal of the Royal Meteorological Society*, 146(730), pp. 1999-2049. <https://doi.org/10.1002/qj.3803>
9. Dorofeev, V.L. and Sukhikh, L.I., 2016. Analysis of Variability of the Black Sea Hydrophysical Fields in 1993-2012 Based on the Reanalysis Results. *Physical Oceanography*, (1), pp. 33-47. <https://doi.org/10.22449/1573-160X-2016-1-33-47>
10. Dorofeev, V.L. and Korotaev, G.K., 2004. Assimilation of the Data of Satellite Altimetry in an Eddy-Resolving Model of Circulation of the Black Sea. *Physical Oceanography*, 14(1), pp. 42-56. <https://doi.org/10.1023/B:POCE.0000025369.39845.c3>
11. Mizyuk, A.I., Korotaev, G.K., Grigoriev, A.V., Puzina, O.S. and Lishaev, P.N., 2019. Long-Term Variability of Thermohaline Characteristics of the Azov Sea Based on the Numerical Eddy-Resolving Model. *Physical Oceanography*, 26(5), pp. 438-450. <https://doi.org/10.22449/1573-160X-2019-5-438-450>
12. Korotaev, G.K., Lishaev, P.N. and Knysh, V.V., 2016. Reconstruction of Three-Dimensional Fields of Temperature and Salinity Based on Satellite Altimetry. *Issledovanie Zemli iz Kosmosa*, (1-2), pp. 199-212. <https://doi.org/10.7868/S0205961416010073> (in Russian).
13. Dobricic, S. and Pinardi, N., 2008. An Oceanographic Three-Dimensional Variational Data Assimilation Scheme. *Ocean Modelling*, 22(3-4), pp. 89-105. <https://doi.org/10.1016/j.ocemod.2008.01.004>
14. Storto, A., Dobricic, S., Masina, S. and Di Pietro, P., 2011. Assimilating Along-Track Altimetric Observations through Local Hydrostatic Adjustment in a Global Ocean Variational Assimilation

System. *Monthly Weather Review*, 139(3), pp. 738-754.  
<https://doi.org/10.1175/2010MWR3350.1>

15. Balmaseda, M.A., Hernandez, F., Storto, A., Palmer, M.D., Alves, O., Shi, L., Smith, G.C., Toyoda, T., Valdivieso, M. [et al.], 2015. The Ocean Reanalyses Intercomparison Project (ORA-IP). *Journal of Operational Oceanography*, 8(1), pp. 80-97.  
<https://doi.org/10.1080/1755876X.2015.1022329>
16. Simonov, A.I. and Altman, E.N., eds., 1991. *Hydrometeorology and Hydrochemistry of Seas in the USSR. Vol. 4. Black Sea. Issue 1. Hydrometeorological Conditions*. Saint Petersburg: Gidrometeoizdat, 429 p. (in Russian).

Submitted 24.10.2024; approved after review 05.03.2025;  
accepted for publication 13.03.2025.

*About the authors:*

**Gennady K. Korotaev**, Academic Advisor, Marine Hydrophysical Institute of RAS (2 Kapitanskaya Str., Sevastopol, 299011, Russian Federation), Corresponding Member of RAS, DSc. (Phys.-Math.), Professor, **Scopus Author ID: 7004998153**, **ResearcherID: K-3408-2017**, [gkorotaev@gmail.com](mailto:gkorotaev@gmail.com)

**Vladimir N. Belokopytov**, Head of Oceanography Department, Marine Hydrophysical Institute of RAS (2 Kapitanskaya Str., Sevastopol, 299011, Russian Federation), DSc. (Geogr.), **ORCID ID: 0000-0003-4699-9588**, **ResearcherID: ABA-1230-2020**, **Scopus Author ID: 6602381894**, [v.belokopytov@gmail.com](mailto:v.belokopytov@gmail.com)

**Viktor L. Dorofeev**, Leading Research Associate, Marine Hydrophysical Institute of RAS (2 Kapitanskaya Str., Sevastopol, 299011, Russian Federation), CSc. (Phys.-Math.), **ORCID ID: 0000-0001-7979-8235**, **Scopus Author ID: 16411510200**, **ResearcherID: G-1050-2014**, [viktor.dorofeev@mhi-ras.ru](mailto:viktor.dorofeev@mhi-ras.ru)

**Artem I. Mizyuk**, Leading Research Associate, Marine Hydrophysical Institute of RAS (2 Kapitanskaya Str., Sevastopol, 299011, Russian Federation), CSc. (Phys.-Math.), **ORCID ID: 0000-0003-4885-354X**, **ResearcherID: C-6125-2016**, **Scopus Author ID: 36446217200**, [artem.mizyuk@mhi-ras.ru](mailto:artem.mizyuk@mhi-ras.ru)

**Oksana S. Puzina**, Junior Research Associate, Marine Hydrophysical Institute of RAS (2 Kapitanskaya Str., Sevastopol, 299011, Russian Federation), **ORCID ID: 0000-0002-1637-4475**, **Scopus Author ID: 57205120208**, [oksana\\_puzina@mhi-ras.ru](mailto:oksana_puzina@mhi-ras.ru)

**Anton L. Kholod**, Research Associate, Department of Dynamics of the Oceanic Processes, Marine Hydrophysical Institute of RAS (2 Kapitanskaya Str., Sevastopol, 299011, Russian Federation), CSc. (Tech.), **Scopus Author ID: 55632951600**, **ORCID ID: 0000-0003-4694-8406**, **ResearcherID: ABA-3482-2020**, [antonholod@mail.ru](mailto:antonholod@mail.ru)

*Contribution of the co-authors:*

**Gennady K. Korotaev** – development of the article concept and structure; selection of illustrative materials; analysis and generalization of the results under consideration; critical analysis and revision of the text

**Vladimir N. Belokopytov** – preparation of data array of temperature and salinity measurements on a regular grid; participation in the discussion of the article materials; participation in the analysis of the results; participation in the text editing

**Viktor L. Dorofeev** – reanalysis based on the MHI Black Sea circulation model; participation in the discussion of the article materials; participation in the analysis of the results; preparation of the article text; text editing and refinement

**Artem I. Mizyuk** – preparation of a regional configuration of the NEMO ocean dynamics numerical modeling complex; reanalysis based on it; participation in the discussion of the article materials and analysis of the results; participation in the text editing

**Oksana S. Puzina** – preparation of atmospheric impact for the NEMO ocean dynamics numerical modeling complex; conducting numerical experiments; participation in the analysis of the results

**Anton L. Kholod** – preparation of data from the CMEMS reanalysis array for research purposes; preparation of illustrative materials for the article; participation in discussion of materials; participation in analysis of results

*The authors have read and approved the final manuscript.*

*The authors declare that they have no conflict of interest.*

## Estimation of the Stationarity Interval of Wind Wave Field

Ya. V. Saprykina , B. V. Divinsky, M. N. Shtremel, O. A. Likutova

*Shirshov Institute of Oceanology, Russian Academy of Sciences, Moscow, Russian Federation*

 [saprykina@ocean.ru](mailto:saprykina@ocean.ru)

### Abstract

**Purpose.** The wind wave field is non-stationary due to variability of wave formation factors such as wind action and the processes of non-linear wave interactions. However, for many practical applications, it is assumed that the wind wave process, described by some time record of waves, is quasi-stationary. Globally, there is no generally accepted length of a wave record for which the conditions of homogeneity and stationarity of the wave field would be valid. Therefore, the main purpose of the work is to estimate the interval of wave field stationarity based on the data of field contact measurements carried out in the deep-water and coastal zones of the Black Sea in different years and seasons.

**Methods and Results.** The data from two long-term field experiments in the Black Sea were analyzed. Waves in the open sea were measured using a Directional Waverider buoy, and in the coastal zone – a Spoondrifter Spotter buoy and a resistive string wave gauge, installed on a specialized marine trestle offshore. Spectral analysis methods were applied to the data. The spectral peak width, defined as the peakedness parameter, was used to characterize the homogeneity of wind waves. Wave records containing high values of the peakedness parameter and characterized by a narrow-band spectral distribution, were classified as the cases of quasi-stationary waves homogeneous in their spectral composition close to regular stationary waves. As a result, the characteristic time intervals were obtained for which the wave field could be assumed to be homogeneous and quasi-stationary.

**Conclusions.** Regardless of the conditions of wave formation, the interval of wave stationarity in the Black Sea can be taken equal to 8–12 minutes. These estimates are the same for the deep-water and coastal parts of the sea, and qualitatively correspond to the theoretical ones.

**Keywords:** wind waves, wave parameters, wave record length, wave field homogeneity, wave spectrum, stationarity interval

**Acknowledgements:** The study was carried out with the support of RSF, grant No. 24-27-00082.

**For citation:** Saprykina, Ya.V., Divinsky, B.V., Shtremel, M.N. and Likutova, O.A., 2025. Estimation of the Stationarity Interval of Wind Wave Field. *Physical Oceanography*, 32(3), pp. 297-311.

© 2025, Ya. V. Saprykina, B. V. Divinsky, M. N. Shtremel, O. A. Likutova

© 2025, Physical Oceanography

### Introduction

Understanding the key parameters of wind waves and their spatiotemporal variability patterns is crucial for numerous applications, including forecasting waves, assessing the impact on coastal structures and mitigating operational risks during marine activities. Wind wave field exhibits non-stationary behavior due to variability in wave generation factors, primarily wind forcing and ongoing nonlinear wave interaction processes. Nevertheless, many practical applications employ the assumption that wave processes described by time series records are stationary (or quasi-stationary). This means that their statistical properties remain time-invariant relative to the initial measurement point. This requirement for stationarity is essential for determining wave height probability distributions, which represent



the proportion of time during which the recorded wave heights in a time series remain below specified thresholds. The temporal window of wave stationarity is particularly critical for validating satellite wave measurements against *in situ* observations under non-simultaneous sampling conditions. However, empirical evidence demonstrates that wave fields only maintain stationarity within limited temporal windows at any given location. As specified in the international *Coastal Engineering Manual*, wind-generated waves can be considered approximately stationary for periods not exceeding 3 h, beyond this, their properties are expected to change <sup>1</sup>.

During the stationarity time interval, the characteristics of the wave record should not change significantly if the duration of the record was slightly shorter or longer, or if sampling was initiated at a slightly different time offset (earlier or later by some fraction of time). If the above-stated assumptions are not satisfied, it signifies that the wave field is non-stationary and cannot therefore be adequately characterized by conventional statistical methods.

From a statistical perspective, an irregular wave field can be fully characterized by a two-dimensional frequency-directional spectrum [1]. Although the sea surface spectrum lacks a precise mathematical form, various empirical models that approximate wave spectra are commonly employed in oceanographic research. These are referred to as parametric spectral models and prove useful for conventional engineering applications. One of the most successful and widely adopted approximations of surface wave frequency spectra is the JONSWAP spectrum, which was proposed in 1973 based on field observations in the North Sea. In its generalized form, it is expressed as [2]:

$$S(f) = \frac{\alpha g^2}{(2\pi)^4} f^{-5} \exp\left(-\frac{5}{4}\left(\frac{f}{f_m}\right)^{-4}\right) \gamma^{\exp\left(-\frac{1}{2\sigma^2}\left(\frac{f}{f_m}-1\right)^2\right)},$$

where  $\alpha$  is the Phillips constant ( $\alpha = 0.0081$ );  $f_m$  is the spectral peak frequency;  $\gamma$  is the peak enhancement coefficient. The  $\gamma$  parameter represents an extremely important spectral characteristic that controls the shape of the spectrum and determines the distribution of wave energy across the frequency range.

Fig. 1 presents examples of surface wave spectra and their corresponding JONSWAP approximations. The experimental spectra were obtained in the Black Sea using a Datawell Waverider buoy [3]. For the wind waves (shown in Fig. 1, *a* and *b*), the significant wave heights  $h_s$  and spectral peak frequencies  $f_p$  are identical ( $\sim 2.6$  m and 0.15 Hz, respectively), while their shape parameters  $\gamma$  differ substantially (2.6 vs. 5.1).

In other words, Fig. 1 demonstrates that, despite having identical integral wave characteristics ( $h_s$  and  $f_p$ ), the spectral energy distribution differs substantially across frequencies. Higher  $\gamma$  values correspond to a greater concentration of wave energy in the spectral peak region. The absence of anomalously high individual waves in the wave record indicates spectrally homogeneous wave conditions, which are dominated by a single frequency component and thus approximate regular stationary

---

<sup>1</sup> U.S. Army Corps of Engineers, 2004. *Coastal Engineering Manual*. [online] Available at: <https://coastalengineeringmanual.tpub.com> [Accessed: 10 May 2025].

waves. This example further reveals that neither wave height nor period can serve as a reliable indicator of wave regularity (homogeneity or stationarity) alone, as neither provides information about spectral composition. The spectral width, which is indirectly characterized by the shape parameter  $\gamma$ , is a more informative metric and is used in wave height distribution assessments [4]. It should be emphasized that, in order to perform a proper spectral analysis of wave records, the data must satisfy the assumptions of wave field stationarity. For example, the *Coastal Engineering Manual*<sup>1</sup> recommends using wave records with durations between 17 and 68 min for spectral analysis.

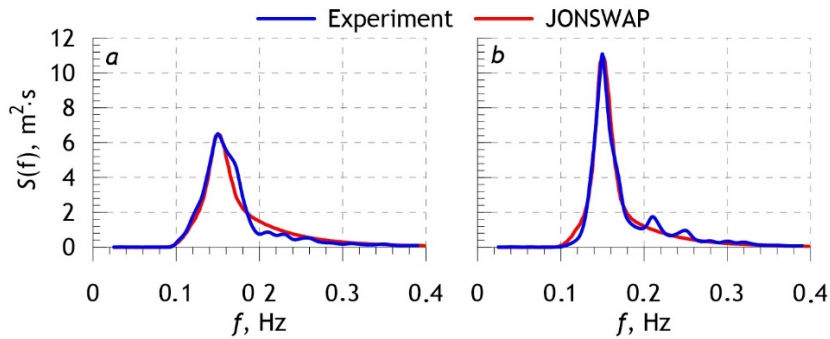


**Fig. 1.** Experimental spectra of wind waves and their approximations by the JONSWAP spectrum at  $h_s = 2.6$  m,  $f_p = 0.15$  Hz,  $\gamma = 2.6$  (a) and  $\gamma = 5.1$  (b)

In international engineering practice, the concept of a ‘quasi-stationarity interval’ is used for wave processes. This is conventionally set at 20 min and corresponds to constant external wave generation factors<sup>2</sup>. This terminology has been standardized and widely adopted for instrumental observations of wind wave parameters. Most specialized ocean wave buoys record 20-minute time series of surface elevation data with precision, from which key wave parameters are subsequently derived and statistical analyses are performed. However, these recommendations have traditionally been applied only to deep-water waves. It is questionable whether the ‘quasi-stationarity interval’ concept can be applied to wind waves in coastal zones. Notably, some wave buoy software (e.g., Datawell systems) calculates wave statistics based on 30-minute measurement series. Scientific literature also employs shorter wave record durations – typically 5, 6, 10, or 15 min – for spectral and statistical characterization, as longer series may be non-stationary [5–7]. Theoretical estimates suggest that the quasi-stationarity interval ranges from 10 to 100 characteristic wave period scales  $\tau$ , where  $1 < \tau < 10$  s [5].

The accuracy of spectral estimates depends on the record length, the temporal resolution (i.e. the sampling frequency) and the method used to smooth the spectral window, in order to achieve an optimal balance between spectral smoothness and the resolution of key components. It should be noted that the specific choice of window function has been shown to have a negligible influence [8].

<sup>2</sup> Lopatukhin, L.I., Bukhanovskii, A.V. and Chernysheva, E.S., 2013. *Reference Data on the Wind and Wave Regime of the Shelf of the Barents and Kara Seas: ND No. 2-029901-01*. Russian Maritime Register of Shipping, St. Petersburg: Publishing Center “Academy”, 335 p. (in Russian).

As previously mentioned, the stationarity assumption is the theoretical basis for deriving wave statistics from field measurements, based on the implicit premise that it is true for all possible sea states. Nevertheless, this assumption has never been systematically validated using extensive field datasets representing diverse wave generation conditions. Consequently, the principal objective of this study is to quantitatively evaluate the duration of wave field stationarity by analyzing direct *in situ* measurements obtained in the Black Sea in different years and seasons, in both the deepwater area and the coastal zone.

### ***In situ* data and research methods**

The analysis incorporated data from two field experiments conducted at different times in the Black Sea. The first experiment was conducted from 1996 to 2003 and covered all seasonal conditions. Wave parameter measurements were obtained as part of the NATO TU-WAVES international program using a Directional Waverider buoy deployed in the open waters near Gelendzhik (44°30'40N, 37°58'70E). With an installation depth of 85 m, deep-water conditions were ensured for all observed waves, except for anomalous wave events. The buoy operated on a standard 3-hour measurement cycle, transmitting 20-minute records of surface elevation data sampled at a frequency of 1.28 Hz. During periods when the significant wave height exceeded 1.5 m the measurement interval decreased to an hour. The experiment captured a comprehensive range of wave conditions, with measured heights varying from 0.1 to 12 m, and periods ranging from 2.5 to 11.4 s. Full details of the experimental procedures and results can be found in reference [9]. A continuous 70-hour dataset was acquired in April 1998 when the buoy was switched to uninterrupted recording mode. We used this record for detailed analysis.

The second experiment was carried out from September to October 2016 in the coastal area of the Black Sea near the village of Shkorpilovtsi, close to Varna. Wave measurements were taken using three Spooindrifter Spotter buoys, which recorded chronograms of the three components of its displacement at sampling frequency of 2.5 Hz. Simultaneous measurements were performed by an array of four contact wire wave gauges installed on a specialized marine trestle 200 m from the shore.

For the analysis, we used data from a buoy moored at the coordinates 42°95'85N, 27°90'35E at a depth of 12 m, as well as data from a wire wave gauge positioned at the end of the trestle at a depth of 4.5 m, as shown in Fig. 2. During the experiment, measured wave heights ranged from 0.1 to 3 m, with wave periods varying between 2.5 and 10 s.

The key wave parameters were determined by analyzing the frequency spectra and their corresponding spectral moments. These spectral moments are expressed as follows:

$$M_n = \int f^n S(f) df.$$

The significant wave height

$$h_s = 4\sqrt{M_0} \tag{1}$$

and the mean wave period were calculated using them

$$t = M_0/M_1. \tag{2}$$

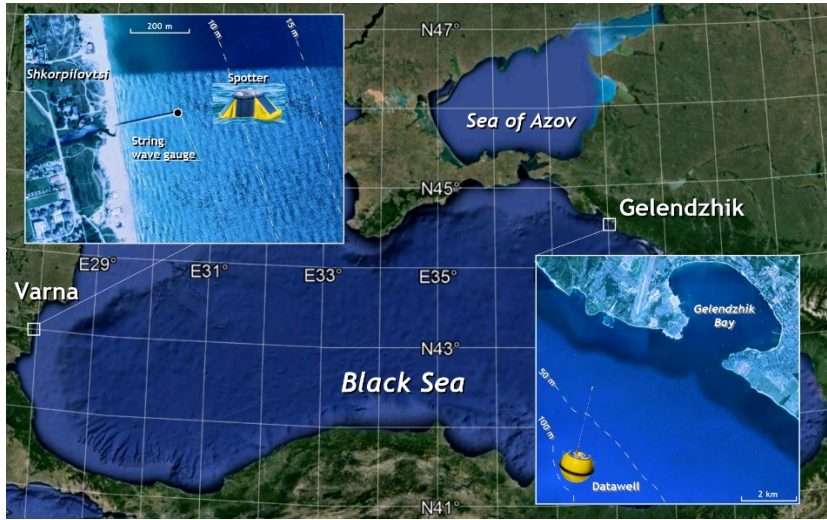


**Fig. 2.** Location of wave recording devices

The spectral peak width, as defined in the manual<sup>3</sup>, was considered a characteristic of the irregularity of wind waves in the form

$$\varepsilon = \sqrt{\frac{M_0 M_4 - M_2^2}{M_0 M_4}}. \quad (3)$$

The parameter  $\varepsilon$  ranges from 0, which corresponds to a narrow spectrum of regular waves, to 1, which is characteristic of a broad spectrum representing an irregular wave field. Since the spectral width in formula (3) is highly sensitive to the quality of the input data, reference [10] proposed an alternative metric: the spectral peakedness parameter, which is defined as the ratio

$$Q = \frac{2}{M_0^2} \int_0^\infty f S(f)^2 df. \quad (4)$$

The peakedness parameter  $Q$  assumes values greater than one. Increasing  $Q$  values correspond to progressively narrower spectra.

As already noted in the introduction, a narrow spectrum indicates a wave field that is fairly uniform in composition and close to the property of stationarity found in regular waves.

Two methods were used for spectrum construction: parametric spectral analysis (for deep-water waves) and the Welch method with a Hamming window (for coastal zone waves) [11]. The Welch method averages spectral estimates over overlapping segments of the wave record. Thus, the frequency resolution of the obtained spectral estimates is determined by the length of these segments. In this study, this remained constant at 0.02 Hz, independent of the duration of the wave record. The same

<sup>3</sup> WMO, 2018. *Guide to Wave Analysis and Forecasting*. Geneva: World Meteorological Organization, 208 p. (WMO-No. 702). [online] Available at: <https://library.wmo.int/records/item/31871-guide-to-wave-analysis-and-forecasting> [Accessed: 10 May 2025].

frequency resolution was adopted for the parametric method. Assessments were made of the influence of the spectrum construction method on the obtained spectral characteristics.

The analysis demonstrated that spectral estimates are practically independent of the spectrum construction method, particularly the shape of the smoothing window, but depend significantly on the frequency resolution. This is fully consistent with the theoretical concepts outlined in reference [8]. For instance, a frequency resolution of 0.1 Hz yields identical spectral estimates regardless of record length, as the resulting spectrum is excessively smoothed and broad. As noted in references [8, 11], selecting spectral estimation parameters involves compromising between resolving power and spectrum smoothing when considering the characteristics of the target process under study. In our study, we specifically chose a resolution of 0.02 Hz to clearly identify the second nonlinear harmonic in the spectrum, which influences many dynamic processes in the coastal zone of the sea [12].

Additionally, assessments were made of the variability of higher-order wave moments for coastal zone conditions. These moments serve as specific indicators of nonlinear wave interactions and are frequently used in engineering and predictive models. Applications include determining the direction and magnitude of bedload sediment transport in coastal areas [13–15] and estimating the probability of abnormally high waves [16].

The study examined the third-order wave moments, namely vertical axis asymmetry  $As$  and horizontal axis skewness  $Sk$ , as well as the fourth-order moment  $K$ , kurtosis. These parameters were calculated using the formulas presented in references [16; 17, p. 1726]:

$$As = \frac{\langle H(\xi)^3 \rangle}{\langle \xi^2 \rangle^{3/2}}, \quad (5)$$

$$Sk = \frac{\langle \xi^3 \rangle}{\langle \xi^2 \rangle^{3/2}}, \quad (6)$$

$$K = \frac{\langle \xi^4 \rangle}{\langle \xi^2 \rangle^2}, \quad (7)$$

where  $\xi$  is the chronogram of the free surface elevation (wave);  $H$  is the Hilbert transform; angle brackets indicate time averaging.

## Results and discussion

### Temporal wave field homogeneity in the deepwater area

We analyzed a continuous 70-hour record from the Datawell buoy and generated 140 time series of surface elevation, each lasting 30 min. For each 30-minute time series, we first calculate the spectral characteristics for the first 5 minutes of the record. We then incrementally increase the length  $L$  of the wave chronogram by 1 min until it reaches 30 min. Fig. 3 shows an example of this processing for one 30-minute record.

As evident from Fig. 3, increasing the chronogram length from 5 to 30 min has a negligible influence on the calculated significant wave heights (1) and mean periods (2). The spectral bandwidth (3) (Fig. 3, *d*) initially increases, but then stabilizes after  $L = 17$  min. At the same time, the  $\varepsilon$  parameter varies insignificantly

in absolute value. In contrast, the peakedness parameter  $Q$  demonstrates a slight increase at record lengths of 8–9 minutes, followed by a decrease until  $L$  reaches 14 min. When the chronogram length  $L$  increases from 14 to 30 min, the value of the peakedness parameter remains almost unchanged.

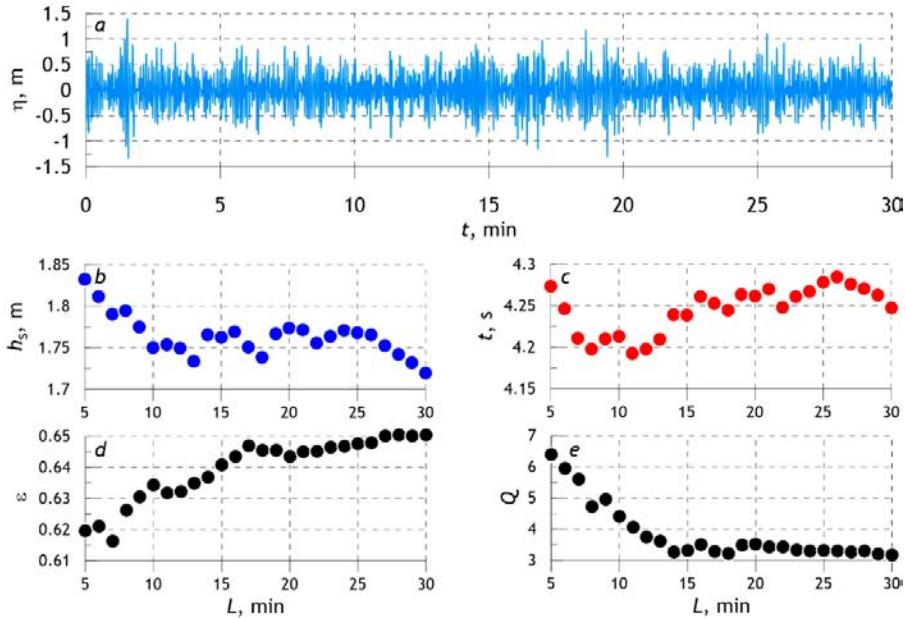


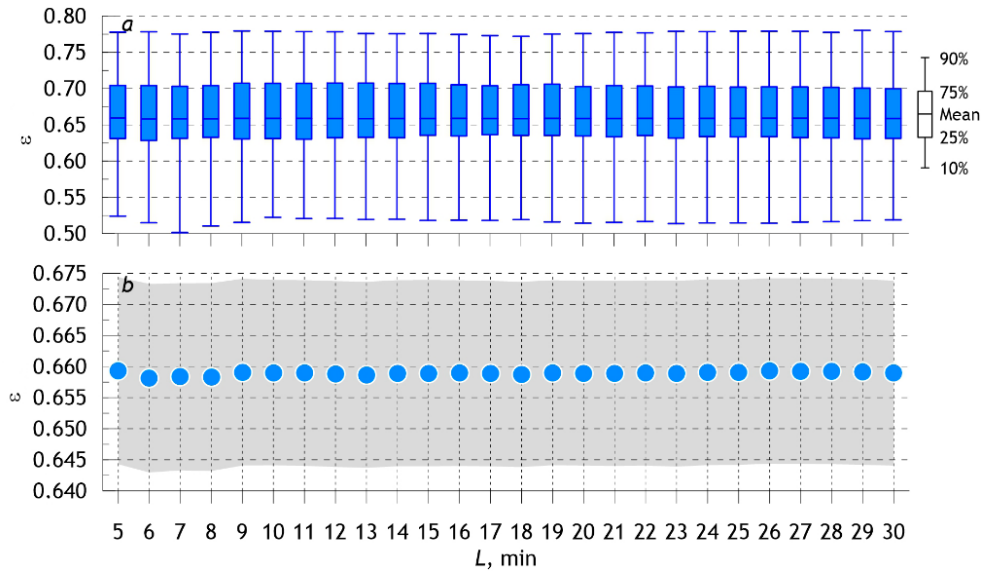
**Fig. 3.** Free surface elevation (a), significant wave heights (b), average periods (c), spectrum width (d), and peakedness parameter (e) for successive chronograms of  $L$  length

These patterns, however, reflect just a single observational series. To derive statistically robust conclusions, we aggregated the results from all the available records (140 chronograms of 30-minute waves).

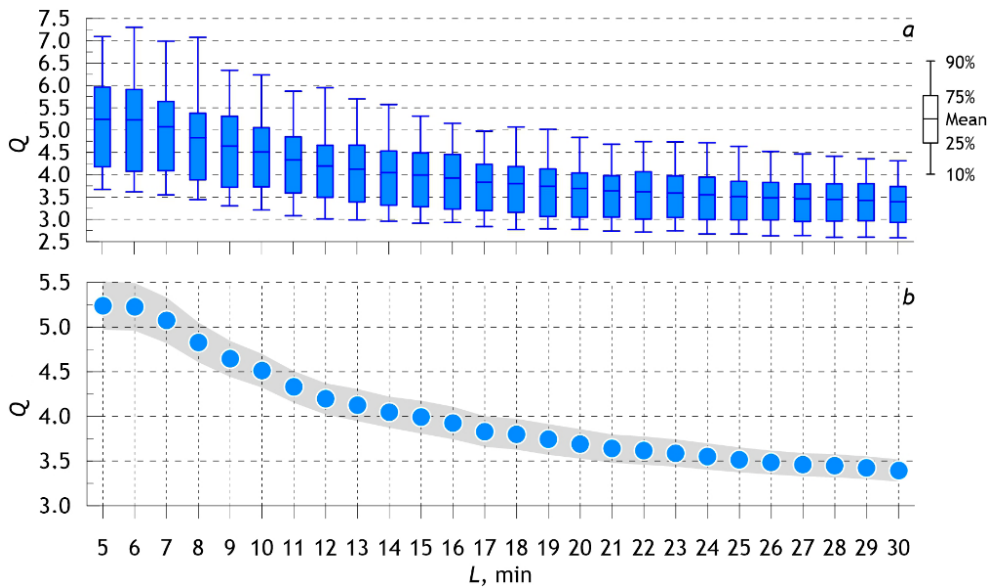
Fig. 4, a presents graphical estimates of the mean value of spectral bandwidth, along with the 10<sup>th</sup>, 25<sup>th</sup>, 75<sup>th</sup>, and 90<sup>th</sup> quantiles of the distribution. Fig. 4, b displays the mean values alongside the 95% confidence intervals (gray shaded area). As can be seen clearly from Fig. 4, the statistical characteristics of spectral bandwidth remain independent of realization length. Therefore, the spectrum width determined by formula (3) is uninformative for our purposes and not suitable for analyzing wave irregularity.

Fig. 5 presents similar plots for the peakedness parameter  $Q$ , which is calculated using formula (4). As can be seen in Fig. 5, there is a relatively sharp decrease in the mean value of the peakedness parameter in the range where the chronogram length  $L$  increases from 6 to 12 min. For record lengths  $L > 12$  min, the  $Q$  parameter also decreases, but much more slowly. For record lengths  $L > 22$  min,  $Q$  remains almost unchanged, apparently due to the increasing spectral bandwidth preventing detailed resolution of its shape. We also observe the narrow range of 95% confidence intervals (grey area in Fig. 5, b) for the mean value.

To expand the statistical basis of the study, we used archival data comprising 20-minute surface elevation records from 1998. These records cover the entire range of observed wind-wave conditions, from calm to stormy. There are a total of 1,100 of such records.



**Fig. 4.** Statistical characteristics of the distributions of spectrum width values (a) as well as the average spectrum width values (b) for successive series of free surface elevations of  $L$  length



**Fig. 5.** Statistical characteristics of the distributions of peakedness parameter values (a) as well as the average spectrum width values (b) for successive series of  $L$  length equal to 5, 6, ..., 30 min

Fig. 6 shows the results of analyzing all these records. The analysis reveals that, as the chronogram length increases from 7 to 20 min, the peakedness parameter decreases. This process is two-stage: a rapid increase in the parameter is observed as the chronogram length increases from 7 to 12 min, while a slower decrease takes place as it increases to 20 min. This is consistent with the patterns identified for continuous recording (Fig. 6). The  $Q$  values remain relatively high for record lengths up to approximately 8 min, indicating a narrow spectral bandwidth characteristic of

regular wave conditions. Based on this, we can conclude that the wave field has a uniform spectral composition for a time interval of up to 8 min. When the record is extended to 12 min, the  $Q$  parameter values decrease but still remain high. Therefore, we can assume that the wave field will be close to uniform for no more than 12 min.

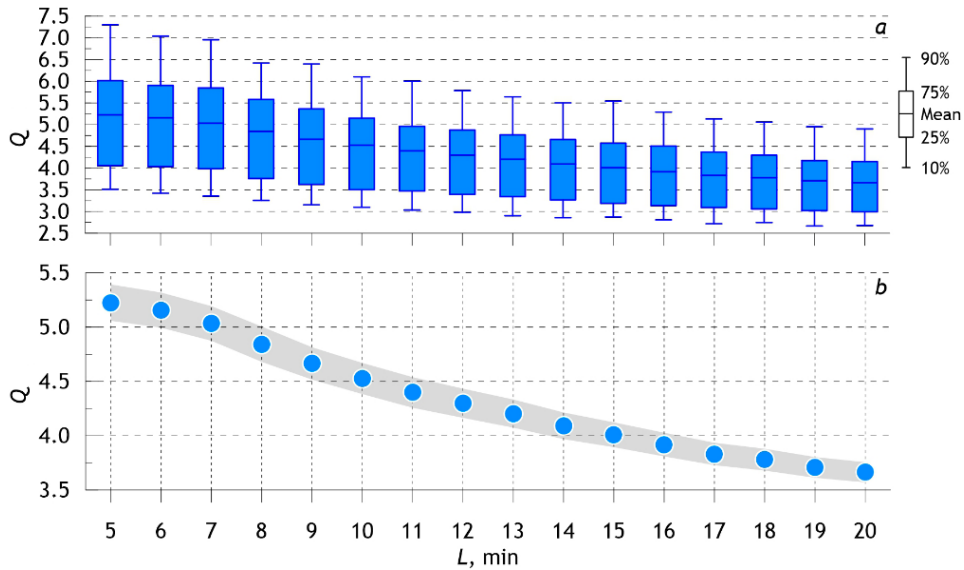


**Fig. 6.** Statistical characteristics of the distributions of peakedness parameter values (a) as well as the average spectrum width values (b) for successive series of free surface elevations of  $L$  length

Thus, the peakedness parameter proves to be an effective tool for analyzing the spectral structure of waves in terms of their irregularity. Surface elevation records with durations of up to 12 min can be classified as spectrally quasi-homogeneous wave cases and treated as nearly stationary wave conditions. These findings are notable because they remain independent of wave generation conditions and the development stage of wind waves.

### Temporal homogeneity of the wave field in the coastal zone of the sea

The results obtained for waves in deepwater area in the previous section are fully confirmed for waves in the coastal zone of the sea. We will consider them using two daily chronograms as an example. To assess the influence of wave formation conditions more precisely, we selected two 24-hour wave records corresponding to an increase (3–4 November 2018) and a decrease (7–8 November 2018) in wave height (Fig. 7).

Since the position of the buoy relative to the anchor changes depending on the direction of the wind and currents, synchronous records of surface elevation obtained from a stationary resistive wave gauge on 7–8 November 2018 were used to assess the influence of buoy mobility on the obtained data. The wave gauge was installed at the end of the trestle at a depth of 4.5 m.

Fig. 8 shows how significant wave height, mean period and parameter  $Q$  vary with the length of the record used for estimation when comparing data from the buoy and the stationary wave gauge.

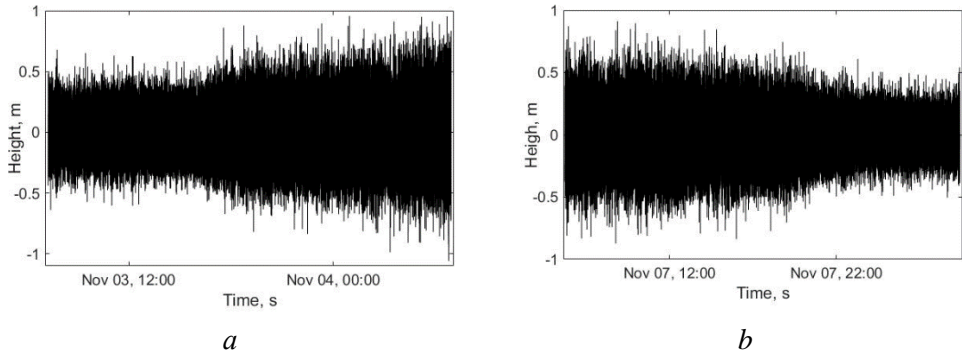


**Fig. 7.** Wave chronograms recorded by the Spoodrifter buoy in the Black Sea coastal zone on 3–4 November (*a*) and 7–8 November (*b*) 2018 and used for analysis

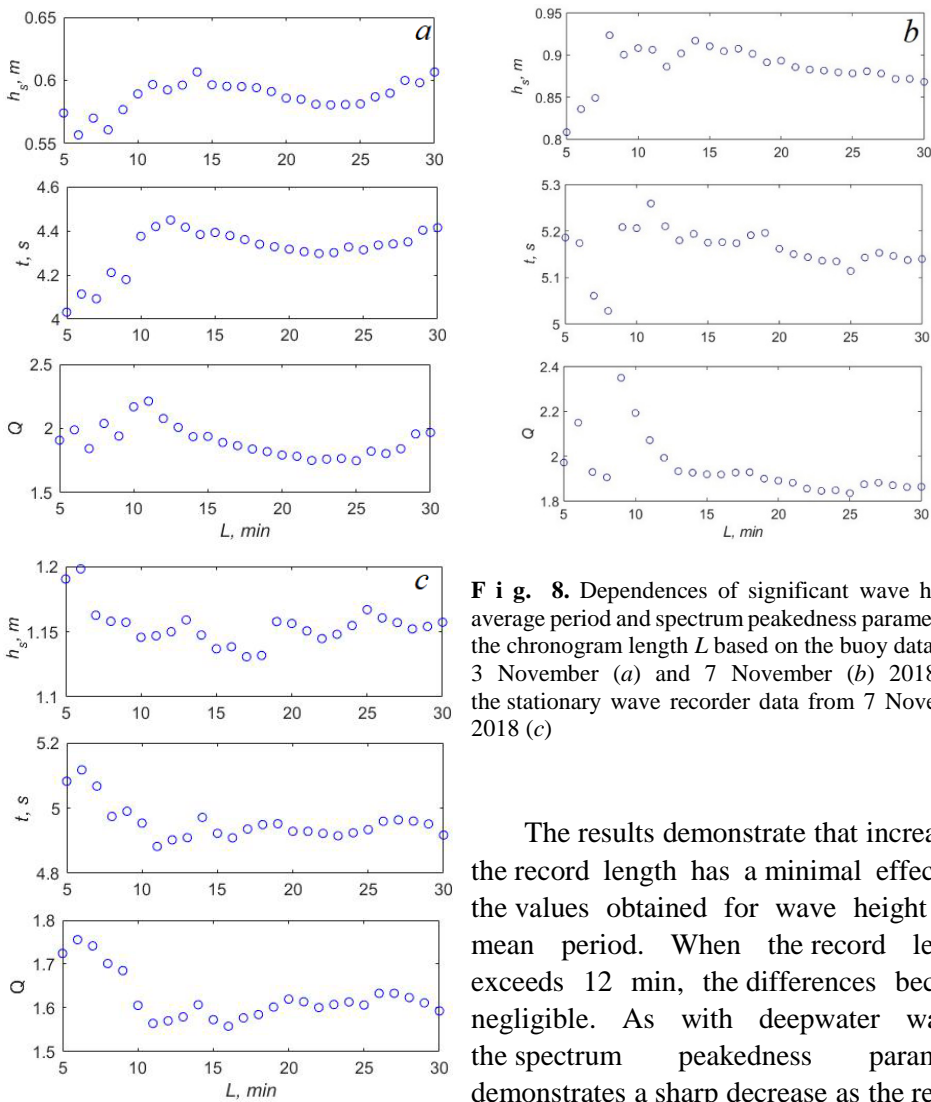


**Fig. 8.** Dependences of significant wave height, average period and spectrum peakedness parameter on the chronogram length  $L$  based on the buoy data from 3 November (*a*) and 7 November (*b*) 2018 and the stationary wave recorder data from 7 November 2018 (*c*)

The results demonstrate that increasing the record length has a minimal effect on the values obtained for wave height and mean period. When the record length exceeds 12 min, the differences become negligible. As with deepwater waves, the spectrum peakedness parameter demonstrates a sharp decrease as the record

length increases from approximately 7–9 min to 12 min, followed by insignificant subsequent changes. The variations observed for record lengths shorter than 8 min (Fig. 8, *a, b*) may be attributed to the specific characteristics of these records. The duration of the records may be insufficient to mitigate the effects of buoy mobility, as such variations are not present in measurements obtained from the stationary wire wave gauge. Furthermore, these deviations are not observed when averaging across all realizations.

The average values of peakedness parameter for the selected 24-hour records are given in Fig. 9.

As with deep-water waves (see Fig. 6), the decrease in the peakedness parameter with increasing chronogram length occurs in two distinct temporal phases: a rapid reduction when extending the record from 6 to 12 min, followed by a more gradual decline as the record length increases to 20 min. The absolute  $Q$  parameter values remain relatively high (indicating a narrow spectrum) for records shorter than 8 min, suggesting that the wave field maintains spectral homogeneity for approximately 8 min and near-homogeneity for up to 12 min. Records extending beyond 20 min do not allow us to identify the features of the spectrum shape, providing almost identical  $Q$  parameter values.

Thus, regardless of the conditions of wave generation and propagation (in deep water or in the coastal zone), the approximate duration of homogeneity, and consequently of stationarity, for surface elevation records is about 8 min. Records of up to 12 min can be considered to be approximately homogeneous (quasi-stationary). These estimates are in full agreement with theoretical predictions [5]. The examined wave conditions had characteristic time periods (spectral peak periods) ranging from 5 to 7 s, and theoretical estimates suggest maximum quasi-stationarity durations of 100 characteristic periods (from 500 to 700 s, or approximately 8 to 12 min).

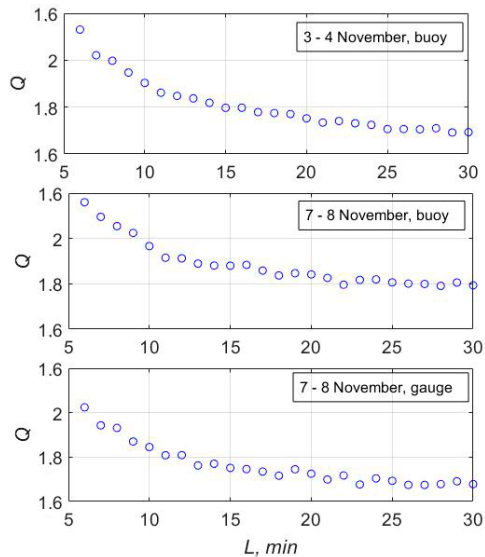


**Fig. 9.** Dependence of the average values of spectrum  $Q$  peakedness parameter upon the  $L$  length of successive series of free surface elevations in the Black Sea coastal zone

### Analysis of higher spectral moments

Using a daily record of decaying waves measured by a buoy on 7–8 November 2018 (Figs. 10, 11), we consider how the length of the record affects the obtained estimates of wave height, average period, and the value of higher wave moments that determine the shape of the waves.

In general, the trend in variation of the selected wave parameters over the 24-hour period is the same, regardless of the duration of the chronogram used. However, the shorter the chronogram used for assessment, the greater the absolute changes for all parameters. As the length of the record used for calculation increases, the spread of absolute values decreases. Therefore, the spread of values for 5- and 30-minute records is up to 10% for height variation and up to 50% for changes in the average wave period, regardless of the wave attenuation stage. Values of selected wave parameters calculated from 10- to 20-minute records differ by only 2–3%. Values obtained from 30-minute records are smoother.

Wave shape parameters, obtained from 30-minute chronograms, such as wave asymmetry values relative to the vertical and horizontal axes, practically never take negative values. This can lead to incorrect estimates of sediment transport direction.

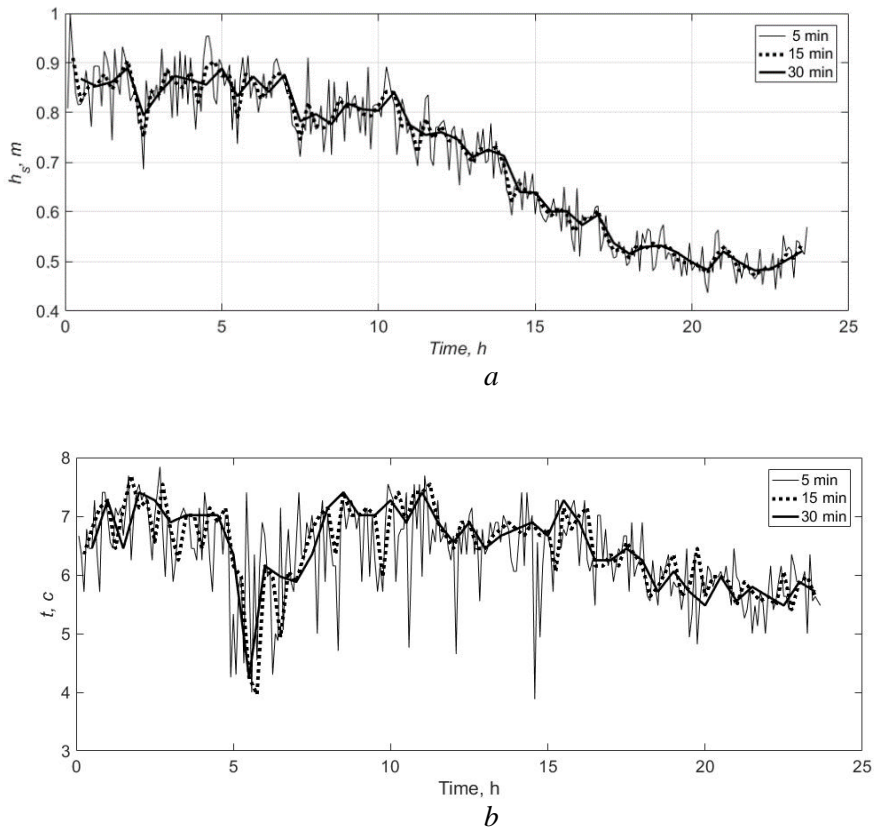


**Fig. 10.** Changes in significant wave height (*a*) and average wave period (*b*) based on the chronograms of different lengths for a 24-hour record made on 7–8 November 2018

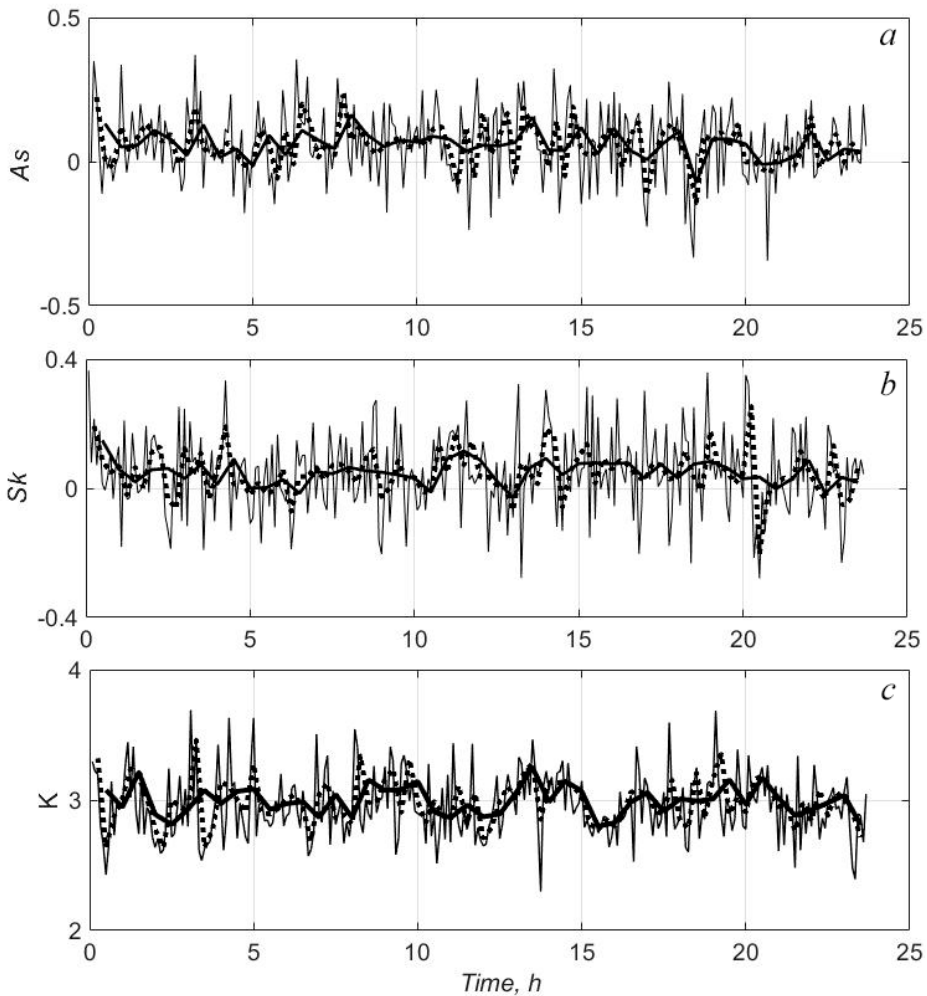


**Fig. 11.** Change in wave asymmetry described by formulas (5)–(7) and calculated using the chronograms of different lengths for a 24-hour record made on 7–8 November 2018: *a* –  $A_s$ ; *b* –  $S_k$ ; *c* –  $K$

### Conclusions

The research results indicate that the period of wave field stationarity in the Black Sea can be reliably established as 8–12 min, independent of wave generation conditions. These estimates demonstrate complete consistency between the deepwater and coastal zones of the sea. Their qualitative correspondence with theoretical estimates suggests that this result is universal across the entire World Ocean.

Analysis of higher-order wave moments and spectral shape characteristics using the peakedness parameter  $Q$  reveals greater variability when derived from wave records shorter than the determined period of stationarity.

## REFERENCES

1. Longuet-Higgins, M.S., Cartwright, D.E. and Smith, N.D., 1963. Observation of the Directional Spectrum of Sea Waves Using the Motions of a Floating Buoy. In: National Academy of Sciences, 1963. *Ocean Wave Spectra: Proceedings of a Conference*. Prentice-Hall, Englewood Cliffs, N.J., pp. 111-132.
2. Hasselmann, K., Barnett, T., Bouws, E., Carlson, H., Cartwright, D., Enke, K., Ewing, J.A., Gienapp, H., Hasselmann, D.E. [et al.], 1973. Measurements of Wind-Wave Growth and Swell Decay during the Joint North Sea Wave Project (JONSWAP). *Erganzungsheft zur Deutschen Hydrographischen Zeitschrift*. Reihe A, Nr. 12, 95 p.
3. Divinsky, B.V., 2003. Results of Measuring of Surface Waves Parameters with Help of Buoy in Gelendzhik Area. In: R. D. Kos'yan, I. S. Podymov and N. V. Pykhov, eds., 2003. *Dynamical Processes in the Sea Nearshore Zone*. Moscow: Scientific World. pp. 70-91 (in Russian).
4. Tayfun, M.A., 1983. Effects of Spectrum Band Width on the Distribution of Wave Heights and Periods. *Ocean Engineering*, 10(2), pp. 107-118. [https://doi.org/10.1016/0029-8018\(83\)90017-3](https://doi.org/10.1016/0029-8018(83)90017-3)
5. Efimov, V.V. and Polnikov, V.G., 1991. *Numerical Modeling of Wind Waves*. Kiev: Naukova Dumka, 238 p. (in Russian).
6. Trubkin, I.P., 2003. [Method and some Results of Directional Spectra Estimations of Random Waves Field in the Coastal Zone]. *Ecological Systems and Devices*, (9), pp. 47-53 (in Russian).
7. Vapnyar, M.U. and Tatlyeva, Z.I., 1989. [On the Nature of the Long-Term Distribution of Wave Heights in the Caspian Sea]. *Trudy GOIN*, 188, pp. 132-137 (in Russian).
8. Jenkins, G.M. and Watts, D.G., 1969. *Spectral Analysis and Its Applications*. Holden-Day, San Francisco, 541 p.
9. Divinskii, B.V., Kos'yan, R.D., Podymov, I.C. and Pushkarev, O.V., 2003. Extreme Waves in the Northeastern Black Sea in February 2003. *Oceanology*, 43(6), pp. 891-893.
10. Goda, Y., 1970. Numerical Experiments on Wave Statistics with Spectral Simulation. *Report of the Port and Harbour Research Institute*, 9(3), pp. 3-57.
11. Marple, S.L.Jr., 1987. *Digital Spectral Analysis with Applications*. Prentice-Hall, Inc., Englewood Cliffs, New Jersey, 492 p.
12. Saprykina, Ya.V., Kuznetsov, S.Yu., Andreeva, N.K. and Shtremel, M.N., 2013. Scenarios of Nonlinear Wave Transformation in the Coastal Zone. *Oceanology*, 53(4), pp. 422-431. <https://doi.org/10.1134/S0001437013040103>
13. Bailard, J.A., 1981. An Energetics Total Load Sediment Transport Model for a Plane Sloping Beach. *Journal of Geophysical Research: Oceans*, 86(C11), pp. 10938-10954. <https://doi.org/10.1029/JC086iC11p10938>
14. Ruessink, B.G., Van Den Berg, T.J.J. and Van Rijn, L.C., 2009. Modeling Sediment Transport beneath Skewed Asymmetric Waves above a Plane Bed. *Journal of Geophysical Research: Oceans*, 114(C11), C11021. <https://doi.org/10.1029/2009JC005416>
15. Saprykina Y., 2020. The Influence of Wave Nonlinearity on Cross-Shore Sediment Transport in Coastal Zone: Experimental Investigations. *Applied Sciences*, 10(12), 4087. <https://doi.org/10.3390/app10124087>
16. Wang, L., Zhou, B., Jin, P., Li, J., Liu, S. and Ducrozet, G., 2022. Relation between Occurrence Probability of Freak Waves and Kurtosis/Skewness in Unidirectional Wave Trains under Single-Peak Spectra. *Ocean Engineering*, 248, 110813. <https://doi.org/10.1016/j.oceaneng.2022.110813>
17. Elgar, S., 1987. Relationships Involving Third Moments and Bispectra of a Harmonic Process. *IEEE Transactions on Acoustics, Speech, and Signal Processing*, 35(12), pp. 1725-1726. <https://doi.org/10.1109/TASSP.1987.1165090>

*About the authors:*

**Yana V. Saprykina**, Leading Research Associate, Shirshov Institute of Oceanology, Russian Academy of Sciences (36 Nakhimovsky Avenue, Moscow 117997, Russian Federation), CSc. (Phys.-Math.), **Scopus Author ID: 57217957923**, **ORCID ID: 0000-0003-0357-0773**, [saprykina@ocean.ru](mailto:saprykina@ocean.ru)

**Boris V. Divinsky**, Leading Research Associate, Laboratory of Geology and Lithodynamics, Shirshov Institute of Oceanology, Russian Academy of Sciences (36 Nakhimovsky Avenue, Moscow 117997, Russian Federation), CSc. (Geogr.), **ORCID ID: 0000-0002-2452-1922**, **Scopus Author ID: 6508359174**, **ResearcherID: C-7262-2014**, divin@ocean.ru

**Margarita N. Stremel**, Senior Research Associate, (36 Nakhimovsky Avenue, Moscow 117997, Russian Federation), CSc. (Geogr.), **Scopus Author ID: 55844240900**, **ORCID ID: 0000-0003-0045-0282**, shtremel@ocean.ru

**Olga A. Likutova**, Junior Research Associate, Shirshov Institute of Oceanology, Russian Academy of Sciences (36 Nakhimovsky Avenue, Moscow 117997, Russian Federation), CSc. (Geogr.), **Scopus Author ID: 57104743100**, **ORCID ID: 0000-0002-7013-339X**, olga.ku-ocean@yandex.ru

*Contribution of the co-authors:*

**Yana V. Saprykina** – developing the main idea and concept of the paper, obtaining and analyzing data for waves in the coastal zone, figure preparation, writing the text and working on the reviewer's comments, writing the final version of the paper

**Boris V. Divinsky** – proposing and discussing analysis methods, analyzing data for deepwater waves, figure preparation, writing a part of the text

**Margarita N. Stremel** – obtaining and pre-processing experimental data in the coastal zone, figure preparation

**Olga A. Likutova** – writing part of the introduction, preliminary processing of experimental data in the coastal zone

*The authors have read and approved the final manuscript.*

*The authors declare that they have no conflict of interest.*

## Upwelling Index at the Southern Coast of Crimea in the Black Sea

I. G. Shokurova <sup>1, ✉</sup>, T. V. Plastun <sup>1</sup>, Yu. V. Simonova <sup>1</sup>,  
V. Yu. Kasianenko <sup>2</sup>

<sup>1</sup> Marine Hydrophysical Institute of RAS, Sevastopol, Russian Federation

<sup>2</sup> V. I. Vernadsky Crimean Federal University, Simferopol, Russian Federation

✉ igshokurova@mail.ru

### Abstract

**Purpose.** The purpose of the study is to analyze wind conditions leading to the occurrence of coastal upwelling events off the Southern Coast of Crimea (Katsiveli) in the Black Sea based on the calculations of wind upwelling index.

**Methods and Results.** The 6-hour ERA5 reanalysis data of surface wind speed components, long-term measurements of seawater and air temperature near the coast in Katsiveli (1992–2021), as well as satellite maps of sea surface temperature are used. The upwelling index is calculated as Ekman transport driven by alongshore winds. The index is considered to be positive when the transport is directed offshore. For the Katsiveli area, this condition corresponds to winds with a western component. Negative values of the index and onshore water transport correspond to eastern winds. Calculations of the upwelling index shown that the most favorable wind conditions for upwelling events are observed in winter (December and January) and summer (June and July), driven by the high frequency of western winds. The maximum value of the upwelling index is noted in June. The statistical relationship between the monthly mean upwelling index, water temperature, number of upwellings, and the frequency and speed of western winds is analyzed for this month. It is found that the upwelling index in June correlates with the number of low water temperature events (indicative of upwelling). The correlation coefficient between them is 0.88. During the years characterized by high frequency and speed of western winds, the number of upwellings increased, whereas it was minimal when eastern winds predominated. Analysis of the variability of wind index and seawater temperature based on the 6-hour data shows that high positive values of the index correspond to the onset of upwellings, while a negative index indicates their cessation.

**Conclusions.** Good agreement between the wind index variability and the number of measurements at low water temperature in summer demonstrates the potential of the index for studying wind conditions resulting in the development of upwelling events, as well as for forecasting their occurrence.

**Keywords:** coastal upwelling, upwelling index, sea water temperature, wind speed, wind direction, Katsiveli, Southern Coast of Crimea, Black Sea

**Acknowledgements:** the study was carried out within the framework of state assignments of FSBSI FRC MHI: FNNN-2024-0014 and FNNN-2024-0016.

**For citation:** Shokurova, I.G., Plastun, T.V., Simonova, Yu.V. and Kasianenko, V.Yu., 2025. Upwelling Index at the Southern Coast of Crimea in the Black Sea. *Physical Oceanography*, 32(3), pp. 312-325.

© 2025, I. G. Shokurova, T. V. Plastun, Yu. V. Simonova, V. Yu. Kasianenko

© 2025, Physical Oceanography

### Introduction

The Black Sea waters adjacent to the Southern Coast of Crimea are a natural marine ecosystem [1], and an area for the development of aquaculture [2]. Productivity of the marine waters depends on the concentration of biogenic elements in the upper photic layer of the sea [3]. Since there are no large rivers in



this area, the enrichment of surface waters with biogenic elements can be due to the inflow from deeper layers where their concentration is higher [4]. In winter, strong winds and winter convection cause the upper layer to mix well, enriching it with nutrients [5] throughout the entire water area. In summer, however, water mixing is weakened [6]. At this time, the role of coastal upwelling, an important factor in ensuring vertical water exchange, increases significantly [7].

Information on the frequency of upwelling events affecting the living conditions of marine organisms can be used to analyze monitoring results relating to the vital activity of the marine ecosystem off the coast of Crimea [8, 9]. In addition, the Southern Coast of Crimea is a popular tourist destination, so understanding the features and intensity of changes in water temperature during the summer is also of interest to researchers [10].

Upwelling is defined as the movement of water from deeper layers to the sea surface. According to Ekman's theory, which was formulated for the deep sea, coastal upwelling can be caused by alongshore winds with the coast to the left (in the Northern Hemisphere) or to the right (in the Southern Hemisphere). In this case, Ekman transport, which is perpendicular to the wind and moves from the coast, shifts the upper layer of water towards the sea, resulting in a compensatory rise in deep waters [11]. The shelf off the Southern Coast of Crimea is narrow with a steep drop-off, so upwelling here is caused by alongshore winds. In the Katsiveli area, these are westerly winds. The occurrence and scale of upwelling depend on the wind speed, duration of action, seasonal stratification of waters, and dynamic processes in the sea [12–14].

In winter, upwellings in the Black Sea are not recorded by temperature since the upper layer is mixed [6]. In summer, however, coastal upwelling events can be clearly visible by the lower water temperature in comparison with the surrounding warm waters [15–17]. On the Southern Coast of Crimea, the area of low-temperature water can extend 60–80 km into the sea [17, 18].

A large number of works has been devoted to studying upwelling off the coast of Crimea. The wind conditions associated with upwelling events were studied based on data from coastal weather stations [19], temperature measurements at the Hydrophysical Polygon in Katsiveli [20–23], ship measurements [15], satellite data [16–18], and data from moored buoys [24]. Upwellings were studied based on numerical modeling in [18, 25, 26]. Statistics on the number of upwellings are given in [17, 19, 20]. Statistics on the frequency and speed of winds favorable for upwelling, based on ERA5 reanalysis data, are presented in [21].

The wind conditions necessary for upwelling are often studied using the wind upwelling index, which is calculated based on the Ekman transport [27]. This index is widely used to study upwelling in different areas of the World Ocean [28–31], including the Black Sea [32]. There are also improved modifications of the wind index [33]. A criterion for the wind upwelling development taking into account the speed and direction of currents in the sea was proposed in [13] and applied in [14, 24]. A number of studies use the temperature upwelling index [30]. It is defined as the difference in water temperature between the upwelling zone near the coast and open waters, usually at a distance sufficient to avoid the influence of upwelling waters captured by currents or eddies.

Studies of the conditions for upwelling events using indices have not yet been carried out for the Southern Coast of Crimea. This paper analyzes the conditions for upwelling events using the wind upwelling index (UI) [27]. The paper compares natural data on the temperature of the upper layer of seawater with index values. In the future, the index could be used to clarify the features of upwelling occurrence depending on wind conditions, and to investigate the climatic conditions affecting the functioning of the coastal ecosystem in Crimea.

The study aims to analyze the wind conditions that lead to coastal upwelling events off the Southern Coast of Crimea (Katsiveli) in the Black Sea, based on the calculations of wind upwelling index.

### Research data and methods

**Water and air temperature.** To identify upwelling events, we used the following data:

- daytime measurements (08:00, 14:00 and 17:00) of seawater temperature  $T_w$  and air temperature  $T_A$  ( $^{\circ}\text{C}$ ) for June 1992–2021, conducted at the Black Sea Hydrophysical Sub-Satellite Polygon of Marine Hydrophysical Institute of the Russian Academy of Sciences in Katsiveli, Crimea [34]. Water temperature was measured near the shore from a pier at a depth of 0.75 m;
- maps of the Black Sea surface temperature from the website archive ([http://dvs.net.ru/mp/index\\_ru.shtml](http://dvs.net.ru/mp/index_ru.shtml)).

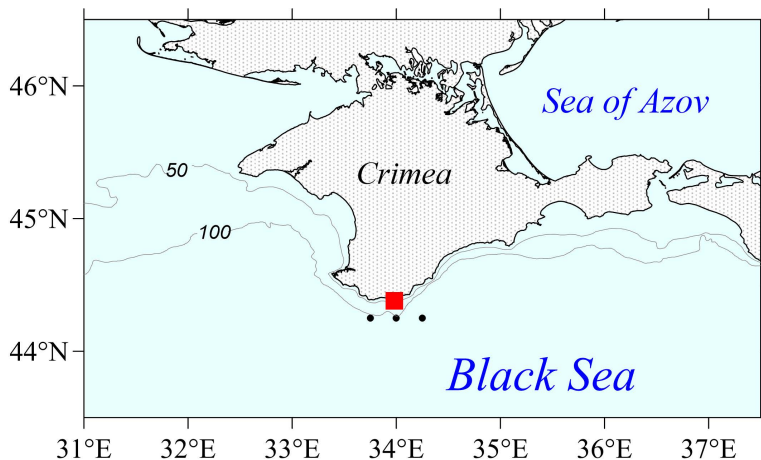


**Fig. 1.** Spatial distribution of ERA5 reanalysis data [36] used to calculate wind characteristics (black dots). Red square indicates the location of the Black Sea Hydrophysical Sub-Satellite Polygon in Katsiveli

**Upwelling.** It was defined as a sharp drop in water temperature of  $5^{\circ}\text{C}$  or more, lasting from six hours to several days [19]. *In situ* measurements were taken in Katsiveli. The total number of upwelling events was determined by counting the number of measurements taken at low water temperatures. This included measurements at which the water temperature dropped sharply, corresponding to the onset of upwelling, as well as subsequent measurements at which the low

temperature was maintained, indicating the upwelling-supporting effect of the wind. An increase in water temperature and its maintenance at high values meant the termination of upwelling.

**Wind.** The study employed 6-hourly ERA5 atmospheric reanalysis data on the  $u$  and  $v$  (m/s) wind speed components at a height of 10 m for the period 1979–2021, with a spatial resolution of  $0.25 \times 0.25^\circ$  [35].

Wind characteristics were calculated for each 6-hour period based on wind speed components averaged over three ERA5 grid nodes in the sea area closest to Katsiveli, with coordinates of  $44.25^\circ$  N and  $33.75^\circ$ ;  $34^\circ$  and  $34.25^\circ$  E (Fig. 1).

For simplicity, winds with a positive zonal component in the speed vector will be called ‘western’ or ‘westerly’ winds, and those with a negative component will be called ‘eastern’ or ‘easterly’ winds.

**Wind upwelling index.** To estimate the wind conditions necessary for an upwelling event, the wind upwelling index was used [27]. This index is based on the calculation of the zonal  $U^{Ek}$  and meridional  $V^{Ek}$  components of the Ekman transport  $\mathbf{V}^{Ek} = (U^{Ek}, V^{Ek})$ ,  $m^2 \cdot s^{-1}$ , which is an integral flow of 1 m width, directed at a  $90^\circ$  angle to the wind direction:

$$U^{Ek} = \frac{\tau_y}{\rho_w f}, \quad V^{Ek} = -\frac{\tau_x}{\rho_w f},$$

where  $\boldsymbol{\tau} = (\tau_x, \tau_y)$  is the wind stress:  $\tau_x = \rho_a C_d |\mathbf{v}|u$ ,  $\tau_y = \rho_a C_d |\mathbf{v}|v$ ,  $u$  is the zonal and  $v$  is the meridional wind speed components  $\mathbf{v} = (u, v)$  at a 10 m height above the sea level;  $\rho_a = 1.2 \text{ kg} \cdot \text{m}^{-3}$  is the air density;  $\rho_w = 1012 \text{ kg} \cdot \text{m}^{-3}$  is the sea water density;  $C_d = 1.3 \cdot 10^{-3}$  is the dimensionless empirical drag coefficient, was taken as constant;  $f$  is the Coriolis parameter.

In the Northern Hemisphere, the Ekman transport  $\mathbf{V}^{Ek} = (U^{Ek}, V^{Ek})$  is directed at a  $90^\circ$  angle to the right of the wind direction. If the coastline is inclined at the  $\alpha$  angle relative to the line of latitude, the  $V^{Ek'}$  transport component (perpendicular to the coastline) is calculated using the zonal and meridional components of the Ekman transport as  $V^{Ek'} = V^{Ek} \cos \alpha - U^{Ek} \sin \alpha$ . In this paper, we do not take into account the small slopes of the coastline from Cape Sarych to Cape Ai-Todor (Fig. 1). It is assumed that the coastline runs parallel to the line of latitude; therefore  $\alpha = 0$ , and  $V^{Ek'} = V^{Ek}$ .

The upwelling index is defined as a transport  $V^{Ek}$  ( $m^3 \cdot s^{-1} \cdot km^{-1}$ ) and calculated per kilometer of the coastline [29, 30]. In addition, the upwelling index is usually defined as positive when the Ekman transport is directed offshore. In the present case, however, the negative transfer is directed offshore, so the index will be defined as  $UI = -V^{Ek}$ . Positive values of the  $UI$  index correspond to the presence

of a western wind. In this case, the Ekman transport is directed offshore, creating conditions for the rise of deep waters (upwelling). Conversely, negative  $UI$  values correspond to an eastern wind, indicating that the Ekman transport is directed onshore, creating conditions for the sinking of surface waters (downwelling).

## Results and discussion

### Seasonal variability of the upwelling index

Calculations of the upwelling index revealed two seasons near the Southern Coast of Crimea during which the wind most often creates conditions conducive to upwelling events: winter (December, January) and summer (June, July) (Fig. 2, *a*). During these months, the zonal component of wind speed is dominated by the westerly direction. Dependence of the seasonal variability of the index on the frequency of westerly winds is clearly evident when comparing Figs. 2, *a* and 2, *b*. The correlation coefficient between them is 0.95. Despite the higher wind speeds in December and January (Fig. 2, *c*), the absolute value of the upwelling index in these months is lower than in June (Fig. 2, *a*). Therefore, on seasonal timescales, the frequency of winds favorable to upwelling events plays a more important role than wind speed.

The most favorable conditions for upwelling are observed in June, when the positive upwelling index reaches its maximum absolute value (Fig. 2, *a*). During this month, the frequency of westerly winds exceeds 60% (Fig. 2, *b*). A local increase in the speed of westerly winds is also observed in June (Fig. 2, *c*). By August, the speed decreases sharply.

Meanwhile, negative values of the upwelling index prevail throughout the year, caused by winds with an easterly component in the velocity vector (Fig. 2, *a*). In other words, downwelling occurs more frequently than upwelling, which is consistent with long-term water temperature observations conducted at the offshore stationary platform in Katsiveli [20]. In addition, eastern winds are faster than western ones in all months (Fig. 2, *c*). Wind conditions favorable for downwelling occur most frequently in October (Fig. 2, *a, b*), as confirmed by observation data [20].

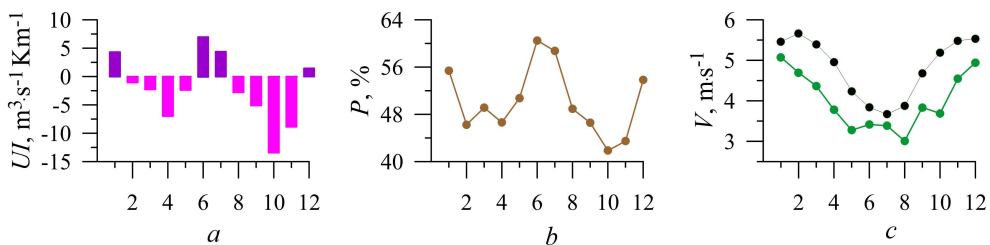


**Fig. 2.** Monthly average values of the upwelling index (*a*), frequency of western winds (*b*), speed of western (green curve) and eastern (black curve) winds (*c*) near the Southern Coast of Crimea in 1979–2021

Taking into account the obtained feature of seasonal variability of the upwelling index, the interannual variability of the conditions for an upwelling event was analyzed based on the data for June. It was considered that, in June:

- the maximum positive upwelling index is reached, corresponding to surface water transfer from the coast and deep-water rise;
- the highest frequency of alongshore westerly winds is observed near the Southern Coast of Crimea (Fig. 2, *b*) [21];
- upwelling is well detected by water temperature [17], since in summer the rising waters from the underlying layers have a lower temperature compared to the temperature of the heated surface waters;
- stratification in the thermocline, which prevents vertical exchange, has not yet reached its maximum value, observed in August [6].

### **Interannual variability of the number of upwelling events and the upwelling index in June**

During the period under consideration (1992–2021), 467 measurements corresponded to upwelling events were recorded in Katsiveli in June. This equates to 17.3% of the total number of measurements (2,700). There were 74 independent upwelling events. On average, 2.4 independent upwelling events and 15.6 low-temperature measurements were observed per month (Table 1). The highest number of upwellings occurred in June in 1993, 2000, 2001, 2005, 2011 and 2021 (Fig. 3, *a*). The maximum number was recorded in 2005: 43. A small number of upwellings or their complete absence were noted in 1999, 2009 and 2016.

Table 1

**Monthly average characteristics of upwelling conditions in June, 1992–2021**

Characteristic	Average	Maximum	Minimum
Total number of daytime observations of low water temperature (upwelling) in month, <i>N</i>	15.6	43.0	1.0
Water temperature, $T_w$ , °C	19.5	23.8	15.0
Speed of western winds, $V$ , $\text{m}\cdot\text{s}^{-1}$	3.1	5.3	2.1
Frequency of western winds, $P$ , %	73.0	83.3	39.2
Upwelling index, $\text{m}^3\cdot\text{s}^{-1}\cdot\text{km}^{-1}$	70.0	255	–107.0

The average water temperature in June during the years under study was 19.5 °C. The highest maximum temperature was recorded in 2019 at an average of 23.8 °C per month (Fig. 3, *c*). Temperatures over 22 °C were also observed in 2007, 2009, 2010, 2013, 2016 and 2018. The lowest average temperature was recorded in 1993 and 2001, at 15 °C.

The most frequent occurrence of winds with a westerly component in the velocity vector (83.3%) was observed in 2021 (Fig. 3, *e*), while the minimum (39.2%) was observed in 2018. The average monthly speed of westerly winds peaked at 5.3  $\text{m}\cdot\text{s}^{-1}$  in 2001 (Fig. 3, *d*). The lowest speed of 2.1  $\text{m}\cdot\text{s}^{-1}$  was recorded in 1998.

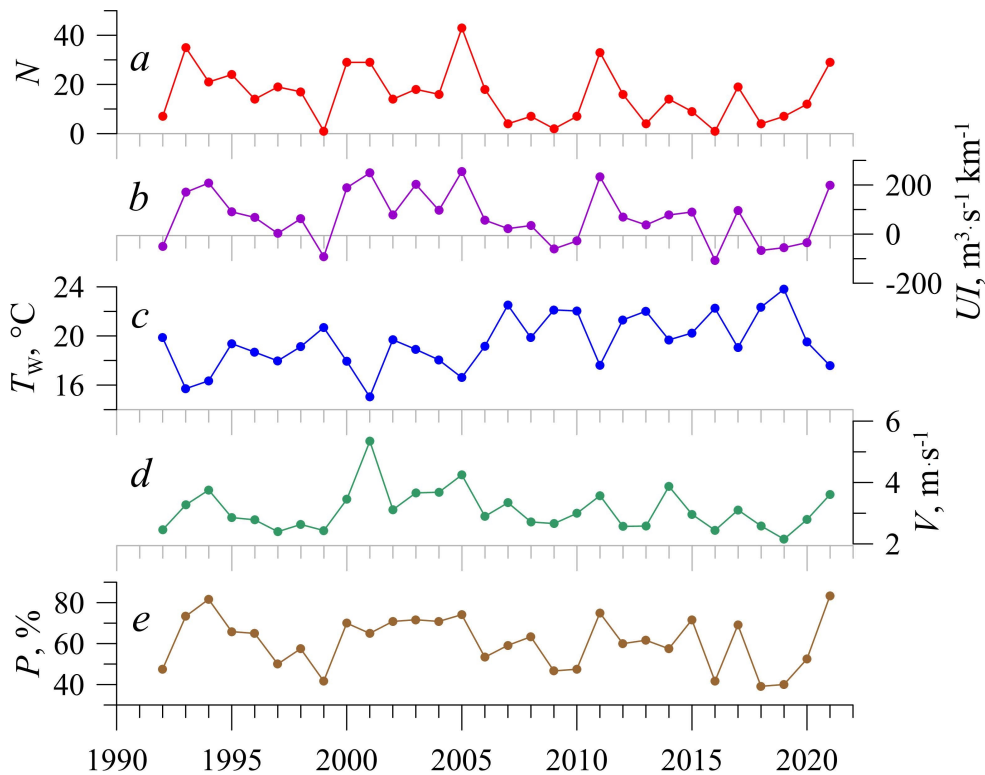


**Fig. 3.** Total number of daytime observations of low water temperature (upwelling) for June (a); June average values of upwelling index  $UI$  (b), water temperature  $T_w$  (c), speed  $V$  (d) and frequency  $P$  (e) of westerly winds

The excess of positive values of the upwelling index over negative values indicates stable wind conditions favorable for upwelling near the Southern Coast of Crimea in June (Table 1, Fig. 3, b). The maximum number of upwellings, in combination with low water temperature, occurred in 2001 and 2005, which correspond to the maximum positive values of the upwelling index (Fig. 3, a, b). The absence of upwelling in 1999 and 2016 is consistent with the low values of the upwelling index.

Table 2

**Correlation coefficients between the time series (1992–2021): number of observations of low water temperature (upwelling)  $N$ , June average water temperature  $T_w$ , upwelling index  $UI$ , speed  $V$  and frequency  $P$  of the westerly winds**

Time series	$T_w$	$UI$	$V$	$P$
$N$	-0.84	0.88	0.69	0.71
$T_w$	1.00	-0.81	-0.68	-0.71
$UI$	-0.81	1.00	0.83	0.89

There is a highly significant relationship between the time series of the monthly total number of upwelling measurements and the upwelling index. The correlation coefficient is 0.88 (Table 2). The correlation coefficient of

the upwelling index with the average water temperature is  $-0.81$ , and with the speed and frequency of western winds is  $0.83$  and  $0.89$ , respectively.

Therefore, the upwelling index describes effectively the variability of wind conditions conducive to upwelling based on monthly averages and can be employed in climate studies in areas where regular measurements are unavailable.

### Upwelling events in June 2001 and 2019

The conditions for the occurrence of upwellings in individual years are considered in more detail in cases:

- high speed and frequency of westerly winds and minimum average water temperature (2001);
- low frequency of westerly winds and maximum average water temperature (2019).

*Upwellings in June 2001.* In June 2001, the lowest average water temperature ( $15\text{ }^{\circ}\text{C}$ ) and the highest average wind speed ( $5.3\text{ m}\cdot\text{s}^{-1}$ ) were observed during the study period. Two independent upwellings were recorded in this month (Fig. 4, c). The first, which was accompanied by a sharp drop in temperature from  $17$  to  $9.3\text{ }^{\circ}\text{C}$ , developed on 5 June during the day with a stable southwesterly wind (Fig. 4, a). The upwelling occurred after an increase in wind speed to  $16\text{ m}\cdot\text{s}^{-1}$ . At the same time, the upwelling index reached an unusually high value of  $3600\text{ m}^3\cdot\text{s}^{-1}\cdot\text{km}^{-1}$  (Fig. 4, b). The upwelling ended on 10 June when the wind direction changed to the southeasterly.

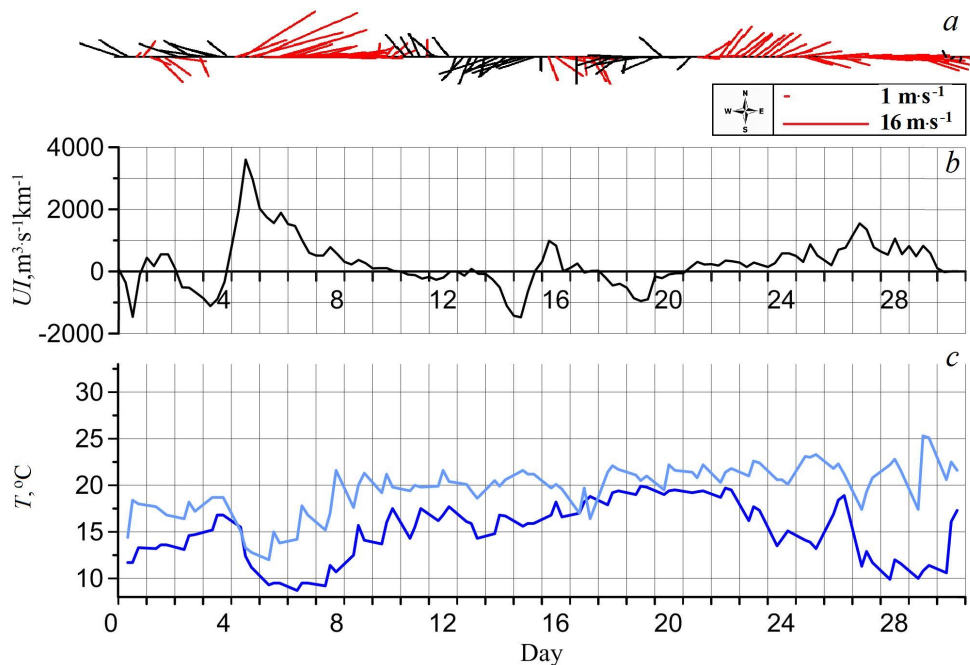


**Fig. 4.** Wind direction (red color indicates westerly winds, black color – easterly winds) (a), upwelling index  $UI$  (b), water temperature  $T_W$  (blue line) and air temperature  $T_A$  (light blue line) based on the daytime measurements in Katsiveli (c) in June 2001

Similar wind conditions (a prolonged southwesterly wind with speeds over  $6\text{--}10\text{ m}\cdot\text{s}^{-1}$ ) caused long-term upwelling from 23 to 30 June, resulting in a decrease in water temperature of almost  $10\text{ }^{\circ}\text{C}$  (Fig. 4, *a, c*). The onset of upwelling at Katsiveli is clearly visible in the 24 June satellite image (Fig. 5, *a*). On 26 June, a short-term weakening of the western wind (no more than half a day) was followed by an increase in the surface water temperature near the shore. On 27 June, when the western wind increased to a speed of  $10\text{ m}\cdot\text{s}^{-1}$ , the temperature dropped again to  $10\text{ }^{\circ}\text{C}$ . Positive values of the index during the third ten-day period of June are consistent with a decrease in water temperature during this period (Fig. 4, *b*).

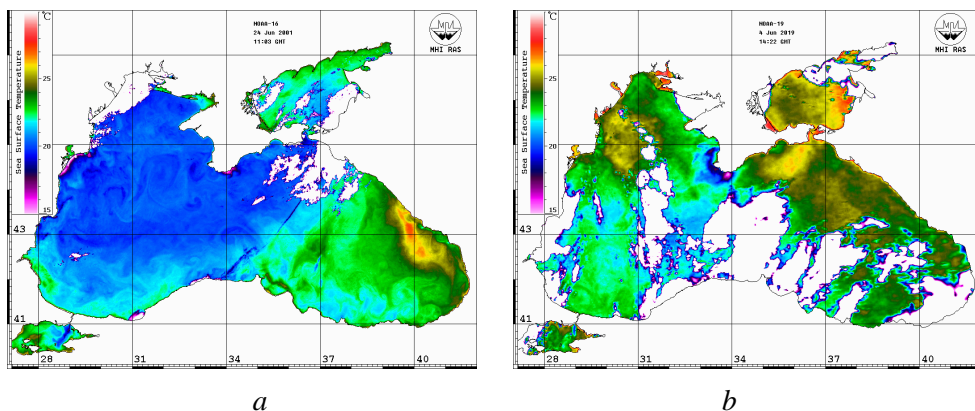


**Fig. 5.** Sea surface temperature at 11:03 GMT on June 24, 2001 (NOAA 16) (*a*) and at 14:22 GMT on June 4, 2019 (NOAA-19) (*b*) taken from the satellite map archive (available at: [http://dvs.net.ru/mp/index\\_ru.shtml](http://dvs.net.ru/mp/index_ru.shtml))

*Upwelling events in June 2019.* According to coastal measurements, the maximum average water temperature of  $23.8\text{ }^{\circ}\text{C}$  was observed in June 2019 (Table 1). The only upwelling occurred at the beginning of the month, from 3 to 5 June (Fig. 6, *c*). During this period, the temperature fell from  $22$  to  $14\text{ }^{\circ}\text{C}$ . This was caused by a sharp increase in the westerly wind to  $5\text{ m}\cdot\text{s}^{-1}$  (Fig. 6, *a*). The decrease in water temperature on 4 June is clearly seen in the satellite image (Fig. 5, *b*). No upwelling was observed during the remaining days of the month. The northwesterly winds observed at the end of the month, from 27 June, were accompanied by only a slight decrease in temperature.

This situation, characterized by a small number of upwelling events, was associated with the low frequency of westerly winds (Fig. 6, *a*). During the month, the northeasterly wind contributed to a surge of warm surface water towards the shore and its subsequent descent (downwelling). The upwelling index was negative for most of the month (Fig. 6, *b*).

An analysis of June data from all years (1992–2021) showed that the wind speed leading to upwelling in June mostly exceeds  $5\text{--}6\text{ m}\cdot\text{s}^{-1}$ , with an index value exceeding  $520\text{ m}\cdot\text{s}^{-1}\cdot\text{km}^{-1}$ . This wind speed is consistent with the results obtained in [13]. It should be noted that these values may increase with a growth in the thickness of the heated sea layer and increased stratification of waters in the thermocline in July and August.

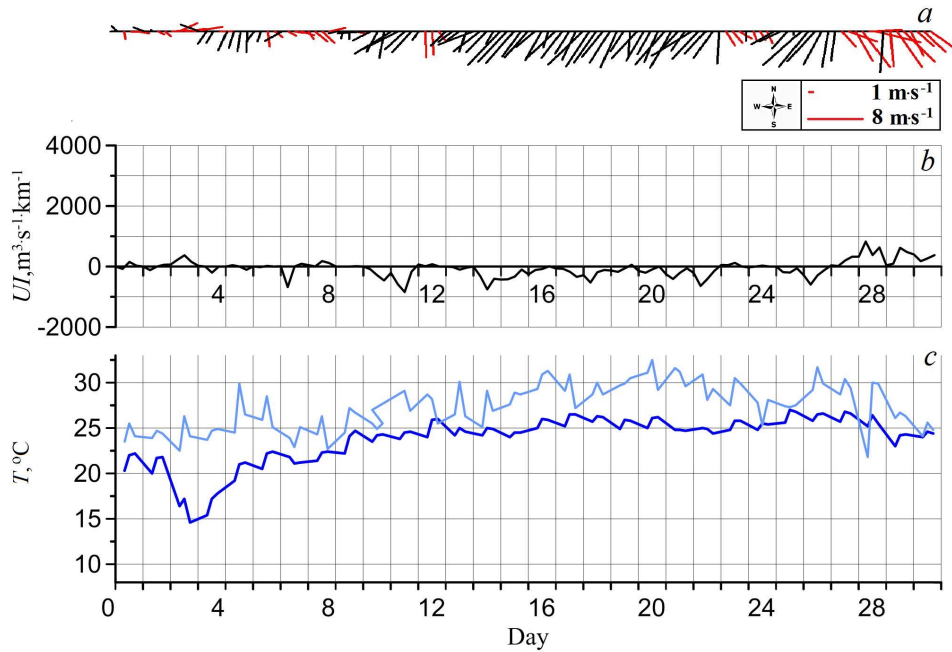


**Fig. 6.** The same as in Fig. 4, June 2019

According to daytime measurements, the air temperature in June was generally higher than the water temperature. In the absence of upwelling, the difference is 1–5 °C; with upwelling, it increases to 10 °C or more.

### Conclusion

This paper studies the wind conditions necessary for upwelling to occur near the Southern Coast of Crimea, in the Katsiveli area, using the wind upwelling index. This index represents the value of Ekman water transfer towards or away from the coast depending on the direction and speed of the alongshore wind.

It was found that conditions for an upwelling event vary by season. In December, January, June and July, the average upwelling index is positive, and the Ekman transport is mainly directed offshore due to the high frequency of westerly winds. This creates favorable conditions for the development of upwelling. In other months, the index is negative. The Ekman transfer of water to the coast predominates, which creates conditions for the development of downwelling.

A comparison of the interannual variability of the monthly average values of the upwelling index and the number of *in situ* coastal upwelling observations in June showed a high correlation between these characteristics, with a correlation coefficient of 0.88. Analysis of 6-hour observation data demonstrated good agreement between upwelling index values and measured water temperature. A decrease in temperature starts with a sharp increase in westerly wind speed. High

positive values of the wind index, corresponding to high wind speeds, precede the appearance of low sea surface temperatures in summer. Stable westerly winds can support long-term upwelling. A weakening of the westerly winds or a change in wind direction to the east leads to the termination of upwelling.

The results of this paper demonstrate the potential for using the wind index to study and forecast coastal Ekman upwelling, as well as for climate studies along the Southern Coast of Crimea. However, further analysis of wind-driven upwelling processes on hourly and daily time scales is actual.

#### REFERENCES

1. Ereemeev, V.N., Boltachev, A.R., Aleksandrov, B.G., Alyomov, S.V., Zagorodnya, Yu.A., Karpova, E.P., Manzhos, L.A. and Gubanov, V.V., 2012. *Biological Diversity of the Coastal Zone of the Crimean Peninsula: Problems, Preservation and Restoration Pathways*. Sevastopol: Institute of Biology of the Southern Seas, 92 p.
2. Massa, F., Aydın, I., Fezzardi, D., Akbulut, B., Atanasoff, A., Beken, A.T., Bekh, V., Buhlak, Y., Burlachenko, I. [et al.], 2021. Black Sea Aquaculture: Legacy, Challenges & Future Opportunities. *Aquaculture Studies*, 21(4), pp. 181-220. [http://doi.org/10.4194/2618-6381-v21\\_4\\_05](http://doi.org/10.4194/2618-6381-v21_4_05)
3. Arrigo, K.R., 2005. Marine Microorganisms and Global Nutrient Cycles. *Nature*, 437(7057), pp. 349-355. <https://doi.org/10.1038/nature04159>
4. Varenik, A.V., Kondratyev, S.I., Medvedev, E.V., Khoruzhiy, D.S. and Orekhova, N.A., 2023. Characteristics of State and Evolution of the Black Sea Hydrochemical Structure. *Physical Oceanography*, 30(6), pp. 826-850.
5. Kubryakov, A.A., Belokopytov, V.N., Zatsepin, A.G., Stanichny, S.V. and Piotukh, V.B., 2019. The Black Sea Mixed Layer Depth Variability and Its Relation to the Basin Dynamics and Atmospheric Forcing. *Physical Oceanography*, 26(5), pp. 397-413. <https://doi.org/10.22449/1573-160X-2019-5-397-413>
6. Ivanov, V.A. and Belokopytov, V.N., 2013. *Oceanography of the Black Sea*. Sevastopol: MHI, 210 p.
7. Checkley, D.M. and Barth, J.A., 2009. Patterns and Processes in the California Current System. *Progress in Oceanography*, 83(1-4), pp. 49-64. <https://doi.org/10.1016/j.pocean.2009.07.028>
8. Stelmakh, L.V., 2020. Methodology of Comprehensive Monitoring of Modern Black Sea Phytoplankton Community Status. *Monitoring Systems of Environment*, (1), pp. 21-26. <https://doi.org/10.33075/2220-5861-2020-1-21-26> (in Russian).
9. Finenko, Z.Z., Mansurova, I.M., Kovalyova, I.V. and Georgieva, E.Yu., 2021. Development of Phytoplankton in the Winter-Spring Period in the Coastal Waters of Crimea. *Marine Biological Journal*, 6(1), pp. 102-114. <https://doi.org/10.21072/mbj.2021.06.1.08> (in Russian).
10. Kostianiaia, E.A. and Kostianoy, A.G., 2021. Regional Climate Change Impact on Coastal Tourism: A Case Study for the Black Sea Coast of Russia. *Hydrology*, 8(3), 133. <https://doi.org/10.3390/hydrology8030133>
11. Kämpf, J. and Chapman, P., 2016. *The Functioning of Coastal Upwelling Systems*. In: J. Kämpf and P. Chapman, 2016. *Upwelling Systems of the World. A Scientific Journey to the Most Productive Marine Ecosystems*. Cham: Springer, pp. 31-65. [https://doi.org/10.1007/978-3-319-42524-5\\_2](https://doi.org/10.1007/978-3-319-42524-5_2)

12. Jacox, M.G. and Edwards, C.A., 2011. Effects of Stratification and Shelf Slope on Nutrient Supply in Coastal Upwelling Regions. *Journal of Geophysical Research: Oceans*, 116(C3), C03019. <https://doi.org/10.1029/2010JC006547>
13. Zatsepin, A.G., Silvestrova, K.P., Piotoukh, V.B., Kuklev, S.B. and Podymov, O.I., 2016. Observations of a Cycle of Intense Coastal Upwelling and Downwelling at the Research Site of the Shirshov Institute of Oceanology in the Black Sea. *Oceanology*, 56(2), pp. 188-199. <https://doi.org/10.1134/S0001437016020211>
14. Silvestrova, K.P., Zatsepin, A.G. and Myslenkov, S.A., 2017. Coastal Upwelling in the Gelendzhik Area of the Black Sea: Effect of Wind and Dynamics. *Oceanology*, 57(4), pp. 469-477. <https://doi.org/10.1134/S0001437017040178>
15. Gawarkiewicz, G., Korotaev, G., Stanichny, S., Repetin, L. and Soloviev, D., 1999. Synoptic Upwelling and Cross-Shelf Transport Processes along the Crimean Coast of the Black Sea. *Continental Shelf Research*, 19(8), pp. 977-1005. [https://doi.org/10.1016/S0278-4343\(99\)00003-5](https://doi.org/10.1016/S0278-4343(99)00003-5)
16. Goryachkin, Yu.N., 2018. Upwelling nearby the Crimea Western Coast. *Oceanography*, 25(5), pp. 368-379. <https://doi.org/10.22449/1573-160X-2018-5-368-379>
17. Stanichnaya, R.R. and Stanichny, S.V., 2021. Black Sea Upwellings. *Current Problems in Remote Sensing of the Earth from Space*, 18(4), pp. 195-207. <https://doi.org/10.21046/2070-7401-2021-18-4-195-207> (in Russian).
18. Kubryakov, A., Aleskerova, A. and Mizyuk, A., 2024. Submesoscale Features of Coastal Upwellings in the Black Sea: Observations and Modeling. *Continental Shelf Research*, 279, 105291. <https://doi.org/10.1016/j.csr.2024.105291>
19. Lovenkova, E.A. and Polonskii, A.B., 2005. Climatic Characteristics of Upwelling near the Crimean Coast. *Russian Meteorology and Hydrology*, (5), pp. 31-37.
20. Kuklin, A.K., Kuklina, N.Ya. and Shabalina, O.A., 2014. [Sea Water Temperature near the Oceanographic Platform in Katsiveli]. *Ecological Safety of Coastal and Shelf Zones and Comprehensive Use of Shelf Resources*, 28, pp. 186-194 (in Russian).
21. Shokurova, I.G., Plastun, T.V., Kasianenko, T.E., Stanichnaya, R.R., Krashennnikova, S.B. and Simonova, Yu.V., 2023. Winds Favorable for Upwellings near the Southern Coast of Crimea. *Physical Oceanography*, 30(4), pp. 398-409.
22. Tolstosheev, A.P., Motyzhev, S.V. and Lunev, E.G., 2020. Results of Long-Term Monitoring of the Shelf Water Vertical Thermal Structure at the Black Sea Hydrophysical Polygon of RAS. *Physical Oceanography*, 27(1), pp. 69-80. <https://doi.org/10.22449/1573-160X-2020-1-69-80>
23. Simonova, Yu.V., Stanichny, S.V. and Lemeshko, E.M., 2024. The Features of Anomalies in Surface Temperature of the Black Sea in the Area of the Southern Coast of Crimea. *Sovremennye Problemy Distantionnogo Zondirovaniya Zemli iz Kosmosa*, 21(3), pp. 234-243. <https://doi.org/10.21046/2070-7401-2024-21-3-234-243> (in Russian).
24. Silvestrova, K.P., Myslenkov, S.A. and Repkov, D.S., 2022. Wind Upwelling Forecast for the Russian Black Sea Coast. *Hydrometeorological Research and Forecasting*, 1(383), pp. 89-107. <https://doi.org/10.37162/2618-9631-2022-1-89-107>
25. Ivanov, V.A. and Mikhailova, E.N., 2008. *Upwelling in the Black Sea*. Sevastopol: ECOSI-Gidrofizika, 92 p. (in Russian).
26. Polonskii, A.B. and Muzyleva, M.A., 2016. Modern Spatial-Temporal Variability of Upwelling in the North-Western Black Sea and off the Crimea Coast. *Izvestiya Rossiiskoi Akademii Nauk*.

- Seriya Geograficheskaya*, (4), pp. 96-108. <https://doi.org/10.15356/0373-2444-2016-4-96-108> (in Russian).
27. Bakun, A., 1973. *Coastal Upwelling Indices, West Coast of North America, 1946–71*. NOAA Technical Report NMFS SSRF. Seattle, WA: National Marine Fisheries Service, 103 p.
  28. Pérez, F.F., Padín, X.A., Pazos, Y., Gilcoto, M., Cabanas, M., Pardo, P.C., Doval, M.D. and Farina-Busto, L., 2010. Plankton Response to Weakening of the Iberian Coastal Upwelling. *Global Change Biology*, 16(4), pp. 1258-1267. <https://doi.org/10.1111/j.1365-2486.2009.02125.x>
  29. González-Nuevo, G., Gago, J. and Cabanas, J.M., 2014. Upwelling Index: A Powerful Tool for Marine Research in the NW Iberian Upwelling System. *Journal of Operational Oceanography*, 7(1), pp. 47-57. <https://doi.org/10.1080/1755876X.2014.11020152>
  30. Ferreira, S., Sousa, M., Picado, A., Vaz, N. and Dias, J.M., 2022. New Insights about Upwelling Trends off the Portuguese Coast: An ERA5 Dataset Analysis. *Journal of Marine Science and Engineering*, 10(12), 1849. <https://doi.org/10.3390/jmse10121849>
  31. Zhabin, I.A., Dmitrieva, E.V., Dubina, V.A. and Luchin, V.A., 2022. Variability of Summer Wind-Driven Upwelling along the Koryak Coast in the Northwestern Bering Sea Based on Satellite Data. *Izvestiya, Atmospheric and Oceanic Physics*, 58(12), pp. 1438-1449. <https://doi.org/10.1134/S0001433822120283>
  32. Mihailov, M.E., 2024. *The Black Sea Upwelling System: Analysis on the Western Shallow Waters*. *Atmosphere*, 15(8), 999. <https://doi.org/10.3390/atmos15080999>
  33. Jacox, M.G., Edwards, C.A., Hazen, E.L. and Bograd, S.J., 2018. Coastal Upwelling Revisited: Ekman, Bakun, and Improved Upwelling Indices for the U.S. West Coast. *Journal of Geophysical Research: Oceans*, 123(10), pp. 7332-7350. <https://doi.org/10.1029/2018JC014187>
  34. Zhuk, E., Khaliulin, A., Zodiatis, G., Nikolaidis, A. and Isaeva, E., 2016. Black Sea GIS Developed in MHI. In: SPIE, 2016. *Proceedings of SPIE*. Volume 9688, Fourth International Conference on Remote Sensing and Geoinformation of the Environment (RSCy2016), 96881C. <https://doi.org/10.1117/12.2241631>
  35. Hersbach, H., Bell, B., Berrisford, P., Hirahara, S., Horányi, A., Muñoz-Sabater, J., Nicolas, J., Peubey, C., Radu, R. [et al.], 2020. The ERA5 Global Reanalysis. *Quarterly Journal of the Royal Meteorological Society*, 146(730), pp. 1999-2049. <https://doi.org/10.1002/qj.3803>

Submitted 18.11.2024; approved after review 29.11.2024;  
accepted for publication 13.03.2025.

*About the authors:*

**Irina G. Shokurova**, Senior Researcher, Marine Hydrophysical Institute of RAS (2 Kapitanskaya Str., Sevastopol, 299011, Russian Federation), CSc. (Geogr.), **ORCID ID: 0000-0002-3150-8603**, **WOS ResearcherID: C-8223-2016**, [igshokurova@mail.ru](mailto:igshokurova@mail.ru)

**Tatyana V. Plastun**, Junior Researcher, Marine Hydrophysical Institute of RAS (2 Kapitanskaya Str., Sevastopol, 299011, Russian Federation), **ORCID ID: 0000-0001-7685-7455**, **WOS ResearcherID: AAC-1888-2022**, [ptv63@inbox.ru](mailto:ptv63@inbox.ru)

**Yulia V. Simonova**, Junior Researcher, Black Sea Sub-Satellite Polygon, Marine Hydrophysical Institute of RAS (2 Kapitanskaya Str., Sevastopol, 299011, Russian Federation), **ORCID ID: 0000-0002-8075-8748**, **WoS ResearcherID: GYU-2700-2022**, [julia.simonova.0502@gmail.com](mailto:julia.simonova.0502@gmail.com)

**Valeria Yu. Kasianenko**, Student, V.I. Vernadsky Crimean Federal University (5/7 Lenina Blvd., Simferopol, 295051, Russian Federation)

*Contribution of the co-authors:*

**Irina G. Shokurova** – wind and temperature data processing, visualization, writing and editing of the text, literature review, discussion of results

**Tatyana V. Plastun** – wind and temperature data processing, visualization, writing and editing of the text, literature review, discussion of results

**Yulia V. Simonova** – water and air temperature data collection and processing, visualization, text editing, discussion of results

**Valeria Yu. Kasianenko** – work with satellite map archive, visualization, discussion of results

*The authors have read and approved the final manuscript.*

*The authors declare that they have no conflict of interest.*

Original article

## Accumulation of Heavy Metals and Distribution of the Areas of Technogenic Loads in Balaklava Bay: Results of Long-Term Research

K. I. Gurov , E. A. Kotelyanets, Yu. S. Gurova

*Marine Hydrophysical Institute of RAS, Sevastopol, Russian Federation*

 [gurovki@gmail.com](mailto:gurovki@gmail.com)

### Abstract

**Purpose.** The purpose of the study is to define the spatial distribution of heavy metal concentrations in bottom sediments and identify areas of technogenic load in Balaklava Bay in 2005–2019, using different geochemical coefficients and indices.

**Methods and Results.** The samples of the surface layer of bottom sediments (0–5 cm) were collected using a Peterson bottom grab in 2005, 2015, 2018 and 2019 and analyzed. The bulk content of elements was determined by the method of X-ray fluorescence analysis using a Spectroscan MAKS-G spectrometer. In order to assess the contribution of anthropogenic sources to bottom sediment pollution relative to the background content of metals in the coastal zone of the Crimean Peninsula shelf, the following indicators were applied: element concentration levels in sediments, total pollution indices, enrichment factors and geoaccumulation index. According to estimates of the degree of bottom sediments pollution in Balaklava Bay obtained from 2005 to 2019, the pollution level varied from low for elements such as V, Cr and Ni, to high for Cu, Zn and Pb. The most polluted areas were noted in the northern part of the basin, specifically in its central and apex parts. Bottom sediments in the Balaklava Bay basin southern part remained unpolluted throughout the period under study.

**Conclusions.** It has been shown that the elevated level of pollution in the bottom sediments of the northern part of the bay is the result of a complex impact of natural and anthropogenic factors. However, the proximity of the polluted areas to municipal and storm water runoffs and yacht marinas suggests that the anthropogenic contribution exceeds the natural one. Furthermore, the increase in the values of the studied indices and parameters indicates that this contribution is growing over time.

**Keywords:** Balaklava Bay, bottom sediments, heavy metals, contamination factors, enrichment factor, geoaccumulation index

**Acknowledgements:** The study was carried out within the framework of state assignments of FSBSI FRC MHI FNNN-2024-0016 “Studies of spatial and temporal variability of oceanological processes in the coastal, near-shore and shelf zones of the Black Sea influenced by natural and anthropogenic factors on the basis of in situ measurements and numerical modelling“ and FNNN-2025-0001 on theme “Monitoring of CO<sub>2</sub> concentrations in the surface water layer and atmosphere in the inland seas of Russia”.

**For citation:** Gurov, K.I., Kotelyanets, E.A. and Gurova, Yu.S., 2025. Accumulation of Heavy Metals and Distribution of the Areas of Technogenic Loads in Balaklava Bay: Results of Long-Term Research. *Physical Oceanography*, 32(3), pp. 326-346.

© 2025, K. I. Gurov, E. A. Kotelyanets, Yu. S. Gurova

© 2025, Physical Oceanography

### Introduction

Bottom sediments represent a relatively stable yet complex multicomponent system capable of accumulating various chemical substances, particularly heavy metals, and acting as a source of secondary pollution in water bodies through physicochemical processes such as desorption, diffusion and resuspension, as well



as biological processes such as bioturbation and bioirrigation [1, 2]. Once heavy metal compounds enter an aquatic environment, they undergo various transport and transformation processes, which are influenced by multiple factors. The danger posed by heavy metals as pollutants is exacerbated by their long-term redistribution across components of the marine ecosystem, with accumulation occurring in hydrobionts at different levels of the food chain [3–5].

Monitoring the levels of pollutants and heavy metals in bottom sediments is highly relevant for the coastal areas of the Black Sea, particularly the Crimean Peninsula, which is renowned for its resorts. Of particular interest are observations of self-purification and secondary pollution processes in water bodies subjected to anthropogenic pressure. Balaklava Bay is a characteristic example of a semi-enclosed water area exposed to prolonged and intensive anthropogenic impact.

While studies of Balaklava Bay were sporadic in the 20<sup>th</sup> and early 21<sup>st</sup> centuries, the bay is now being examined in detail and on a regular basis by researchers from Marine Hydrophysical Institute (MHI) of the Russian Academy of Sciences and Institute of Biology of the Southern Seas (IBSS) RAS [6–18]. The increased interest in researching Balaklava Bay in recent years is linked to its use as an active yacht marina, which has led to greater anthropogenic pressure on the bay ecosystem and consequently a decline in its ecological state. To date, the oceanographic, hydrological and hydrochemical characteristics [6–8] of the bay waters and the adjacent part of Megalo-Yalo Gulf have been thoroughly investigated, as have wave dynamics and water circulation using mathematical modeling [9–11]. Important studies on the physicochemical [12–16] and radiochemical [17] properties of bottom sediments have also been conducted over the past decade. Studies [12–15] have examined the granulometric composition of sediments and their dynamics [16] in detail. The accumulation patterns of various organic [13, 15, 18] and inorganic [14, 17] pollutants have also been investigated. Research [14, 15] has focused on identifying correlations between the accumulation of different elements and the physical (granulometric composition and moisture content) and chemical (organic matter and carbonate content) characteristics of bottom sediments.

However, a comprehensive study of the spatial variability of microelement pollution levels in bottom sediments, or an assessment of temporal changes in this pollution, has not yet been conducted in Balaklava Bay. It is crucial to evaluate spatial and temporal variations in the intensity of anthropogenic pollution in order to determine the rate and direction of changes in the anthropogenic load on the ecosystem.

According to [19], the total content of heavy metals (Cr, Cu, Ni, Pb, Zn) in the bottom sediments of Balaklava Bay in 2005 was 558 mg/kg, which is higher than the levels found in Sevastopol Bay (431 mg/kg) [19], the coastal areas of Crimea (281 mg/kg) [20] and Turkey (260 mg/kg) [21], as well as in the northeastern part of the Black Sea (163 mg/kg, excluding Ni) [22]. By way of comparison, the total microelement content of bottom sediments in some Mediterranean coastal areas

ranged from 30–163 mg/kg [23–25], while the levels in Al-Harar Lagoon in the Red Sea and the South China Sea shelf were 136 mg/kg [26] and 125 mg/kg [27], respectively. However, the values obtained in Balaklava Bay are comparable to those in Tokyo Bay (536 mg/kg) [28] and Boston Harbor (689 mg/kg) [29], but significantly lower than in New York Harbor (1270 mg/kg) [30] or in sediments from industrial centers such as Birmingham, UK (1090 mg/kg) [31], Baoji, China (1296 mg/kg) [32], and Seoul, South Korea (4494 mg/kg) [33].

Current regulatory standards for permissible metal levels in bottom sediments do not account for regional variations in pollutant accumulation. Such an assessment can be performed using geochemical indices, such as the Enrichment Factor (*EF*) and the Geoaccumulation Index ( $I_{geo}$ ), which reflect the concentration of an element in sediments relative to its background level [34–36]. According to [37], since anthropogenic anomalies are polyelemental, cumulative pollution indices must be calculated. The Pollution Load Index (*PLI*) and the Degree of Contamination ( $C_{deg}$ ) are two widely used indices for assessing pollution in coastal sediments worldwide [38–40]. In this study, the following metals were selected to calculate cumulative pollution indices: V, Cr, Ni, Cu, Zn, Pb, Sr, Fe, Mn and Ti. This selection is based on previous research into sediments from Balaklava [14, 15] and Sevastopol Bays [19], as well as the Crimean shelf [20], in which these metals were analyzed.

This paper aims to identify features of microelement and heavy metal accumulation in the bottom sediments of Balaklava Bay, and to assess the spatial distribution of areas of technogenic loads between 2005 and 2018, using various geochemical indices.

### **Materials and methods**

The study used data obtained during field expeditions carried out by Marine Hydrophysical Institute (MHI) in Balaklava Bay in 2005, 2015, 2018, and 2019 (Fig. 1). Data on the granulometric composition of the sediments and their organic carbon ( $C_{org}$ ) content in Balaklava Bay was obtained from previous studies [12, 14, 15].

Based on the bottom morphometry, shoreline configuration and hydrodynamic features of the water masses and bottom sediments, the bay water area was divided into several zones: a shallow northern basin with an isolated apex in the innermost part of the bay; a central section; a southern basin; and a knee-shaped narrowness connecting the latter two zones [7].

Surface sediment samples (from the 0–5 cm layer) were collected using a Petersen grab sampler (coverage area: 0.025 m<sup>2</sup>). For metal analysis, the top 5 cm of sediment was subsampled from the central part of the grab using a plastic spoon and placed into pre-labeled zip-lock polyethylene bags. The samples were then transported to the laboratory, where they were oven-dried at 105°C until they reached constant weight and were homogenized.

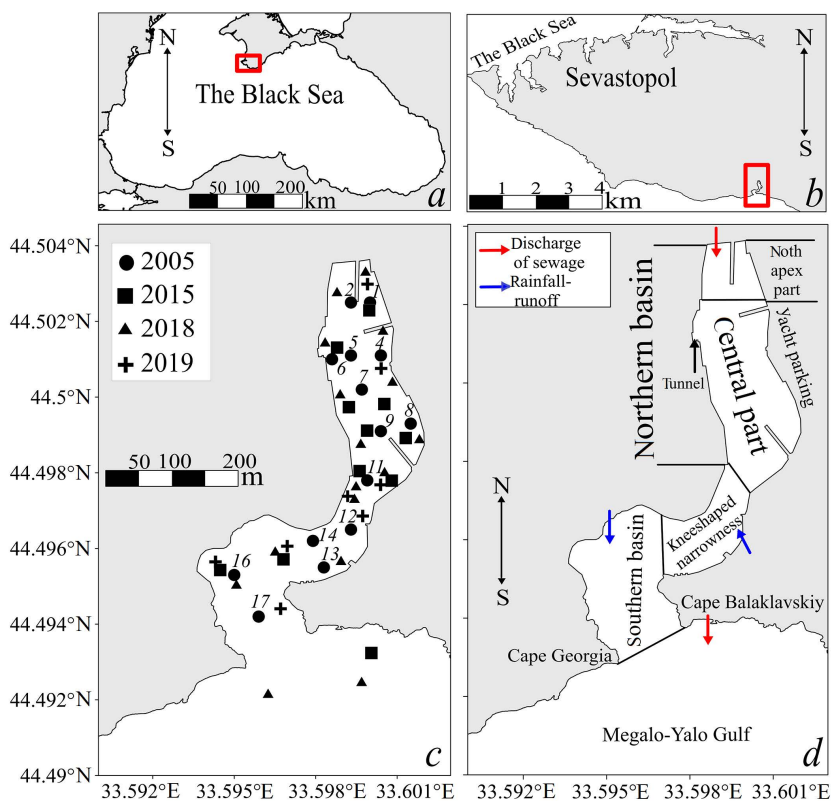


**Fig. 1.** Location of the Sevastopol region under study (highlighted in red rectangle) (a), its enlarged image (red rectangle marks Balaklava Bay) (b), scheme of the bottom sediment sampling stations in Balaklava Bay (c), zoning of the bay water area and location of the main storm and sewage water runoffs (d)

The total content of chemical elements (Fe, Mn, Ti, V, Cr, Ni, Cu, Zn, Sr, Pb) was determined using X-ray fluorescence (XRF) spectroscopy on a Spectroscan Max-G spectrometer (Spectron, Russia). This method enables the total concentration of elements (from Be to U) to be determined in various natural substances in the range of 0.0001–100%<sup>1</sup>. Calibration curves were constructed using certified reference soil samples, including typical black soil, sod-podzolic sandy loam, red soil and carbonate gray soil. The calibration was validated using certified reference materials (CRMs) DSZU 163.1-98 and DSZU 163.2-98. To assess the reproducibility and accuracy of measurements, the certified bottom sediment (DSZU 163.1-98) was analyzed eight times. The minimum standard deviation was 0.003% for MnO and the maximum was 7.62% for Cr.

<sup>1</sup> NPO Spektron, 2016. *Methodology for Measuring the Mass Fraction of Metals and Metal Oxides in Powdered Soil Samples by X-ray Fluorescence Analysis M049-P/16*. Saint Petersburg: NPO Spektron LLC, 18 p. (in Russian).

To evaluate the intensity of microelement accumulation in the surface sediment layer between 2005–2015 and 2015–2018, the percentage increase in concentration was calculated using the following formula:

$$\Delta = (C_{\text{end}} - C_{\text{start}}) / C_{\text{start}} \cdot 100,$$

where  $\Delta$  is the increase in concentration, %;  $C_{\text{start}}$  and  $C_{\text{end}}$  are the initial and final metal concentrations (mg/kg), respectively.

For the period from 2005 to 2015, the increase in concentration was calculated as the difference between concentrations in 2015 and 2005. For the period from 2015 to 2018, the increase in concentration was calculated as the difference between the concentration in 2018 and 2015.

The Pollution Load Index (*PLI*), which is a cumulative indicator of sediment pollution by metals, was calculated according to [35]:

$$PLI = \sqrt[n]{CF_1 \cdot CF_2 \cdot CF_3 \cdot \dots \cdot CF_n},$$

where  $CF_{1,2,3,\dots}$  are the contamination factors for each metal;  $n$  is the number of metals analyzed (here,  $n = 10$ ).  $PLI > 1$  indicates polluted sediments;  $PLI \leq 1$  indicates unpolluted sediments.

Degree of Contamination ( $C_{\text{deg}}$ ), which assesses overall pollution levels, was calculated according to [34]:

$$C_{\text{deg}} = \sum_{i=1}^n CF_i,$$

where  $C_{\text{deg}}$  at a low level – less than 10, at a moderate level – in the range of 10–20, at a significant level – 20–40, at a very high level it is 40 or more.

The Enrichment Factor (*EF*), first introduced in [40], quantifies the normalized accumulation level of an element in bottom sediments relative to its background concentration. This enables the evaluation of anthropogenic contributions. Initially, EF calculations initially used average metal concentrations in the upper continental crust as a reference. However, crustal averages often fail to accurately represent regional geochemical baselines. To improve accuracy, we adopted average values of metal concentrations for the coastal region of Crimea [20], obtained by the authors using methodology <sup>1</sup> (consistent with the analytical protocol of the present study).

The Enrichment Factor (*EF*) is calculated using the following equation:

$$EF = \frac{(EL/EL_{\text{ind}})_{\text{sample}}}{(EL/EL_{\text{ind}})_{\text{background}}},$$

where  $(EL/EL_{\text{ind}})_{\text{sample}}$  is the ratio of the target element concentration to the concentration of the indicator element (titanium was selected for this study) in the sediment sample (mg/kg);  $(EL/EL_{\text{ind}})_{\text{background}}$  is the ratio of the background concentrations of the target element to titanium (mg/kg) in the coastal regions of the Crimean Peninsula [20]. The rationale for selecting titanium as the indicator element is also explained by the fact that it is a major constituent of soils and

sediments, and is highly resistant to weathering and anthropogenic influences [41]. The *EF* is commonly used in marine and estuarine sediment studies as an indicator of pollution [42–46].

The *EF* values were interpreted according to [46] using the following classification: *EF* values not exceeding 1 indicate no accumulation; *EF* values in the range 1–3 indicate insignificant accumulation; *EF* values in the range 3–5 indicate moderate accumulation; *EF* values in the range 5–10 indicate moderately heavy accumulation; *EF* values in the range 10–25 indicate heavy accumulation; *EF* values in the range 25–50 indicate very heavy accumulation; *EF* values exceeding 50 indicate extremely heavy accumulation.

The Geoaccumulation Index ( $I_{geo}$ ), originally proposed by G. Müller [36], was calculated as:

$$I_{geo} = \log_2 \left( \frac{El_{sample}}{1,5 \cdot El_{background}} \right),$$

where  $El_{sample}$  and  $El_{background}$  are the concentrations of the element in the sediment (mg/kg) and the background concentration of the element [20] (mg/kg), respectively. The correction factor of 1.5 accounts for natural variations in background levels and minimal anthropogenic influences [47]. Depending on the value of the geoaccumulation index, the following pollution classes are distinguished:  $I_{geo} \leq 0$ : practically unpolluted; 0–1: unpolluted to moderately polluted; 1–2: moderately polluted; 2–3: moderately polluted; 3–4: heavily polluted; 4–5: heavily to extremely polluted; more than 5: extremely polluted [36].

Statistica software was used to compute the correlation coefficients and their significance levels. A 95% confidence level was applied to evaluate the reliability of the correlations.

## Results and discussion

**Granulometric composition of bottom sediments.** The surface layer of the bottom sediments in Balaklava Bay is predominantly composed of fine-grained silt sediments. Coarse-grained gravel-sand material accumulates only locally near the shoreline, primarily due to the elevated concentrations of shell gravel and detritus found there.

Studies [12, 14, 15] have shown that the granulometric composition of the bottom sediments in Balaklava Bay changed considerably between 2005 and 2018. Firstly, the proportion of fine silty material in the bottom sediments of the bay increased: the average proportion of the silty fraction was 58% in 2005, increasing to 66% in 2015 and reaching 76% in 2018. This indicates a clear siltation of the bay. Additionally, the ratio of silty sediment fractions changed significantly, with an increase in the proportion of pelitic material (averaging 13% in the bay in 2005, 50% in 2015 and 62% in 2018), particularly in the northern part of the basin: the ratio of pelitic to silty fraction (in %) was 19/58 in 2005; 71/17 – in 2015 and 81/11 – in 2018.

The increased accumulation of silty material in the northern part of Balaklava Bay is due to a combination of natural and anthropogenic factors. Natural factors

include the isolation of this part of the bay from open-sea wave action and weak hydrodynamics and water circulation, while anthropogenic factors include the input of terrigenous material and organic matter with stormwater and municipal wastewater discharges.

In contrast, the average content of gravel-sand material decreased from 42% in 2005 to 34% in 2015, declining further to 23% by 2018.

**Distribution of metals in surface sediment layer.** The analysis of the spatial distribution features of the microelements studied in the surface layer of the bottom sediments of Balaklava Bay was carried out based on data from 2018. The sampling stations are shown in Fig. 1, c.

Concentrations of heavy metals showed considerable variability: 0.1–0.3% (Ti), 0.3–3.8% (Fe), 5–76 mg/kg (V), 5–80 mg/kg (Ni), 40–123 mg/kg (Cr), 148–399 mg/kg (Mn), 10–483 mg/kg (Cu), 15–560 mg/kg (Pb), 183–803 mg/kg (Sr), 38–869 mg/kg (Zn). The spatial distribution of heavy metals in the 0–5 cm sediment layer is presented in Fig. 2.

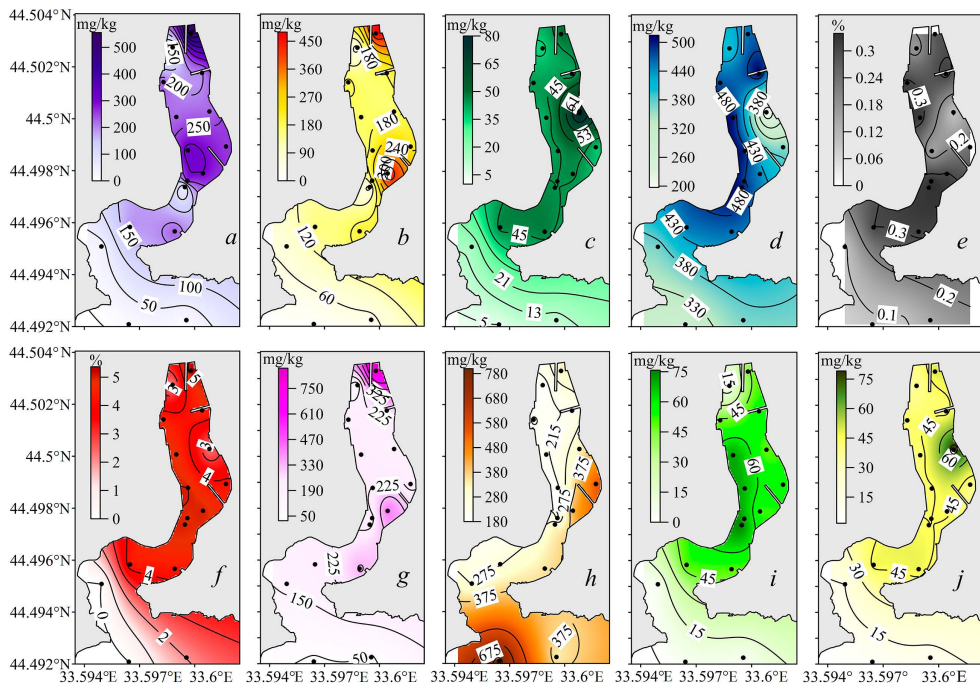


**Fig. 2.** Spatial distribution of Pb (a), Cu (b), Ni (c), Mn (d), Ti (e), Fe (f), Zn (g), Sr (h), V (i), Ni (j) contents in the bottom sediments of Balaklava Bay (2018)

The maximum concentrations of Fe, Cu, Pb, and Zn were recorded in the sediments of the northern basin, particularly in the apex part. Mn and V accumulated preferentially along the western shore of the northern basin (Fig. 2). Elevated levels of Cr and Ni were observed near the eastern shore in the central part of the northern basin. Meanwhile, Ti accumulated predominantly in the knee-shaped

narrowness area, and Sr concentrations peaked in the sediments of the southern basin and the bay mouth.

A clear relationship emerged between sediment granulometry and metal accumulation. The highest elemental concentrations were consistently recorded at stations dominated by fine-grained silty material. Conversely, the lowest concentrations were recorded in the southern basin, where gravel-sand deposits containing only a 20–30% silt fraction prevail [15]. The table below shows the correlation coefficients between the studied parameters.

**Pearson correlation coefficients between concentrations of heavy metals, fractional content of particle size distribution fractions and  $C_{org}$  content. Correlation coefficients statistically significant at the 95% level are marked in red**

Parameters	Fe	Mn	Cr	V	Cu	Ni	Zn	Pb	Sr	Ti
Gravel	-0.2	-0.7	-0.3	0.0	0.0	0.2	-0.1	0.0	0.5	-0.3
Sand	-0.8	-0.5	-0.6	-0.7	-0.5	-0.8	-0.4	-0.6	0.6	-0.7
Silt	0.8	0.7	0.7	0.7	0.4	0.6	0.4	0.5	-0.7	0.7
Aleurite	0.4	0.1	0.5	0.4	0.6	0.6	0.4	0.4	-0.2	0.4
Pelite	0.7	0.7	0.6	0.6	0.3	0.5	0.3	0.5	-0.7	0.7
$C_{org}$	0.7	0.1	0.6	0.7	0.6	0.9	0.5	0.7	-0.1	0.5
Fe	1	0.8	0.9	0.9	0.7	0.6	0.6	0.8	-0.4	0.8
Mn		1	0.8	0.6	0.4	0.1	0.3	0.4	-0.6	0.8
Cr			1	0.8	0.8	0.4	0.7	0.8	-0.2	0.9
V				1	0.5	0.7	0.3	0.7	-0.4	0.7
Cu					1	0.5	0.9	0.9	-0.1	0.5
Ni						1	0.4	0.6	-0.4	0.4
Zn							1	0.8	-0.1	0.4
Pb								1	-0.2	0.6
Sr									1	-0.4
Ti										1

Correlation analysis revealed that all the studied heavy metals, except Sr ( $r = -0.4$ ), showed direct correlations with Fe ( $r = 0.6...0.9$ ). All the metals also correlated with both the silt fraction content and organic carbon content ( $C_{org}$ ) ( $r = 0.3...0.7$  for silt and  $r = 0.1...0.9$  for  $C_{org}$ ), with the exception of Sr ( $r = -0.7$  and  $r = -0.1$ , respectively). However, statistically significant correlations (at 95% confidence level) were absent between silt content and Cu, Zn, as well as between  $C_{org}$  content and Mn, Ti, Zn. The difference in correlation patterns between metals and total silt versus pelitic material fractions reflects the specific features of trace element accumulation in different fine-grained sediment fractions [48–50]. No correlation was found between metal concentrations and gravel fraction content ( $r = -0.3...0.0$ ), except for Mn ( $r = -0.7$ ), while the correlation for Sr ( $r = 0.5$ ) was statistically insignificant. This can be explained by the low gravel content, its uneven distribution within the sediment samples and the poor sorption capacity [50].

Similar positive correlations have been documented between heavy metal concentrations,  $C_{org}$  silt fraction content and Fe in sediments in various regions of the World Ocean, including the Red Sea [26, 38], the Bohai Sea [27], the Pacific Ocean [44], the South China Sea [45], the Atlantic Ocean [46], among others.

### Comparative analysis of metal concentrations over the study period.

A comparative analysis of mean concentrations of the studied elements in 2005, 2015, 2018, and 2019 is presented in Fig. 3.

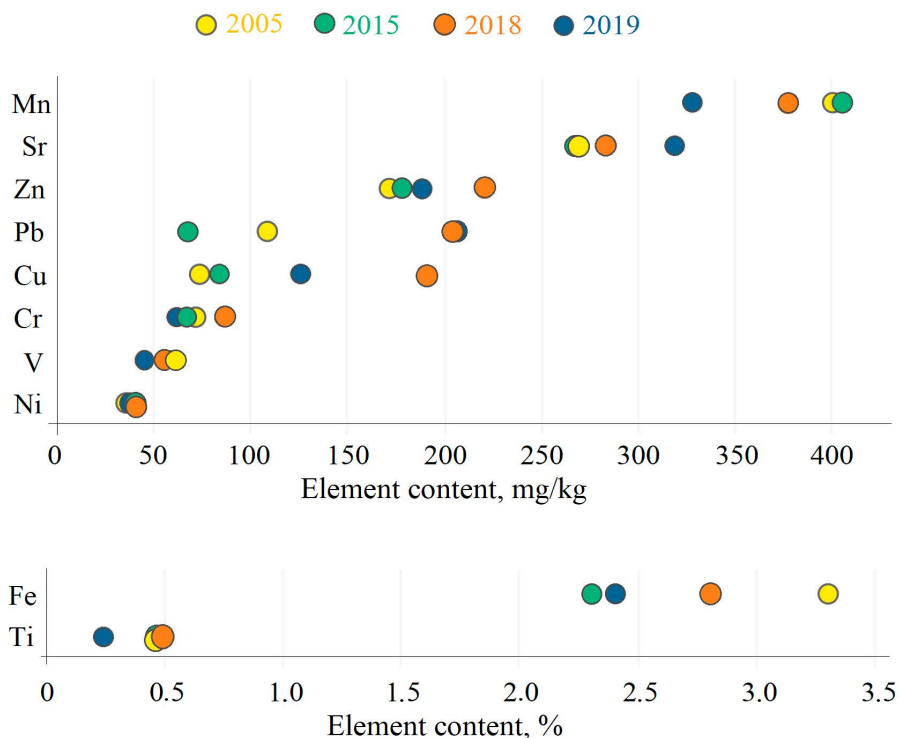


**Fig. 3.** Average values of metal concentrations based on the data for 2005, 2015, 2018 and 2019

The study revealed that concentrations of Zn, Cu, Cr, and Ti in 2018 were higher than in 2005 (171–220 mg/kg for Zn, 73–190 mg/kg for Cu, 71–86 mg/kg for Cr, and 0.46–0.48% for Ti), followed by a decrease in 2019 (188 mg/kg for Zn, 125 mg/kg for Cu, 61 mg/kg for Cr, and 0.23% for Ti). The lowest average Pb concentration in the bay sediments was recorded in 2015 (67 mg/kg), while the highest values occurred in 2018 and 2019 (204 mg/kg). Maximum average concentrations for Mn, V, and Fe were observed in 2005 (400 mg/kg, 60 mg/kg, and 3.3%, respectively), with minima recorded in 2019 (327 mg/kg, 44 mg/kg, and 2.4%, respectively). Sr showed an inverse pattern, with the lowest value (268 mg/kg) in 2005 and the highest (318 mg/kg) in 2019. The average Ni concentration remained relatively stable throughout the study

period, ranging from a minimum of 35 mg/kg in 2005 to maxima of 40 mg/kg in 2015 and 2018.

For comparison: the total content of trace elements (Cr, Cu, Ni, Pb, Zn) in Balaklava Bay sediments was 558 mg/kg in 2005 [19]. However, following numerous dredging and cleanup operations in the northern basin between 2005 and 2015, concentrations decreased to 414 mg/kg by 2015. Nevertheless, the year-round presence of numerous boats and yachts in the bay, along with hull maintenance and painting activities near quay walls, combined with multiple sources of stormwater runoff and wastewater discharges (including untreated effluents), led to deteriorating conditions by 2018, resulting in an increased total content of studied trace elements reaching 763 mg/kg.

**Assessment of sediment pollution levels. Growth rate values.** The spatial distribution features of the estimated growth rates for Cu, Pb, and Zn are presented in Fig. 4. Analysis reveals that during 2005–2015, all the studied elements showed negative growth rates (–5% to –30%) in the central part of the northern basin (Fig. 1, *d*), likely attributable to dredging operations conducted during this period.

Concentrations have increased positively (by 15–150%) in the northern apex part and the southern part of the northern basin. For copper (Fig. 4, *a*), concentrations have also increased in the southern basin. In the northern part of the bay, this is explained by the location of the ship berths and repair facilities that were operational until 2015. In the southern part of the northern basin, it is explained by the features of water circulation and sedimentation in the bay. In the southern basin, it is explained by the additional contribution of terrigenous material that comes with stormwater runoff.

Between 2015 and 2018, the situation changed dramatically. Throughout the water area of the bay, except for the northern part, three zones can be identified where each of the selected trace elements showed significant concentration increases (Fig. 4, *b, d, f*). The first zone is the western shore of the northern basin. An increase of 100–150% was observed for Cu in this zone, 430–1200% for Pb and 30–90% for Zn. This increase in trace element concentrations is apparently explained by the significant accumulation of the pelite-aleurite fraction (up to 0.05 mm), whose concentrations in this area increased from 2–19% in 2005 to 84–87% in 2018.

The second zone is the southeastern part of the northern basin. The increase here is due to the combined influence of stormwater runoff, the dense location of small craft berths and the features of water circulation that determine the inflow and accumulation of fine-grained sediments in this area [5, 14]. The increase amounts to 150–440% for Cu, 160–760% for Pb, and 10–50% for Zn.

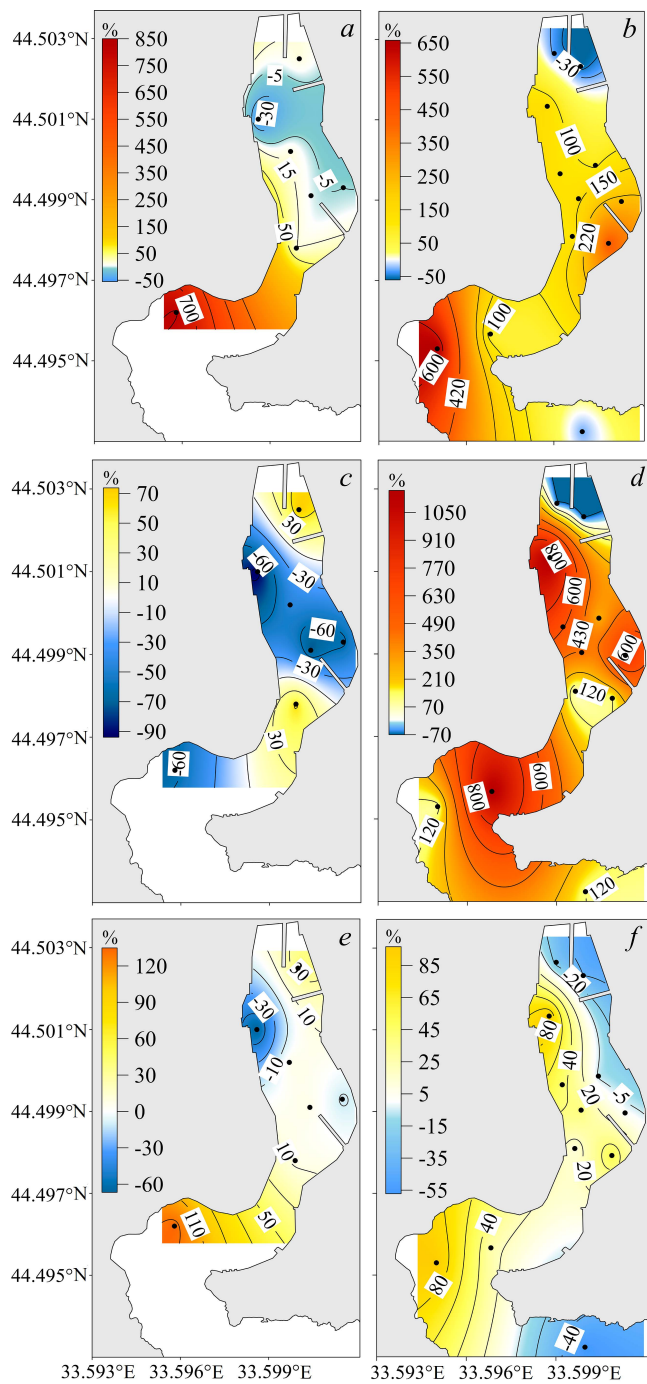


**Fig. 4.** Spatial distribution of the values of increase in trace element concentrations: *a, b* – copper; *c, d* – lead; *e, f* – zinc in the bottom sediments of Balaklava Bay in 2005–2015 (*a, c, e*) and 2015–2018 (*b, d, f*)

The third zone comprises the northwestern part of the southern basin. Research results show that, for Cu and Zn, concentration growth values were lower in 2015–2018 than in 2005–2015. On the contrary, a significant increase in Pb concentration was noted, rising from 65% in 2005–2015 (Fig. 4, *c*) to 130–1150% in 2015–2018 (Fig. 4, *d*). The main sources of pollutant input into the bottom sediments of this zone are stormwater runoff from the northern part of the southern basin and municipal wastewater discharged into the bay exit.

The significant increase in the growth rates of Pb and Cu content in the central part of the bay indicates intensive siltation, which is partly a natural process caused by the regulated nature of the bay and the inflow of untreated wastewater. The deterioration of the natural environment is also due to the increasing number of small vessels, boats and other means of marine transport, as well as painting and cleaning work conducted in the bay.

**Integrated pollution indices (*PLI*,  $C_{deg}$ ).** The integrated pollution indices (*PLI* and  $C_{deg}$ ) were calculated for each sampling station. The spatial distribution of these indices in the bay surface sediment layer over different years is presented in Fig. 5.

According to the *PLI* and  $C_{deg}$  values, the total pollution level of the bottom sediments in 2005 was classified as unpolluted to moderately polluted, with values of 1.0 and 13.9 respectively. The minimum values were recorded in the southern basin and the knee-shaped narrowness (0.5–0.9 and 6–8), while the maximum values occurred in the sediments of the northern basin (0.7–1.6 and 12–30). By 2015, the average bay-wide index values had decreased to 0.86 and 12; however, they increased again to 1.2 and 23 by 2018. Notably, the  $C_{deg}$  index for northern basin sediments averaged 27 (indicating significant pollution), with a local maximum of 54 (high pollution level) in the northern apex area.

While the maximum *PLI* index values were observed in the sediments of the central part of the northern basin in 2005, anthropogenic anomalies had completely spread across the entire water area of the northern basin and the knee-shaped narrowness by 2018. This redistribution of the index values is determined by the specific water circulation patterns of the water in the northern basin [10] and the dynamics of the bottom sediments within the bay [16]. Additionally, Balaklava's main recreational infrastructure (cafes, restaurants, hotels, and residential buildings) and primary ship berthing facilities are located on the eastern shore of the northern basin.

The maximum *PLI* index values recorded in the northern apex in 2018 differ from previous results and can be attributed to the relocation of sampling stations closer to potential pollution sources, such as the mouth of the Balaklavka River. The minimum index values observed in 2015 were likely the result of dredging operations and bay bottom cleaning measures carried out between 2005 and 2015. Excluding the 2015 calculations and comparing values from 2005 and 2018 reveals that the overall pollution level of Balaklava Bay bottom sediments has increased by an average factor of 1.5.

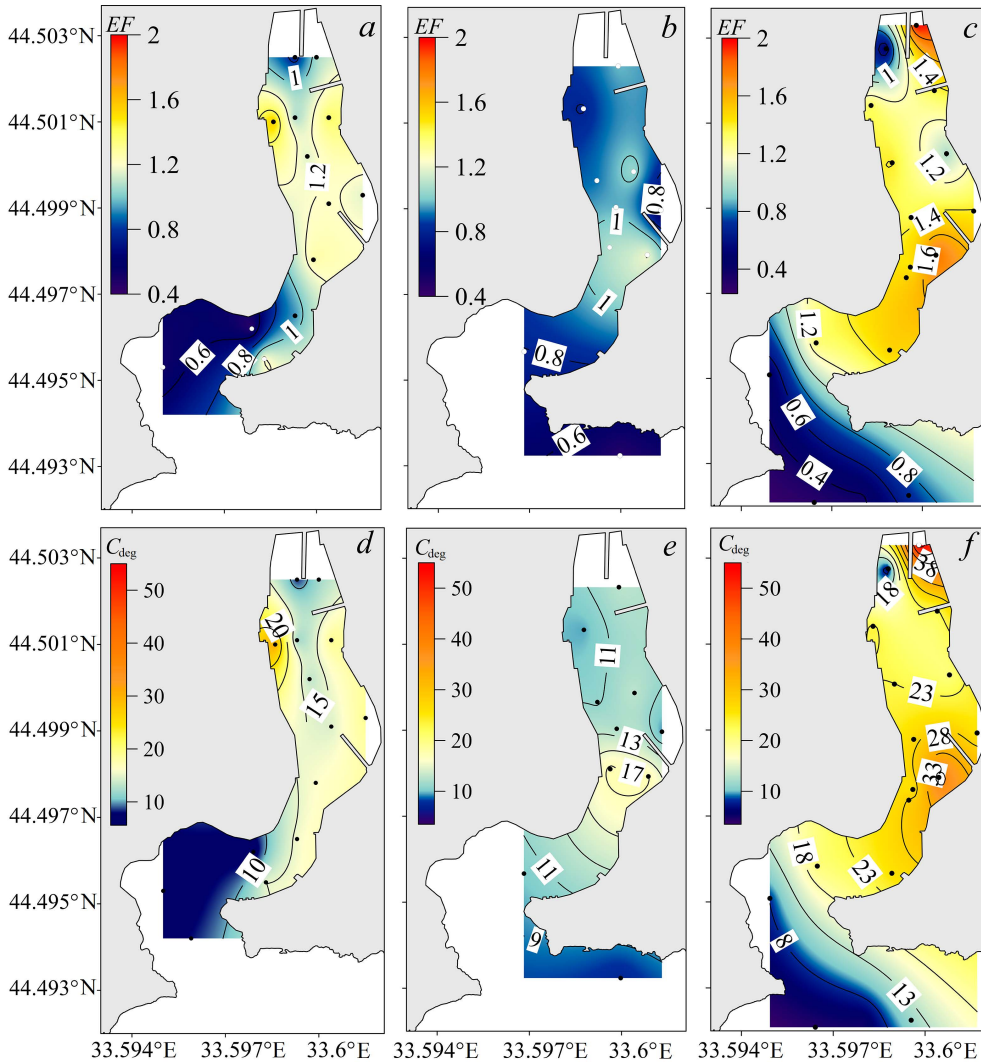


**Fig. 5.** Distribution of total pollution indices  $PLI$  (*a, b, c*) and  $C_{deg}$  (*d, e, f*) in the bottom sediments of Balaklava Bay in 2005 (*a, d*), 2015 (*b, e*) and 2018 (*c, f*)

The consistently low  $PLI$  (less than 1) and  $C_{deg}$  (less than 10) index values observed in southern waters (Fig. 5) and at the bay exit from 2005 to 2018 are explained by the unique water circulation patterns in the open part of the bay, which is exposed to storm wave activity [9–11], as well as by the granulometric composition of sediments at the sampling stations [12, 14, 15].

**Enrichment Factor.** This study presents  $EF$  calculations for Zn, Cu and Pb, as these elements showed the highest average values across the bay during the study period (2005, 2015, 2018): 2–10, 2–4 and 3–12, respectively. Fig. 6 shows the spatiotemporal variability of  $EF$  values in surface sediments of Balaklava Bay.

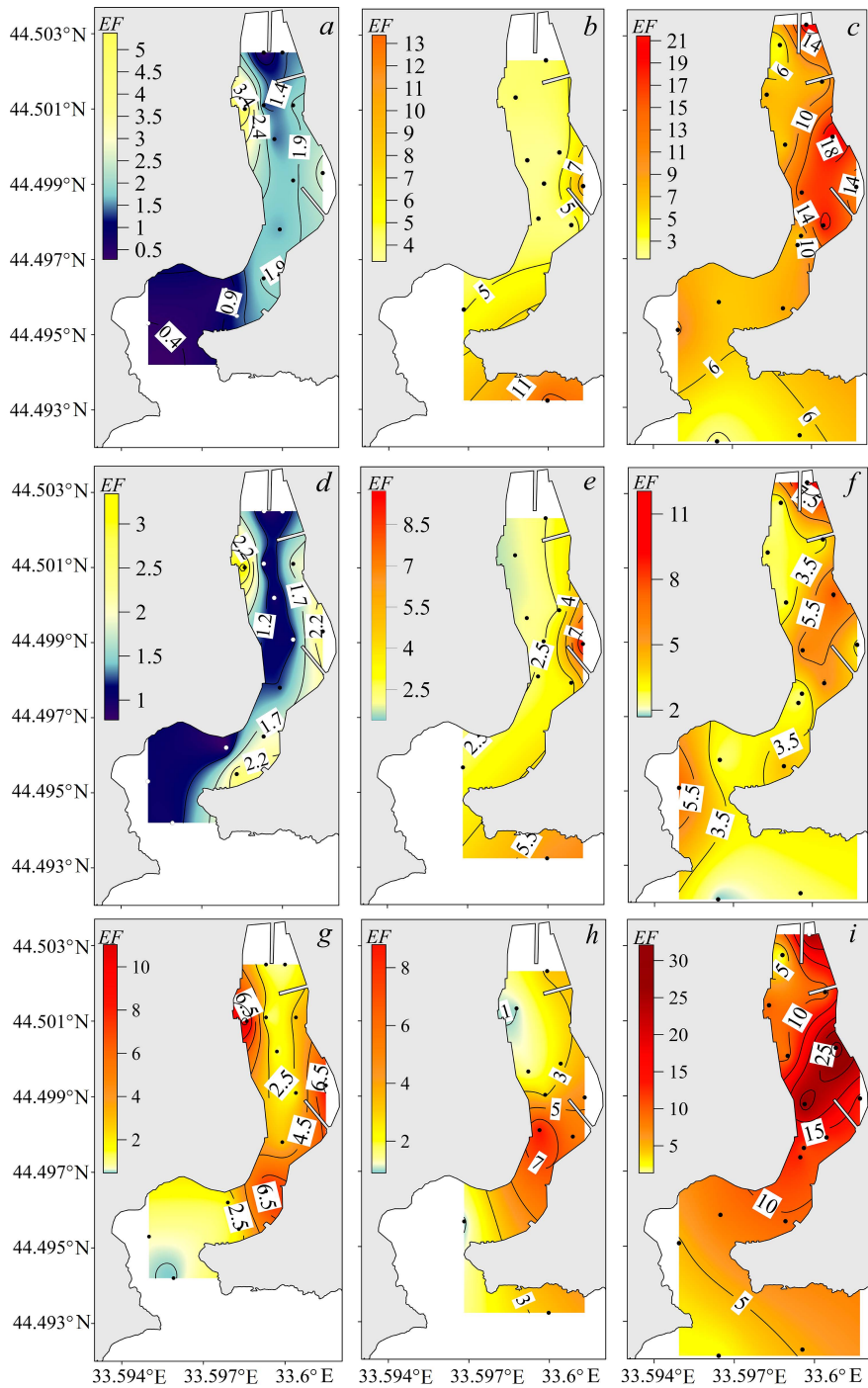


**Fig. 6.** Distribution of the EF for copper (a, b, c), zinc (d, e, f) and lead (g, h, i) in the bottom sediments of Balaklava Bay in 2005 (a, d, g), 2015 (b, e, h) and 2018 (c, f, i)

Analysis revealed that the *EF* values of all the studied elements increased from 2005 to 2018, with average multiplication factors of 7, 3 and 4 for Cu, Zn and Pb, respectively.

In 2005, the *EF* values ranged from 0.3–5.4 for Cu (Fig. 6, *a*), 0.8–3.4 for Zn (Fig. 6, *d*) and 0.5–11.1 for Pb (Fig. 6, *g*). No enrichment was observed in the southern basin and northern apex of the bay, while local maxima indicating moderate Zn enrichment, moderately severe Cu enrichment and severe Pb enrichment were noted near the tunnel outlet. Moderately severe Pb enrichment was also noted in the central bay area ( $EF=9.2$ ) and the knee-shaped narrowness ( $EF=8.3$ ). By 2015, the *EF* values for Cu and Zn had increased by factors of 3.4 and 2.4, respectively, while Pb showed little change (3.2 in 2005 vs 3.5 in 2015). Overall, the bay-wide Cu enrichment level increased to moderate, reaching severe levels at some stations in the central area ( $EF=10.3$ ) and the bay exit ( $EF=13.4$ ) (Fig. 6, *b*). Zn maintained minor enrichment in the central area, with local maxima of moderately severe enrichment in the central bay ( $EF=9.9$ ) and the bay exit area ( $EF=6.5$ ) (Fig. 6, *e*). Pb enrichment ranged from minor/moderate in the central areas and at the outlet, to severe ( $EF=8.5$ ) in the knee-shaped narrowness (Fig. 6, *h*). By 2018, only minor enrichment levels persisted at stations near the bay exit for all metals and in some central and southern basin areas for Zn. The maximum *EF* values were recorded in the central bay areas and corresponded to heavy ( $EF=10\dots22$ ) Cu enrichment (Fig. 6, *c*), moderately heavy ( $EF=5.5\dots7.7$ ) Zn enrichment (Fig. 6, *f*) and very heavy ( $EF=27.6\dots32.6$ ) Pb enrichment (Fig. 6, *i*).

The study revealed that, while elevated *EF* values were observed in close proximity to the main sources of substance input into bottom sediments in 2005, by 2018 these values had become distributed throughout the entire bay area.

The spatial distribution patterns of metal accumulation zones in the bay bottom sediments are explained by the combined influence of natural and anthropogenic factors. In particular, the increase in silt fraction content from 58% in 2005 [12] to 66% in 2015 [14] and further to 76% in 2018 [15] enhanced the sediments' sorption capacity, thereby accounting for the overall increase in metal accumulation across the entire bay area. Furthermore, the concentration of local pollution sources in the central part of the bay indicates its intensive use as a yacht marina and growing anthropogenic pressure on the aquatic environment.

A comparison of the values obtained for Balaklava Bay with those recorded in the coastal areas of Crimea [20] showed significantly higher levels of contamination (with Pb concentrations exceeding the reference values by an order of magnitude). These findings demonstrate the severe pollution of the bay bottom sediments and the substantial anthropogenic impact on this marine ecosystem.

**Geoaccumulation index.** Following the same approach as for the *EF* parameter, the  $I_{geo}$  index was applied to visualize heavy metal pollution in Balaklava Bay bottom sediments, focusing on Zn, Cu, and Pb (Fig. 7). This selection was primarily motivated by the fact that, for other studied trace elements,  $I_{geo} \leq 0$  indicated practically uncontaminated sediments.

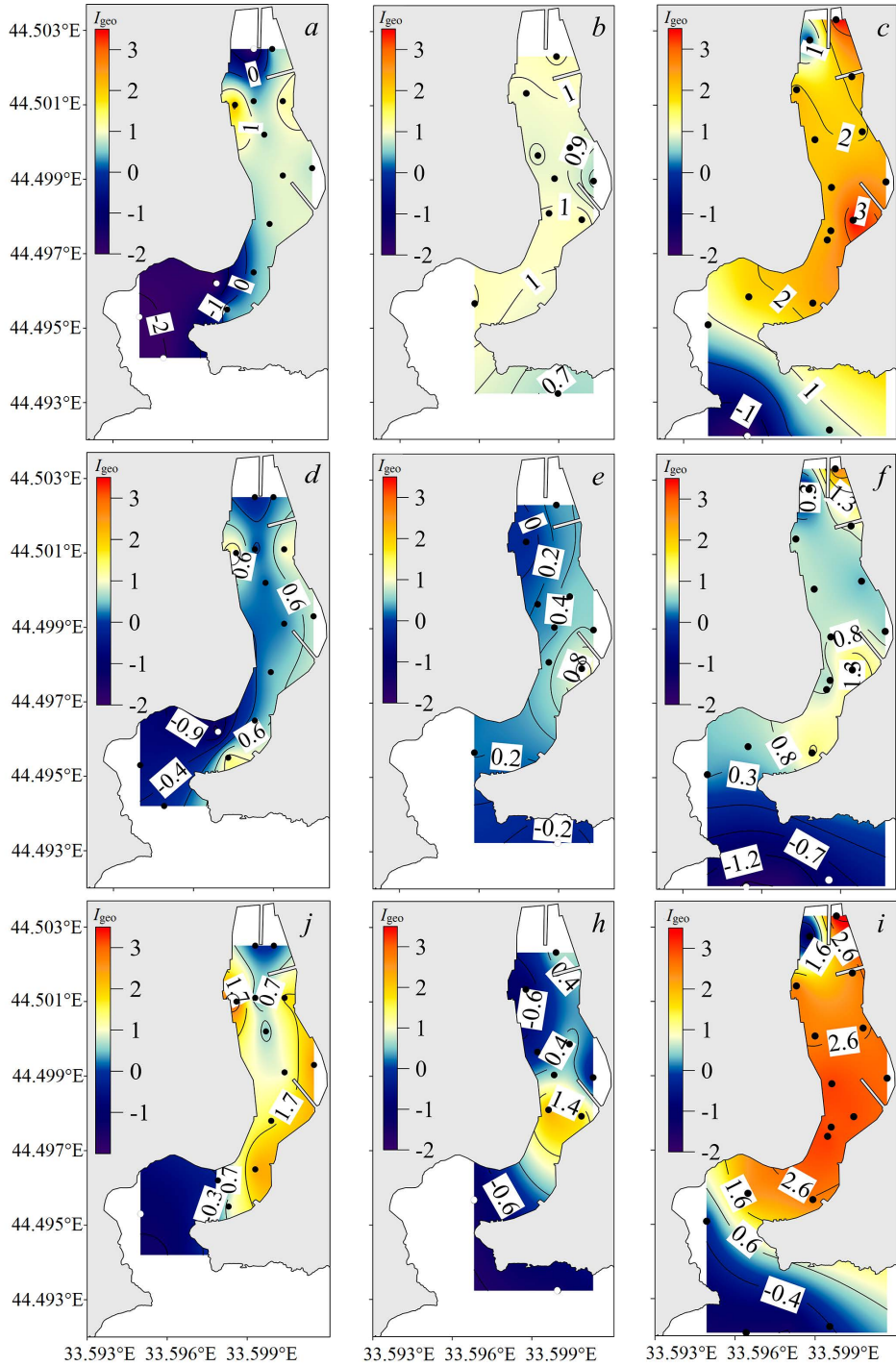


**Fig. 7.** Distribution of  $I_{geo}$  parameter for copper (a, b, c), zinc (d, e, f) and lead (g, h, i) in the bottom sediments of Balaklava Bay in 2005 (a, d, g), 2015 (b, e, h) and 2018 (c, f, i)

The geoaccumulation index of the 2005 samples revealed that the sediments ranged from nearly uncontaminated ( $-2.1 \dots -0.2$ ) in the southern basin to moderately polluted ( $2.1-3.2$ ) in the northern basin (Fig. 7, *a, d, g*). The average  $I_{geo}$  values were 0.0 for Cu, 0.2 for Zn and 0.8 for Pb. By 2015, the average  $I_{geo}$  value had increased to 0.9 for Cu and 0.3 for Zn, while decreasing to 0.1 for Pb. This shift was also evident in the sediments of the southern basin, where Cu and Zn accumulation rose to moderate levels.

Local decreases in Pb  $I_{geo}$  values were traced to dredging activities in the northern basin, near the tunnel outlet ( $3.2$  in 2005 versus  $-1.1$  in 2015), and in the municipal beach/small craft mooring area ( $2.5$  in 2005 versus  $-0.5$  in 2015).

By 2018, the  $I_{geo}$  values for Cu and Pb had increased markedly, averaging 1.7 and 1.8, respectively, while the rise in Zn was modest, from 0.3 to 0.5. Although the average  $I_{geo}$  value indicated moderate pollution, specific stations in the northern basin were heavily contaminated ( $3.0-3.8$ ) (Fig. 7, *c, f, j*).

As previously noted, the elevated pollution levels in the northern basin stem from a combination of natural and anthropogenic influences. Comparative data from Crimean coastal sediments [20] showed significantly lower averages:  $-1.44$  for Cu,  $-0.4$  for Zn and  $0.03$  for Pb. The spatial correlation of peak contamination with municipal/stormwater outfalls and yacht moorings demonstrates anthropogenic dominance over natural factors. Consistent upward trends in all calculated indices ( $PLI$ ,  $C_{deg}$ ,  $EF$ ,  $I_{geo}$ ) confirm that this anthropogenic contribution is progressively intensifying.

## Conclusion

Balaklava Bay was used as a case study to investigate the distribution features of trace elements in bottom sediments, assess the spatial distribution of enrichment and pollution zones, and evaluate changes in anthropogenic pressure between 2005 and 2019. Various geochemical coefficients and indices were employed for this study.

To assess the anthropogenic contribution to sediment pollution in relation to the average composition of trace elements in Crimean coastal shelf areas, the study used contamination and enrichment factors, as well as integrated pollution and geoaccumulation indices.

The research established that the level of sanitary-toxicological hazard posed by sediment pollution in Balaklava Bay shifted from acceptable/moderately hazardous to hazardous/severe during the study period.

Elevated concentrations of the studied elements were consistently observed in samples that were dominated by fine-grained silty material. A comparative analysis of metal concentrations revealed an increasing trend for Cu, Zn, Sr and Pb from 2005 to 2019, whereas Mn, V and Fe showed an opposite, decreasing pattern.

The pollution assessment indicated low levels of accumulation and enrichment for V, Cr and Ni, which did not exceed background values for Crimean coastal areas. Localized exceedances of background levels were noted for Fe, Mn, Sr and Ti, primarily in the fine-grained silts of the northern basin. Pollution levels for Cu, Zn and Pb varied widely, ranging from low levels in the sediments of the southern basin and the bay mouth areas, to high levels in the waters of the northern basin.

The study confirmed that elevated pollution levels in sediments of the northern basin result from a combination of natural and anthropogenic factors. However, the spatial correlation between contamination hotspots and municipal/stormwater discharge points and yacht mooring areas demonstrates that anthropogenic contributions outweigh natural influences. Increasing index values clearly indicate the progressive intensification of this anthropogenic impact. This comprehensive analysis reveals the spatial dynamics of sediment pollution and its temporal evolution in the bay ecosystem under growing anthropogenic pressure.

#### REFERENCES

1. Duan, L., Song, J., Liang, X., Yin, M., Yuan, H., Li, X., Ren, C., Zhou, B., Kang, X. [et al.], 2019. Dynamics and Diagenesis of Trace Metals in Sediments of the Changjiang Estuary. *Science of the Total Environment*, 675, pp. 247-259. <https://doi.org/10.1016/j.scitotenv.2019.04.190>
2. Cukrov, N., Cindrić, A.-M., Omanović, D. and Cukrov, N., 2024. Spatial Distribution, Ecological Risk Assessment, and Source Identification of Metals in Sediments of the Krka River Estuary (Croatia). *Sustainability*, 16(5), 1800. <https://doi.org/10.3390/su16051800>
3. Matishov, G.G., Bufetova, M.V. and Egorov, V.N., 2017. The Regulation of Flows of Heavy Metals into the Sea of Azov According to the Intensity of Sedimentation of Water Self-Purification. *Science in the South of Russia*, 13(1), pp. 44-58 (in Russian).
4. Ledin, M., 2000. Accumulation of Metals by Microorganisms – Processes and Importance for Soil Systems. *Earth-Science Reviews*, 51(1-4), pp. 1-31. [https://doi.org/10.1016/S0012-8252\(00\)00008-8](https://doi.org/10.1016/S0012-8252(00)00008-8)
5. Gnanasekaran, S. and Amal Raj, S., 2023. Heavy Metal Bioaccumulation in Sediment and Benthic Biota. In: B. A. Almayahi, ed., 2023. *Heavy Metals – Recent Advances*. London: IntechOpen, pp. 1-15. <https://doi.org/10.5772/intechopen.110015>
6. Kovrigina, N.P., Popov, M.A., Lisitskaya, E.V., Kuftarkova, E.A. and Gubanov, V.I., 2010. Complex Monitoring of Balaklava Bay (Black Sea) in 2000-2007. *Marine Ecological Journal*, 9(4), pp. 62-75 (in Russian).
7. Lomakin, P.D. and Popov, M.A., 2011. *Oceanological Characteristic and Estimation of the Water Pollution in the Balaklava Bay*. Sevastopol: ECOSI-Gidrofizika, 184 p. (in Russian).
8. Mukhametov, S.S. and Kondratev, S.I., 2018. Extreme Values of Hydrochemical Parameters in the Balaklava Bay Water in February 2015. *Vestnik Moskovskogo Universiteta. Seriya 5, Geografiya*, (5), pp. 14-21 (in Russian).
9. Kubryakov, A.I. and Popov, M.A., 2005. Modeling of Circulation and Propagation of Contaminating Impurities in the Balaklava Bay. *Physical Oceanography*, 15(3), pp. 180-191. <https://doi.org/10.1007/s11110-005-0040-3>
10. Fomin, V.V. and Repetin, L.N., 2005. Numerical Simulation of Wind Currents and Propagation of Impurities in the Balaklava Bay. *Physical Oceanography*, 15(4), pp. 232-246. <https://doi.org/10.1007/s11110-005-0045-y>
11. Fomin, V.V. and Polozok, A.A., 2020. Wind Wave Regime in the Area of Balaklava Bay. *Ecological Safety of Coastal and Shelf Zones of Sea*, (2), pp. 53-67. <https://doi.org/10.22449/2413-5577-2020-2-53-67> (in Russian).
12. Gurov, K.I., Ovsyany, E.I., Kotelyanets, E.A. and Konovalov, S.K., 2015. Factors of Formation and Features of Physical and Chemical Characteristics of the Bottom Sediments in the Balaklava Bay (the Black Sea). *Physical Oceanography*, (4), pp. 46-52. <https://doi.org/10.22449/1573-160X-2015-4-46-52>
13. Orekhova, N.A., Ovsyany, E.I., Gurov, K.I. and Popov, M.A., 2018. Organic Matter and Grain-Size Distribution of the Modern Bottom Sediments in the Balaklava Bay (the Black Sea). *Physical Oceanography*, 25(6), pp. 479-488. <https://doi.org/10.22449/1573-160X-2018-6-479-488>

14. Kotelyanets, E.A., Gurov, K.I., Tikhonova, E.A. and Kondratev, S.I., 2019. Pollutants in Bottom Sediments in the Balaklava Bay (the Black Sea). *Physical Oceanography*, 26(5), pp. 414-424. <https://doi.org/10.22449/1573-160X-2019-5-414-424>
15. Tikhonova, E.A., Kotelyanets, E.A. and Gurov, K.I., 2019. Content of Organic Compounds and Trace Metals in Bottom Sediments of the Balaklava Bay (the Black Sea). *Ecological Safety of Coastal and Shelf Zones of Sea*, (3), pp. 82-89. <https://doi.org/10.22449/2413-5577-2019-3-82-89> (in Russian).
16. Gurov, K.I. and Fomin, V.V., 2021. Mathematical Modeling the Dynamics of the Bottom Sediments Granulometric Composition in the Balaklava Bay Affected by the Wind Waves. *Physical Oceanography*, 28(1), pp. 78-89. <https://doi.org/10.22449/1573-160X-2021-1-78-89>
17. Kremenchutskii, D.A. and Gurov, K.I., 2021. Distribution of <sup>137</sup>Cs and <sup>40</sup>K in the Bottom Sediments of the Balaklava Bay (the Black Sea). *Physical Oceanography*, 28(2), pp. 191-204. <https://doi.org/10.22449/1573-160X-2021-2-191-204>
18. Soloveva, O.V., Tikhonova, E.A., Gurov, K.I. and Kotelyanets, E.A., 2023. Hydrocarbons Composition of Sea Bottom Sediments (Balaklava Bay, Black Sea). *International Journal of Environmental Science and Technology*, 20(3), pp. 2405-2416. <https://doi.org/10.1007/s13762-022-04167-y>
19. Burgess, R.M., Terletskaia, A.V., Milyukin, M.V., Povolotskii, M., Demchenko, V.Y., Bogoslavskaya, T.A., Topkin, Y.V., Vorobyova, T.V., Petrov, A.N. [et al.], 2009. Concentration and Distribution of Hydrophobic Organic Contaminants and Metals in the Estuaries of Ukraine. *Marine Pollution Bulletin*, 58(8), pp. 1103-1115. <https://doi.org/10.1016/j.marpolbul.2009.04.013>
20. Gurov, K.I., Kurinnaya, Yu.S. and Kotelyanets, E.A., 2021. Features of Accumulation and Spatial Distribution of Microelements in Bottom Sediments of the Crimea Coastal Regions. In: T. Chaplina, ed., 2021. *Processes in GeoMedia – Volume III*. Springer Geology Series. Cham: Springer, pp. 119-130. [https://doi.org/10.1007/978-3-030-69040-3\\_12](https://doi.org/10.1007/978-3-030-69040-3_12)
21. Bat, L., Özkan, E.Y. and Öztekin, H.C., 2015. The Contamination Status of Trace Metals in Sinop Coast of the Black Sea, Turkey. *Caspian Journal of Environmental Sciences*, 13(1), pp. 1-10.
22. Korablina, I.V., Barabashin, T.O. and Katalevsky, N.I., 2021. Heavy Metals in the Bottom Sediments of the Black Sea Northwestern Shelf in Recent Years. *Physical Oceanography*, 28(5), pp. 549-566. <https://doi.org/10.22449/1573-160X-2021-5-549-566>
23. Ardila, P.A.R., Alonso, R.Á., Valsero, J.J.D., García, R.M., Cabrera, F. Á., Cosío, E.L. and Laforet, S.D., 2023. Assessment of Heavy Metal Pollution in Marine Sediments from Southwest of Mallorca Island, Spain. *Environmental Science and Pollution Research*, 30(7), pp. 16852-16866. <https://doi.org/10.1007/s11356-022-25014-0>
24. Soliman, N.F., Nasr, S.M. and Okbah, M.A., 2015. Potential Ecological Risk of Heavy Metals in Sediments from the Mediterranean Coast, Egypt. *Journal of Environmental Health Science and Engineering*, 13(1), 70. <https://doi.org/10.1186/s40201-015-0223-x>
25. Chifflet, S., Tedetti, M., Zouch, H., Fourati, R., Zaghden, H., Elleuch, B., Quéméneur, M., Karray, F. and Sayadi, S., 2019. Dynamics of Trace Metals in a Shallow Coastal Ecosystem: Insights from the Gulf of Gabès (Southern Mediterranean Sea). *AIMS Environmental Science*, 6(4), pp. 277- 297. <https://doi.org/10.3934/environsci.2019.4.277>
26. Youssef, M. and El-Sorogy, A., 2016. Environmental Assessment of Heavy Metal Contamination in Bottom Sediments of Al-Kharrar Lagoon, Rabigh, Red Sea, Saudi Arabia. *Arabian Journal of Geosciences*, 9(6), 474. <https://doi.org/10.1007/s12517-016-2498-3>
27. Zhang, J. and Gao, X., 2015. Heavy Metals in Surface Sediments of the Intertidal Laizhou Bay, Bohai Sea, China: Distributions, Sources and Contamination Assessment. *Marine Pollution Bulletin*, 98(1-2), pp. 320-327. <https://doi.org/10.1016/j.marpolbul.2015.06.035>
28. Fukushima, K., Saino, T. and Kodama, Y., 1992. Trace Metal Contamination in Tokyo Bay, Japan. *Science of the Total Environment*, 125, pp. 373-389. [https://doi.org/10.1016/0048-9697\(92\)90402-E](https://doi.org/10.1016/0048-9697(92)90402-E)

29. Bothner, M.H., Buchholtz Ten Brink, M. and Manheim, F.T., 1998. Metal Concentrations in Surface Sediments of Boston Harbor: Changes with Time. *Marine Environmental Research*, 45(2), pp. 127-155. [https://doi.org/10.1016/S0141-1136\(97\)00027-5](https://doi.org/10.1016/S0141-1136(97)00027-5)
30. Ho, K.T., Burgess, R.M., Pelletier, M.C., Serbst, J.R., Ryba, S.A., Cantwell, M.G., Kuhn, A. and Raczekowski, P., 2002. An Overview of Toxicant Identification in Sediments and Dredged Materials. *Marine Pollution Bulletin*, 44(4), pp. 286-293. [https://doi.org/10.1016/S0025-326X\(01\)00251-X](https://doi.org/10.1016/S0025-326X(01)00251-X)
31. Charlesworth, S., Everett, M., McCarthy, R., Ordóñez, A. and De Miguel, E., 2003. A Comparative Study of Heavy Metal Concentration and Distribution in Deposited Street Dusts in a Large and a Small Urban Area: Birmingham and Coventry, West Midlands, UK. *Environment International*, 29(5), pp. 563-573. [https://doi.org/10.1016/S0160-4120\(03\)00015-1](https://doi.org/10.1016/S0160-4120(03)00015-1)
32. Lu, X., Wang, L., Lei, K., Huang, J. and Zhai, Y., 2009. Contamination Assessment of Copper, Lead, Zinc, Manganese and Nickel in Street Dust of Baoji, NW China. *Journal of Hazardous Materials*, 161(2-3), pp. 1058-1062. <https://doi.org/10.1016/j.jhazmat.2008.04.052>
33. Chon, H.-T., Kim, K.-W. and Kim, J.-Y. Metal Contamination of Soils and Dusts in Seoul Metropolitan City, Korea. *Environmental Geochemistry and Health*, 17(3), pp. 139-146. <https://doi.org/10.1007/BF00126082>
34. Hakanson, L., 1980. An Ecological Risk Index for Aquatic Pollution Control. A Sedimentological Approach. *Water Research*, 14(8), pp. 975-1001. [https://doi.org/10.1016/0043-1354\(80\)90143-8](https://doi.org/10.1016/0043-1354(80)90143-8)
35. Tomlinson, D.L., Wilson, J.G., Harris, C.R. and Jeffrey, D.W., 1980. Problems in the Assessment of Heavy-Metal Levels in Estuaries and the Formation of a Pollution Index. *Helgoländer Meeresuntersuchungen*, 33(1-4), pp. 566-575. <http://dx.doi.org/10.1007/BF02414780>
36. Muller, G., 1979. Schwermetalle in den Sedimenten des Rheins: Veränderungen seit 1971. *Umschau*, 79, pp. 778-783 (in German).
37. Ovsyany, E.I., Kotelyanets, E.A. and Orekhova, N.A., 2009. Arsenic and Heavy Metals in the Bottom Sediments of the Balaklava Bay (Black Sea). *Physical Oceanography*, 19(4), pp. 254-266. <https://doi.org/10.1007/s11110-009-9048-4>
38. Bantan, R.A., Al-Dubai, T.A. and Al-Zubieri, A.G., 2020. Geo-Environmental Assessment of Heavy Metals in the Bottom Sediments of the Southern Corniche of Jeddah, Saudi Arabia. *Marine Pollution Bulletin*, 161, part A, 111721. <https://doi.org/10.1016/j.marpolbul.2020.111721>
39. Habib, S.B., Hossain, M.B., Hossain, Md.S., Jolly, Y.N. and Sarker, S., 2021. Ecological Risk Evaluation in Bottom-Surface Sediments and Sub-Surface Water in the Subtropical Meghna Estuarine System. *Heliyon*, 7(11), e08324. <https://doi.org/10.1016/j.heliyon.2021.e08324>
40. Zoller, W.H., Gladney, E.S. and Duce, R.A., 1974. Atmospheric Concentrations and Sources of Trace Metals at the South Pole. *Science*, 183(4121), pp. 198-200. <https://doi.org/10.1126/science.183.4121.198>
41. Liu, R., Bao, K., Yao, S., Yang, F. and Wang, X., 2018. Ecological Risk Assessment and Distribution of Potentially Harmful Trace Elements in Lake Sediments of Songnen Plain, NE China. *Ecotoxicology and Environmental Safety*, 163(10), pp. 117-124. <https://doi.org/10.1016/j.ecoenv.2018.07.037>
42. Mehlhorn, P., Newman, B. and Haberzettl, T., 2024. Comparison of Different Normalisers for Identifying Metal Enrichment of Sediment: A Case Study from Richards Bay Harbour, South Africa. In: G.P. von Maltitz, G.F. Midgley, J. Veitch, C. Brümmer, R.P. Rötter, F.A. Veihberg and M. Veste, eds., 2024. *Sustainability of Southern African Ecosystems under Global Change*. Ecological Studies Series, vol. 248. Cham: Springer, pp. 787-814. [https://doi.org/10.1007/978-3-031-10948-5\\_27](https://doi.org/10.1007/978-3-031-10948-5_27)
43. Jaskuła, J., Sojka, M., Fiedler, M. and Wróżyński, R., 2021. Analysis of Spatial Variability of River Bottom Sediment Pollution with Heavy Metals and Assessment of Potential Ecological Hazard for the Warta River, Poland. *Minerals*, 11(3), 327. <https://doi.org/10.3390/min11030327>
44. Ontiveros-Cuadras, J.F., Ruiz-Fernández, A.C., Pérez-Bernal, L.H., Raygoza-Viera, J.R. and Sanchez-Cabeza, J.-A., 2021. Historical Reconstruction of Trace Element Concentrations and

- Fluxes in a Tropical Coastal Lagoon (Mexican Pacific) Derived from  $^{210}\text{Pb}$  Radiochronology. *Continental Shelf Research*, 213, 104315. <https://doi.org/10.1016/j.csr.2020.104315>
45. Zhang, J. and Liu, C.L., 2002. Riverine Composition and Estuarine Geochemistry of Particulate Metals in China – Weathering Features, Anthropogenic Impact and Chemical Fluxes. *Estuarine, Coastal and Shelf Science*, 54(6), pp. 1051-1070. <https://doi.org/10.1006/ecss.2001.0879>
  46. Essien, J.P., Antai, S.P. and Olajire, A.A., 2009. Distribution, Seasonal Variations and Ecotoxicological Significance of Heavy Metals in Sediments of Cross River Estuary Mangrove Swamp. *Water, Air, and Soil Pollution*, 197(1-4), pp. 91-105. <https://doi.org/10.1007/s11270-008-9793-x>
  47. Salomons, W. and Förstner, U., 1984. *Metals in the Hydrocycle*. Berlin, Heidelberg: Springer-Verlag, 352 p. <https://doi.org/10.1007/978-3-642-69325-0>
  48. Özşeker, K., Erüz, C. and Terzi, Y., 2022. Evaluation of Toxic Metals in Different Grain Size Fractions of Sediments of the Southeastern Black Sea. *Marine Pollution Bulletin*, 182, 113959. <https://doi.org/10.1016/j.marpolbul.2022.113959>
  49. Que, W., Yi, L., Wu, Y. and Li, Q., 2024. Analysis of Heavy Metals in Sediments with Different Particle Sizes and Influencing Factors in a Mining Area in Hunan Province. *Scientific Reports*, 14(1), 20318. <https://doi.org/10.1038/s41598-024-71502-3>
  50. Abdallah, M.A.M., 2023. Accumulation and Distribution of Heavy Metals in Surface Sediments from the Continental Shelf Adjacent to Abu Qir Bay, Egypt, as a Function of Grain Size. *Geo-Marine Letters*, 43(1), 2. <https://doi.org/10.1007/s00367-022-00743-w>

Submitted 16.08.2024; approved after review 25.09.2024;  
accepted for publication 13.03.2025.

*About the authors:*

**Konstantin I. Gurov**, Researcher, Marine Hydrophysical Institute of RAS (2 Kapitanskaya Str., Sevastopol 299011, Russian Federation), CSc. (Geogr.), **ORCID ID: 0000-0003-3460-9650**, **Scopus Author ID: 57200248245**, **ResearcherID: L-7895-2017**, [gurovki@gmail.com](mailto:gurovki@gmail.com)

**Ekaterina A. Kotelyanets**, Junior Researcher, Marine Hydrophysical Institute of RAS (2 Kapitanskaya Str., Sevastopol 299011, Russian Federation), CSc. (Geogr.), **ORCID ID: 0009-0007-1921-3566**, **Scopus Author ID: 36059344400**, **ResearcherID: AAA-8699-2019**, [plistus@mail.ru](mailto:plistus@mail.ru)

**Yulia S. Gurova**, Researcher, Marine Hydrophysical Institute of RAS (2 Kapitanskaya Str., Sevastopol 299011, Russian Federation), CSc. (Geogr.), **ORCID ID: 0000-0002-9826-4789**, **Scopus Author ID: 57964475800**, **ResearcherID: AAB-5628-2019**, [gurova@mhi-ras.ru](mailto:gurova@mhi-ras.ru)

*Contribution of the co-authors:*

**Konstantin I. Gurov** – general scientific supervision of the research, formulation of goals and objectives of the study, data preparation, analysis and synthesis of research result, interpretation of the results, processing and description of the study results, preparation of graphic and text materials, writing of the original draft

**Ekaterina A. Kotelyanets** – sampling, conceptualization, data preparation; analysis and synthesis of research results; presentation of data in the text and their analysis; article correction; advisory assistance

**Yulia S. Gurova** – data processing, analysis and interpretation of data, participation in the discussion of the paper materials, paper correction, formulation of the conclusions

*The authors have read and approved the final manuscript.*

*The authors declare that they have no conflict of interest.*

## Parameterization of the Dependence of Integral Phytoplankton Biomass on Chlorophyll Concentration at the Black Sea Surface Based on Expeditionary Research Data

I. V. Kovalyova

A. O. Kovalevsky Institute of Biology of the Southern Seas of RAS,  
Sevastopol, Russian Federation  
✉ [ilonavk@ibss-ras.ru](mailto:ilonavk@ibss-ras.ru)

### Abstract

**Purpose.** The purpose of the study is to present an algorithm for calculating the integral phytoplankton biomass in the Black Sea euphotic layer using expeditionary data, and to perform a comparative analysis of the variability of the studied characteristics obtained by means of calculations in two ways: using direct measurements of chlorophyll concentration along the horizons, and based on the parameterization results. **Methods and Results.** The algorithm for calculating the integral biomass of phytoplankton is presented. Data from Crimean coastal waters at the depths of 20–1500 m, collected during R/V *Professor Vodyanitsky* cruises for different seasons of 2018–2022, were used in this study. The estimates resulted from parameterization and those obtained from calculations based on direct measurements of the individual input parameters at different depths are compared. The results of parameterization statistical analysis show that the determination coefficients varied in the range 0.70–0.74. In the photosynthesis zone, the monthly averages of integral phytoplankton biomass (calculated from the expeditionary data) in June and October constitute  $768 \pm 283$  and  $2277 \pm 726$  mg C/m<sup>2</sup>, respectively. In the upper mixed layer, in June they are  $556 \pm 270$  mg C/m<sup>2</sup>, and in October –  $2023 \pm 725$  mg C/m<sup>2</sup>. The parameterization-derived monthly averages for the whole water area under study differ from the ones calculated using the direct measurements of input parameters at different depths by 0.9–4%. The chlorophyll a concentration profiles for individual months in 2018–2022 are considered and mathematically described using the function obtained in earlier studies. In autumn, maximum values of chlorophyll a are observed mainly in the upper mixed layer. In summer, they occur at the lower boundary of the euphotic zone, where up to ~0.1% of light reaching the sea surface penetrates.

**Conclusions.** The above parameterization of integral phytoplankton biomass is applicable to all the seasons, easy to use and agrees well with the results of calculations based on direct measurements of chlorophyll concentration at different depths. In the future, the calculation algorithm will be refined to facilitate computations based on satellite data.

**Keywords:** integral biomass, phytoplankton, Black Sea, calculation algorithm, chlorophyll a concentration profiles

**Acknowledgements:** The study was funded by the Russian Science Foundation and the Government of Sevastopol (Grant No. 24-27-20014, “Transformation of the structure and functional characteristics of the Black Sea phytoplankton off the Crimea coast in modern environmental conditions. Fundamental role and applied importance”, <https://rscf.ru/project/24-27-20014/>). The work was carried out at the Center for Collective Use of R/V *Professor Vodyanitsky*. The author expresses gratitude to N. V. Minina, Leading Engineer, for collecting data during the cruises.

**For citation:** Kovalyova, I.V., 2025. Parameterization of the Dependence of Integral Phytoplankton Biomass on Chlorophyll Concentration at the Black Sea Surface Based on Expeditionary Research Data. *Physical Oceanography*, 32(3), pp. 347-360.

© 2025, I. V. Kovalyova

© 2025, Physical Oceanography



## Introduction

Phytoplankton form the primary link in the trophic chain of aquatic ecosystems. One of the most important indicators of this is biomass. Changes in phytoplankton biomass affect the development of all subsequent trophic levels. Many studies have been carried out for many years on changes in phytoplankton biomass over time and its spatial distribution in the sea [1–12]. Microalgae biomass is usually determined by direct measurement of cell volume, followed by recalculation in various dimensions [1, 3, 4, 13, 14]. In addition to these direct methods, models are being developed that allow the ratio of chlorophyll to organic carbon and phytoplankton biomass to be estimated [9, 15–17]. Models for calculating phytoplankton biomass using a minimum number of easily accessible input parameters can significantly simplify the task, especially when analyzing spatial and temporal changes. Models for calculating phytoplankton parameters are also necessary for studies that use satellite data. Estimates of integral phytoplankton characteristics in the photosynthetic zone are of particular interest. For example, simple, user-friendly models for calculating integral primary production have been developed for the Black Sea <sup>1</sup> [18, 19]. However, similar calculation algorithms for integral phytoplankton biomass with easily accessible input parameters have been presented poorly in the literature. Although model data are inferior in accuracy to direct measurements, direct estimation methods are labor-intensive. Calculating the integral phytoplankton biomass in the euphotic zone and the upper mixed layer (UML) allows for the prompt and extensive analysis of water ecosystems and their use in calculations with satellite observation data.

The study aims to present an algorithm for calculating integral phytoplankton biomass in the euphotic layer of the Black Sea using expeditionary data, and to conduct a comparative analysis of the variability of the studied characteristics obtained through two calculation methods: direct chlorophyll concentration measurements along the horizons and parameterization results.

## Materials and methods

The measurements used in this paper were carried out at the Collective Use Data Center of R/V *Professor Vodyanitsky* during cruises No. 122 (June 7 – July 2, 2022) and No. 124 (October 3–20, 2022) in the Black Sea off the southern and southeastern coasts of Crimea. Sampling was performed at station depths of 32–1500 m, with samples collected at 10–20 m below the surface, near the thermocline at deep-water stations, and in the bottom layer at stations with depths of  $\leq 100$  m.

Surface light intensity was measured daily between 08:00 to 20:00 using a LI-1500 illuminance recorder with a LI-190R quantum sensor (LI-COR, USA). Daily integral irradiance was then calculated.

---

<sup>1</sup> Demidov, A.B., 2001. [*Seasonal Variations in Primary Production and Chlorophyll a in Open Areas of the Black Sea*]. Thesis Cand. Biol. Sci. Moscow: Moscow State University, 188 p. (in Russian).

The UML was determined using data from an IDRONAUT OCEAN SEVEN 320 Plus M probe, based on a water density increase of 0.07 relative to the surface [20].

The relative water transparency was assessed using a Secchi disk during daylight hours. The euphotic zone depth ( $Z_{eu} = 3Z_s$ )<sup>2</sup>, where up to 1% of the light falling on the surface penetrates, was determined based on the Secchi disk visibility depth ( $Z_s$ ) data. The light diffusion attenuation indicator  $k_d$  ( $m^{-1}$ ) was estimated using the formula obtained from the data<sup>3, 4</sup>:

$$k_d = 4.6/Z_{eu} \quad (r^2 = 0.96).$$

The methodology for determining the concentration of chlorophyll a (hereinafter referred to as ‘chlorophyll a’ throughout this paper), the measurement data collected during the voyages and the areas of water studied are described in [21].

To analyze the chlorophyll concentration profiles, data obtained on R/V *Professor Vodyanitsky* during cruises No. 105, 106, 108, 110, 122 and 124 in November–December, April, July–August, October, June and October 2018–2022 are used. Concentration measurements were usually taken at 10 m intervals down to a depth of 40–50 m and, in some cases, deeper.

Statistical data processing was carried out using Excel, SigmaPlot, Grapher, and OriginLab software.

## Results

In this study we modified the previously developed algorithm for calculating phytoplankton biomass in the surface layer of the Black Sea [15], which was adjusted in [22], to estimate integral indicators. Input parameters were calculated for each horizon and then the biomass was integrated by depth.

The following equation to calculate phytoplankton biomass  $B_z$  ( $mg\ C/m^3$ ) at  $z$  depth (m) was used:

$$B_z = Chl_z/Chl:C_z, \quad (1)$$

where  $Chl_z$  ( $mg/m^3$ ) is the chlorophyll concentration at  $z$  depth;  $Chl:C_z$  is the ratio of chlorophyll concentration to organic carbon, calculated at each horizon:

$$Chl:C_z = 0.0072(E_z a_{phz})^{-0.395} \quad (r^2 = 0.78), \quad (2)$$

$$a_{phz} = 0.017 Chl_z^{-0.29}. \quad (3)$$

<sup>2</sup> Man'kovskiy, V.I., Soloviev, M.V. and Man'kovskaya, E.V., 2009. [*Hydrooptical Properties of the Black Sea. Handbook*]. Sevastopol: MHI NAS of Ukraine, 92 p. (in Russian).

<sup>3</sup> Vedernikov, V.I., 1989. [Primary Production and Chlorophyll in the Black Sea in Summer–Autumn Period]. In: M. E. Vinogradov and M. V. Flint, eds., 1989. *Structure and Production Characteristics of Plankton Communities of the Black Sea*. Moscow: Nauka, pp. 65–83 (in Russian).

<sup>4</sup> Voznyak, B., Kopter, R. and Vedernikov, V.I., 1986. [Input of Photosynthetically Active Radiation into the Euphotic Zone of the Black Sea in April–May 1984]. In: IO AN SSSR, 1986. *Study of the Ecosystem of the Pelagic Zone of the Black Sea*. Moscow: IO AN SSSR-KOTS “World Ocean”, pp. 198–221 (in Russian).

The equation parameters for Chl:C were obtained from algae cultures in laboratory experiments under different illumination conditions, as described in [15]. To estimate Chl:C at different horizons, the illumination at each depth was determined using the following equation:

$$E_z = 0.94E_0 \exp(-k_d z), \quad (4)$$

where  $E_z$ ,  $E_0$  (mol quanta/m<sup>2</sup>-day) represents the intensity of photosynthetically active radiation (PAR) at depth  $z$  and at the sea surface, respectively; the coefficient 0.94 accounts for 6% surface light reflection<sup>5</sup>;  $a_{phz}$  (m<sup>2</sup>/mg Chl) is the indicator of light absorption by algae pigments, normalized to the chlorophyll concentration.

The integral biomass of phytoplankton was calculated using distribution equations for the necessary indicators. For chlorophyll concentration, the Gaussian curve proposed in [23] was used:

$$\text{Chl}_z = (h/\sigma(2\pi)^{1/2}) \exp[-(z - z_m)^2/2\sigma^2], \quad (5)$$

$$h = (55.73 \pm 1.40) \text{Chl}_0^{(0.56 \pm 0.008)} \quad (r^2 = 0.75), \quad (6)$$

$$z_m = (11.1 \pm 0.75) - (10.46 \pm 0.45) \ln(\text{Chl}_0) \quad (r^2 = 0.61), \quad (7)$$

where  $h$  is the total chlorophyll content (mg/m<sup>3</sup>) in the maximum layer;  $\sigma$  (m) is the index of the deep chlorophyll maximum width;  $z_m$  (m) is the depth of the chlorophyll maximum;  $\text{Chl}_0$  (mg/m<sup>3</sup>) is the chlorophyll concentration in the surface layer. When estimating the depth of the chlorophyll maximum, according to function (7), it is assumed that the maximum will always be at the surface if  $\text{Chl}_0 > 2.89$  mg/m<sup>3</sup>. However, when calculating equation (5),  $z_m$  is used as function (7). The maximum width of the  $\sigma$  is equal to  $20 \pm 10$  m at  $\text{Chl}_0 < 1$  mg/m<sup>3</sup> and  $13 \pm 8$  m at  $\text{Chl}_0 > 1$  mg/m<sup>3</sup> [23]. This value was calculated to be 68% of the chlorophyll peak height according to the law of Gaussian distribution. Formula (5), when applied to the input components, is valid for chlorophyll concentration values in the surface layer typical of the Black Sea. This distribution is typical of the warm period of the year (April–October, and sometimes November); whereas for the cold period (December–March) it is considered that chlorophyll is distributed uniformly [18, 23]. The nutritional conditions during the development of the model were assumed to be optimal.

For each depth, the parameters  $a_{phz}$ ,  $\text{Chl:C}_z$ ,  $B_z$ ,  $E_z$  were calculated, taking into account the direct measurements obtained during the cruises. The integral biomass calculation was carried out in two ways: the first included direct measurements of chlorophyll concentration in the algorithm; the second used equation (5) to calculate the distribution of this parameter with depth; the remaining parameters were calculated identically. Then, the biomass was integrated by depth for the euphotic zone and UML.

---

<sup>5</sup> Mankovsky, V.I., 1996. *Fundamentals of Ocean Optics. Methodical Manual*. Sevastopol: MHI NAS of Ukraine, 119 p. (in Russian).

The results of the integral phytoplankton biomass comparison, obtained by calculation using the presented algorithm and equation (5), showed high consistency with the biomass calculated using direct measurements of chlorophyll concentration for the coastal area along Crimea and the open coast (depths greater than 500 m) of the northern Black Sea. The statistical characteristics of the compared values for the photosynthesis zone and the UML are presented in Fig. 1 and in the accompanying table.

**Statistical indicators and average values obtained by the algorithm and calculated using direct measurements of chlorophyll concentration at horizons for the integral phytoplankton biomass averaged based on the data collected in cruises No. 122 and 124 of R/V *Professor Vodyanitsky***

Zones	$r$	$r^2$	$F$	$P$	$\langle B \rangle_{122}$	$\langle B \rangle_{124}$	$\langle B_p \rangle_{122}$	$\langle B_p \rangle_{124}$
Euphotic zone	0.84	0.70	75.4	< 0.0001	768 ± 283	2277 ± 726	776 ± 276	2212 ± 759
UML	0.86	0.74	89.5	< 0.0001	556 ± 270	2023 ± 725	561 ± 240	1942 ± 719

Note:  $r$  is the correlation coefficient,  $r^2$  is the determination coefficient,  $F$  is the Fisher criterion,  $P$  is the importance level,  $\langle B \rangle$  and  $\langle B_p \rangle$  (mg C/m<sup>2</sup>) are the average values of integral phytoplankton biomass obtained using direct measurements and parameterization results, respectively.

The differences between the model and the measured data for the chlorophyll concentration profiles are reflected in the results of the biomass calculation using the two methods. These differences appear when the maximum chlorophyll concentration on the surface is quite high and then decreases sharply with depth, or when there are low values on the surface and a maximum with a high chlorophyll concentration at depth. Significant differences in the results of the biomass calculation by the two methods are also observed in the presence of two-peak chlorophyll concentration profiles. Compared to direct measurements, model calculations can overestimate or underestimate phytoplankton biomass by up to one and a half times in the cases described above. However, the number of chlorophyll concentration profiles that deviate so markedly from the parameterized description is small: 18% according to data from two cruises in the euphotic zone, and 15% in the UML. Measurements were carried out almost daily during the cruises at various stations in the coastal and deep-water areas near the Crimean coast. Consequently, when averaging is applied, the results obtained using the distribution function and those obtained using direct measurement data will be smoothed and approximated (Table and Fig. 1).

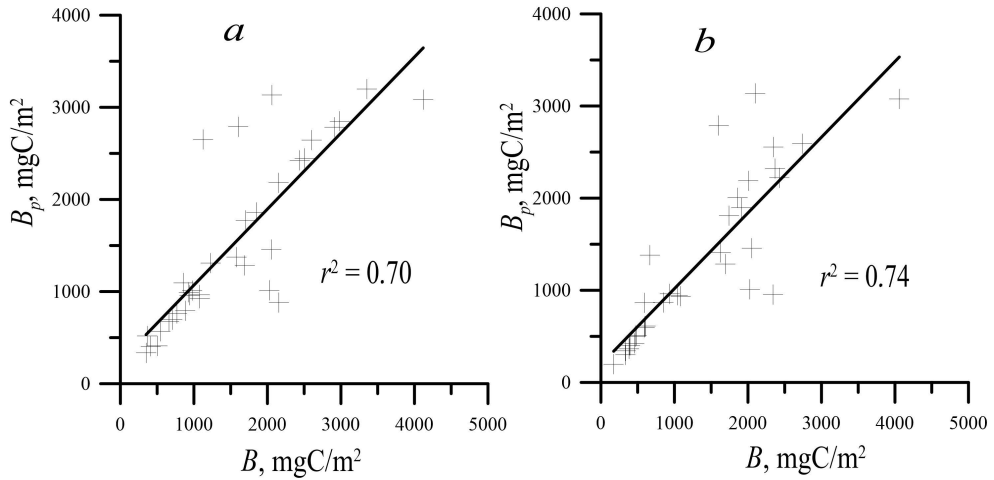


**Fig. 1.** Comparison of the values of integral phytoplankton biomass obtained by parameterization ( $B_p$ ) and calculated using direct measurements of input parameters ( $B$ ) for the euphotic zone (a) and UML (b)

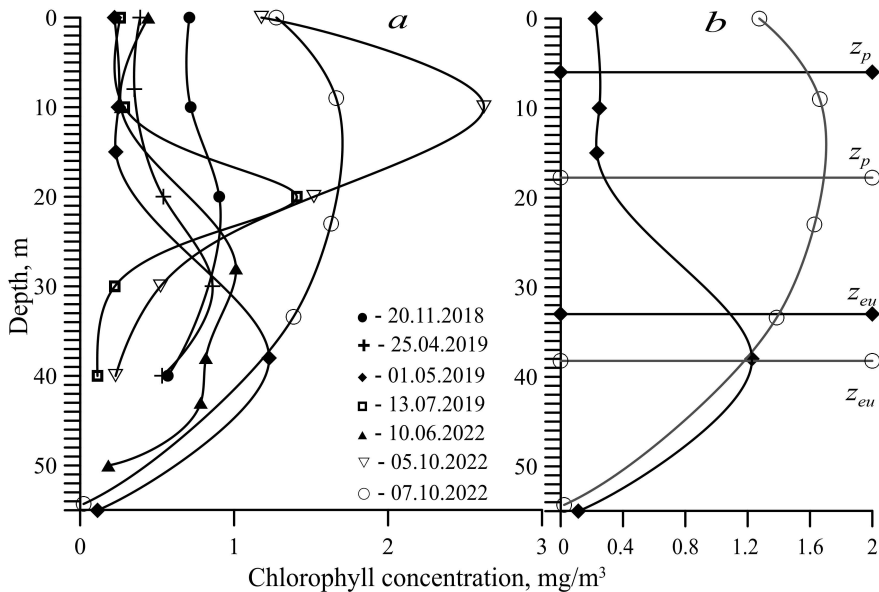


**Fig. 2.** Change in chlorophyll concentration with depth based on the data obtained during the cruises of R/V *Professor Vodyanitsky* in 2018–2022: a – for selected days in different months; b – showing data from 7 October 2022 (○) and 1 May 2019 (◆) with UML ( $z_p$ ) and euphotic zone ( $z_{eu}$ ) boundaries

The present paper analyzes 88 chlorophyll concentration profiles from April to December. Some examples are shown in Fig. 2. Over the entire period under consideration, two-peak profiles were observed 9 times and a three-peak profile was observed once. These profiles were mainly observed in October (6 times), as well as in June (3 times) and August (once). Maximum chlorophyll concentrations were usually observed within the UML zone in October, November and December (Fig. 2). However, during cruise No. 110 in October, the maximum was more often

noted at the lower boundary of the UML or below this zone. In June and April, the maximum chlorophyll concentration was below the UML at the lower boundary of the euphotic layer (Fig. 2), and was sometimes below 1% of the PAR illumination falling on the sea surface. In July–August, the chlorophyll peak was also observed within the euphotic zone or at its lower boundary. Equation (5) of the chlorophyll concentration distribution [23], presented above, provided a description of the profiles that was close to the measurement data. According to our data, which used all the points from two cruises, testing showed  $r = 0.68$  in June and  $r = 0.64$  in October (Fig. 3). Of the 218 points used in the calculations for the two cruises (No. 122 and 124), the correlation coefficient varied for 21 profiles in the range of 0.80–0.99, for five profiles – in the range of 0.60–0.8, for five profiles – in the range of 0.30–0.60 and for three profiles it was less than 0.10.

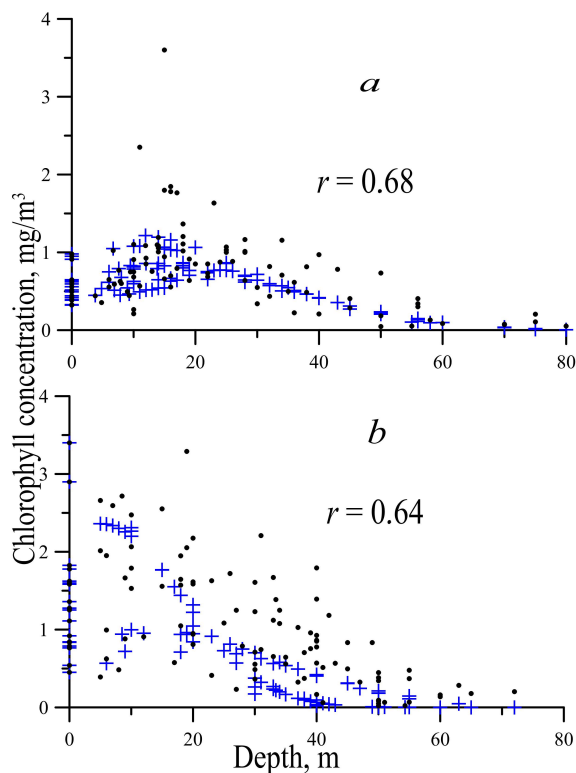


**Fig. 3.** Change in chlorophyll concentration with depth in cruises No. 122 (a) and 124 (b) of R/V *Professor Vodyanitsky* (data obtained using the distribution function (5) are indicated with a cross, and the direct measurement data – with a circle)

The relationship between  $\sigma$  and  $\text{Chl}_0$ , the UML, the euphotic zone depth and the temperature of the sea surface layer, as well as with  $E_0$  and  $k_d$ , was considered. The  $\sigma$  indicator showed the best agreement with the UML, euphotic zone depth and  $\text{Chl}_0$ , but no reliable correlation with the analyzed parameters was revealed in the sample. According to the multiple correlation results, the influence of the three specified parameters explained 20% of the variability

in  $\sigma$ , while the influence of six parameters explained 25%. The average value of  $\sigma$  was  $25 \pm 10$  m across all the months considered, varying in the 2–48 m range. In the autumn months, the  $\sigma$  width was comparable with the UML values; however, in the summer months, it could exceed them several times over. Compared with the width of the euphotic zone, the  $\sigma$  parameter was almost always smaller than or comparable with it. It can be assumed that  $\sigma$  depends on the amount of nutrients and the characteristics of the hydrological conditions since no obvious correlation was found with the six considered parameters. These parameters were chosen for estimating  $\sigma$  because they can be easily determined and calculated using satellite data, which will facilitate more extensive studies in the future.

Also, studies of chlorophyll concentration profiles revealed that the maximum concentration in spring (from April) and summer can be observed at approximately up to the 0.1% light penetration from the surface values. Accordingly, the euphotic zone boundary will be below 1% PAR in these months.

### Discussion

There are very few data on the integral biomass of phytoplankton in the literature, particularly with regard to the Black Sea. For example, the authors of [24] estimate the integral biomass of diatoms using models from [17, 25], comparing the results with chlorophyll concentrations obtained from satellite data. An earlier study [26] used a simplified approach to calculate integral biomass when analyzing expeditionary studies carried out in winter and spring. However, the calculation methods used in these studies did not consider the depth distribution of important phytoplankton characteristics and optical indicators when estimating biomass. The calculations were carried out in different areas and the results were difficult to compare with each other.

The phytoplankton biomass distribution function is given in [23]. This requires nitrate concentration and water temperature measurements by horizon, which are not always possible. Another function from this paper requires the determination of optical depth and provides rough estimates of integral biomass compared to direct measurements, as indicated by the authors themselves. For example, we compared calculated integral phytoplankton biomass data using the specified function, which includes optical depth and integral biomass values obtained by our algorithm, with data obtained by direct chlorophyll concentration measurements at different horizons. We analyzed 34 biomass profiles obtained from the results of cruises No. 122 and 124 of R/V *Professor Vodyanitsky* in June and October. Their comparison showed the consistency of the two calculation methods for June ( $r^2 = 0.63$ ) and October ( $r^2 = 0.19$ ). It was also found that, compared to our calculations, the values obtained using the biomass function from [23] in October were often approximately twice as high.

Direct determinations of phytoplankton biomass, particularly integral determinations, are labor-intensive and carried out extremely rarely. No such measurements have been taken in the Black Sea for 10–15 years. Therefore, it is not

possible to obtain or compare direct measurements of integral biomass with calculation results due to the absence of such measurements. The consistency of the measured and calculated phytoplankton biomass values for the surface layer obtained using the algorithm described earlier in [15, 22, 27] has been demonstrated. The distribution function (5) of chlorophyll concentration was also compared with direct measurement data at the horizons in the present paper and in [23]. Based on this consistency, it is assumed that the calculated values at the horizons, taking into account different illumination, are adequate.

Our research builds upon the works of [15, 23]. The algorithm we have developed for calculating integral biomass is based on laboratory and expeditionary studies. It is easy to use and shows good comparability with calculation data, including direct measurements of chlorophyll concentration at different horizons (Table). The algorithm considers the depth distribution of important input parameters such as Chl,  $a_{ph}$ , Chl:C, as well as the illumination variation with depth. The algorithm used for the surface layer was developed based on 10 species of algae found in the Black Sea (*Nitschia sp.*, *Pseudonitschia delicatissima*, *Skeletonema costatum*, *Talasiossira parva*, *Coscinodiscus granii*, *Phaeodactylum tricornerutum*, *Prorocentrum micans*, *Isochrysis galbana*, *Dunaliella tertiolecta*, *Glenodinium foliaceum*), including species from the dominant taxonomic groups (diatoms and dinoflagellates), which were available for experimentation. For these species, the aforementioned dependencies of the physiological and structural parameters of microalgae and their average coefficients were obtained (equations (1) – (7)). In this model, the nutritional conditions are assumed to be optimal at different illumination levels.

In our algorithm, we rely on measurements of chlorophyll concentration and the previously obtained dependence of the average specific content of chlorophyll in cells of different types of algae in individual groups. The Chl:C estimation in the model from [15] was performed by taking into account light absorption by microalgae, enabling an approximate total phytoplankton biomass estimate despite the absence of other species in the parameterization.

One limitation of our algorithm is that it does not consider coccolithophores, which dominate at the beginning of summer [11, 28–30]. Therefore, phytoplankton biomass values may be underestimated during their ‘blooming’ period. According to the results of our earlier studies presented in [21], coccolithophores dominated in June compared to other microalgae groups. The integral biomass data calculated in two ways showed high consistency, and the phytoplankton biomass values were not low. This can be explained by the relatively close average specific chlorophyll content values in the cell <sup>6</sup> of the considered diatoms and coccolithophores. The algorithm provides general estimates of phytoplankton biomass without dividing microalgae into groups and types. Therefore, the results should be analyzed taking into account the limitations and assumptions of this model.

---

<sup>6</sup> Stelmakh, L.V., 2017. [*Patterns of Phytoplankton Growth and Its Consumption by Microzooplankton in the Black Sea*]. Doctor of Biological Sciences Dissertation. Sevastopol, 310 p. (p. 37) (in Russian).

Analysis of the chlorophyll concentration profiles reveals that, in most cases, maximum formation occurs in the UML zone in autumn. This may be due to increased mixing of water masses, the flow of biogenic substances into the upper water layers, and expansion of the UML zone. At the same time, dissolved organic matter resulting from the activity of marine organisms remains in the surface layer. Decreased solar radiation also allows the photosynthesis zone to rise higher, enabling the development of algae species that experienced photoinhibition in the UML zone in summer. The same reasons can also cause two peaks to form in the chlorophyll profiles during this period. The formation of chlorophyll maxima in April and in the summer outside the UML, at the lower boundary of the euphotic zone, is mainly associated with high levels of illumination, pronounced temperature stratification in the water column, and a narrow UML zone. For example, in June, peaks in the chlorophyll profiles were observed at less than 1% illumination, which indicates euphotic zone expansion due to the high level of PAR falling on the sea surface.

Mathematically describing chlorophyll concentration profiles remains problematic in cases where there are two or even three maxima in the water column or the profile is atypically single-peaked. This problem is simplified by the fact that complex profiles are uncommon, and differences are smoothed out during averaging. The same thing happens when recalculating other phytoplankton parameters.

When constructing models of the Black Sea that take many factors into account, such as hydrological conditions and nutrient levels (including nitrogen, phosphorus and silicon compounds), it is necessary to take contact measurements of these parameters. Studies and data collection were conducted over several years to identify relationship between parameters such as dominant species and nutrients, taking wind activity into account [12], as well as the relationship between river runoff and phytoplankton community structure [31]. Considering all these factors will lead to the development of more complex models in the future. However, not all of the specified input parameters will currently or in the near future be available to estimate integral values based on satellite data. Although there are complex global models of marine ecosystems that include a large number of input parameters [17, 32–34], they do not describe all cases either and also have their own assumptions, limitations and errors.

Our current task is to create a simple algorithm for estimating total phytoplankton biomass and integral values within the water column, taking into account the average ratios of specific chlorophyll within cells of certain dominant microalgae groups (equation (2)). The proposed algorithm is applicable to all seasons and considers the distribution of chlorophyll concentration (equation (5)) from April to November, as well as its uniform distribution from December to March [23]. The results were analyzed using data from two seasons. Thus, the average monthly integral phytoplankton biomass values obtained from our parameterization differ by 0.9–4% from those obtained from calculations using measured input parameters at different depths (Table). With a limited supply of individual nutrients, deviations in the Chl:C ratio are possible. In real conditions, changes in species

composition also occur. However, the parameterization proposed in this paper does not take such factors into account. The algorithm only allows estimation of variability in total phytoplankton biomass based on the average characteristics described above (equations (1) – (7)). The proposed parameterization can be applied to estimate integral biomass. This calculation algorithm will be useful for future calculations based on satellite data that take into account the hydrooptical characteristics of the Black Sea [35].

### Conclusion

The presented algorithm was used to calculate the integral biomass of phytoplankton in the coastal and open coastal zones (at depths over 500 m) of the northern Black Sea. The results of the integral biomass calculation obtained using two methods are in good agreement: one method used data from direct measurements of input parameters at different depths in expeditionary studies, while the other method used equations for the distribution of input parameters. According to the statistical analysis, the determination coefficients for the data from the two cruises are 0.7 and 0.74, respectively. The average monthly values and standard deviations of the integral phytoplankton biomass, calculated based on the results of expeditionary studies, are  $768 \pm 283$  mg C/m<sup>2</sup> in the photosynthesis zone in June and  $2277 \pm 726$  mg C/m<sup>2</sup> in October, and  $556 \pm 270$  mg C/m<sup>2</sup> in June and  $2023 \pm 725$  mg C/m<sup>2</sup> in October in the upper quasi-homogeneous layer. The average monthly values calculated using the two methods varied by 0.9–4%.

The presented algorithm includes distribution equations for all input parameters and is user-friendly and convenient for working with satellite data. Analysis of chlorophyll concentration profiles revealed that the peak is typically observed in the UML zone in autumn and at the lower boundary of the euphotic layer in April – July, when up to 0.1% of the PAR reaching the sea surface is absorbed. Multiple correlation analysis revealed no reliable correlation between the width of the deep maximum of chlorophyll concentration in the water layer and any of the following six parameters: chlorophyll concentration at the surface; UML and euphotic layer depth; temperature; illumination on the sea surface; and the diffuse light attenuation coefficient. It was found that these parameters influence the variability of the width of the chlorophyll maximum by 25%.

### REFERENCES

1. Selifonova, Zh.P. and Yasakova, O.N., 2012. Phytoplankton of Areas of the Seaports of the Northeastern Black Sea. *Marine Ecological Journal*, 11(4), pp. 67-77 (in Russian).
2. Krasheninnikova, S.B., Minkina, N.I., Samyshev, E.Z. and Shokurova, I.G., 2019. The Influence of the Complex of Environmental Factors on the Phytoplankton and Zooplankton Biomass in the Black Sea in Spring. *Ekologiya i Stroitelstvo*, (4), pp. 14-21. <https://doi.org/10.35688/2413-8452-2019-04-002>
3. Stelmakh, L.V. and Mansurova, I.M., 2020. Long-Term Dynamics of Phytoplankton and Chlorophyll a Concentration in the Surface Layer of the Coastal Waters of the Black Sea (Sevastopol Region). *Issues of Modern Algology*, 1(22), pp. 66-81. [https://doi.org/10.33624/2311-0147-2020-1\(22\)-66-81](https://doi.org/10.33624/2311-0147-2020-1(22)-66-81) (in Russian).

4. Stelmakh, L.V., 2019. Effect of Phytoplankton Adaptation on the Distribution of Its Biomass and Chlorophyll-a Concentration in the Surface Layer of the Black Sea. *Monitoring Systems of Environment*, 1(5), pp. 106-114. <https://doi.org/10.33075/2220-5861-2019-1-106-114> (in Russian).
5. Morozova-Vodyanitskaya, N.V., 1948. [Phytoplankton of the Black Sea. Part I. Phytoplankton in the Sevastopol Region and a General Overview of the Phytoplankton of the Black Sea]. In: SBS, 1948. *Trudy Sevastopolskoj Biologichskoj Stantsii*. Moscow-Leningrad: AS USSR Publishing. Vol. 6, pp. 39-172 (in Russian).
6. Morozova-Vodyanitskaya, N.V., 1954. [Phytoplankton of the Black Sea. Part 2. Phytoplankton in the Sevastopol Region and a General Overview of the Phytoplankton of the Black Sea]. In: SBS, 1948. *Trudy Sevastopolskoj Biologichskoj Stantsii*. Moscow-Leningrad: AS USSR Publishing. Vol. 8, pp. 11-99 (in Russian).
7. Marañón, E., Holligan, P.M., Varela, M., Mouriño, B. and Bale, A.J., 2000. Basin-Scale Variability of Phytoplankton Biomass, Production and Growth in the Atlantic Ocean. *Deep Sea Research Part I: Oceanographic Research Papers*, 47(5), pp. 825-857. [https://doi.org/10.1016/S0967-0637\(99\)00087-4](https://doi.org/10.1016/S0967-0637(99)00087-4)
8. Pérez, V., Fernández, E., Marañón, E., Morán, X.A.G. and Zubkov, M.V., 2006 Vertical Distribution of Phytoplankton Biomass, Production and Growth in the Atlantic Subtropical Gyres. *Deep Sea Research I: Oceanographic Research Papers*, 53(10), pp. 1616-1634. <https://doi.org/10.1016/j.dsr.2006.07.008>
9. Behrenfeld, M.J., Boss, E., Siegel, D.A. and Shea, D.M., 2005. Carbon-Based Ocean Productivity and Phytoplankton Physiology from Space. *Global Biogeochemical Cycles*, 19(1), GB1006. <https://doi.org/10.1029/2004GB002299>
10. Stelmakh, L.V., 2015. Spatial and Temporal Variability of Carbon to Chlorophyll a Ratio in Phytoplankton of the Surface Layer in Shallow Water Areas of the Black Sea (Crimea). *International Journal on Algae*, 17(4), pp. 385-396. <https://doi.org/10.1615/InterJAlgae.v17.i4.60>
11. Mikaelyan, A.S., Pautova, L.A., Chasovnikov, V.K., Mosharov, S.A. and Silkin, V.A., 2015. Alternation of Diatoms and Coccolithophores in the North-Eastern Black Sea: A Response to Nutrient Changes. *Hydrobiologia*, 755(1), pp. 89-105. <https://doi.org/10.1007/s10750-015-2219-z>
12. Silkin, V.A., Pautova, L.A., Giordano, M., Chasovnikov, V.K., Vostokov, S.V., Podymov, O.I., Pakhomova, S.V. and Moskalenko, L.V., 2019. Drivers of Phytoplankton Blooms in the Northeastern Black Sea. *Marine Pollution Bulletin*, 138, pp. 274-284, <https://doi.org/10.1016/j.marpolbul.2018.11.042>
13. Zhitina, L.S., Ilyash, L.V., Belevich, T.A., Klyuvitkin, A.A., Kravchishina, M.D., Tolstikov, A.V. and Tchultsova, A.L., 2016. Phytoplankton Structure in the White Sea after Summer Bloom: Spatial Heterogeneity in Relation to Hydrophysical Conditions. *Sibirskiy Ekologicheskij Jurnal*, 23(6), pp. 888-899. <https://doi.org/10.15372/SEJ20160608> (in Russian).
14. Menden-Deuer, S. and Lessard, E.J., 2000. Carbon to Volume Relationships for Dinoflagellates, Diatoms, and Other Protist Plankton. *Limnology & Oceanography*, 45(3), pp. 569-579. <https://doi.org/10.4319/lo.2000.45.3.0569>
15. Finenko, Z.Z., Kovalyova, I.V. and Suslin, V.V., 2018. A New Approach to Estimate Phytoplankton Biomass and Its Variability in the Black Sea Surface Water Layer Based on Satellite Data. *Uspekhi Sovremennoi Biologii*, 138(3), pp. 294-307. <https://doi.org/10.7868/S0042132418030079> (in Russian).
16. Abakumov, A.I. and Pak, S.Ya., 2021. Modeling of Photosynthesis Process and Assessing of Phytoplankton Dynamics Based on Droop Model. *Mathematical Biology and Bioinformatics*, 16(2), pp. 380-393. <https://doi.org/10.17537/2021.16.380> (in Russian).

17. Oguz, T., Ducklow, H.W. and Malanotte-Rizzoli, P., 2000. Modeling Distinct Vertical Biogeochemical Structure of the Black Sea: Dynamical Coupling of the Oxidic, Suboxic, and Anoxic Layers. *Global Biogeochemical Cycles*, 14(4), pp. 1331-1352. <https://doi.org/10.1029/1999GB001253>
18. Finenko, Z.Z., Suslin, V.V. and Churilova, T.Ya., 2009. The Regional Model to Calculate the Black Sea Primary Production Using Satellite Color Scanner SeaWiFS. *Morskoy Ekologicheskii Zhurnal*, 8(1), pp. 81-106 (in Russian).
19. Kovalyova, I.V. and Suslin, V.V., 2022. Integrated Primary Production in the Deep-Sea Regions of the Black Sea in 1998–2015. *Physical Oceanography*, 29(4), pp. 404-416. <https://doi.org/10.22449/1573-160X-2022-4-404-416>
20. Kubryakov, A.A., Belokopytov, V.N., Zatsepin, A.G., Stanichny, S.V. and Piotukh, V.B., 2019. The Black Sea Mixed Layer Depth Variability and Its Relation to the Basin Dynamics and Atmospheric Forcing. *Physical Oceanography*, 26(5), pp. 397-413. <https://doi.org/10.22449/1573-160X-2019-5-397-413>
21. Stelmakh, L.V., Mansurova, I.M., Farber, A.A., Kovaleva, I.V. and Borisova, D.S., 2024. Structural and Functional Parameters of the Black Sea Phytoplankton during the Summer Bloom of the Coccolithophore *Emiliana Huxleyi*. *Regional Studies in Marine Science*, 76, 103594. <https://doi.org/10.1016/j.rsma.2024.103594>
22. Kovalyova, I.V. and Suslin, V.V., 2023. Seasonal Variability of Biomass and Specific Growth Rate of Phytoplankton for 2016-2020 in the Deep-Water Zone of the Black Sea. *Sovremennye Problemy Distantionnogo Zondirovaniya Zemli iz Kosmosa*, 20(4), pp. 250-262. <https://doi.org/10.21046/2070-7401-2023-20-4-250-262> (in Russian).
23. Finenko, Z.Z., Churilova, T.Ya. and Li, R.I., 2005. Vertical Distribution of Chlorophyll and Fluorescence in the Black Sea. *Morskoy Ekologicheskii Zhurnal*, 4(1), pp. 15-46 (in Russian).
24. Kubryakova, E.A., Kubryakov, A.A. and Stanichny, S.V., 2018. Impact of Winter Cooling on Water Vertical Entrainment and Intensity of Phytoplankton Bloom in the Black Sea. *Physical Oceanography*, 25(3), pp. 191-206. <https://doi.org/10.22449/1573-160X-2018-3-191-206>
25. Mellor, G.L., 2001. One-Dimensional, Ocean Surface Layer Modeling: A Problem and a Solution. *Journal of Physical Oceanography*, 31(3), pp. 790-809. [https://doi.org/10.1175/1520-0485\(2001\)0312.0.CO;2](https://doi.org/10.1175/1520-0485(2001)0312.0.CO;2)
26. Finenko, Z.Z., Mansurova, I.M., Kovalyova, I.V. and Georgieva, E.Yu., 2021. Development of Phytoplankton in the Winter-Spring Period in the Coastal Waters of Crimea. *Marine Biological Journal*, 6(1), pp. 102-114. <https://doi.org/10.21072/mbj.2021.06.1.08> (in Russian).
27. Finenko, Z.Z., Mansurova, I.M. and Suslin, V.V., 2022. Temporal Dynamics of Phytoplankton Biomass in the Surface Layer of the Black Sea According to Satellite Observations. *Oceanology*, 62(3), pp. 358-368. <https://doi.org/10.1134/S0001437022030043>
28. Pautova, L.A., Mikaelyan, A.S. and Silkin, V.A., 2007. Structure of Plankton Phytocoenoses in the Shelf Waters of the Northeastern Black Sea during the *Emiliana Huxleyi* Bloom in 2002–2005. *Oceanology*, 47(3), pp. 377-385. <https://doi.org/10.1134/S0001437007030101>
29. Mikaelyan, A.S., Silkin, V.A. and Pautova, L.A., 2011. Coccolithophorids in the Black Sea: Their Interannual and Long-Term Changes. *Oceanology*, 51(1), pp. 39-48. <https://doi.org/10.1134/S0001437011010127>
30. Silkin, V.A., Pautova, L.A., Pakhomova, S.V., Lifanchuk, A.V., Yakushev, E.V. and Chasovnikov, V.K., 2014. Environmental Control on Phytoplankton Community Structure in the NE Black Sea. *Journal of Experimental Marine Biology and Ecology*, 461, pp. 267-274. <https://doi.org/10.1016/j.jembe.2014.08.009>
31. Sergeeva, V.M., Mosharov, S.A., Shulga, N.A., Kremenetskiy, V.V., Khlebopashev, P.V. and Matorin, D.N., 2023. Response of the Coastal Phytoplankton Community to the Runoff from Small Rivers in the Northeastern Black Sea. *Diversity*, 15(7), 857. <https://doi.org/10.3390/d15070857>

32. Vichi, M., Pinardi, N. and Masina, S., 2007. A Generalized Model of Pelagic Biogeochemistry for the Global Ocean Ecosystem. Part I: Theory. *Journal of Marine Systems*, 64(1-4), pp. 89-109. <https://doi.org/10.1016/j.jmarsys.2006.03.006>
33. Dorofeev, V.L., Korotaev, G.K. and Sukhikh, L.I., 2017. Analysis-Forecast System of the Black Sea Ecosystem State. *Problems of Ecological Monitoring and Ecosystem Modelling*, 28(2), pp. 71-85. <https://doi.org/10.21513/0207-2564-2017-2-71-85> (in Russian).
34. Belyaev, V.I. and Konduforova, N.V., 1990. *Mathematical Modelling of the Ecological Shelf Systems*. Kiev: Naukova Dumka, 240 p. (in Russian).
35. Suslin, V.V., Churilova, T.Ya. and Pryahina, S.F., 2012. The Black Sea IOPs Based on SeaWiFS Data. *Ecological Safety of Coastal and Shelf Zones and Comprehensive Use of Shelf Resources*, 26(2), pp. 204-223 (in Russian).

Submitted 16.08.2024; approved after review 03.03.2025;  
accepted for publication 13.03.2025.

*About the author:*

**Iлона В. Ковалыова**, Senior Researcher, Algae Eco-Physiology Department, A.O. Kovalevsky A. O. Kovalevsky Institute of Biology of the Southern Seas of RAS (2 Nakhimova Ave., Sevastopol, 299011, Russian Federation), CSc. (Biol.), **ORCID ID: 0000-0001-5430-2002**, **Scopus Author ID: 57211264299**, **ResearcherID: AAB-4397-2019**, **SPIN-code: 2356-4570**, [ilonavk@ibss-ras.ru](mailto:ilonavk@ibss-ras.ru)

*The author has read and approved the final manuscript.*

*The author declares that she has no conflict of interest.*

---

---

Original article

## Arakawa–Lamb Scheme in Application to Stratified Incompressible Fluid in the Absence of Friction

S. G. Demyshev

*Marine Hydrophysical Institute of RAS, Sevastopol, Russian Federation*

✉ demyshev@gmail.com

### Abstract

**Purpose.** The study is aimed at generalizing the Arakawa–Lamb scheme for discrete equations of the horizontal components of three-dimensional absolute vorticity of an ideal fluid and analyzing its features.

**Methods and Results.** To derive the finite-difference three-dimensional equations of absolute vorticity, a grid containing more unknowns than equations is applied, that permits obtaining the discrete motion equations which, in their turn, yield the equation for absolute vorticity. The resulting expression is presented in the form of three terms reflecting different features of the discrete equations. The first term provides the fulfillment of the energy conservation law for discrete statement, the second term represents the presence of two quadratic invariants for a divergence-free flow, the addition of the third term results in the Arakawa–Lamb scheme under the shallow water approximation. It follows from the presented expression that the second and third terms, which have no analogues in the continuous statement, can be interpreted as a zero approximation with the second order of accuracy. Thus, selection of these expressions makes it possible to construct the schemes with the required features of the conservation laws.

**Conclusions.** The presented form of the discrete equation for three-dimensional absolute vorticity enables the construction of schemes with the desired features. The difference equations for the horizontal components of absolute vorticity are derived, which possess two quadratic invariants.

**Keywords:** Arakawa-Lamb scheme, discrete equations of model, sea dynamics, kinetic energy, absolute vortex, quadratic invariants

**Acknowledgments:** The study was carried out as part of the state assignment of FSBSI FRC MHI under theme FNNN- 2021-0004.

**For citation:** Demyshev, S.G., 2025. Arakawa–Lamb Scheme in Application to Stratified Incompressible Fluid in the Absence of Friction. *Physical Oceanography*, 32(3), pp. 361-371.

© 2025, S. G. Demyshev

© 2025, Physical Oceanography

### Introduction

One of the fundamental results in the study of partial differential equations is Noether's theorem [1], which establishes a one-to-one correspondence between the properties of solutions to such systems and the conservation laws they possess. A clear example of its application to shallow water equations is the energy and potential enstrophy preserving scheme (conservation laws), which ensures the constancy of the mean wavenumber weighted by energy (a solution property).

For the two-dimensional dynamics finite-difference system of equations, work [2] derived schemes that preserve energy and the square of vorticity for non-divergent motion. For the shallow water approximation, work [3] presents a discrete system of equations with two quadratic invariants: energy and potential enstrophy. As a consequence of this property, in accordance with the differential



formulation, energy transfer towards small scales is prohibited. In [4], the Nambu bracket was discretized while preserving the antisymmetry property. This made it possible to generalize the Arakawa–Lamb scheme and derive a fully discrete (in time and space) finite-difference scheme possessing two quadratic invariants: energy and potential enstrophy. Building on this, we derived explicit finite-difference shallow water equations that conserve mass, circulation, energy and potential enstrophy on both a regular square grid and an unstructured triangular grid. The latter includes a regular hexagonal grid as a special case.

In [5], the classical Arakawa–Lamb scheme, which was originally formulated for orthogonal square grids, is extended to arbitrary non-orthogonal polygonal grids. The scheme obtained in [4] is also generalized to arbitrary orthogonal spherical polygonal grids in such a way as to ensure the conservation of energy and potential enstrophy. For the shallow water equations in the case of generalized curvilinear coordinates, work [6] derives an energy- and potential enstrophy-preserving finite-difference scheme based on tensor analysis. The paper demonstrates that exact conservation of discrete energy and potential enstrophy prevents distortion of the forward and inverse energy cascades in quasi-two-dimensional turbulent flow, thereby enhancing the stability of the scheme.

For shallow water equations that incorporate the full Coriolis force and bottom topography, work [7] presents a scheme conserving energy and potential enstrophy. The authors observe that preserving discrete energy and potential enstrophy prevents distortion of the forward and inverse energy cascades in quasi-two-dimensional turbulence, thereby improving the stability of the scheme.

This paper is a continuation of studies [8, 9] and presents a specific rewriting of the Arakawa–Lamb scheme. This allows the terms responsible for different conservation properties to be explicitly isolated in the equation for absolute velocity vorticity, and the scheme to be generalized for discrete equations of the horizontal components of velocity vorticity.

### Discrete equations of motion

Let us consider the differential equations of an incompressible fluid in a potential force field, assuming the absence of viscosity and external sources. In the Boussinesq approximation, in a Cartesian coordinate system and for a domain  $\Omega$  with boundary  $\partial\Omega$ , the velocity of motion satisfies the following system of equations in the Gromeka–Lamb form:

$$\frac{\partial \vec{U}}{\partial t} + \vec{\xi} \times \vec{U} = -\frac{1}{\rho_0} \nabla(P + E) + \vec{g} \frac{\rho}{\rho_0}, \quad (1)$$

$$\nabla \vec{U} = 0. \quad (2)$$

The following notations are introduced:  $\vec{U} = (u, v, w)$  – components of the flow velocity vector along the  $(x, y, z)$  axes, directed eastward, northward, and vertically downward, respectively;  $\vec{g} = (0, 0, g)$  – free fall acceleration;  $(P, \rho)$  – pressure and density of seawater;  $\rho_0 = 1 \text{ g/cm}^3$  (henceforth, pressure and density are assumed to be normalized by  $\rho_0$ );  $\vec{f} = (0, 0, f^z)$  – Coriolis parameter, where  $f^z = 2\omega \sin\varphi$ ;  $\omega$  – angular velocity of Earth’s rotation;  $\varphi$  – latitude.

In equation (1), the absolute vorticity and kinetic energy of motion are introduced:

$$\bar{\xi} = \text{rot } \bar{U} + \bar{f}, \quad \xi^x = \frac{\partial w}{\partial y} - \frac{\partial v}{\partial z}, \quad \xi^y = \frac{\partial u}{\partial z} - \frac{\partial w}{\partial x}, \quad \xi^z = \frac{\partial v}{\partial x} - \frac{\partial u}{\partial y} + f^z, \quad (3)$$

$$E = \rho_0 \frac{u^2 + v^2 + w^2}{2}. \quad (4)$$

In terms of tensor analysis,

$$\xi^\alpha = \varepsilon^{\alpha\beta\gamma} \partial_\beta v^\gamma + f^\alpha, \quad \text{where } (v^x, v^y, v^z) = (u, v, w).$$

Here and henceforth,  $\alpha, \beta, \gamma$  can only take distinct values of  $x, y, z$  simultaneously;  $\varepsilon^{\alpha\beta\gamma}$  is the Levi-Civita tensor and for each fixed  $\alpha$ , summation is performed over  $\beta$  and  $\gamma$ .

$$\text{At } z = 0 \quad w = -\zeta, \quad \text{at } z = H(x, y) \quad w = 0. \quad (5)$$

No-penetration conditions are imposed on lateral walls: for meridional boundaries  $u = 0$ , for zonal boundary segments  $v = 0$ . (6)

Initial conditions:

at  $t = t_0 \quad u = u^0, v = v^0, w = w^0$ .

The equation for absolute vorticity takes the following form:

$$\frac{\partial \bar{\xi}}{\partial t} + \nabla \times (\bar{\xi} \times \bar{U}) = \nabla \times (\bar{g} \rho). \quad (7)$$

We approximate the uneven-bottom basin using boxes whose centers correspond to the integer values of the indices  $i, j, k$  ( $i = i_1, \dots, i_N, j = j_1, \dots, j_M, k = 1, \dots, K_{i,j}$ ), while their faces correspond to the values  $i+1/2, j+1/2, k+1/2$ . The horizontal box dimensions  $(h_x, h_y)$  are constant, while the vertical approximation uses non-uniform spacing ( $h_z^k = z_{k+1/2} - z_{k-1/2}, h_z^{k+1/2} = z_{k+1} - z_k$ ).

Finite-difference operators are expressed as (similarly for  $j, k$ ):

$$\bar{\phi}_{i,j,k}^x = \frac{\phi_{i+1/2,j,k} + \phi_{i-1/2,j,k}}{2}, \quad \delta_x \phi_{i,j,k} = \frac{\phi_{i+1/2,j,k} - \phi_{i-1/2,j,k}}{h_x}, \quad (8)$$

$$\nabla_{x,y}^2 \phi_{i,j,k} = \delta_x^2 \phi_{i,j,k} + \delta_y^2 \phi_{i,j,k},$$

$$\{\phi\}^{\Omega_k} = \frac{1}{\Omega_k} \sum_{i,j} \phi_{i,j,k} h_x h_y, \quad \{\phi\}^V = \frac{1}{V} \sum_{i,j} \sum_{k=1}^{K_{i,j}} \phi_{i,j,k} h_z^k h_x h_y, \quad V = \sum_{i,j} \sum_{k=1}^{K_{i,j}} h_z^k h_x h_y.$$

Horizontal velocity components are calculated at  $z_k$  horizons, while vertical velocity is computed at  $z_{k+1/2}$  horizons – vertical velocity,  $\Omega_k$  denotes the surface area at  $k$  horizon. The distribution of the variables is shown in Fig. 1.

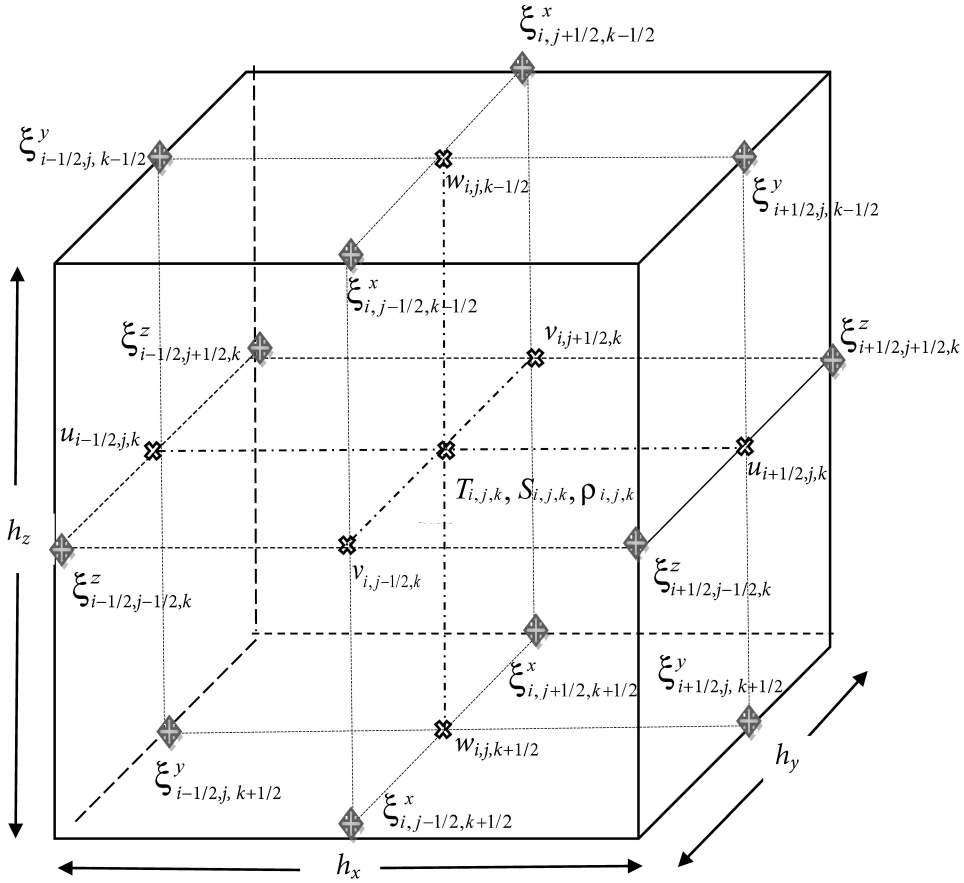


**Fig. 1** Distribution of variables in the box  $(i, j, k)$  and on its edges represents the absolute vorticity components  $\xi^x, \xi^y, \xi^z$

The differential-difference equations of motion (differential in time) [3, 9] are written below:

$$\frac{du_{i+1/2,j,k}}{dt} - [v, \xi^z]_{i+1/2,j,k} + [w, \xi^y]_{i+1/2,j,k} = -\delta_x (E_{i+1/2,j,k} + P_{i+1/2,j,k}), \quad (9)$$

$$\frac{dv_{i,j+1/2,k}}{dt} + [u, \xi^z]_{i,j+1/2,k} - [w, \xi^x]_{i,j+1/2,k} = -\delta_y (E_{i,j+1/2,k} + P_{i,j+1/2,k}), \quad (10)$$

$$\frac{dw_{i,j,k+1/2}}{dt} - [u, \xi^y]_{i,j,k+1/2} + [v, \xi^x]_{i,j,k+1/2} = -\delta_z (E_{i,j,k+1/2} + P_{i,j,k+1/2}) + g\rho_{i,j,k+1/2}. \quad (11)$$

Notations have been introduced for discrete analogs of nonlinear terms:

$$[v, \xi^z]_{i+1/2,j,k}, [w, \xi^y]_{i+1/2,j,k}, [u, \xi^z]_{i,j+1/2,k}, [w, \xi^x]_{i,j+1/2,k},$$

$[u, \xi^y]_{i,j,k+1/2}, [v, \xi^x]_{i,j,k+1/2}$ , whose specific form will be presented later.

In accordance with notations (3), (4), (8), the components of velocity vorticity (see Figure) and kinetic energy take the following form:

$$\begin{aligned}\xi_{i,j+1/2,k+1/2}^x &= \delta_y(w_{i,j+1/2,k+1/2}) - \delta_z(v_{i,j+1/2,k+1/2}), \\ \xi_{i+1/2,j,k+1/2}^y &= \delta_z(u_{i+1/2,j,k+1/2}) - \delta_x(w_{i+1/2,j,k+1/2}), \\ \xi_{i+1/2,j+1/2,k}^z &= \delta_x(v_{i+1/2,j+1/2,k}) - \delta_y(u_{i+1/2,j+1/2,k}) + f_{j+1/2}^z, \\ E_{i,j,k} &= \frac{\overline{u_{i,j,k}^2}^x + \overline{v_{i,j,k}^2}^y + \overline{w_{i,j,k}^2}^z}{2}.\end{aligned}\tag{12}$$

From approximation (5) it follows that at points  $i+1/2, j+1/2, k+1/2$  the following holds:

$$\delta_x \xi_{i,j+1/2,k+1/2}^x + \delta_y \xi_{i+1/2,j,k+1/2}^y + \delta_z \xi_{i+1/2,j+1/2,k}^z = 0.\tag{13}$$

Let us consider motion in the  $(x, y)$  plane. Unlike in the classical work [3], we write the nonlinear term  $[v, \xi^z]_{i+1/2,j,k}$  in the first equation and  $[u, \xi^z]_{i,j+1/2,k}$  in the second equation in the following form:

$$\begin{aligned}-[\xi, v]_{i+1/2,j,k} &= -\underbrace{\overline{v_{i+1/2,j} \xi_{i+1/2,j,k}^z}}_I - \underbrace{\frac{h_x^2 h_y^2}{48} \delta_x [(\delta_y v_{i+1/2,j,k})(\delta_x \delta_y \xi_{i+1/2,j,k}^z)]}_{II} + \\ &+ \underbrace{\frac{h_x h_y}{6} \{[\delta_x (\overline{u_{i+1/2,j,k} \delta_y \xi_{i+1/2,j,k}^z})] - \frac{1}{2} [u_{i+1/2,j,k} \delta_x \delta_y \xi_{i+1/2,j,k}^z]\}}_{III},\end{aligned}\tag{14}$$

$$\begin{aligned}[\xi, u]_{i,j+1/2,k} &= \underbrace{\overline{u_{i,j+1/2,k} \xi_{i,j+1/2,k}^z}}_I + \underbrace{\frac{h_x^2 h_y^2}{48} \delta_y [(\delta_x u_{i,j+1/2,k})(\delta_x \delta_y \xi_{i,j+1/2,k}^z)]}_{II} - \\ &- \underbrace{\frac{h_x h_y}{6} \{[\delta_y (v_{i,j+1/2,k} \delta_x \xi_{i,j+1/2,k}^z)] + \frac{1}{2} [v_{i,j+1/2,k} \delta_x \delta_y \xi_{i,j+1/2,k}^z]\}}_{III}.\end{aligned}\tag{15}$$

After standard transformations taking into account equality (13), we proceed to discrete equations of nondivergent flow in the  $(x, y)$  plane and obtain the equation for velocity vorticity. This equation possesses conservation laws for energy, vorticity and enstrophy (squared vorticity), all of which must be maintained in the finite-difference formulation. The significance of expressing nonlinear terms in equations (9) and (10) as expressions (14) and (15), respectively, is as follows. The finite-difference term marked with the numeral I corresponds to the differential analogue of horizontal advection. In the finite-difference equation for velocity vorticity, it ensures conservation of discrete energy; however, vorticity

and enstrophy are not invariants. The term marked with the numeral II is of fourth-order smallness and therefore does not change the order of the finite-difference scheme. However, its presence in expressions (14) and (15) ensures that the discrete equation for velocity vorticity in non-divergent flow satisfies the conservation laws for vorticity, energy and enstrophy [2].

The third term of second-order smallness is fundamentally different from the other two. While the first two can be interpreted as approximations of  $v\xi^z$ , the third term does not formally correspond to any component. It emerges as a consequence of conservativity being required in the discrete vorticity equation, which, along with the first term, ensures the conservation of energy and potential enstrophy in the shallow water model (divergent motion in the  $(x, y)$  plane) [3].

Based on these considerations, the equations of motion in the shallow water approximation can be expressed as follows:

$$\frac{du_{i+1/2,j}}{dt} - v_{i+1/2,j} \overline{\overline{\xi_{i+1/2,j}^z}}^{xy,x} = -\delta_x(\eta_{i+1/2,j} + E_{i+1/2,j}) + \Phi_{i+1/2,j}^x, \quad (16)$$

$$\frac{dv_{i,j+1/2}}{dt} + u_{i,j+1/2} \overline{\overline{\xi_{i,j+1/2}^z}}^{xy,y} = -\delta_y(\eta_{i,j+1/2} + E_{i,j+1/2}) + \Phi_{i,j+1/2}^y, \quad (17)$$

where  $\eta_{i,j}$  is the elevation of the free surface. The  $\Phi_{i+1/2,j}^x, \Phi_{i,j+1/2}^y$  form is obvious in equations (16) and (17).

Two conclusions can be drawn from the above. Firstly, constructing finite-difference schemes with the required conservation properties may involve selecting suitable expressions of  $\Phi^x, \Phi^y$  type, which do not change the order of the problem and can be interpreted as approximating zero with the corresponding order. Secondly, equations (16) and (17) can be expressed using tensor analysis:

$$\frac{d\mathbf{v}_{n^\alpha}^\alpha}{dt} - \varepsilon^{\alpha\beta\gamma} \overline{\overline{\mathbf{v}_{n^\alpha}^\beta \xi_{n^\alpha}^\gamma}}^{\alpha\beta} = -\delta^\alpha(h_{n^\alpha} + E_{n^\alpha}) + \Phi_{n^\alpha}^\alpha, \quad (18)$$

where  $\alpha, \beta, \gamma$  can only take distinct values of  $x, y, z$  simultaneously.

Expressions for  $\Phi_{n^\alpha}^\alpha$  will be provided later.

The following notations are introduced:  $(\mathbf{v}_{n^x}^x, \mathbf{v}_{n^y}^y, \mathbf{v}_{n^z}^z) = (u_{i+1/2,j,k}, v_{i,j+1/2,k}, w_{i+1/2,j+1/2,k})$ ,

where  $n^x, n^y, n^z$  correspond to the points  $(i+1/2, j, k), (i, j+1/2, k), (i, j, k+1/2)$ .

Setting  $\alpha = x$  in equation (18) yields equation (16), while setting  $\alpha = y$  yields equation (17). In other words, swapping  $\alpha$  and  $\beta$  gives us system (16), (17).

Taking the introduced notations into account, we can write equations (9)–(11) as a single equation:

$$\frac{d\mathbf{v}_{n^\alpha}^\alpha}{dt} - \varepsilon^{\alpha\beta\gamma} \overline{\overline{\mathbf{v}_{n^\alpha}^\beta \xi_{n^\alpha}^\gamma}}^{\alpha\beta} - \varepsilon^{\alpha\gamma\beta} \overline{\overline{\mathbf{v}_{n^\alpha}^\gamma \xi_{n^\alpha}^\beta}}^{\alpha\gamma} = -\delta_\alpha(E_{n^\alpha} + P_{n^\alpha}) + \bar{g}\rho_{n^\alpha} + \Phi_{n^\alpha}^\alpha. \quad (19)$$

If we set  $\alpha = x, \beta = y, \gamma = z$  in equation (19), we obtain:

$$\frac{du_{i+1/2,j,k}}{dt} - v_{i+1/2,j,k} \overline{\overline{\xi_{i+1/2,j,k}^z}}^{xy,x} + w_{i+1/2,j,k} \overline{\overline{\xi_{i+1/2,j,k}^y}}^{xz,x} =$$

$$= -\delta_x (E_{i+1/2,j,k} + P_{i+1/2,j,k}) + \Phi_{i+1/2,j,k}^x, \quad (20)$$

at  $\alpha = y, \beta = x, \gamma = z$

$$\begin{aligned} \frac{dv_{i,j+1/2,k}}{dt} + u_{i,j+1/2,k} \overline{\overline{\xi_{i,j+1/2,k}^{xz}}}^{xy} - w_{i,j+1/2,k} \overline{\overline{\xi_{i+1/2,j,k}^{xz}}}^{xy} &= \\ = -\delta_y (E_{i,j+1/2,k} + P_{i,j+1/2,k}) + \Phi_{i,j+1/2,k}^y, \end{aligned} \quad (21)$$

at  $\alpha = z, \beta = y, \gamma = x$

$$\begin{aligned} \frac{dw_{i,j,k+1/2}}{dt} - u_{i,j,k+1/2} \overline{\overline{\xi_{i,j,k+1/2}^{yz}}}^{xz} + v_{i,j,k+1/2} \overline{\overline{\xi_{i,j,k+1/2}^{yz}}}^{xz} &= \\ = -\delta_z (E_{i,j,k+1/2} + P_{i,j,k+1/2}) + g\rho_{i,j,k+1/2} + \Phi_{i,j,k+1/2}^z. \end{aligned} \quad (22)$$

Let us examine the last term in equation (19). We represent it in the form:

$$\Phi_{n^\alpha}^\alpha = \Phi_{n^\alpha}^1 + \Phi_{n^\alpha}^2 + \Phi_{n^\alpha}^3. \quad (23)$$

Then, in accordance with expressions (14) and (15), the terms in equality (23) can be written as follows:

$$\begin{aligned} \Phi_{n^\alpha}^1 &= \varepsilon^{\alpha\beta\gamma} \frac{h_\alpha^2 h_\beta^2}{48} \delta_\alpha \left[ (\delta_\beta \mathbf{v}_{n^\alpha}^\beta) (\delta_\alpha \delta_\beta \overline{\overline{\xi_{n^\alpha}^\gamma}}) \right], \\ \Phi_{n^\alpha}^2 &= -\varepsilon^{\alpha\beta\gamma} \frac{h_\alpha h_\beta}{6} [\delta_\alpha (\mathbf{v}_{n^\alpha}^\alpha \delta_\beta \overline{\overline{\xi_{n^\alpha}^\gamma}})], \\ \Phi_{n^\alpha}^3 &= \varepsilon^{\alpha\beta\gamma} \frac{h_\alpha h_\beta}{12} [\mathbf{v}_{n^\alpha}^\alpha \delta_\alpha \delta_\beta \overline{\overline{\xi_{n^\alpha}^\gamma}}]. \end{aligned} \quad (24)$$

Note that, from this point onwards, summation is performed for a fixed  $\alpha$  over two permutations:  $\beta, \gamma$  and  $\gamma, \beta$ . Therefore, taking expression (24) into account, equations (21) and (22) can be written as a single equation:

$$\begin{aligned} \frac{d\mathbf{v}_{n^\alpha}^\alpha}{dt} - \underbrace{\varepsilon^{\alpha\beta\gamma} \mathbf{v}_{n^\alpha}^\beta \overline{\overline{\xi_{n^\alpha}^\gamma}}^{\alpha\beta}}_I + \delta_\alpha (E_{n^\alpha} + P_{n^\alpha}) - \bar{g}\rho_{n^\alpha} &= \underbrace{\varepsilon^{\alpha\beta\gamma} \frac{h_\alpha h_\beta}{12} [\mathbf{v}_{n^\alpha}^\alpha \delta_\alpha \delta_\beta \overline{\overline{\xi_{n^\alpha}^\gamma}}]}_{II} + \\ + \underbrace{\varepsilon^{\alpha\beta\gamma} \frac{h_\alpha^2 h_\beta^2}{48} \left( \delta_\alpha \langle (\delta_\beta \mathbf{v}_{n^\alpha}^\beta) (\delta_\alpha \delta_\beta \overline{\overline{\xi_{n^\alpha}^\gamma}}) \rangle - 2\delta_\alpha (\mathbf{v}_{n^\alpha}^\alpha \delta_\beta \overline{\overline{\xi_{n^\alpha}^\gamma}}) \right)}_{III}. \end{aligned} \quad (25)$$

The discrete equation (25) possesses the following features. Term I is a discrete analogue of the nonlinear term in the equation of motion. In the shallow water approximation, it satisfies the energy conservation law, but does not guarantee the conservation of potential enstrophy (the second quadratic invariant). Adding the term marked as II yields a scheme that provides two discrete invariants: energy and enstrophy (squared vorticity) for non-divergent flow. However, the property of potential enstrophy conservation in the shallow water approximation is still absent. Finally, term III yields the Arakawa–Lamb scheme [3].

Although the right-hand side does not formally correspond to the differential form of equation (1), yet it does not alter the order of the scheme and can be interpreted as a second-order accurate spatial approximation of zero.

In the specified notation, the absolute velocity vorticity (12) can be rewritten as a finite-difference analogue of (3):

$$\xi_{n^\alpha}^\alpha = \varepsilon^{\alpha\beta\gamma} \delta_\beta v_{n^\alpha}^\gamma + f^\alpha. \quad (26)$$

By performing the appropriate operations, we obtain a differential-difference (time-differential) equation for absolute velocity vorticity (a discrete analogue of equation (7)):

$$\frac{d\xi_{n^\alpha}^\alpha}{dt} + \delta_\beta [v_{n^\beta}^\beta, \xi_{n^\alpha}^\alpha] - \delta_\gamma [v_{n^\alpha}^\alpha, \xi_{n^\gamma}^\gamma] = \bar{g} \vartheta_{n^\alpha}^\alpha - \frac{\varepsilon^{\alpha\beta\gamma}}{2} [\delta_\beta (\Phi_{n^\gamma}^\gamma) - \delta_\gamma (\Phi_{n^\beta}^\beta)]. \quad (27)$$

### Quasi-static approximation

Let us consider a special case of motion in the quasi-static approximation, taking into account the boundary conditions (6) and initial conditions. In this case,

$$\xi^x = -\frac{\partial v}{\partial z}, \quad \xi^y = \frac{\partial u}{\partial z}, \quad \xi^z = \frac{\partial v}{\partial x} - \frac{\partial u}{\partial y} + f^z, \quad E = \rho_0 \frac{u^2 + v^2}{2}. \quad (28)$$

The continuity equation retains its original form (2).

Note that we assume  $\rho_0 = 1 \text{ g / cm}^3$ .

In accordance with the C-grid (Fig. 1), the finite-difference analogues of velocity vorticity (26) in the form (28), as well as the kinetic energy, can be written as follows:

$$\xi_{i,j+1/2,k+1/2}^x = -\delta_z (v_{i,j+1/2,k+1/2}), \quad \xi_{i+1/2,j,k+1/2}^y = \delta_z (u_{i+1/2,j,k+1/2}), \quad (29)$$

$$\xi_{i+1/2,j+1/2,k}^z = \delta_x (v_{i+1/2,j+1/2,k}) - \delta_y (u_{i+1/2,j+1/2,k}) + f_{j+1/2}^z.$$

$$E_{i,j,k} = \frac{\overline{u_{i,j,k}^2} + \overline{v_{i,j,k}^2}}{2}.$$

The discrete equation of motion (25), with  $\alpha = x, \beta = y, \gamma = z$  and  $\alpha = y, \beta = x, \gamma = z$ , leads to the system of equations (20) and (21), where the components of absolute vorticity take the form (29).

Let us rewrite the obtained equations as follows:

$$\frac{du_{i+1/2,j,k}}{dt} + N_{i+1/2,j,k}^u(u,v) + \left( \overline{w_{i+1/2,j,k}^{-x} \xi_{i+1/2,j,k}^y h_z^k} (h_z^k)^{-1} \right) = -\delta_x (E_{i+1/2,j/k} + P_{i+1/2,j,k}), \quad (30)$$

$$\frac{dv_{i,j+1/2,k}}{dt} + N_{i,j+1/2,k}^v(u,v) - \left( \overline{w_{i,j+1/2,k}^{-y} \xi_{i,j+1/2,k}^x h_z^k} (h_z^k)^{-1} \right) = -\delta_y (E_{i,j+1/2,k} + P_{i,j+1/2,k}). \quad (31)$$

To describe vertical advection, we selected a scheme based on a minimal difference stencil to ensure energy conservation in the equations of motion. This is a special case of the scheme presented in equations (21)–(24). The horizontal advective terms in equations (30) and (31) can be verified to have the following form:

$$\begin{aligned}
 N_{i+1/2,j,k}^u(u,v) = & -(\alpha_{i+1,j+1/2,k}^1 v_{i+1,j+1/2,k} + \alpha_{i+1,j-1/2,k}^2 v_{i+1,j-1/2,k} + \alpha_{i,j+1/2,k}^3 v_{i,j+1/2,k} + \\
 & + \alpha_{i,j-1/2,k}^4 v_{i,j-1/2,k}) + \alpha_{i+3/2,j,k}^5 u_{i+3/2,j,k} - \alpha_{i-1/2,j,k}^6 u_{i-1/2,j,k}, \\
 N_{i,j+1/2,k}^v(u,v) = & \beta_{i+1/2,j+1,k}^1 u_{i+1/2,j+1,k} + \beta_{i-1/2,j+1,k}^2 u_{i-1/2,j+1,k} + \beta_{i+1/2,j,k}^3 u_{i+1/2,j,k} + \\
 & + \beta_{i-1/2,j,k}^4 u_{i-1/2,j,k}) - \beta_{i,j+3/2,k}^5 v_{i,j+3/2,k} + \beta_{i,j-1/2,k}^6 v_{i,j-1/2,k},
 \end{aligned} \tag{32}$$

where

$$\begin{aligned}
 \alpha_{i+1,j+1/2,k}^1 &= \frac{1}{24} (2\xi_{i+3/2,j+1/2,k}^z + \xi_{i+3/2,j-1/2,k}^z + \xi_{i+1/2,j+1/2,k}^z + 2\xi_{i+1/2,j-1/2,k}^z), \\
 \alpha_{i+1,j-1/2,k}^2 &= \frac{1}{24} (\xi_{i+3/2,j+1/2,k}^z + 2\xi_{i+3/2,j-1/2,k}^z + 2\xi_{i+1/2,j+1/2,k}^z + \xi_{i+1/2,j-1/2,k}^z), \\
 \alpha_{i,j+1/2,k}^3 &= \frac{1}{24} (\xi_{i+1/2,j+1/2,k}^z + 2\xi_{i+1/2,j-1/2,k}^z + 2\xi_{i-1/2,j+1/2,k}^z + \xi_{i-1/2,j-1/2,k}^z), \\
 \alpha_{i,j-1/2,k}^4 &= \frac{1}{24} (2\xi_{i+1/2,j+1/2,k}^z + \xi_{i+1/2,j-1/2,k}^z + \xi_{i-1/2,j+1/2,k}^z + 2\xi_{i-1/2,j-1/2,k}^z), \\
 \alpha_{i+3/2,j,k}^5 &= \frac{1}{24} (\xi_{i+3/2,j+1/2,k}^z - \xi_{i+1/2,j-1/2,k}^z + \xi_{i+1/2,j+1/2,k}^z - \xi_{i-1/2,j-1/2,k}^z), \\
 \alpha_{i-1/2,j,k}^6 &= \frac{1}{24} (\xi_{i+1/2,j+1/2,k}^z - \xi_{i+1/2,j-1/2,k}^z + \xi_{i-1/2,j+1/2,k}^z - \xi_{i-1/2,j-1/2,k}^z), \\
 \beta_{i+1/2,j+1,k}^1 &= \frac{1}{24} (2\xi_{i+1/2,j+3/2,k}^z + \xi_{i+1/2,j+1/2,k}^z + \xi_{i-1/2,j+3/2,k}^z + 2\xi_{i-1/2,j+1/2,k}^z), \\
 \beta_{i-1/2,j+1,k}^2 &= \frac{1}{24} (\xi_{i+1/2,j+3/2,k}^z + 2\xi_{i+1/2,j+1/2,k}^z + 2\xi_{i-1/2,j+3/2,k}^z + \xi_{i-1/2,j+1/2,k}^z), \\
 \beta_{i-1/2,j,k}^3 &= \frac{1}{24} (\xi_{i+1/2,j+1/2,k}^z + 2\xi_{i+1/2,j-1/2,k}^z + 2\xi_{i-1/2,j+1/2,k}^z + \xi_{i-1/2,j-1/2,k}^z), \\
 \beta_{i-1/2,j,k}^4 &= \frac{1}{24} (2\xi_{i+1/2,j+1/2,k}^z + \xi_{i+1/2,j-1/2,k}^z + \xi_{i-1/2,j+1/2,k}^z + 2\xi_{i-1/2,j-1/2,k}^z), \\
 \beta_{i,j+3/2,k}^5 &= \frac{1}{24} (\xi_{i+1/2,j+3/2,k}^z - \xi_{i-1/2,j+3/2,k}^z + \xi_{i+1/2,j+1/2,k}^z - \xi_{i-1/2,j+1/2,k}^z), \\
 \beta_{i,j-1/2,k}^6 &= \frac{1}{24} (\xi_{i+1/2,j+1/2,k}^z - \xi_{i-1/2,j+1/2,k}^z + \xi_{i+1/2,j-1/2,k}^z - \xi_{i-1/2,j-1/2,k}^z).
 \end{aligned} \tag{33}$$

The equation for the vertical component of absolute velocity vorticity at the point  $i + 1/2, j + 1/2, k + 1/2$  is written as ( $\alpha = z$  in the equation (27)):

$$\frac{d\xi^z}{dt} + \delta_x[N^u(u, v)] + \delta_y([N^v(u, v)]) - \delta_x([w, \xi^x]) - \delta_y([w, \xi^y]) = 0. \quad (34)$$

The form of the last two terms in equation (34) is clear.

Approximation (32)–(34) corresponds exactly to the Arakawa–Lamb scheme. Therefore, in the shallow water approximation, equation (34) possesses two quadratic invariants: energy and potential enstrophy. When these two quadratic conservation laws are satisfied, the mean wavenumber remains time-independent. This consequently prevents systematic energy transfer to motions with high wavenumbers, thereby enhancing the stability of the numerical solution.

The formulation obtained in equations (25) and (27) enables us to derive analogous schemes for the other two velocity vorticity components.

### Conclusion

This paper presents the Arakawa–Lamb scheme as comprising three distinct terms that reflect the different properties of the discrete equations. The first term ensures energy conservation in the discrete formulation; the second leads to a scheme with two quadratic invariants for non-divergent flow; and the addition of the third term corresponds to the full Arakawa–Lamb scheme. A crucial feature of this representation is that the second and third terms are not directly analogous to any terms in the system of differential equations. Although they do not affect the order of approximation, they do significantly influence the properties of the scheme. As the grid spacing decreases, these terms tend towards zero and can therefore be interpreted as being equal to zero when expressed as a function  $h^2\varphi_{i,j,k}$ . Consequently, appropriate finite-difference approximations of the zero right-hand side can be selected to construct difference schemes with various conservation properties. As there is an infinite number of such variants, it is necessary to develop a formalism that can identify schemes with specific characteristics.

The fundamental result is that the presented formulation enables the derivation of difference equations for the horizontal vorticity components, which, like the Arakawa–Lamb scheme, possess two quadratic invariants.

### REFERENCES

1. Noether, E., 1918. Invariante Variationsprobleme. *Nachrichten von der Gesellschaft der Wissenschaften zu Göttingen – Mathematisch-Physikalische Klasse*, pp. 235-257 (in German).
2. Arakawa, A., 1966. Computational Design for Long-Term Numerical Integration of the Equations of Fluid Motion: Two-Dimensional Incompressible Flow. Part I. *Journal of Computational Physics*, 1(1), pp. 119-143. [https://doi.org/10.1016/0021-9991\(66\)90015-5](https://doi.org/10.1016/0021-9991(66)90015-5)
3. Arakawa, A. and Lamb, V.R., 1981. A Potential Enstrophy and Energy Conserving Scheme for the Shallow Water Equations. *Monthly Weather Review*, 109(1), pp. 18-36. [https://doi.org/10.1175/1520-0493\(1981\)109<0018:APEAEC>2.0.CO;2](https://doi.org/10.1175/1520-0493(1981)109<0018:APEAEC>2.0.CO;2)

4. Salmon, R., 2007. A General Method for Conserving Energy and Potential Enstrophy in Shallow-Water Models. *Journal of the Atmospheric Sciences*, 64(2), pp. 515-531. <https://doi.org/10.1175/JAS3837.1>
5. Sugibuchi, Y., Matsuo, T. and Sato, S., 2018. Constructing Invariant-Preserving Numerical Schemes Based on Poisson and Nambu Brackets. *JSIAM Letters*, 10, pp. 53-56. <https://doi.org/10.14495/jsiaml.10.53>
6. Toy, M.D. and Nair, R.D., 2016. A Potential Enstrophy and Energy Conserving Scheme for the Shallow-Water Equations Extended to Generalized Curvilinear Coordinates. *Monthly Weather Review*, 145(3), pp. 751-772. <https://doi.org/10.1175/MWR-D-16-0250.1>
7. Stewart, A.L. and Dellar, P.J., 2016. An Energy and Potential Enstrophy Conserving Numerical Scheme for the Multi-Layer Shallow Water Equations with Complete Coriolis Force. *Journal of Computational Physics*, 313, pp. 99-120. <https://doi.org/10.1016/j.jcp.2015.12.042>
8. Demyshev, S.G., 2005. Numerical Experiments Aimed at the Comparison of Two Finite-Difference Schemes for the Equations of Motion in a Discrete Model of Hydrodynamics of the Black Sea. *Physical Oceanography*, 15(5), pp. 299-310. <https://doi.org/10.1007/s11110-006-0004-2>
9. Demyshev, S.G., 2023. Nonlinear Invariants of a Discrete System of the Sea Dynamics Equations in a Quasi-Static Approximation. *Physical Oceanography*, 30(5), pp. 523-548.

Submitted 06.11.2024; approved after review 05.12.2024;  
accepted for publication 13.03.2025.

*About the author:*

**Sergey G. Demyshev**, Head of Wave Theory Department, Chief Researcher, Marine Hydrophysical Institute of RAS (2 Kapitanskaya Str., Sevastopol, 299011, Russian Federation), DSc. (Phys.-Math.), **Scopus Author ID: 6603919865**, **SPIN-code: 1848-2350**, **ResearcherID: C-1729-2016**, **ORCID ID: 0000-0002-5405-2282**, [demyshev@gmail.com](mailto:demyshev@gmail.com)

*The author has read and approved the final manuscript.*

*The author declares that he has no conflict of interest.*

Original article

## Model of the Lagrangian Particle Transport in a Quasi-Two-Phase Ocean – Ice Medium in a Parallel Ocean Dynamics Model

S. V. Semin<sup>1, 2, ✉</sup>, L. Yu. Kalnitskii<sup>1</sup>, K. V. Ushakov<sup>1</sup>,  
R. A. Ibrayev<sup>3, 1</sup>

<sup>1</sup> Shirshov Institute of Oceanology, Russian Academy of Sciences, Moscow, Russian Federation

<sup>2</sup> Nuclear Safety Institute, Russian Academy of Sciences, Moscow, Russian Federation

<sup>3</sup> Marchuk Institute of Numerical Mathematics, Russian Academy of Sciences, Moscow,  
Russian Federation

✉ svsemin@unistemlab.com

### Abstract

**Purpose.** The purpose of the study is to develop the model of impurity transport in the ocean – sea ice system based on the Lagrangian approach.

**Methods and Results.** The Lagrangian transport of particles is considered in the approximation of a quasi-two-phase ocean – ice medium (particles are subject to the ice formation and melting processes, but actually remain in the ocean model). For the first time, the Lagrangian model over an arbitrary computational grid taking into account the quadratic correction of turbulent diffusion is described in detail. A synchronous model for the Lagrangian transport and the ocean – sea ice model (INMIO – CICE5.1) is constructed. The test calculations of particle transport in the field of a static vortex in the Cartesian and spherical coordinate systems demonstrate the correctness of the presented method. The results of the experiment on particle cloud transport in the Laptev Sea have shown both the fundamental possibilities of using the approach to solve applied problems and a good scalability of the model’s parallel implementation for a large (up to  $10^6$ ) number of particles.

**Conclusions.** The model developed on the basis of the Eulerian and Lagrangian approaches, makes it possible to solve comprehensively the problems related to water circulation and spread of impurities of various types (radioactive and stable isotopes, soluble and insoluble elements of anthropogenic and natural origin, etc.) and, consequently, to assess their impact on the environment.

**Keywords:** computer modeling, Lagrangian transport, ocean dynamics model, ocean – ice model, two-phase medium, turbulent mixing, parallel calculations

**Acknowledgments:** The work was conducted at the Nuclear Safety Institute, RAS, with financial support from the Russian Science Foundation (grant No. 20-19-00615, sections 2-5), and at the Shirshov Institute of Oceanology, RAS, under state assignment theme FMWE-2024-0017 (section 1). Computational resources were provided by the Interdepartmental Supercomputer Center, RAS.

**For citation:** Semin, S.V., Kalnitskii, L.Yu., Ushakov, K.V. and Ibrayev, R.A., 2025. Model of the Lagrangian Particle Transport in a Quasi-Two-Phase Ocean – Ice Medium in a Parallel Ocean Dynamics Model. *Physical Oceanography*, 32(3), pp. 372-391.

© 2025, S. V. Semin, L. Yu. Kalnitskii, K. V. Ushakov, R. A. Ibrayev

© 2025, Physical Oceanography

### Introduction

Two traditional approaches are conventionally used when solving hydrodynamic problems: the Eulerian approach and the Lagrangian approach. These methods are generally effective for different classes of problems and have a wide range of applications. They can also complement each other to provide a more



complete picture of processes occurring in the fluid. The Eulerian approach is mainly used when constructing most modern ocean circulation models and when describing the general dynamics of a continuous medium. By contrast, the Lagrangian approach involves tracking the trajectory of an infinitesimal fluid particle in the presence of specified forces. This makes it possible to evaluate the details of individual currents or specific structures (for example, surface and underwater currents, oceanic vortices) during the evolution of the internal state of the continuous medium. It also enables the evaluation of specific features of currents or particular structures (such as surface and subsurface currents, oceanic vortices, etc.) during the evolution of the continuum medium's internal state. At the same time, various properties can be assigned to the particles, including characteristic of local biogenic and anthropogenic processes and real or hypothetical sources of pollution, including radioactive ones. This allows the dynamics of impurity propagation in a given current to be reconstructed. Since ocean dynamics modeling often considers water in two states (liquid and solid), the dynamic properties of which are fundamentally different, studying particle transport within both thermodynamic phases is of particular scientific interest. To the best of our knowledge, there are currently no publicly available models that consider such processes [1].

Combining Eulerian and Lagrangian approaches provides comprehensive solutions to problems involving water circulation and the dispersion of various types of impurities (radioactive and stable isotopes, soluble and insoluble elements of anthropogenic and natural origin). Consequently, it is possible to assess their environmental impact. This tool is particularly relevant due to the development of the Northern Sea Route <sup>1</sup> and the Arctic region <sup>2</sup> as a whole in terms of logistical and military-political potential. Floating nuclear power plants are already being actively utilized during the development of resources in the Arctic Ocean (AO). Due to various risk factors, a detailed study of their environmental impact is necessary [2]. Particular attention should be given to potential emergency situations involving the release of radioactive isotopes into the AO waters. Research is required to assess the long-term consequences of such an event [3]. A tool based on a coupled Lagrangian-Eulerian ocean model would be optimally suited to solving these problems. In this context, developing such a tool using domestic software platforms is particularly relevant <sup>3</sup>.

When developing coupled Lagrangian-Eulerian models, particles are typically treated as passive tracers that do not affect the properties of the carrying flow. In such configurations, the Eulerian model is primary in the sense that the accuracy and reliability of the calculated velocity field determine the predictability of particle transport. The Eulerian ocean dynamics model involves the numerical solution of

---

<sup>1</sup> Government of the Russian Federation, 2019. [*Northern Sea Route Infrastructure Development Plan until 2035 (Order No. 3120-r of December 21, 2019). Collected Legislation of the Russian Federation*]. No. 52 (Part V), Article 8053 (in Russian).

<sup>2</sup> Government of the Russian Federation, 2021. [*Socio-Economic Development of the Arctic Zone of the Russian Federation. Resolution of the Government of the Russian Federation No. 484, 30 March. Collected Legislation of the Russian Federation*]. No. 14, Article 2411 (in Russian).

<sup>3</sup> Government of the Russian Federation, 2023. [*Concept of Technological Development until 2030. Order of the Government of the Russian Federation No. 1315-r, 20 May, Moscow*] (in Russian).

the full set of fluid dynamics equations for a specified body of water with a defined spatial resolution, as well as the parameterization of internal and boundary processes. Coupling this approach with ice and/or atmospheric models demonstrates its high effectiveness in forecasting regional and global climate dynamics [4–10]. Combining such models with Lagrangian transport modeling is the most appropriate approach, as evidenced by the numerous existing implementations reviewed in [1].

There are two subclasses of numerical models that support Lagrangian particle transport: autonomous and synchronous. In the former, the Eulerian and Lagrangian models run independently of each other (usually sequentially). The velocity field obtained from the first model is then used in the second model. Examples of the first subclass include TRACMASS [11], Ariane [12], CMS [13], and the SibCIOM-based Lagrangian model [14]. In the second subclass, the modeling of fluid dynamics and particles is carried out synchronously. The complete set of current data for the entire computational domain is used in the Lagrangian model at each time step, providing the maximum possible temporal resolution. Examples of implementations can be found in the MRI.COM<sup>4</sup>, NEMO<sup>5</sup>, HYCOM [15], ROMS [16], and MITgcm [17] models.

Compared to synchronous models, autonomous models have several disadvantages. Specifically, three-dimensional velocity fields are always time-averaged (and sometimes spatially averaged), which reduces the accuracy with which dynamic processes can be described [1]. Storing current data in four-dimensional arrays requires substantial disk space. This limits the ability to study temporally extended and spatially detailed processes. Secondly, reading data from external storage is a relatively slow process that significantly impacts post-processing performance and the computational efficiency of the autonomous model. While synchronous models offer many advantages, they also have certain drawbacks, including placing an additional load on high-performance computing system resources and making implementation somewhat more complex.

The aim of this work is to develop and implement a Lagrangian transport model within the INMIO ocean dynamics model [18], which forms part of the integrated ocean – ice – atmosphere – land modeling system [5, 6, 9, 19]. The Lagrangian particle transport model must have the following features: synchronous execution with the ocean dynamics model, incorporation of two-phase transport capability for ocean – ice system simulations, enabling of particle injection at specified coordinates and times, support for particle classification into groups based on individual properties (including lifetime duration, buoyancy characteristics, and bottom adhesion conditions), a total number of particles of up to  $10^6$ .

---

<sup>4</sup> Sakamoto, K., Nakano, H., Urakawa, S., Toyoda, T., Kawakami, Y., Tsujino, H. and Yamanaka, G., 2023. *Reference Manual for the Meteorological Research Institute Community Ocean Model Version 5 (MRI.COMv5)*. MRI, 334 p. (Technical Reports of the Meteorological Research Institute; No. 87).

<sup>5</sup> Madec, G. and the NEMO Team, 2016. *NEMO Ocean Engine: Technical Report*. 300 p. (Note du Pôle de Modélisation de l'Institut Pierre-Simon Laplace; No. 27). <https://doi.org/10.5281/ZENODO.3248739>

## Data and methods

**Coupled ocean – ice model.** The implementation of a synchronous Lagrangian transport model depends directly on the ‘parent’ Eulerian model and its specific architecture. This study focuses on developing a particle transport model for a two-phase medium, representing aspects that are particularly important from the standpoint of the Lagrangian model for implementing both components in the ocean – ice modeling system.

The basic ocean model of the joint modeling complex is represented by the INMIO numerical model of ocean dynamics [18]. This model belongs to the 3D PEM (3-Dimensional Primitive Equation Models) class. It is based on the classical system of Reynolds equations under the Boussinesq, hydrostatic and incompressible fluid approximations. The free boundary of the atmosphere – ocean interface is described by a nonlinear kinematic condition that explicitly describes the flows of water, heat, salt and momentum. At rigid boundaries, the free-slip condition and zero heat and salinity flow are specified.

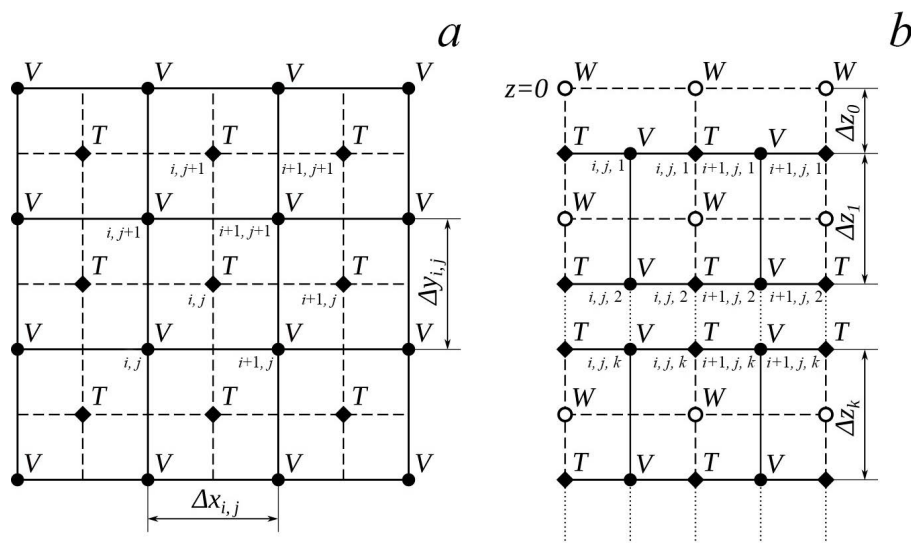


**Fig. 1.** Calculation grid in the INMIO model: scheme of the arrangement of grid nodes in the horizontal (a) and vertical (b) planes

The original differential equations are approximated using the finite volume method on a  $B$ -type horizontal grid (Fig. 1), which uses  $z$ -coordinates in the vertical dimension and an arbitrary orthogonal coordinate system in the horizontal plane. Currently, Cartesian, spherical and tripolar coordinate systems are supported. The numerical model is optimized for parallel execution on high-performance computing systems via two-dimensional domain decomposition.

The coupled ocean – ice model incorporates sea ice dynamics via the CICE5.1 model<sup>6</sup>. It characterizes the state of ice and snow using a distribution function

<sup>6</sup> Hunke, E.C. and Lipscomb, W.H., 2013. *CICE: The Los Alamos Sea Ice Model Documentation and Software User's Manual Version 5.1. LA-CC-06-012*. Los Alamos National Laboratory, 115 p.

$g(t, x, h)$  that depends on time, geographical coordinates and ice thickness. The primary prognostic variables include ice concentration, averaged thickness values, the internal energy of ice and snow, ice salinity, temperature, and the ice velocity vector. The original thermodynamic and ice transport equations are approximated using the finite difference method on a  $B$ -type grid in Cartesian, polar or tripolar coordinate systems at the ocean surface.

The coupled ocean – ice modeling system has been implemented using the compact computational platform CMF3.0 [5]. In addition to centralized and parallel input/output operations, CMF3.0 integrates multiple models into a unified geophysical modeling system by reinterpolating the components participating in modeling onto different grids.

Based on the abovementioned information, more detailed requirements for implementing the Lagrangian model can be formulated. The implementation must support centralized input/output with specified discretization through CMF3.0 procedures. As the formulation of the ocean – ice system does not include the transport of particles into the atmosphere, it is sufficient to implement support for Lagrangian transport in the ocean model, ensuring the reinterpolation of the velocity field and the ice formation/melting potential from the ice model using the compact computational platform's method. Finally, as the INMIO model is defined in an arbitrary orthogonal coordinate system, the Lagrangian model must support particle transport in any coordinate system.

Taking these requirements into account, the procedure for calculating the trajectories of Lagrangian particles in the ocean model can be represented as two fundamental operations: the interpolation of the discrete velocity field to an arbitrary coordinate point (particle coordinates) within a specific coordinate system; and the integration of the equation describing the motion of the particles in the given current field.

**The model of Lagrangian particle transport.** As mentioned in the introduction, from a practical standpoint, it is interesting to track not only the movement of water, but also that of dissolved trace elements in the ocean, such as radionuclides, nutrients, plankton and minerals. However, it is insufficient to simply compute the displacement of fluid particles under the influence of a given velocity field, since the mass of dissolved material in a given volume is generally not constant due to turbulent mixing. As small-scale processes are difficult to describe within the framework of a general ocean circulation model, the mixing effect must be represented directly in the Lagrangian model as particle transport under the influence of diffusion [1]. Thus, the Lagrangian model accounts for the transport of a fluid particle with fixed physical properties within a given velocity field, taking into account the effects of turbulent mixing. The concentration of dissolved material can then be determined by counting the number of particles in a given volume. This approach was first introduced in [20] and has since become standard practice for modeling dissolved substance transport [1].

Since turbulent mixing processes are random by nature and liquid particle transport and diffusion are assumed to be linearly independent processes, stochastic differential equations can be used to model Lagrangian transport. In general, this equation is represented by formula (1). This is a stochastic differential equation,

which is a special case of the Langevin equation. The additional term in this equation describes the random fluctuations of a particle caused by turbulent processes [21]:

$$\frac{d\vec{x}(t)}{dt} = \vec{A}(\vec{x}, t) + B(\vec{x}, t)\vec{L}(t), \quad (1)$$

where  $\vec{x}(t) = (x^l(t), y^l(t), z^l(t))$  are the coordinates of a particle in a given space;  $\vec{A}(\vec{x}, t)$  is a vector representing a deterministic force field that governs the evolution of  $\vec{x}(t)$ ;  $B(\vec{x}, t)$  is a predefined tensor that characterizes the stochastic influence on the particle (in this case, turbulence);  $\vec{L}(t)$  is a random vector representing the chaotic nature of these influences (turbulent diffusion). The components of  $\vec{L}(t)$  are independent random variables with zero expected mean.

Particle displacement under the effect of turbulent diffusion effect can be represented as a Markov process, in which predicting the subsequent position of the particle requires only information about its current state. Random fluctuations in this process are described by a Wiener process, which is a function of a normally distributed random variable with zero expected mean and dispersion  $- dt$ . The relation between equation (1) and the advection-diffusion equation is demonstrated through the Kolmogorov forward equation (or Fokker–Planck equation) in works <sup>7</sup> [1]. According to work <sup>6</sup>, the Lagrangian particle transport equation along the three coordinate axes can then be expressed as follows:

$$\begin{aligned} dx^l(t) &= u(\vec{x}, t)dt + \frac{\partial K_x(\vec{x}, t)}{\partial x} dt + \xi_x \sqrt{2K_x(\vec{x}, t)} dt, \\ dy^l(t) &= v(\vec{x}, t)dt + \frac{\partial K_y(\vec{x}, t)}{\partial y} dt + \xi_y \sqrt{2K_y(\vec{x}, t)} dt, \\ dz^l(t) &= w(\vec{x}, t)dt + \frac{\partial K_z(\vec{x}, t)}{\partial z} dt + \xi_z \sqrt{2K_z(\vec{x}, t)} dt, \end{aligned} \quad (2)$$

where  $u, v, w$  are velocity vector components;  $K_x, K_y, K_z$  are turbulent diffusion coefficients;  $\xi_x, \xi_y, \xi_z$  are independent, normally distributed random variables with a zero mean and unit dispersion. Note that the second term on the right-hand side of equations (2) has been introduced artificially to compensate for the unrealistic particle accumulation in regions of low diffusivity <sup>6</sup> [23, 24], ensuring that turbulent diffusion processes are modelled correctly within the framework of the advection-diffusion equation.

We introduced several modifications to the aforementioned Lagrangian particle transport model to optimize it for the processes of interest. Firstly, in the context of an eddy-resolving ocean model, the effects of horizontal turbulent diffusion can be disregarded, as advective processes largely dominate weak horizontal plane fluctuations <sup>6</sup>. Secondly, studies <sup>8</sup> [24] suggest that the vertical turbulent diffusion term, which is responsible for random fluctuations, should be adjusted to second-

<sup>7</sup> Wolk, F., 2003. *Three-Dimensional Lagrangian Tracer Modelling in Wadden Sea Areas: Diploma Thesis*. Hamburg, Germany: Carl von Ossietzky University Oldenburg, 77 p.

<sup>8</sup> Ermak, D.L., Nasstrom, J.S. and Taylor, A.G., 1995. *Implementation of a Random Displacement Method (RDM) in the ADPIC Model Framework*. Lawrence Livermore National Laboratory, 16 p. (Report UCRL-ID-121742). <https://doi.org/10.2172/103520>

order accuracy. This improves the representation of diffusive processes in the bottom boundary layer, where  $K_z$  approaches zero. Thirdly, in practice, the presence of dissolved substances in a given volume alters the density of the solution. In most cases, however, this can be disregarded. In certain applications, particularly those involving long-term simulations or significant concentrations of passive tracers (such as sediment transport studies <sup>6</sup>), the effect of buoyancy variation may become non-negligible. To account for this, an additional term has been introduced into the third equation (2) to describe particle motion along the vertical axis at a constant velocity  $w^s$ , reflecting this process in the first-order approximation. Considering all these modifications, the final system of Lagrangian particle transport equations takes the following form:

$$\begin{aligned}
 dx^l(t) &= u^o(\vec{x}, t)dt, \\
 dy^l(t) &= v^o(\vec{x}, t)dt, \\
 dz^l(t) &= (w^o(\vec{x}, t) + w^s)dt + \frac{\partial K_z(\vec{x}, t)}{\partial z}dt + \\
 &+ \xi_z \sqrt{2K_z(\vec{x}, t)dt + \left(\frac{\partial K_z(\vec{x}, t)}{\partial z}dt\right)^2}, \quad (3)
 \end{aligned}$$

where  $u^o$ ,  $v^o$ ,  $w^o$  are components of the fluid velocity vector at a given coordinate point.

According to [1], it is particularly noteworthy that there are currently no publicly available implementations of synchronous Lagrangian-Eulerian ocean models that can compute particle trajectories based on stochastic differential equations, explicitly accounting for turbulent diffusion. Furthermore, we have been unable to find ocean circulation models that support Lagrangian particle transport in this formulation. In this respect, the particle transport functionality in the INMIO model is unique.

Equations of the form (3) only apply to particle transport in a liquid ocean environment where turbulent diffusion is caused by mesoscale vortex processes. However, if a particle becomes trapped in an ice cover, turbulent mixing is absent. In this case, particles move along the ice velocity vector. This motion can be described by a simple Lagrangian transport equation:

$$\begin{aligned}
 dx(t) &= u^i(\vec{x}, t)dt, \\
 dy(t) &= v^i(\vec{x}, t)dt, \\
 dz(t) &= 0, \quad (4)
 \end{aligned}$$

where  $u^i$ ,  $v^i$  are the horizontal components of the ice velocity. Since our model does not consider particle transport processes beyond the ocean surface, vertical particle movement in the ice cover can be disregarded. The transition between oceanic and ice-bound transport modes occurs when particles cross the ice-ocean interface, which requires special treatment in numerical implementations to ensure the conservation of particle properties. In this case, the moment at which particles transition into and out of a frozen state can be estimated using a probabilistic approach based on the intensity of ice formation and melting processes.

As noted earlier, the ocean – ice modeling system comprises two models that are managed by the compact computational platform CMF3.0. This enables each model to obtain the necessary information from the other with a specified discreteness. Within the framework of Lagrangian transport in a two-phase

environment, our focus is on the ice velocity field, as well as on the potential for ice formation and melting. The first quantity will obviously be used directly in equations (4) to calculate particle displacement. The second quantity, the ice formation and melting potential, determines the procedures in the ice model for forming frozen structures on the ocean surface. When this quantity is positive, it indicates that the water temperature has fallen below the freezing point. This leads to the formation of ice proportional to the magnitude of the potential, and the subsequent accumulation of ice crystals on the surface, gradually forming an ice cover. Negative potential values correspond to melting processes. In dimensionless form, this parameter enables the approximate estimation of the probability of a Lagrangian particle freezing or thawing if it is located in the ocean surface layer:

$$P(\vec{x}, t) = \left| 1 - \frac{T^o(\vec{x}, t)}{T^f(\vec{x}, t)} \right|, \quad (5)$$

where  $T^o$  is the fluid temperature at the current coordinates of the Lagrangian particle;  $T^f$  is the freezing temperature at that point; formula (5) defines the probability function for particle freezing if it is located in the surface layer when  $T^o < T^f$ , as well as the probability function for particle thawing if it was already frozen when  $T^o \geq T^f$ .

Thus, the general model of Lagrangian transport in the quasi-two-phase ocean – ice environment can be represented as follows:

1. If the particle is in a frozen state, its movement is described by equations (4) and the probability of thawing is determined by function (5) when  $T^o \geq T^f$ .
2. Otherwise, the particle moves freely in the liquid phase according to equations (3) and may freeze with a probability (5) if located in the surface layer of the fluid (in the uppermost grid cell of the numerical model) when  $T^o < T^f$ .

This approach enables the model to be implemented without the need to transfer particle information to the ice model. This significantly reduces the number of computational resources required and simplifies the program code simultaneously.

For the numerical integration of the equations describing the transport of Lagrangian particles, the explicit Euler scheme or Runge–Kutta schemes [1] of various orders of accuracy are typically used. In the autonomous implementation of coupled models, when temporal discretization of the velocity field is relatively coarse, higher-order time approximation schemes are employed to enhance the accuracy of particle trajectory reconstruction in the original equations (3) and (4). In such cases, methods such as Heun scheme and fourth-order (or higher) Runge–Kutta schemes<sup>6</sup> are commonly applied [1, 25].

In coupled models, the requirement for high-order temporal schemes becomes less critical, enabling the use of the first-order accurate Euler scheme. The accuracy of the numerical integration of the original equations can be adjusted by reducing the time step in the numerical implementation of the Lagrangian model. Numerical tests of particle transport in a static circular current field demonstrate that, regardless of the numerical scheme used (Euler or Runge–Kutta), the integration time step in the Lagrangian transport model must be significantly smaller than in the ocean model to achieve acceptable accuracy in reconstructing circular particle trajectories [1]. Thus, the finite-difference scheme for the original Lagrangian particle transport

equations in the velocity field of the coupled ocean – ice modeling system can be expressed as follows:

$$\begin{aligned}
 x_{n+1}^l &= x_n^l + \begin{cases} u^o(\vec{x}_n)\Delta t^l, & s = \text{ocean}, \\ u^i(\vec{x}_n)\Delta t^l, & s = \text{ice}, \end{cases} \\
 y_{n+1}^l &= y_n^l + \begin{cases} v^o(\vec{x}_n)\Delta t^l, & s = \text{ocean}, \\ v^i(\vec{x}_n)\Delta t^l, & s = \text{ice}, \end{cases} \\
 z_{n+1}^l &= z_n^l + \begin{cases} (w^o(\vec{x}_n) + w_s)\Delta t^l + \frac{\Delta K_z(\vec{x}_n)}{\Delta z(\vec{x}_n)}\Delta t^l + \\ 0, \end{cases} \\
 &+ \begin{cases} \xi_z \sqrt{2K_z(\vec{x}_n)\Delta t^l + \left(\frac{\Delta K_z(\vec{x}_n)}{\Delta z(\vec{x}_n)}\Delta t^l\right)^2}, & s = \text{ocean}, \\ 0 & s = \text{ice}, \end{cases} \\
 P_n(s = \text{ice}) &= 1 - \frac{T^o(\vec{x}_n)}{T^f(\vec{x}_n)}, s = \text{ocean}, T^o \leq T^f, z_n^l < z_2, \\
 P_n(s = \text{ocean}) &= \frac{T^o(\vec{x}_n)}{T^f(\vec{x}_n)} - 1, s = \text{ice}, T^o > T^f, \\
 \Delta t^l &= \Delta t^o / p,
 \end{aligned} \tag{6}$$

where  $\vec{x}_n = \{x_n^l, y_n^l, z_n^l\}$  is the Lagrangian particle coordinate at the  $n$ -th integration step;  $\vec{u}^o = \{u^o(\vec{x}_n), v^o(\vec{x}_n), w^o(\vec{x}_n)\}$  is current velocity at the point with particle coordinates;  $\vec{u}^i = \{u^i(\vec{x}_n), v^i(\vec{x}_n), 0\}$  is ice movement velocity;  $\Delta t^l$  is the time step in the Lagrangian model;  $\Delta t^o$  is the time step in the ocean model;  $p$  is the integer determining the refinement factor for the Lagrangian model integration order relative to the INMIO model. Test calculations demonstrate that acceptable solution accuracy is achieved at  $p \sim 10$ .

**Interpolation in the Lagrangian particle transport model.** The Lagrangian transport modeling involves the movement of particles in a space of continuously defined coordinates (6). This means that, at any given moment, the coordinates of particles may not coincide with those of the grid nodes in the computational domain of the numerical model. Therefore, to achieve greater accuracy, the discrete velocity field of the ocean – ice system must be reconstructed within computational cells. This is typically accomplished using interpolation methods of various orders [1]. In this study, linear interpolation was chosen as it is the most computationally efficient approach while still providing acceptable accuracy [25].

However, applying this approach is complicated by the fact that the INMIO model equations are formulated in an arbitrary orthogonal coordinate system in the horizontal plane. In such a configuration, determining particle positions on the computational grid and performing interpolation becomes non-trivial. One solution to this problem, which preserves the simplicity of linear interpolation formulas, is to consider particle transport equations in logical (computational) space (Fig. 2) [25].

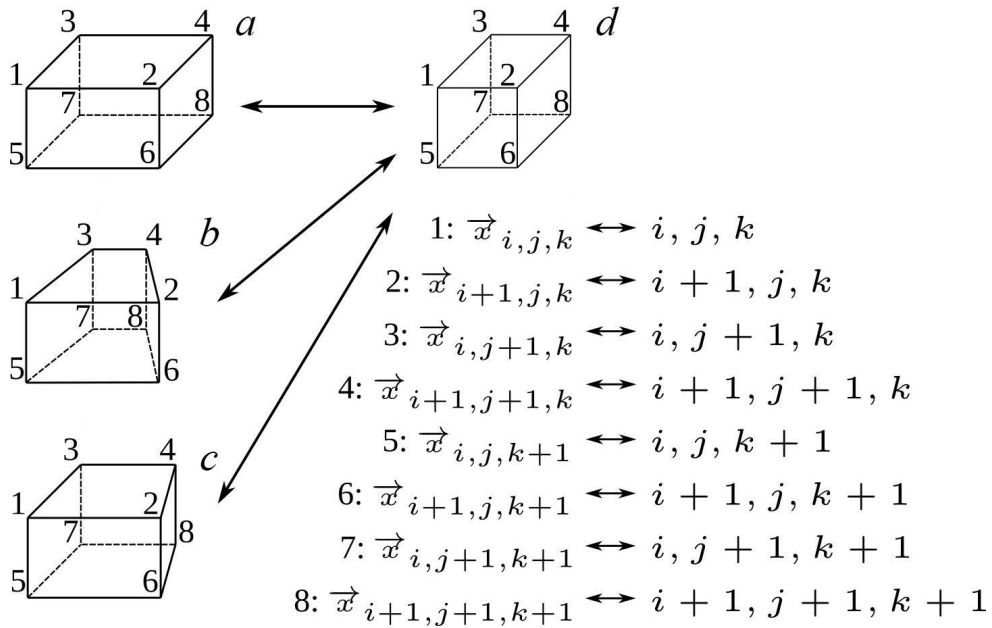


**Fig. 2.** Display of computational cells in different coordinate systems: Cartesian (*a*), polar (*b*), bipolar (*c*) and semi-logical (*d*) ones

This space is a Cartesian coordinate system that arises naturally during the implementation of most numerical models. It is described by the indices of grid nodes. However, the transition to logical coordinates is only meaningful in the horizontal plane, since the INMIO model introduces  $z$ -coordinates in the vertical plane. In this new semi-logical space,  $\bar{C}$  point coordinates can be represented as  $\vec{\xi} = \{\xi, \eta, z\}$ , where  $\xi = i + \alpha$  and  $\eta = j + \beta$ , and the mapping function from this space to physical space  $P$  takes the following form:

$$\begin{aligned}
 \tau(f_{i,j,k}, \xi, \eta, z) &= \sum_{I,J,K=0}^1 f_{i+I,j+J,k+K} \varphi_I(\alpha) \psi_J(\beta) \chi_{k+K}(z), \\
 \varphi_0(\alpha) &= (1 - \alpha), \varphi_1(\alpha) = \alpha, \alpha \in [0,1], \\
 \psi_0(\beta) &= (1 - \beta), \psi_1(\beta) = \beta, \beta \in [0,1], \\
 \chi_k(z) &= \frac{z_{k+1} - z}{z_{k+1} - z_k}, \chi_{k+1}(z) = \frac{z - z_k}{z_{k+1} - z_k}, z \in [z_k, z_{k+1}],
 \end{aligned}
 \tag{7}$$

where  $i, j, k$  are indices of the computational grid cell;  $\alpha, \beta$  are the real-valued displacements of a point in logical space relative to the cell index;  $f_{i,j,k}$  is the function that defines the parameter values at the grid nodes in physical space;  $\varphi, \psi, \chi$  are the basic mapping functions. When the function  $f$  specifies the coordinates of the grid cell nodes in physical space, expression (7) can be used to compute physical coordinates from given semi-logical coordinates. If  $f$  represents velocity vectors, expression (7) performs trilinear velocity interpolation within the specified grid cell (see Fig. 1).

However, when transitioning to semi-logical space, the particle motion vector should be rescaled according to the spatial deformation of the corresponding coordinate axes. Following [25], this rescaling can be implemented through the following transformation within the previously defined mapping framework:

$$\begin{aligned}\vec{u} &= J \cdot \vec{\omega}, \vec{\omega} = J^{-1} \cdot \vec{u}, \\ J &= \left( \frac{\partial \vec{x}}{\partial \xi} \middle| \frac{\partial \vec{x}}{\partial \eta} \middle| \frac{\partial \vec{x}}{\partial z} \right),\end{aligned}\tag{8}$$

where  $\vec{u} = \{u, v, w\}$  is the velocity vector in physical space;  $\vec{\omega} = \{\bar{u}, \bar{v}, \bar{w}\}$  is the velocity vector in semi-logical space;  $J$  is the Jacobian matrix that defines the spatial deformation during transformation from physical to semi-logical coordinates.

On a discrete grid, the Jacobian matrix  $J$  can be computed using finite differences. However, as demonstrated in [25], maximum accuracy requires these differences to be calculated for all nodes of the computational cell using both forward and backward finite difference schemes. This can be achieved using the mapping function  $\tau(\vec{x}, \xi, \eta, z)$  (7), which defines the transformation from semi-logical to physical coordinates. It is straightforward to show that, in the third column and in the third row of the Jacobian matrix, all elements except the last one will be zero, since the given mapping does not affect the  $OZ$  axis. For each computational cell  $(i, j, k)$  the matrix will therefore take the form:

$$J_{i,j,k} = \begin{pmatrix} \frac{\partial \tau(x)}{\partial \alpha} & \frac{\partial \tau(x)}{\partial \beta} & 0 \\ \frac{\partial \tau(y)}{\partial \alpha} & \frac{\partial \tau(y)}{\partial \beta} & 0 \\ 0 & 0 & 1 \end{pmatrix},\tag{9}$$

where partial derivatives are calculated trivially for the mapping function  $\tau(\vec{x}, \xi, \eta, z)$  of form (7).

Equations (6) remain invariant under the above mapping since the  $OZ$  dimension remains unchanged. To obtain the Lagrangian particle coordinates at the next time point, it is sufficient to scale the velocity vector at the cell nodes using formulas (8) and (9), interpolate it to the particle coordinates using formula (7), and then apply the semi-logical coordinates and resulting velocity vector directly to equations (6).

## Results and discussion

**Test calculations of particle transport in a static vortex field.** As various aspects of the mathematical model presented above have been repeatedly verified in previous studies<sup>6, 7</sup> [1, 24], the primary objective of these test calculations is to demonstrate the correct implementation of the Lagrangian transport model and its integration methods on grids supported by the INMIO ocean model, in both Cartesian and geospheric/tripolar coordinate systems.

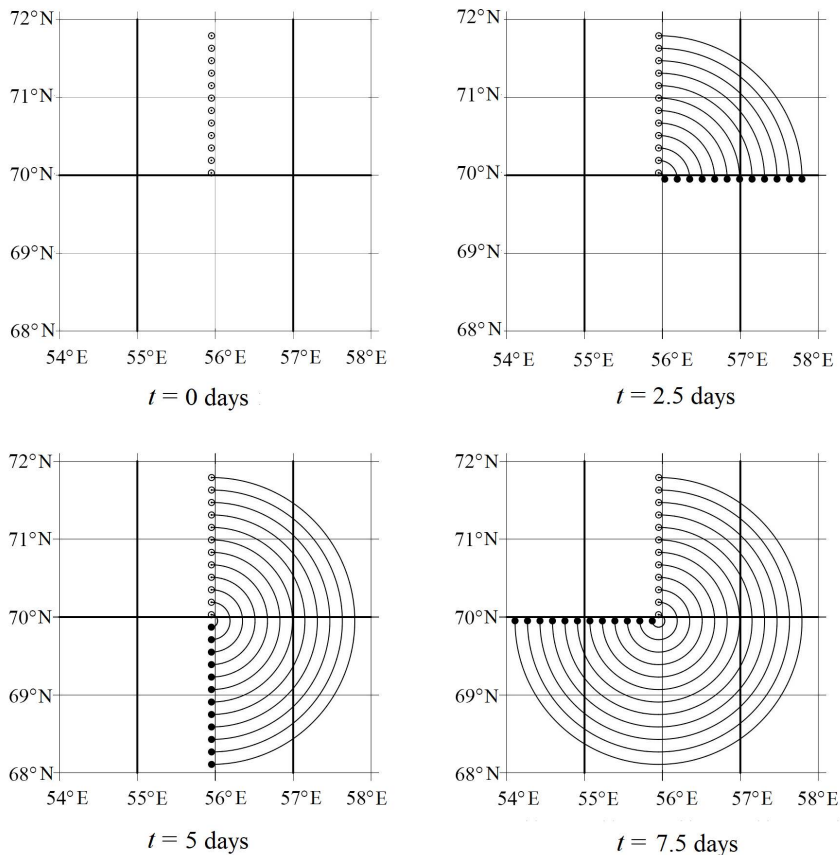


**Fig. 3.** Trajectories of particles moving in the static vortex field on a grid in the Cartesian coordinate system

The INMIO software model was configured to simulate a geographical domain within the rectangle defined by the coordinates 53°–59°E and 68°–72°N. To test particle transport, an artificial velocity field representing a static vortex centered in the middle of the domain was introduced. The vortex had a rotation period of  $\sim 10$  days (angular velocity  $W = 7.27 \cdot 10^{-6}$  rad/s). In the implementation of the Cartesian coordinate system, the linear velocity field was expressed in geographical units (degrees/seconds). In the spherical coordinate system, the velocity field dimensions corresponded to the metric system (m/s) and represented a vortex with the specified angular velocity centered on the Earth’s surface at the aforementioned geographical coordinates. The model was discretized using a  $60 \times 40$  computational grid with a resolution of  $0.1^\circ$ . The ocean model time step was set to  $\Delta t^o = 6'$ . The temporal discretization of the Lagrangian model was varied to obtain the most accurate particle trajectories. As expected, the particle trajectories formed concentric streamlines for this preset velocity field.

The computation was performed in parallel mode using six cores. Fig. 3 presents the results of the Lagrangian particle transport test calculation on the Cartesian grid.

As expected, the particles move synchronously in a circle along the streamlines specified in the computational domain of the vortex velocity field. It is obvious that particle transitions between grid cells and computational domains (indicated by thick lines in Fig. 3) do not distort their trajectories, and their motion in a vortex with a  $\sim 10$ -day period is reflected in the particle coordinates. The trajectories shown in Fig. 3 were obtained using  $p = 5$  in expressions (6).

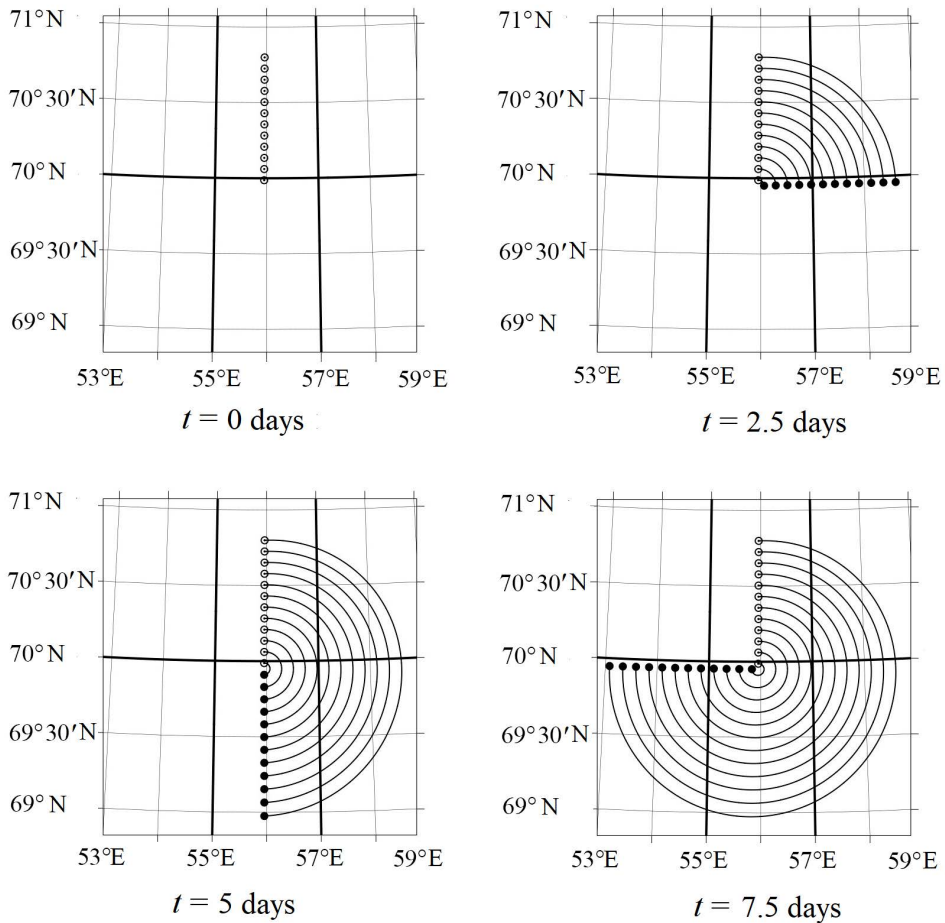


**Fig. 4.** Trajectories of particles moving in the static vortex field on a grid in the geographic coordinate system

In the next numerical test, the particles moved on a grid in a geographic coordinate system.

Fig. 4 shows the results of calculations at various stages of the modeling process. As in the previous case, the particles move synchronously along the streamlines of the vortex velocity field. The trajectories remain circular in metric

space representation only. They no longer appear as circles in geographical coordinates, but instead manifest as elongated ellipsoidal curves elongated along the latitudinal axis. As before, the trajectories shown in Fig. 4 were obtained using  $p = 5$  in equations (6).

To obtain more accurate Lagrangian particle trajectories, special consideration must be given to particle transitions between computational cells, including transfers between subdomains in the two-dimensional decomposition of the ocean model's computational domain. In the former instance, this is due to the peculiarities of modeling in semi-logarithmic space, where the velocity field at cell boundaries is no longer continuous (equations (7) and (8)). Therefore, to achieve maximum accuracy, the particle velocity and path should be recalculated when crossing cell boundaries. This requirement also applies when modeling in physical space, albeit for different reasons. In our implementation, this condition is only partially satisfied by using a time integration step (6) that is smaller than the ocean model time step. Conversely, 'seamless' particle transfer between computational domains would indicate the correct implementation of the parallel computation algorithm for the Lagrangian model.

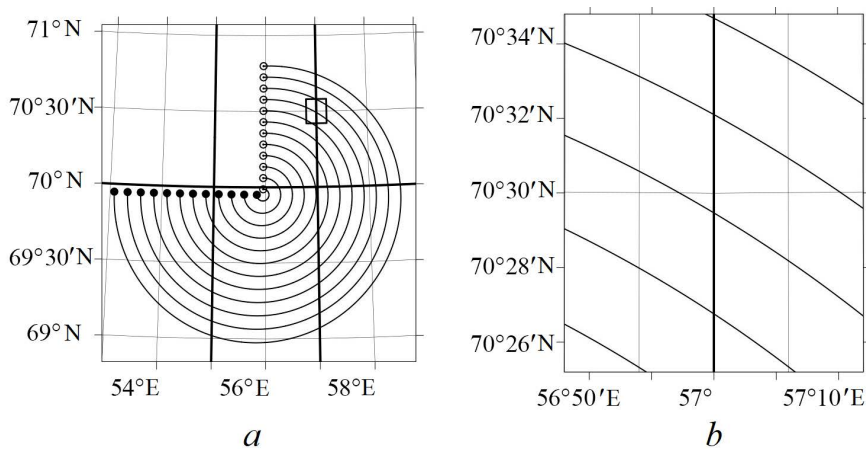


**Fig. 5.** Particle trajectories in the test experiment on a grid in the geographic coordinate system (rectangle highlights the region on the boundary of computational cells and calculation domain) (a), enlarged image of the highlighted area (b)

Fig. 5 shows, for example, particle trajectories crossing boundaries between two computational subdomains and several grid cells. As can be seen, the trajectories demonstrate no visible discontinuities. This indicates firstly that the required level of accuracy has been achieved for the specified  $\Delta t^l$  ( $p = 5$  in equations (6)) and secondly that the interprocessor particle exchange in the parallel Lagrangian transport model has been implemented correctly.

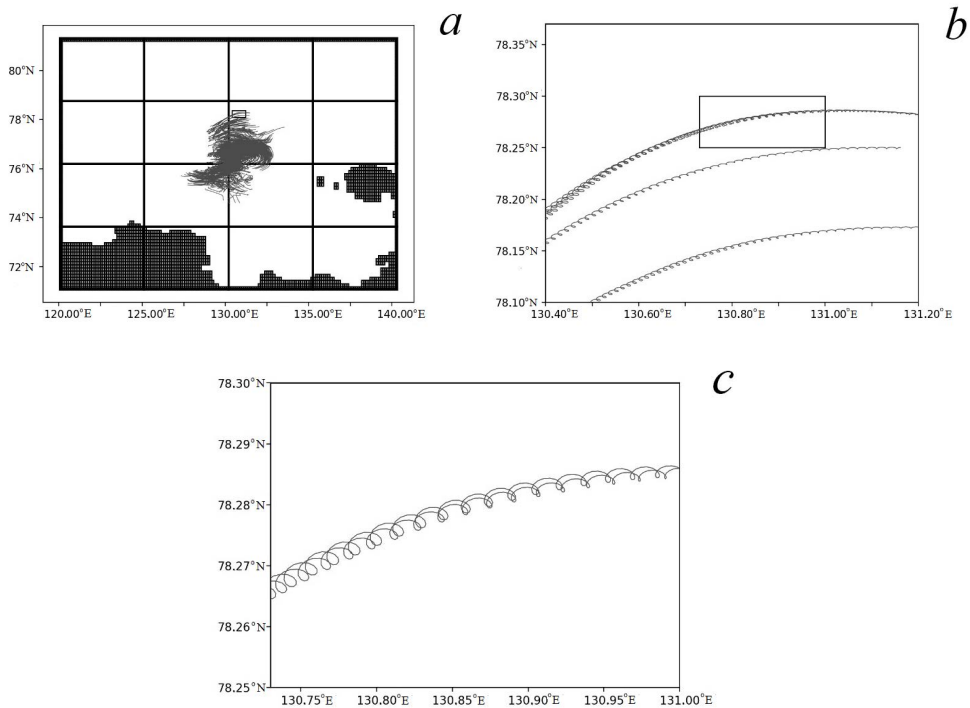


**Fig. 6.** Particle trajectories in the Laptev Sea current model (the study area is shown by a rectangle) (a), enlarged image of the indicated area (rectangle highlights the zone of interest) (b), enlarged image of the highlighted area (c)

### **Test calculation of particle transport in the coupled ocean – ice model.**

The main purpose of this test calculation was to demonstrate the correct implementation of the above-described Lagrangian model within the ocean – ice modeling system consisting of the INMIO ocean model and the CICE5.1 ice thermodynamics model. The configuration of the ocean model for the AO was adopted from [6], but the Laptev Sea (71°–91°N, 120°–140°E) was chosen as the model domain because its waters are ice-covered for most of the year. The model bathymetry was interpolated from ETOPO5<sup>9</sup> data. Atmospheric forcing was specified according to the conditions of the international CORE-I experiment [26] as a normal annual cycle. The horizontal computational grid for the ocean and ice models was defined using a spherical coordinate system with 160 × 80 nodes horizontally and 49 vertical levels. Thus, the coupled ocean – ice model operated at a resolution of 0.125°. The integration step was set identically for the ocean and ice models at  $\Delta t^o = \Delta t^i = 5'$ . In the Lagrangian model, the integration step was set to  $\Delta t^l = 1'$ , and particle coordinates were saved at the same frequency. Physical field

<sup>9</sup> National Oceanic and Atmospheric Administration (NOAA), 1988. *Digital Relief of the Surface of the Earth*. Data Announcement 88-MGG-02. National Geophysical Data Center, Boulder, Colorado.

data, including ice velocity fields, were synchronized every 10' in the coupled ocean – ice system. The ocean – ice system took 1 year to setup; after this, the Lagrangian model was activated synchronously for an additional two model months for  $10^4$  particles initially located in the surface layer at 76°N, 130°E. The calculation was performed in parallel mode using 16 computational cores for the ocean model.

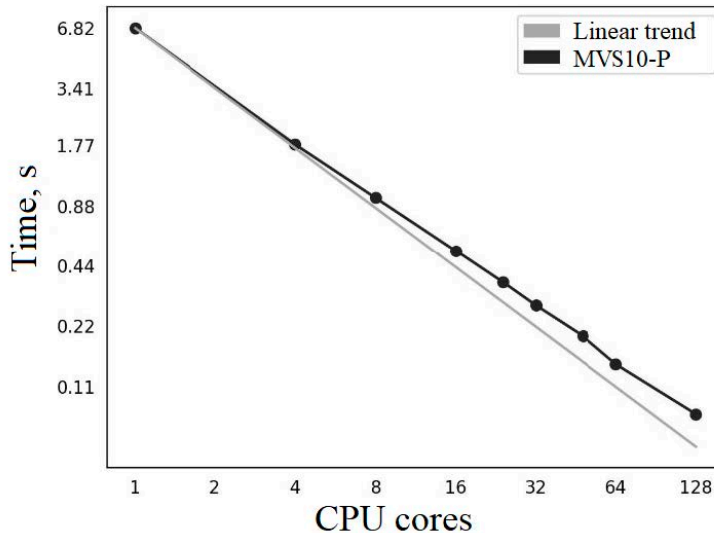


**Fig. 7.** Graph of the dependence of one step duration (in seconds) in the Lagrangian model upon the core number in the experiment with uniform particle distribution in the simulated region

Fig. 6, a displays horizontal trajectories of particles after two months of coupled numerical integration of the ocean – ice dynamics model and the Lagrangian transport model. As can be seen, the particles follow different trajectories under the effect of internal currents, as expected for a model incorporating turbulent mixing effects. Fig. 6, b presents an enlarged view of the trajectories of several particles within the rectangular area indicated in Fig. 6, a. The shapes of the trajectories reflect two primary dynamic processes: a quasi-uniform process in the selected region and circular motions corresponding to inertial oscillations in the current field. A further magnification (Fig. 6, c) reveals the synchronous horizontal movement of two nearby particles.

To evaluate the scalability of the implementation of the Lagrangian transport model, we performed a series of numerical experiments involving  $10^6$  particles that were uniformly distributed over the surface of the domain that was simulated in these experiments (Fig. 7). As can be seen, the dependence of the time taken to calculate

one step in the Lagrangian transport model on the number of computing cores is almost linear, indicating good scalability of the parallel algorithm implemented for calculating the Lagrangian transport. However, it should be noted that this only holds true for the case of uniformly distributed particles, which rarely occurs in actual simulations. Under the influence of currents, particle concentrations within computational domains are not constant, but evolve over time. Consequently, the total computation time per integration step in the Lagrangian model is determined by the domain containing the maximum number of particles.

### Conclusion

This study presents a Lagrangian particle transport model for the quasi-two-phase ocean – ice medium that incorporates vertical turbulent mixing. This model has been implemented in the INMIO ocean general circulation model, which uses arbitrary horizontal coordinate systems. The model's ability to support both two-phase dynamics and turbulent diffusion is a unique feature among existing ocean dynamics models. This modeling tool is particularly relevant given the ongoing intensive development of the Arctic region.

The model implementation supports the parallel computation of the transport of a large number of particles (up to  $10^6$ ) within the framework of a two-dimensional decomposition of the computational domain. For uniformly distributed Lagrangian particles, the algorithm demonstrates near-linear scalability. The particle trajectory calculations are performed on the computational cores of the ocean model, which determines the maximum number of particles. Otherwise, having more than  $10^6$  particles concentrated in one computational domain will inevitably lead to an imbalance in the computational load, negatively affecting the model's performance. However, this worst-case scenario is unlikely, occurring only at the initial moment when particles are concentrated in specific domains according to the conditions of the problem. As the numerical solution evolves, the particles will inevitably be transported to different parts of the computational domain, a process that will be further accelerated by turbulent mixing.

The developed interprocessor exchange algorithm ensures the correct transfer of particle data between subdomains of computing cores, and guarantees the possibility of particle transport throughout the entire ocean model domain. Test calculations demonstrate that setting the integration time step to one-fifth of the ocean model's time step achieves relative trajectory smoothness when crossing the cell boundaries.

### REFERENCES

1. Van Sebille, E., Griffies, S.M., Abernathey, R., Adams, T.P., Berloff, P., Biastoch, A., Blanke, B., Chassignet, E.P., Cheng, Y. [et al.], 2018. Lagrangian Ocean Analysis: Fundamentals and Practices. *Ocean Modelling*, 121, pp. 49-75. <https://doi.org/10.1016/j.ocemod.2017.11.008>
2. Khvostova, M.S., 2018. Environmental Problems of Operation of Floating Nuclear Power Plant in the Arctic Region. *Russian Arctic*, (1), pp. 11-29 (in Russian).

3. Antipov, S.V., Bilashenko, V.P., Vysotskii, V.L., Kalantarov, V.E., Kobrinskii, M.N., Sarkisov, A.A., Sotnikov, V.A., Shvedov, P.A., Ibraev, R.A. [et al.], 2015. Prediction and Evaluation of the Radioecological Consequences of a Hypothetical Accident on the Sunken Nuclear Submarine B-159 in the Barents Sea. *Atomic Energy*, 119(2), pp. 132-141. <https://doi.org/10.1007/s10512-015-0039-x>
4. Ushakov, K.V., Ibrayev, R.A. and Kalmykov, V.V., 2015. Simulation of the World Ocean Climate with a Massively Parallel Numerical Model. *Izvestiya, Atmospheric and Oceanic Physics*, 51(4), pp. 362-380. <https://doi.org/10.1134/S0001433815040131>
5. Kalmykov, V.V., Ibrayev, R.A., Kaurkin, M.N. and Ushakov, K.V., 2018. Compact Modeling Framework v3.0 for High-Resolution Global Ocean–Ice–Atmosphere Models. *Geoscientific Model Development*, 11(10), pp. 3983-3997. <https://doi.org/10.5194/gmd-11-3983-2018>
6. Kalnitskii, L.Y., Kaurkin, M.N., Ushakov, K.V. and Ibrayev, R.A., 2020. Seasonal Variability of Water and Sea Ice Circulation in the High-Resolution Model of the Arctic Ocean. *Известия Российской академии наук. Izvestiya. Atmospheric and Oceanic Physics*, 56(5), pp. 598-610. <https://doi.org/10.31857/S0002351520050065> (in Russian).
7. Kulakov, M.Yu., Makshtas, A.P. and Shutilin, S.V., 2012. AARI–IOCM – Coupled Ice–Ocean Circulation Model for the Arctic Ocean. *Arctic and Antarctic Research*, 2(92), pp. 6-18 (in Russian).
8. Campin, J.-M., Marshall, J. and Ferreira, D., 2008. Sea Ice–Ocean Coupling Using a Rescaled Vertical Coordinate  $z^*$ . *Ocean Modelling*, 24(1-2), pp. 1-14. <https://doi.org/10.1016/j.ocemod.2008.05.005>
9. Fadeev, R.Yu., Ushakov, K.V., Tolstykh, M.A. and Ibrayev, R.A., 2018. Design and Development of the SLAV-INMIO-CICE Coupled Model for Seasonal Prediction and Climate Research. *Russian Journal of Numerical Analysis and Mathematical Modelling*, 33(6), pp. 333-340. <https://doi.org/10.1515/rnam-2018-0028>
10. Warner, J.C., Armstrong, B., He, R. and Zambon, J.B., 2010. Development of a Coupled Ocean–Atmosphere–Wave–Sediment Transport (COAWST) Modeling System. *Ocean Modelling*, 35(3), pp. 230-244. <https://doi.org/10.1016/j.ocemod.2010.07.010>
11. Döös, K., Jönsson, B. and Kjellsson J., 2017. Evaluation of Oceanic and Atmospheric Trajectory Schemes in the TRACMASS Trajectory Model v6.0. *Geoscientific Model Development*, 10(4), pp. 1733-1749. <https://doi.org/10.5194/gmd-10-1733-2017>
12. Blanke, B. and Raynaud, S., 1997. Kinematics of the Pacific Equatorial Undercurrent: An Eulerian and Lagrangian Approach from GCM Results. *Journal of Physical Oceanography*, 27(6), pp. 1038-1053. [https://doi.org/10.1175/1520-0485\(1997\)027<1038:KOTPEU>2.0.CO;2](https://doi.org/10.1175/1520-0485(1997)027<1038:KOTPEU>2.0.CO;2)
13. Paris, C.B., Helgers, J., Van Sebille, E. and Srinivasan, A., 2013. Connectivity Modeling System: A Probabilistic Modeling Tool for the Multiscale Tracking of Biotic and Abiotic Variability in the Ocean. *Environmental Modelling & Software*, 42, pp. 47-54. <https://doi.org/10.1016/j.envsoft.2012.12.006>
14. Golubeva, E. and Gradova, M., 2024. Numerical Study of the Riverine Microplastic Distribution in the Arctic Ocean. *Water*, 16(3), 441. <https://doi.org/10.3390/w16030441>
15. Bleck, R., 2002. An Oceanic General Circulation Model Framed in Hybrid Isopycnic–Cartesian Coordinates. *Ocean Modelling*, 4(1), pp. 55-88. [https://doi.org/10.1016/S1463-5003\(01\)00012-9](https://doi.org/10.1016/S1463-5003(01)00012-9)
16. Shchepetkin, A.F. and McWilliams, J.C., 2005. The Regional Oceanic Modeling System (ROMS): A Split-Explicit, Free-Surface, Topography-Following-Coordinate Oceanic Model. *Ocean Modelling*, 9(4), pp. 347-404. <https://doi.org/10.1016/j.ocemod.2004.08.002>
17. Marshall, J., Adcroft, A., Hill, C., Perelman, L. and Heisey, C., 1997. A Finite-Volume, Incompressible Navier Stokes Model for Studies of the Ocean on Parallel Computers. *Journal of Geophysical Research: Oceans*, 102(C3), pp. 5753-5766. <https://doi.org/10.1029/96JC02775>

18. Ibrayev, R.A., Khabeev, R.N. and Ushakov, K.V., 2021. Eddy-Resolving 1/10° Model of the World Ocean. *Izvestiya, Atmospheric and Oceanic Physics*, 48(1), pp. 37-46. <https://doi.org/10.1134/S0001433812010045>
19. Kalmykov, V.V. and Ibrayev, R.A., 2013. A Framework for the Ocean-Ice-Atmosphere-Land Coupled Modeling on Massively-Parallel Architectures. *Numerical Methods and Programming*, 14(3), pp. 88-95 (in Russian).
20. Maier-Reimer, E. and Sündermann, J., 1982. On Tracer Methods in Computational Hydrodynamics. In: M.B. Abbot and J.A. Cunge, eds., 1982. *Engineering Applications of Computational Hydraulics*. Boston, London, Melbourne: Pitman Advanced Publishing Program. Vol. 1, pp. 198-217.
21. Gardiner, C.W., 1985. *Handbook of Stochastic Methods for Physics, Chemistry and the Natural Sciences*. Springer Series in Synergetics, vol. 13. Berlin, Heidelberg: Springer Berlin Heidelberg, 439 p. <https://doi.org/10.1007/978-3-662-02452-2>
22. Hunter, J.R., Craig, P.D. and Philips, H.E., 1993. On the Use of Random Walk Models with Spatially Variable Diffusivity. *Journal of Computational Physics*, 106(2), pp. 366-376. [https://doi.org/10.1016/S0021-9991\(83\)71114-9](https://doi.org/10.1016/S0021-9991(83)71114-9)
23. Visser, A.W., 1997. Using Random Walk Models to Simulate the Vertical Distribution of Particles in a Turbulent Water Column. *Marine Ecology Progress Series*, 158, pp. 275-281. <https://doi.org/10.3354/meps158275>
24. Sunarko and Zaki Su'ud, 2016. Lagrangian Particle Method for Local Scale Dispersion Modeling. *Journal of Physics: Conference Series*, 739, 012122. <https://doi.org/10.1088/1742-6596/739/1/012122>
25. Sadarjoen, A., Van Walsum, T., Hin, A.J.S. and Post, F.H., 1994. Particle Tracing Algorithms for 3D Curvilinear Grids. In: G. Nielson, H. Müller and H. Hagen, eds., 1994. *Scientific Visualization. Overviews. Methodologies. Techniques*. Delft University of Technology, pp. 299-323.
26. Griffies, S.M., Biastoch, A., Böning, C., Bryan, F., Danabasoglu, G., Chassignet, E.P., England, M.H., Gerdes, R., Haak, H. [et al.], 2009. Coordinated Ocean-Ice Reference Experiments (COREs). *Ocean Modelling*, 26(1-2), pp. 1-46. <https://doi.org/10.1016/j.ocemod.2008.08.007>

Submitted 25.11.2024; approved after review 04.01.2024;  
accepted for publication 13.03.2025.

*About the authors:*

**Sergey V. Semin**, Research Associate, Shirshov Institute of Oceanology, Russian Academy of Sciences (36 Nakhimovskiy ave., Moscow, 117997, Russian Federation) Engineer, Nuclear Safety Institute, Russian Academy of Sciences (52 Bolshaya Tulsкая Str., Moscow, 115191, Russian Federation), CSc. (Phys.-Math.), **Scopus Author ID: 56604365800**, **ORCID ID: 0000-0001-8079-168X**, **ResearcherID: ABH-7440-2020**, svsemin@unistemlab.com

**Leonid Yu. Kalnitskii**, Leading Engineer, Shirshov Institute of Oceanology, Russian Academy of Sciences (36 Nakhimovskiy ave., Moscow, 117997, Russian Federation), **Scopus Author ID: 57219609143**, **ORCID ID: 0009-0005-4023-2257**, leonid.kalnitsckij@yandex.ru

**Konstantin V. Ushakov**, Senior Research Associate, Shirshov Institute of Oceanology, Russian Academy of Sciences (36 Nakhimovskiy ave., Moscow, 117997, Russian Federation), CSc. (Phys.-Math.), **Scopus Author ID: 55015342700**, **ORCID ID: 0000-0002-8454-9927**, **ResearcherID: U-6185-2017**, ushakovkv@mail.ru

**Rashit A. Ibrayev**, Chief Research Associate, Marchuk Institute of Numerical Mathematics, Russian Academy of Sciences (8 Gubkina Str., Moscow, 119333, Russian Federation), Shirshov

Institute of Oceanology, Russian Academy of Sciences (36 Nakhimovskiy ave., Moscow, 117997, Russian Federation), DSc. (Phys.-Math.), Corresponding Member of RAS, **Scopus Author ID: 6602387822**, **ResearcherID: S-6750-2016**, **ORCID ID: 0000-0002-9099-4541**, ibrayev@mail.ru

*Contribution of the co-authors:*

**Sergey V. Semin** – development and adaptation of a Lagrangian model for arbitrary computational grids; integration of the model with the parallel Eulerian INMIO model for quasi-two-phase ocean dynamics; full model debugging; test calculations; processing and interpretation of data; preparation of text and graphical materials; text writing and paper maintenance

**Leonid Yu. Kalnitskii** – development of a Lagrangian particle model in a static vortex; test simulations in the static vortex and the Laptev Sea; data collection and processing; preparation of graphical materials

**Konstantin V. Ushakov** – development of the joint ocean-ice Laptev Sea model; participation in the discussions of the Lagrangian model development and the research results; interpretation of the joint sea-ice model calculation results; detailed paper review

**Rashit A. Ibrayev** – general scientific supervision of the research; formulation of goals and objectives of the study; advisory assistance in the model debug and development; results analysis and interpretation; article review and correction

*The authors have read and approved the final manuscript.*

*The authors declare that they have no conflict of interest.*

## Measuring the Characteristics of Short-Period Internal Waves Using an Array of Drifting Thermoprofiling Buoys

E. I. Svergun<sup>1, ✉</sup>, A. V. Zimin<sup>1, 2</sup>, **S. V. Motyzhev<sup>3, 4</sup>**,  
E. G. Lunev<sup>3, 4</sup>, A. P. Tolstosheev<sup>3, 4</sup>, M. S. Volikov<sup>3, 4</sup>

<sup>1</sup> Shirshov Institute of Oceanology, Russian Academy of Sciences, Moscow, Russian Federation

<sup>2</sup> Saint Petersburg State University, Saint Petersburg, Russian Federation

<sup>3</sup> Sevastopol State University, Sevastopol, Russian Federation

<sup>4</sup> Marlin-Yug LLC, Sevastopol, Russian Federation

✉ Egor-svergun@yandex.ru

### Abstract

**Purpose.** Technical characteristics of a mobile rapidly deployable autonomous hydrophysical measuring system based on an array of drifting buoys, as well as the method for analyzing the obtained measurement data are described to study the characteristics of short-period internal waves.

**Methods and Results.** The developed system is based on the autonomous free-drifting surface thermoprofiling buoys and the automatic receiving station. Each of the buoys is equipped with a measuring line with eighteen temperature sensors and a hydrostatic pressure sensor, a global positioning receiver, a data collection system and a satellite modem for data transmission. The receiving station consists of the information receiving unit, satellite communication antennas and global positioning system, as well as a personal computer with specialized software. A method for assessing the characteristics of short-period internal waves based on the observational data from autonomous hydrophysical system is presented. The novelty of the method consists in determining the time difference between the arrivals of internal wave trains at different measuring lines based on the local maxima of moving dispersion at the pycnocline depth. The examples of analyzing the observational data obtained in the large thermostratified lake (Lake Onega) and in the sea (Kara Gate Strait) are presented. The obtained and submitted estimates of phase velocity and direction of the propagation of internal waves are compared to the simplest model estimates.

**Conclusions.** The developed software and hardware packages significantly simplify the process of studying the characteristics of short-period internal waves in relatively large lakes and distant areas of the World Ocean. The examples of system application have shown its versatility. In future, the buoy group can be supplemented with new buoys with additional sensors that will expand the possibilities for analyzing observational data.

**Keywords:** water temperature, measurement methods, *in situ* measurements, distributed measuring systems, short-period internal waves, signal processing, Lake Onega, Kara Sea

**Acknowledgements:** Measurements in the Kara Sea were carried out within the framework of scientific and educational program “Floating University” (agreement No. 075-01593-23-06). Measurement results were processed within the framework of state assignment of IO, RAS No. FMWE-2024-0028.

**For citation:** Svergun, E.I., Zimin, A.V., Motyzhev, S.V., Lunev, E.G., Tolstosheev, A.P. and Volikov, M.S., 2025. Measuring the Characteristics of Short-Period Internal Waves Using an Array of Drifting Thermoprofiling Buoys. *Physical Oceanography*, 32(3), pp. 392-407.

© 2025, E. I. Svergun, A. V. Zimin, S. V. Motyzhev, E. G. Lunev, A. P. Tolstosheev, M. S. Volikov

© 2025, Physical Oceanography



## Introduction

One of the important current problems in ocean physics is the need to monitor the short-term and submesoscale variability of ocean hydrological field characteristics to determine the geographical features of their contribution to dissipative processes in various areas of the continental shelf [1]. The main difficulty in solving this problem lies in obtaining high-resolution measurements in both space and time simultaneously [2]. A similar problem in local water areas can be solved, for example, using clusters of temperature meters distributed across the area, such as moored chains (thermochains) [3] or integrated sensors [4]. However, setting up and removing moored stations is associated with significant difficulties and risks. Groups of thermochains (thermolines) lowered from [5] or towed behind a vessel [6] can also be used.

Such approaches can be applied anywhere in the World Ocean. However, given the significant labor intensity and cost of such work, questions naturally arise about economic efficiency, selection of areas and the timing of observations. The answers to these questions led to the idea of using autonomous surface-drifting SVP-type buoys. Their successful use in programs such as GDP (Global Drifting Program)<sup>1</sup> and UpTempO<sup>2</sup> confirmed their high efficiency in studying the active layer of the ocean [7]. Therefore, temperature-profiling drifting buoys (SVP BTC60/GPS/ice), which were used to study the Arctic region in the UpTempO program and for which manufacturing experience is available to domestic manufacturers [8], can be considered a prototype for an inexpensive, mobile monitoring system.

The improvement of this type of buoy and the unification of several buoys into a single measuring cluster [9, 10] enabled the development of a prototype monitoring system for short-period variability in the temperature of the active layer of the World Ocean. This prototype enables the characteristics of the field of short-period internal waves (SIW) to be monitored at any point in the World Ocean and the data obtained to be transmitted and processed promptly. The buoy observation facilities are adapted for year-round use in the Arctic. The integrated information system ensures the collection of measurement data, their transmission through the buoy-user communication channels, and the processing and presentation of data at a timescale close to real time. This makes it possible to determine the amplitudes, periods, speeds and directions of propagation of SIW, based on the time difference between wave packets arriving at various buoys in the array.

In [11] it is noted that similar systems were used in 1980–1990s, but their technical imperfections resulted in the method being abandoned. The new generation of systems is now being used more widely to record the spatial characteristics of internal waves in expeditionary practice. Therefore, the methodological basis for their use is only beginning to form. Specialized software needs to be developed from scratch to process data obtained from a specific buoy system.

---

<sup>1</sup> ARGOS. *Global Drifter Program*. [online] Available at: <https://www.argos-system.org/project/global-drifter-program/> [Accessed: 05 September 2024].

<sup>2</sup> UpTempO. *Measuring the Upper Layer Temperature of the Polar Oceans*. [online] Available at: <http://psc.apl.washington.edu/UpTempO/> [Accessed: 05 September 2024].

This paper aims to provide the technical characteristics of a rapidly deployable, autonomous, hydrophysical measuring system based on an array of drifting buoys. It also describes the method used to analyze the obtained measurement data in order to study the characteristics of short-period internal waves.

### Materials and methods

**Array of the drifting buoys used.** To record the SIW characteristics, the Volna-DS-01 hydrophysical measuring system (drifting system) manufactured by Marlin-Yug (Russia) was used. It consists of at least three autonomous, freely drifting Volna-DB-01 surface temperature-profiling buoys (drifting buoys) (the number can be increased several times), and the station for automatic data reception from Volna PS-01 drifting buoys (receiving station). Fig. 1, a shows a diagram of the Volna-DS-01 hydrophysical measuring system.

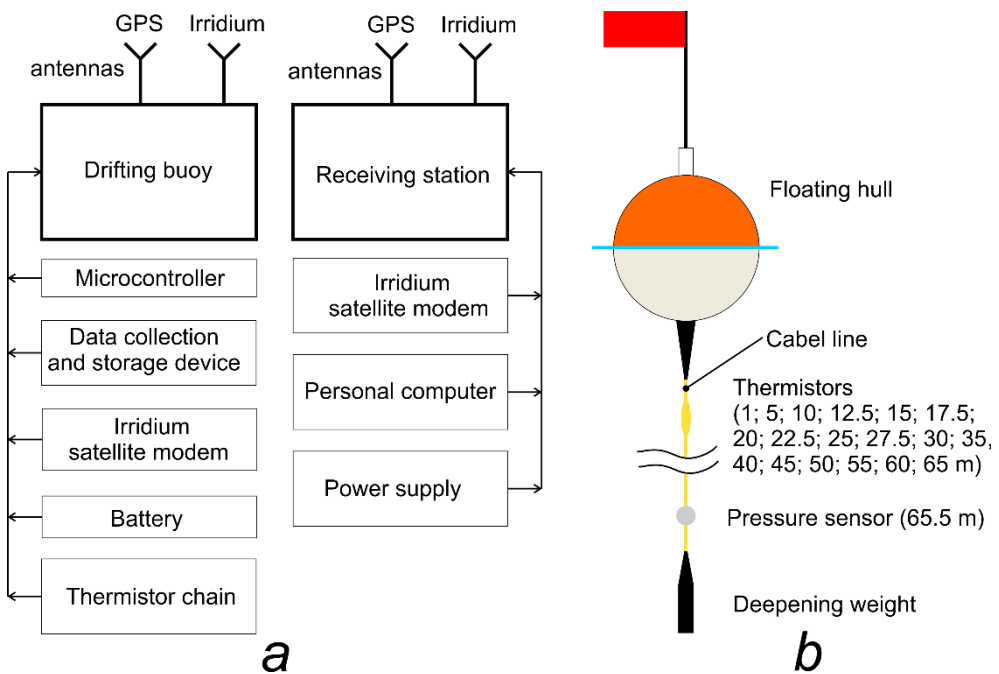


**Fig. 1.** Volna-DS-01 hydrophysical measuring system: *a* – diagram of the components (Volna-DB-01 drifting buoy and Volna-PS-01 receiving station); *b* – schematic diagram of a drifting buoy

Each drifting buoy (Fig. 1, *b*) consists of a floating hull and a measuring line. The hull is made of two polycarbonate hemispheres, hermetically connected by a flange mount. The upper part of the hull contains a hermetically sealed compartment with a USB A interface for connecting a flash drive. A flagpole with a red signal flag is installed on the hull and is equipped with a line to facilitate setting up and retrieving the drifting buoy.

The hermetically sealed hull contains power supply elements that provide at least 1,200 hours of continuous operation, as well as a real-time system controller, a GNSS GLONASS/GPS module with an antenna and an Iridium satellite modem with an antenna. The GNSS module determines the coordinates of each drifting buoy

and synchronizes the measurement time. The satellite modem provides prompt transmission of the geographic coordinates of each drifting buoy with a resolution of 10 minutes. Temperature and hydrostatic pressure profile measurements, buoy power source parameters and additional diagnostic information are transmitted synchronously with the geographic coordinates. The floating hull is equipped with a magnetic power switch and light indicators for the operating mode of the measuring system and the status of satellite data transmission.

The measuring line consists of a twisted pair of cables and a supporting rope. The cable contains 18 digital temperature sensors and a hydrostatic pressure sensor. The readings from these sensors are used to determine their actual horizons when the measuring line deviates from the vertical. The nominal horizons of the sensors are shown in Fig. 1. The design of the temperature sensor housings ensures they are easily washed by the surrounding water, reducing the time constant. A deepening weight is located at the lower end of the measuring line.

The Volna-PS-01 receiving station comprises a data reception unit, Iridium and GNSS satellite system antennas, and a laptop with specialized software. The data reception unit contains an Iridium satellite system modem and a controller, as well as an atmospheric pressure meter designed to correct the readings of the hydrostatic pressure sensors on the buoys. The GNSS antenna includes a BU-353s4/BR-355s4 (GlobalSat) GPS receiver. The software displays the information received by the station in graphic (temperature distribution by depth and drift map) and text (buoy coordinates and station coordinates and speed) formats. The receiving station and the drifting buoys can be in any relative position, which enables the system status to be monitored both from the vessel and from the shore station.

The table below provides information about the characteristics of the sensors used in the drifting system. The minimum possible measurement interval is 10 sec.

#### Technical and metrological characteristics of the drifting system sensors

Measured parameter	Measurement range	Measurement error	Resolution	Time constant
Temperature	-2...35 °C	±0.05 °C	0.015 °C	15 sec
Hydrostatic pressure	850...10000 GPa	±0.4 % of the measured value	1 GPa	2 sec
Location coordinates	Latitude: -90°...+90°, Longitude: 0°...360°	Hit radius of 95 % of locations does not exceed 10 m	0.00001°	–

**Examples of system application.** Fig. 2 shows the location where the Volna-DS-01 hydrophysical measuring system was used.

Tests of the system were carried out in Kondopozhskaya Bay and Bolshoe Onego Bay in Lake Onega in June 2022, as part of the Karelian Scientific Center's expedition aboard the R/V *Ecolog* (point 1 in Fig. 2). Lake Onega was chosen as a test site to minimize the risks of equipment failure or loss and to enable the use of a drifting system to record SIW characteristics in a large stratified water body.

Marine measurements using a drifting system were carried out in July 2023 and 2024 in the Kara Sea as part of the Floating University expeditions on

the R/Vs *Dalniye Zelentsy* and *Professor Molchanov*. The drifting system was deployed in the Kara Gate Strait (points 2 and 3 in Fig. 2), above the Novozemelsky Trench (point 4 in Fig. 2) and near Zhelaniya Cape (point 5 in Fig. 2).

A total of six measurements were taken in Lake Onega with a total duration of 46 hours. The duration of each measurement ranged from 3 to 10 hours. An example of a buoy drift map is shown in the inset of Fig. 2. Five measurements were taken in the Kara Sea, each lasting between 6 and 12 hours, for a total duration of 37 hours.

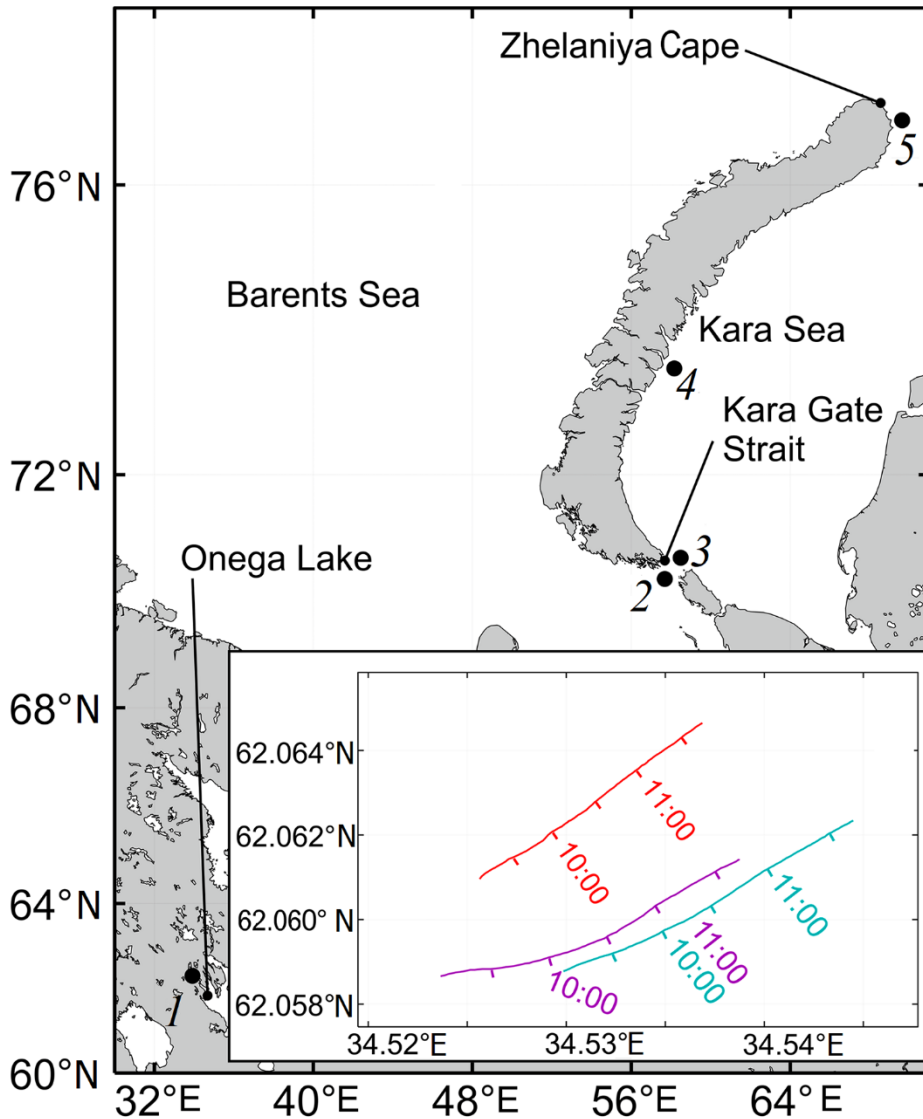


**Fig. 2.** Map of application of the hydrophysical measuring system (1 – Lake Onega; 2, 3 – Kara Gate Strait; 4 – Novozemelsky Trench; 5 – Zhelaniya Cape); *inset* – map of the buoys B<sub>1</sub>–B<sub>3</sub> drifts (1–3 are the manufacturer serial numbers) in Lake Onega on June 16, 2022 (red line shows buoy B<sub>1</sub>, purple line – buoy B<sub>2</sub> and turquoise one – buoy B<sub>3</sub>)

Drifting buoys were installed and removed manually from a working boat at sea states of up to three to avoid damaging the floating housing. During the measurements, each drifting buoy collected data on the vertical temperature distribution in a 1–65 m layer and its own drift coordinates. These were supplemented by the results of control (background) measurements taken by CastAway (USA), CTD48M (Germany) and SBE19plus V2 (USA) CTD probes from other vessels.

The paper will consider as an example the results of recording SIW characteristics in Lake Onega in June 2022 (Fig. 2, inset) and in the eastern part of the Kara Gate Strait in July 2023.

### **Methodology for estimating SIW characteristics using drifting system data.**

In order to record the speed and direction of SIW propagation, simultaneous measurements must be carried out at the location of at least three spaced-apart points. These SIW characteristics are usually assessed based on the time difference between wave packets arrivals at measuring devices positioned at the vertices of a triangle [6]. Therefore, the accuracy of propagation speed and direction estimates depends on the accuracy of determining the arrival delay time of a wave packet.

Various methods can be used to estimate delay time. In [5, 11, 12, 13], the delay time is estimated visually from the temperature fluctuation records directly. This method is effective when clearly distinguishable soliton-like waves are present in the records. However, in the presence of successive wave packets with a complex structure in the records, applying this method may be difficult. Another method of delay time estimation using the cross-correlation function maxima is described in [4, 6]. This method is applicable when the measuring devices are located at the vertices of a triangle, where the side length is much shorter than the length of the recorded waves. However, this configuration is not always convenient for implementation. The delay time can be determined using the integral temperature maxima [14] or the temperature change rate maxima at a certain horizon [3]. However, these methods are mainly described for use with large-amplitude and soliton-like waves.

This paper uses the moving dispersion estimate [15] of the isotherm depth to estimate the arrival delay time of wave packets. The moving dispersion method has previously been used to estimate fluctuations in various ionospheric parameters [16], geochemical parameters [17], and ocean current velocities [9, 18]. Since the moving dispersion reflects local changes in time series properties, its maxima correspond well to solitons and SIW packets.

Let us now take a closer look at the algorithm developed for processing the measurement data of the Volna-DS-01 drifting system (Fig. 3, *a*). The left-hand column of the block diagram shows the processing of data obtained from the vessel (background) and from buoys; the rest of the columns show the data only from the array of drifting buoys.

In the first stage of data analysis, when calculating the moving dispersion, it is necessary to determine the optimal window for the calculation of dispersion at each step. In the present paper, the optimal window was calculated as the ratio of the average buoy-to-buoy distance (based on their geographic coordinates) to the phase velocity of the internal waves, using the two-layer approximation [19] and

background CTD probing data (see the left-hand column of the block diagram in Fig. 3, *a*). The optimal window essentially represents the minimum time during which a wave will propagate from one drifting buoy to another. If the phase velocity is underestimated, the optimal window may exceed the period of the recorded waves. Therefore, the optimal window can also be estimated by calculating the minimum period of the internal waves in the temperature fluctuation record. However, it should be noted that the true period of the waves is distorted by buoy drift due to the Doppler effect.

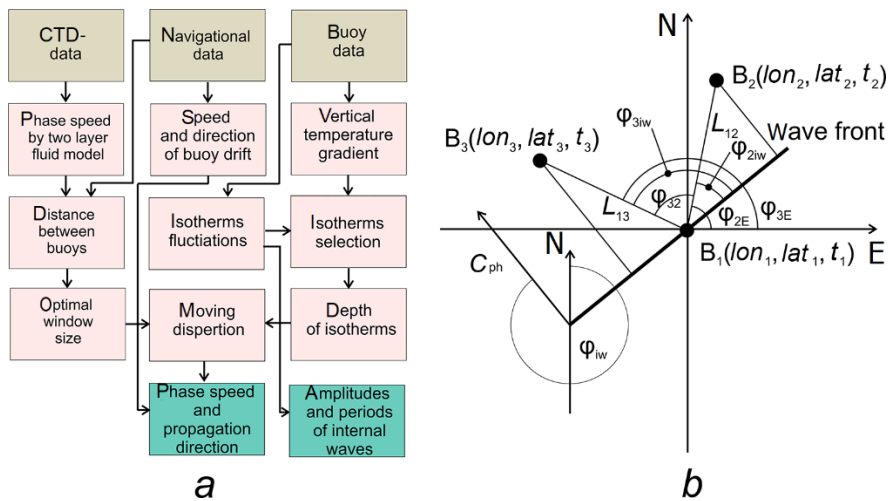


**Fig. 3.** Algorithm for calculating the SIW characteristics based on the drifting system measurements: *a* – block diagram of the algorithm (beige color shows initial data, pink – intermediate results, green – final results); *b* – graph for determining the SIW velocities and directions (letters *N* and *E* indicate the directions to the north and east, large dots labeled *lat* and *lon* show the buoy geographical locations at the time of wave packet recording, and signatures  $B_1$ ,  $B_2$  and  $B_3$  indicate the order of wave packet recording by the buoys of the drifting system where  $B_1$  is the buoy that first recorded the wave packet)

Fig. 3, *a* shows the algorithm for calculating SIW characteristics in the middle and right columns of the block diagram. It should be noted that the accuracy and efficiency of time difference estimation between the wave packet arrivals, based on moving dispersion maxima, is affected by the choice of an isotherm for analysis. The isotherm is selected in the layer with the maximum vertical temperature gradient, where the depth experiences the greatest amplitude fluctuations. Then, with a constant step size equal to the discreteness of the measurements, the depth values are calculated. SIW amplitudes and periods are then determined from these values in accordance with the methodology [20].

The moving dispersion of the isotherm depth is calculated by taking into account the optimal window estimates, and is normalized to the maximum value to facilitate subsequent joint analysis. The graphs showing the temporal variability of the moving dispersion illustrate visual registration of successive local maxima that occur close together in time for different buoys in the drifting system. Moreover, typically, the delay between local dispersion maxima for one pair of buoys out of three is greater than for the other pair.

Next, the positions of the local maxima are validated by direct comparison of the moving dispersion graphs with the isotherm fluctuation records. Firstly, based on the local maxima of the moving dispersion, the order of wave packet recording by the system buoys is determined. Secondly, the moments of wave packet recording by each buoy in the system are determined.

Then, taking into account the distance between the buoys (calculated using their geographic coordinates), the SIW phase velocity is determined [11]:

$$C_{\text{ph}} = \frac{L_{12} \sin \varphi_{2\text{iw}}}{t_2 - t_1} = \frac{L_{13} \sin \varphi_{3\text{iw}}}{t_3 - t_1}, \quad (1)$$

where  $L_{12}$  is the distance between  $B_1$  and  $B_2$  buoys;  $L_{13}$  is the distance between  $B_1$  and  $B_3$  buoys;  $t_1, t_2, t_3$  is the time of wave packet registration by  $B_1, B_2, B_3$  buoy sensors, respectively;  $\varphi_{2\text{iw}}$  is the angle between the wave front line passing through  $B_1$  point and the direction from  $B_1$  point to  $B_2$  point, determined by the following formula

$$\varphi_{2\text{iw}} = \arctg \left( \pm \frac{\sin \varphi_{32}}{\frac{(t_3 - t_1)L_{12} - \cos \varphi_{32}}{(t_2 - t_1)L_{13}}} \right), \varphi_{3\text{E}} > < \varphi_{2\text{E}},$$

where  $\varphi_{32}$  is the angle between the directions from  $B_1$  point to  $B_2$  and  $B_3$  point;  $\varphi_{2\text{E}}$  is the angle between the directions from  $B_1$  point eastward to  $B_2$  point;  $\varphi_{3\text{E}}$  is the angle between the directions from  $B_1$  point eastward to  $B_3$  point;  $\varphi_{3\text{iw}}$  is the angle between the wave front line passing through  $B_1$  point and the direction from  $B_1$  point to  $B_3$  point, determined by the following formula

$$\varphi_{3\text{iw}} = \varphi_{2\text{iw}} \pm \varphi_{32}, \quad \varphi_{3\text{E}} >> \varphi_{2\text{E}}.$$

The SIW propagation direction (Fig. 3b) is determined by the formula [11]

$$\varphi_{\text{iw}} = 2\pi + \varphi_{2\text{iw}} - \varphi_{2\text{E}}. \quad (2)$$

There are also other expressions for calculating SIW characteristics [3, 6]. The expressions from [11] were chosen because the calculations using these expressions do not impose strict requirements on the relative position of the buoys, nor do they require a transition to another coordinate system.

Expressions (1) and (2) are used to calculate the speed and direction of wave propagation in a moving reference system associated with a drifting system. To obtain absolute estimates of these values, the vector sum of the wave speed and drift speed vectors is calculated. It is assumed that the buoys are drifting at the same speed when the wave packet is recorded.

The advantage of the method described in [11] is that the measuring system elements do not need to be rigidly fixed in space. The distance between the elements can be arbitrary and vary depending on the spatial scale of the phenomena being studied. The algorithm for processing the measurement results is implemented in the Matlab environment. The main data processing operations are accompanied by the graphic and text output.

## Results and their discussion

**SIW characteristics in Lake Onega based on drifting system measurements.** The measurement results of June 16, 2022 are given below as an example of the drifting system's use in Lake Onega. The system was deployed over depths of about 36 m in Bolshoe Onego Bay. To ensure stable operation of the drifting system, the working length of the thermal lines was reduced to 30 m by winding the lower part into coils. The distance between the system buoys was  $\sim 300$  m, and the drift velocity varied from 0.05 to 0.1 m/s. According to the background CTD probing data, stable temperature stratification was observed. The upper quasi-homogeneous layer had a thickness of 4 m, and the thermocline layer was located in the layer from 4 to 10 m, coinciding with the pycnocline position. The temperature gradient in the thermocline reached  $0.9\text{ }^{\circ}\text{C/m}$ , corresponding to a density gradient of  $0.08\text{ kg/m}^4$ .

Fig. 4 shows fragments of the measurement results in Lake Onega.

According to the data from each of the three buoys in the layer from 4 to 10 m, a clearly expressed wave packet with wave amplitudes of  $\sim 1$  m and periods of 10–15 min is noted in the records of isotherm fluctuations (Fig. 4, *a*). Based on these records, it is difficult to visually identify the arrival time of the packet at the drifting system buoys. Given the 276 m distance between the buoys and a phase velocity of 0.12 m/s according to the dispersion relation for a two-layer medium, the optimal window of the moving dispersion is 36 min. However, this exceeds the maximum period of the recorded fluctuations. Therefore, the optimal window of moving dispersion was set to the minimum wave period of 5 min.

The moving dispersion calculation for the  $10\text{ }^{\circ}\text{C}$  isotherm depth (thick black line in Fig. 4, *a*), selected based on the maximum vertical temperature gradient, demonstrates successive maxima (Fig. 4, *b*), which corresponds well to the leading waves in the packet when compared with the isotherm fluctuation records. The first local maximum of the moving dispersion ( $t_1$ ) was recorded at buoy 3 at 10:05 (UTC), the second ( $t_2$ ) – at buoy 2 at 10:06, and the third ( $t_3$ ) – at buoy 1 at 10:18.

Using the buoy position data, the phase velocity (0.33 m/s) and propagation direction ( $350^{\circ}$ ) of the leading wave of the packet were estimated in the reference system associated with the moving buoys using expressions (1) and (2), respectively. Taking into account the drift speed of the buoys of 0.08 m/s and the drift direction of  $38^{\circ}$ , the resulting wave packet propagation speed is 0.34 m/s in the direction of  $2^{\circ}$ .

The obtained direction of wave packet propagation is consistent with the spatial position of the local maxima of the normalized moving dispersion (Fig. 4, *c*), the order of wave packet registration, and the estimated time difference between wave packets arriving at the system buoys. The SIW propagation velocity obtained from processing the drifting system data is three times higher than the phase velocity estimated using two-layer stratification (0.34 m/s versus 0.12 m/s). This difference is probably due to the significant nonlinearity of the registered wave packet, or to the fact that the two-layer approximation is not entirely suitable for describing the velocity of internal waves in shallow, weakly stratified waters.

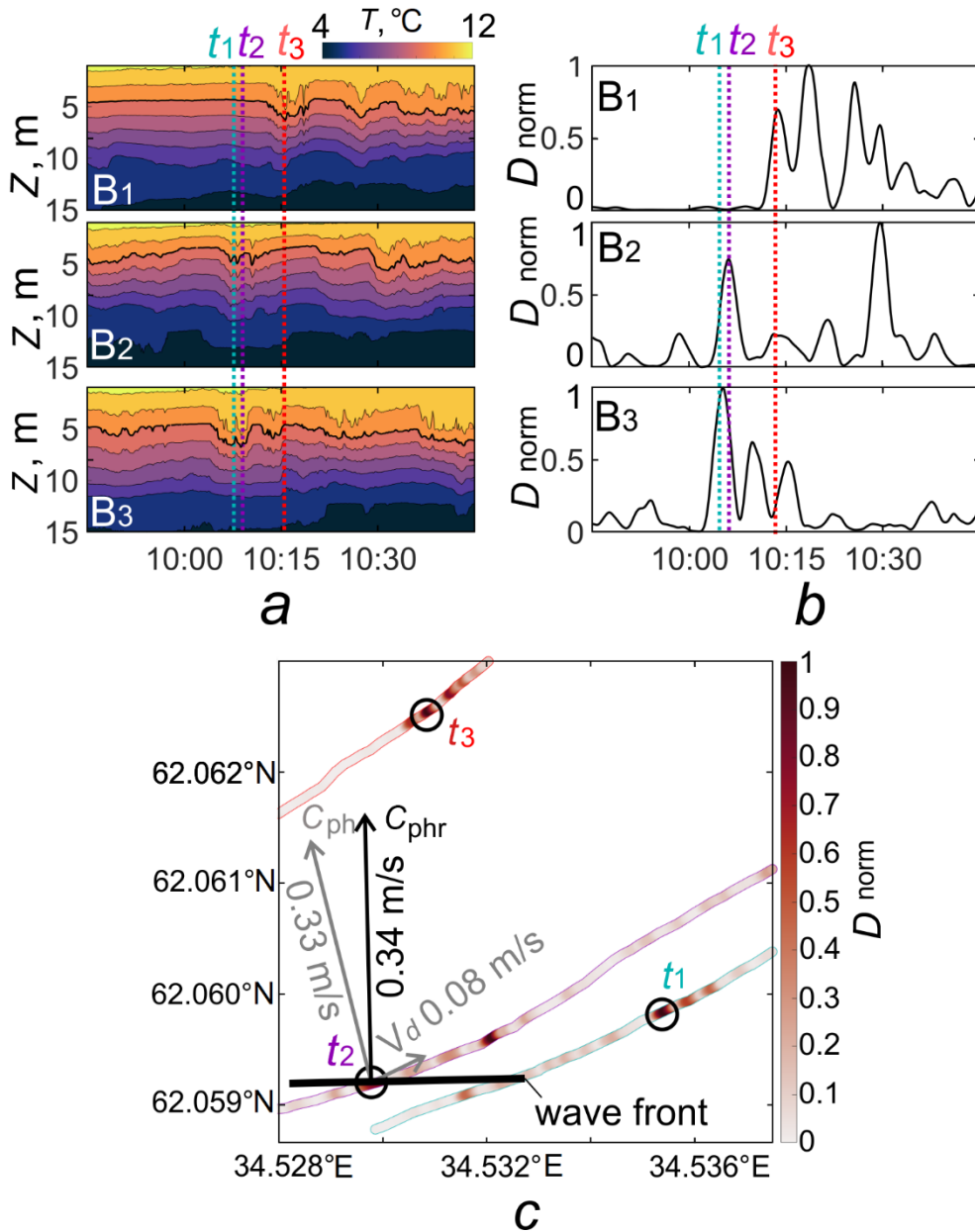


**Fig. 4.** Fragments of the measurement results obtained at R/V *Ecolog* in Lake Onega in June 2022: *a* – records of isotherm fluctuations for three buoys of the drifting system (red dashed line is buoy B1, purple dashed line – buoy B2, turquoise dashed line – buoy B3;  $t_1$ ,  $t_2$ ,  $t_3$  are the designations for the moments of the wave packet arriving at the buoys of the drifting system); *b* – time variations of the moving dispersion normalized to its maximum value for the 10 °C isotherm depths with a 5 min window; *c* – map of the moving dispersion distribution along the buoy drift trajectories with the vectors of buoy drift velocities and SIW phase speeds ( $C_{ph}$  is the phase speed of leading packet wave in the coordinate system related to the moving buoys,  $V_d$  is the buoy drift velocity and  $C_{phr}$  is the resulting phase speed)

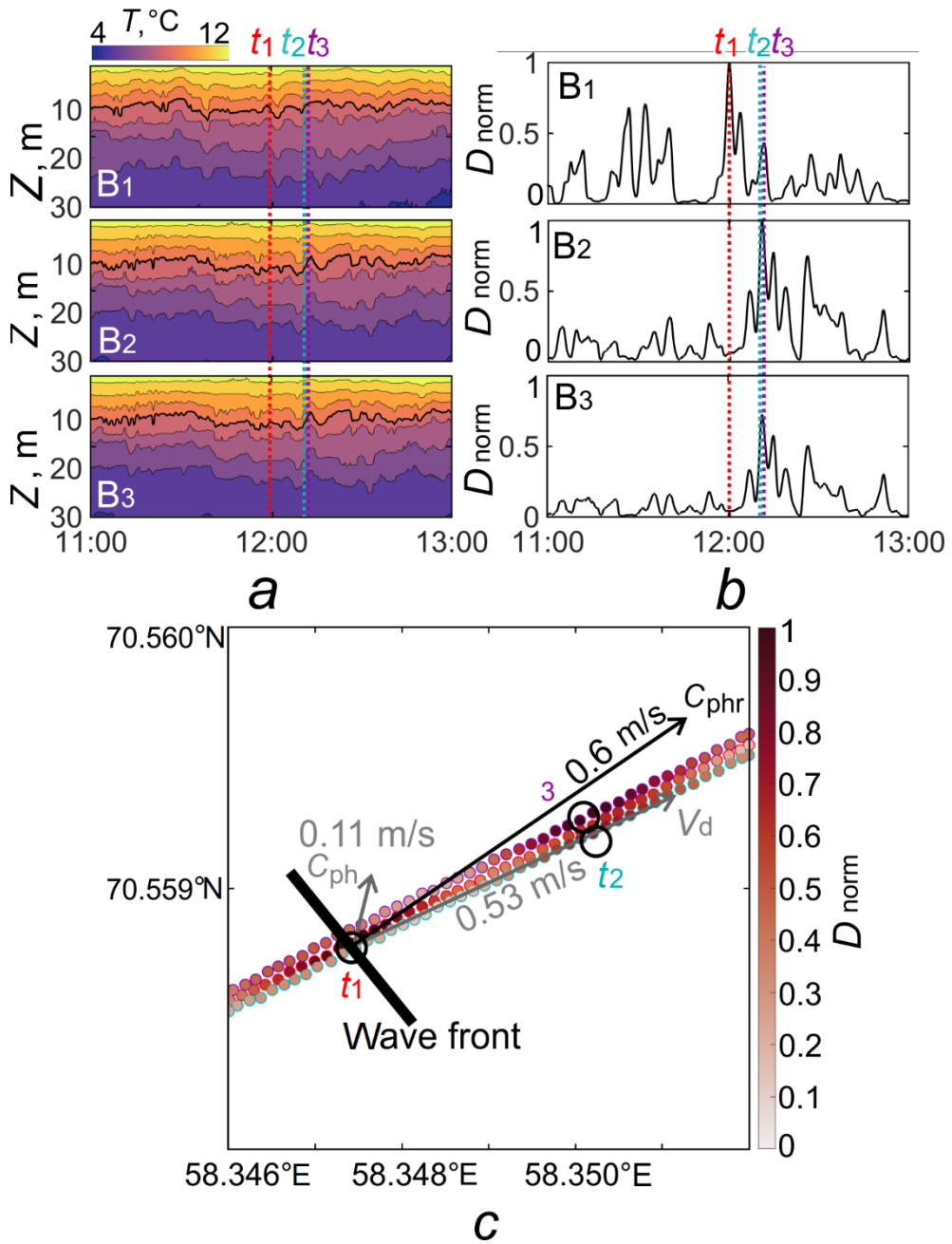


**Fig. 5.** Fragments of the measurement results obtained at R/V *Dalnie Zelentsy* in the Kara Gate Strait in July 2023 (see designations in Fig. 4): a – records of the isotherm fluctuations for three buoys of the drifting system; b – time variations of the moving dispersion normalized to its maximum value for the 9 °C isotherm depths with a 4 min window; c – map of the moving dispersion distribution along the buoy drift trajectories with the vectors of buoy drift velocities and SIW phase speeds (designations are as in Fig. 4)

It should be noted that the relationship between the velocities of linear and nonlinear waves is often discussed in the context of the Kortweg – de Vries (KdV) theory, describing the behavior of nonlinear waves, including solitons [21]. According to this theory, the velocity of nonlinear waves depends on their amplitude, whereas the velocity of linear waves is determined solely by the properties of the medium (stratification and depth).

**SIW characteristics in the Kara Sea according to drifting system measurements.** Let us consider the processing of drifting system measurements in the Kara Gate Strait on July 16, 2023 as an example. The system buoys were installed in the northeastern part of the strait (see Fig. 2), at depths of around 80 m and at a distance of about 140 m from each other. According to background sounding data, pronounced stratification close to a two-layer structure was revealed. The upper quasi-homogeneous layer, which was 5 m thick, and the lower layer were separated by a pycnocline in the 5–11 m layer, which had a density gradient of about  $0.42 \text{ kg/m}^4$ . The positions of the pycnocline and thermocline coincided. Given this stratification and in accordance with the dispersion relation for a two-layer medium, the phase velocity is 0.6 m/s.

Fig. 5 shows fragments of the measurement results in the Kara Gate Strait.

The records of isotherm fluctuations (Fig. 5, *a*) indicate the presence of SIW in a layer from 5 to 15 m, with amplitudes of about half a meter and periods of  $\sim 10$  min. The complex nature of the fluctuations in the records does not allow a reliable estimate of the wave arrival time at the system buoys. The optimal window is the ratio of the distance between the buoys (136 m) to the phase velocity of the wave (0.6 m/s), which, when taking into account the minimum recorded wave period of 5 min, provides an adequate estimate of 4 min. In the maximum gradient area, the  $9^\circ \text{C}$  isotherm was selected (Fig. 5, *a*). The moving dispersion of its occurrence depths is shown in Fig. 5, *b*.

All buoys of the drifting system show successive local maxima, which correspond to waves of a similar shape in the isotherm fluctuation records. Buoy 1 registered a wave at 12:01:00 (UTC) ( $t_1$ ), buoy 3 registered a wave at 12:11:10 ( $t_2$ ), buoy 2 registered a wave at 12:11:40 ( $t_3$ ). Such a small delay is associated with the direction of wave packet propagation, the small distance between the buoys and the relatively high phase velocity of the waves. The phase velocity calculated using expression (1) was 0.11 m/s, and the direction of propagation calculated using expression (2) was  $14^\circ$ . Taking into account the drift speed (0.53 m/s) and direction ( $65^\circ$ ), the resulting wave propagation speed was 0.6 m/s, and the direction was  $57^\circ$  (Fig. 5, *c*). The obtained phase velocity is close to the estimates obtained in the two-layer model. The propagation direction corresponds to the position and order of registration of the dispersion maxima on the buoy drift map (Fig. 5, *c*), and is also similar to the general direction of propagation of SIW packet manifestations recorded from satellite data in the area under consideration [22, 23].

## Conclusion

The paper describes a new hydrophysical measuring system based on an array of surface-drifting temperature-profiling buoys. The main advantages of this system are its mobility, ease of installation, and the ability to track the system's status in real time via a satellite communication channel. The disadvantages include the lack of a standard ability to change the position of the temperature sensors by depth. It is worth noting that the presented measuring system is suitable for recording a wide range of processes and phenomena occurring in the ocean, such as frontal and eddy dynamics.

Methodological features of estimating the speed and direction of internal waves were described. A method for determining the delay time of wave packets arriving to measuring devices was demonstrated based on the results of calculating the moving dispersion with a window determined based on the stratification conditions, the configuration of the drifting system, and the period of the recorded waves.

The results of using the system in Lake Onega and in the Kara Gate Strait are presented. Processing the measurement results using the proposed method based on calculating the moving dispersion allowed to determine the phase velocity and direction of SIW propagation.

Comparing the results obtained in Lake Onega and the Kara Gate Strait, it is worth noting that with a decrease in the distance between the buoys, the estimate of the delay in the arrival of wave packets becomes more complicated, since the difference between the moving dispersion maxima is small. This is important to take into account in subsequent work, deploying the buoys so that the distance between them is approximately equal to the length of the wave being studied.

As a result of using the Volna-DS-01 drifting system in 2022–2024, an extensive database of *in-situ* measurements was accumulated. The obtained wave characteristics in the future, together with the results of satellite observations and calculations using a high-resolution regional tidal model, will allow to determine the prevailing mechanisms of SIW generation in various areas of the Kara Sea.

The presented algorithm will be further improved. A more detailed comparative analysis of various methods for signal delay time estimation is planned, as well as the use of other methods for estimating wave speed and direction. Data on the full density profile will be used to validate phase velocity estimates, and the period of the recorded waves will be adjusted taking into account the Doppler effect.

## REFERENCES

1. Munk, W., Armi, L., Fischer, K. and Zachariasen, F., 2000. Spirals on the Sea. *Proceedings of the Royal Society A: Mathematical, Physical and Engineering Sciences*, 456(1997), pp. 1217-1280. <https://doi.org/10.1098/rspa.2000.0560>
2. Zimin, A.V., 2018. *Sub-Tidal Processes and Phenomena in the White Sea*. Moscow: GEOS Publishing, 220 p. (in Russian).

3. Ocherednik, V.V., Zatsepin, A.G., Kuklev, S.B., Baranov, V.I. and Mashura, V.V., 2020. Examples of Approaches to Studying the Temperature Variability of Black Sea Shelf Waters with a Cluster of Temperature Sensor Chains. *Oceanology*, 60(2), pp. 149-160. <https://doi.org/10.1134/S000143702001018X>
4. Serebryany, A., Khimchenko, E., Popov, O., Denisov, D., and Kenigsberger, G., 2020. Internal Waves Study on a Narrow Steep Shelf of the Black Sea Using the Spatial Antenna of Line Temperature Sensors. *Journal of Marine Science and Engineering*, 8(11), 833. <https://doi.org/10.3390/jmse8110833>
5. Kozlov, I.E., Kopyshov, I.O., Frey, D.I., Morozov, E.G., Medvedev, I.P., Shiryborova, A.I., Silvestrova, K.P., Gavrikov, A.V., Ezhova, E.A. [et al.], 2023. Multi-Sensor Observations Reveal Large-Amplitude Nonlinear Internal Waves in the Kara Gates, Arctic Ocean. *Remote Sensing*, 15(24), 5769. <https://doi.org/10.3390/rs15245769>
6. Stepanyuk, I.A., 2002. *Methods for Measuring the Parameters of Internal Sea Waves*. Saint Petersburg: RGGMU Publishing, 138 p. (in Russian).
7. Motyzhev, S.V., Lunev, E.G. and Tolstosheev, A.P., 2017. The Experience of Using Autonomous Drifters for Studying the Ice Fields and the Ocean Upper Layer in the Arctic. *Physical Oceanography*, (2), pp. 51-64. <https://doi.org/10.22449/1573-160X-2017-2-51-64>
8. Tolstosheev, A.P., Lunev, E.G. and Motyzhev, V.S., 2008. Development of Means and Methods of Drifter Technology Applied to the Problem of the Black Sea Research. *Oceanology*, 48(1), pp. 138-146. <https://doi.org/10.1007/s11491-008-1016-4>
9. Zimin, A.V., Rodionov, A.A., Motyzhev, S.V., Lunev, E.G. and Tolstosheev, A.P., 2021. A System to Monitor Characteristics of Hydrophysical Fields in the Sub-Mesoscale Variability Interval. In: MHI, 2021. *Proceedings of All-Russian Scientific Conference. The Seas of Russia: Year of Science and Technology in the RF – United Nations Decade of Ocean Science for Sustainable Development*. Sevastopol, pp. 246-247 (in Russian).
10. Svergun, E.I., Zimin, A.V., Lunyov, E.G., Tolstosheev, A.P. and Bezgin, A.A., 2023. A Method for Estimating the Characteristics of Short-Period Internal Waves Based on the Data of a Drifting buoy Array. In: MHI, 2023. *Proceedings of All-Russian Scientific Conference. The Seas of Russia: From Theory to Practice of Oceanological Research*. Sevastopol, pp. 102-103 (in Russian).
11. Centurioni, L.R., 2010. Observations of Large-Amplitude Nonlinear Internal Waves from a Drifting Array: Instruments and Methods. *Journal of Atmospheric and Oceanic Technology*, 27(10), pp. 1711-1731. <https://doi.org/10.1175/2010JTECHO774.1>
12. Lee, O.S., 1961. Observations on Internal Waves in Shallow Water. *Limnology and Oceanography*, 6(3), pp. 312-321. <https://doi.org/10.4319/lo.1961.6.3.0312>
13. Johannessen, O.M., Sandven, S., Chunchuzov, I.P. and Shuchman, R.A., 2019. Observations of Internal Waves Generated by an Anticyclonic Eddy: A Case Study in the Ice Edge Region of the Greenland Sea. *Tellus A: Dynamic Meteorology and Oceanography*, 71(1), 1652881. <https://doi.org/10.1080/16000870.2019.1652881>
14. Gong, Q., Chen, L., Diao, Y., Xiong, X., Sun, J. and Lv, X., 2023. On the Identification of Internal Solitary Waves from Moored Observations in the Northern South China Sea. *Scientific Reports*, 13(1), 3133. <https://doi.org/10.1038/s41598-023-28565-5>
15. Sevostyanov, P.A., Samoilova, T.A. and Rodin, A.A., 2019. [Sequential Regressions in the Analysis and Forecasting of Time Series Variability]. In: Vitebsk State Technological University, 2019. *Innovative Technologies in Textile, Shoe, Knitwear and Clothing Industry. Proceedings of Scientific-and-Technical Conference*. Vitebsk, pp. 305-307 (in Russian).
16. Sverdlík, L.G., 2021. Identification of Pre-Seismic Atmospheric Perturbations Using Modified STA/LTA Criterion. *Current Problems of Remote Sensing of the Earth from Space*, 18(3), pp. 141-149. <https://doi.org/10.21046/2070-7401-2021-18-3-141-149> (in Russian).

17. Saidov, O.A., 2014. Monitoring of Geochemical Parameters Variations in the Region of Dagestan Wedge in Connection with Seismic Events. *Monitoring. Science and Technology*, 4(21), pp. 71-75 (in Russian).
18. Khodyaev, A.V., Shevyrnogov, A.P., Vysotskaya, G.S. and Kozikova, O.S., 2011. Using Moving Variance Method to Detect Ocean Currents from Space. *Journal of Siberian Federal University. Engineering and Technologies*, 4(2), pp. 179-184.
19. Konyaev, K.V. and Sabinin, K.D., 1992. *Waves inside the Ocean*. Saint Petersburg: Gidrometeoizdat, 269 p. (in Russian).
20. Zhegulín, G.V., Zimin, A.V. and Rodionov, A.A., 2016. Analysis of the Dispersion Dependence and Vertical Structure of Internal Waves in the White Sea in Experimental Data. *Fundamental and Applied Hydrophysics*, 9(4), pp. 47-59 (in Russian).
21. Meng, J., Zhang, H., Sun, L. and Wang, J., 2024. Remote Sensing Techniques for Detecting Internal Solitary Waves: A Comprehensive Review and Prospects. *IEEE Geoscience and Remote Sensing Magazine*, 12(4), pp. 46-78. <https://doi.org/10.1109/MGRS.2024.3402673>
22. Kozlov, I.E., Kudryavtsev, V.N., Zubkova, E.V., Atadjanova, O.A., Zimin, A.V., Romanenkov, D.A., Shapron, B. and Myasoedov, A.G., 2014. Generation Sites of Nonlinear Internal Waves in the Barents, Kara and White Seas from Spaceborne SAR Observations. *Current Problems of Remote Sensing of the Earth from Space*, 11(4), pp. 338-345 (in Russian).
23. Kopyshov, I.O., Kozlov, I.E., Shiryborova, A.I. and Myslenkov, S.A., 2023. Properties of Short-Period Internal Waves in the Kara Gates Strait Revealed from Spaceborne SAR Data. *Russian Journal of Earth Sciences*, 23, ES0210. <https://doi.org/10.2205/2023ES02S110>

*About the authors:*

**Egor I. Svergun**, Researcher, Shirshov Institute of Oceanology, Russian Academy of Sciences, (30, 1st Line of Vasilievsky Island, Saint Petersburg, 119053, Russian Federation), CSc. (Geogr.), **WoS ResearcherID: AAC-7289-2020**, **Scopus Author ID: 57195066881**, **ORCID ID: 0000-0002-9228-5765**, **SPIN-code: 3212-7041**, [egor-svergun@yandex.ru](mailto:egor-svergun@yandex.ru)

**Alexey V. Zimin**, Senior Researcher, Shirshov Institute of Oceanology, Russian Academy of Sciences (30, 1st Line of Vasilievsky Island, Saint Petersburg, 119053, Russian Federation), DSc. (Geogr.), Professor, Saint Petersburg State University (7/9 Universitetskaya Embankment, Saint Petersburg, 199034, Russian Federation), **ORCID ID: 0000-0003-1662-6385**, **WoS ResearcherID: C-5885-2014**, **Scopus Author ID: 55032301400**, **SPIN-code: 9833-3460**, [zimin2@mail.ru](mailto:zimin2@mail.ru)

**Sergey V. Motyzhev**, Chief Researcher, Sevastopol State University (33 Universitetskaya Str., Sevastopol, 299053, Russian Federation), DSc. (Tech.), **ORCID ID: 0000-0002-8438-2602**, **Scopus Author ID: 6507354504**, **SPIN-code: 1999-2976**, [motyzhev@marlin-yug.com](mailto:motyzhev@marlin-yug.com)

**Aleksey P. Tolstosheev**, Leading Researcher, Sevastopol State University (33 Universitetskaya Str., Sevastopol, 299053, Russian Federation), DSc. (Tech.), **ORCID ID: 0000-0002-0771-0879**, **ResearcherID: G-1901-2014**, **Scopus Author ID: 23994548500**, **SPIN-code: 8885-3906**, [tolstosheev@marlin-yug.com](mailto:tolstosheev@marlin-yug.com)

**Evgeniy G. Lunev**, Leading Researcher, Sevastopol State University (33 Universitetskaya Str., Sevastopol, 299053, Russian Federation), DSc. (Tech.), **ORCID ID: 0000-0002-7138-3024**, **Scopus Author ID: 23994266100**, **SPIN-code: 9627-6497**, [lunev@marlin-yug.com](mailto:lunev@marlin-yug.com)

**Mihail S. Volikov**, Researcher, Sevastopol State University (33 Universitetskaya Str., Sevastopol, 299053, Russian Federation), **ORCID ID: 0000-0003-4307-0423**, **ResearcherID: ABI-9792-2022**, **SPIN-code: 7799-5042**, [volikov@marlin-yug.com](mailto:volikov@marlin-yug.com)

Submitted 19.09.2024; approved after review 11.10.2024;  
accepted for publication 13.03.2025.

*Contribution of the co-authors:*

**Egor I. Svergun** – carrying out experimental studies, data collection and systematization, analysis of measurement data, selection and analysis of literature, preparation of the article text, creation of figures

**Alexey V. Zimin** – carrying out experimental studies, selection and analysis of literature, scientific supervision, critical analysis and revision of the text

**Sergey V. Motyzhev** – general scientific supervision, development and scientific substantiation of the research concept, analysis of materials, discussion of results

**Aleksey P. Tolstosheev** – carrying out laboratory studies, development and implementation of information and measuring system, metrological support, analysis of materials, discussion of the results, updating of the paper text

**Evgeniy G. Lunev** – development and implementation of information and measuring system, analysis of materials, discussion of the results, updating of the paper text

**Mihail S. Volikov** – carrying out experimental studies, development and implementation of information and measuring system, development of software, discussion of the results

*The authors have read and approved the final manuscript.*

*The authors declare that they have no conflict of interest.*

## On Tropical Cyclone Footprints in Sea Surface Height Anomalies

P. D. Pivaev<sup>1,2</sup>✉, V. N. Kudryavtsev<sup>1,2</sup>

<sup>1</sup> *Marine Hydrophysical Institute of RAS, Sevastopol, Russian Federation*

<sup>2</sup> *Russian State Hydrometeorological University, Saint Petersburg, Russian Federation*

✉ [pivaev.pavel@gmail.com](mailto:pivaev.pavel@gmail.com)

### Abstract

**Purpose.** Tropical cyclones leave ‘footprints’ on the ocean surface in the form of sea surface height anomalies, which are well observed by satellite altimeters. Recent studies have shown that the values of these anomalies, normalized by the square of the maximum wind speed in the tropical cyclone and the acceleration due to gravity, are a universal function of a dimensionless parameter composed of the radius of maximum wind speed, translation speed of the tropical cyclone and the buoyancy frequency in the seasonal pycnocline. The purpose of this paper is to investigate physical processes responsible for the formation of tropical cyclone wakes in sea surface height anomalies, assess contribution of barotropic and baroclinic modes, and substantiate and quantify the self-similarity of hurricane-induced sea surface height anomalies revealed in satellite altimetry.

**Methods and Results.** The paper considers sea surface height anomalies in wakes of tropical cyclones observed in different regions of the World Ocean from 2010 to 2020. The modelling is carried out using a simplified model of the baroclinic and barotropic response of the ocean to moving tropical cyclones. Calculations show that the first and second baroclinic modes make a significant contribution to the sea surface height anomaly, and the contribution of the third baroclinic mode is of secondary importance. The relative contribution of the barotropic mode depends substantially on the local ocean depth, and it is greater when the ocean is shallower. However, the contribution of the barotropic mode to satellite altimetry measurements of the ocean surface height in wakes of tropical cyclones can be ignored, since the lifetime of the barotropic perturbation is significantly shorter than a typical time interval between the passage of the tropical cyclone and the measurements.

**Conclusions.** Empirical parameterizations of satellite altimetry measurements of the sea surface height anomaly in wakes of tropical cyclones can be reproduced by superposition of the first three baroclinic modes describing the ocean response to the tropical cyclone passage. In this case, the best fit of the modelling results to the measurement data is achieved if the ocean surface drag coefficient at hurricane-force winds has an approximately constant value of  $2.25 \cdot 10^{-3}$ . This result can be considered as an estimate of the momentum exchange between the ocean and the atmosphere at hurricane-force winds, which remains a subject of present-day scientific effort.

**Keywords:** tropical cyclone, sea surface height, satellite altimeter, sea surface height anomaly, baroclinic mode, barotropic mode, sea surface height parameterization

**Acknowledgements:** This work was supported by the Ministry of Science and Education of the Russian Federation under state assignments No. FNNN-2024-0001 (Marine Hydrophysical Institute of RAS) and No. FSZU-2025-0005 (Russian State Hydrometeorological University).

**For citation:** Pivaev, P.D. and Kudryavtsev, V.N., 2025. On Tropical Cyclone Footprints in Sea Surface Height Anomalies. *Physical Oceanography*, 32(3), pp. 408-426.

© 2025, P. D. Pivaev, V. N. Kudryavtsev

© 2025, Physical Oceanography



## Introduction

Tropical cyclones (TCs) propagating over the ocean result in barotropic and baroclinic disturbances. These disturbances manifest themselves as perturbations of the sea surface height (SSH). The author of [1] was the first to study the impact of the barotropic mode on the ocean surface. Using a two-layer fluid approximation as an example, the author showed that the steady-state displacement of the free surface produced by a point source of vorticity moving in a straight line has the form of a trough along its trajectory. The depth of the trough exponentially decays in the cross-track direction, with the decay rate being the inverse of the barotropic radius of deformation. He also obtained a solution for baroclinic displacements of the interface between the two layers, but the author did not consider the manifestation of these displacements in variations of the SSH. The authors of [2] gave analytical expressions for the SSH anomaly associated with the barotropic mode and the currents corresponding to this mode. The authors derived relations that are applicable to wind fields resembling those of real atmospheric cyclones. Using numerical modelling, the authors also obtained SSH anomalies associated with the baroclinic mode and showed that in the case of a two-layer fluid, baroclinic SSH anomalies are out of phase with and proportional to the displacements of the interface between the two layers (pycnocline) with a proportionality coefficient equal to the relative difference in densities of the two layers.

With the advent of satellite altimetry data, it became possible to experimentally study SSH anomalies produced by moving TCs. At present, surface height anomalies can be considered well documented. The results of [3–5] show that SSH anomalies observed by altimeters are described quite well by the relationship

$$\frac{h_s g}{U_m^2} = c_s \frac{N_1 R_m}{V}, \quad (1)$$

where  $g$  – acceleration due to gravity;  $h_s$  – SSH anomaly;  $U_m$  – maximum wind speed in the TC;  $N_1$  – buoyancy frequency in the seasonal thermocline;  $R_m$  – radius of maximum wind speed in the TC;  $V$  – TC translation speed, and  $c_s$  – empirical constant. Experimental estimates of the proportionality constant in the equation (1) from the works mentioned are  $c_s = 6.9 \cdot 10^{-6}$  [3, 4] and  $c_s = 8.6 \cdot 10^{-6}$  [5].

Expression (1) was obtained in [3] using the condition of pressure continuity across the ocean surface and the pycnocline displacements in a two-layer model, taken from [1], considered as a scale of TC-induced displacements in continuously stratified ocean. Accordingly, equation (1) was initially obtained for the first baroclinic mode, whereas SSH anomalies analyzed in [4, 5] have, as a matter of fact, an unknown mode composition.

In processing altimetry data, the authors of [4, 5] excluded cases with a local ocean depth of less than 2 and 5 km, respectively. The authors assumed that using this depth-based filtration of data allowed them to minimize the contribution of the barotropic mode to the displacement of the ocean surface, and the approximation of SSH anomalies by equation (1) then becomes justified. The assumption that the exclusion of barotropic surface displacements is possible by simply discarding the data according to the ocean depth criterion requires clarification. Indeed, according to [1], the ratio of the barotropic displacement of the ocean surface to

the displacement of the interface in a two-layer fluid is equal to the ratio of the corresponding radii of deformation:

$$\frac{h_{bt}}{\eta_{bc}} = \frac{R_{bc}}{R_{bt}} = \left( \frac{\varepsilon H_1}{H} \right)^{1/2},$$

where  $H_1$  – upper layer thickness;  $H$  – ocean depth;  $\varepsilon$  – relative density difference. As shown in [2], the displacement of the ocean surface associated with the baroclinic mode is well described by the formula  $h_{bc} = \varepsilon \eta_{bc}$ , which means that the ratio of the barotropic SSH anomaly to the baroclinic one is

$$\frac{h_{bt}}{h_{bc}} = \left( \frac{H_1}{\varepsilon H} \right).$$

When substituting values typical for the ocean  $\varepsilon = 10^{-3}$ ,  $H_1 = 200$  m,  $H = 5000$  m, we obtain a ratio of the order of unity, which means that barotropic and baroclinic displacements of the ocean surface are comparable even in conditions of a sufficiently deep ocean. For this reason, the influence of the barotropic mode on SSH anomalies parameterized by formula (1) remains unclear. In addition, the role of higher-order baroclinic modes in the formation of the SSH anomaly is also unclear. If their role is significant, it is necessary to explain why SSH anomalies observed experimentally in [3–5] are well parameterized by the law (1), which assumes the dominant role of the first baroclinic mode.

The aim of our study is to analyze SSH anomalies produced by moving TCs and their parameterization taking into account the barotropic response and the multimode structure of the baroclinic response of the ocean to the passage of the TC.

## Model and input parameters

### Main equations

To model the SSH anomaly, we use a simplified model of the baroclinic and barotropic response of the ocean to a moving TC proposed in [6]. The model equations are written for the unbounded, inviscid fluid consisting of three layers – seasonal, main pycnocline and abyssal. In each layer, buoyancy frequencies are constant (zero in the abyssal). The model is based on the linearized equations of motion in Boussinesq approximations on an  $f$ -plane, written in a coordinate system whose origin is fixed at the TC centre. The initial condition is a horizontally homogeneous ocean at rest. The stationary solution of the problem in coordinate system moving with TC is considered. The driving force is the ‘frozen’ wind stress field of the TC moving along the  $x$ -axis (in opposite direction) with a constant speed  $V$ . The details of constructing the wind vector field in the TC are given in the next section. Equations for the barotropic mode are obtained assuming the ocean with uniform density.

Under the approximations mentioned above, the displacement of the ocean surface relative to the undisturbed state (SSH anomaly) is determined as

$$h(x, y) = \frac{1}{V} \int_{-\infty}^x w(x', y, 0) dx', \quad (2)$$

where  $w(x, y, 0)$  is the vertical velocity at the surface associated with either baroclinic or barotropic modes.

The barotropic vertical velocity is given by the Fourier integral:

$$w_{bt}(x, y) = \frac{-f}{C_{bt}^2} \frac{1}{(2\pi)^2} \iint_{-\infty}^{+\infty} dk dl P(k, l) e^{-i(kx+ly)}. \quad (3)$$

The function  $P(k, l)$  is defined as

$$P(k, l) = \frac{\hat{F}(k, l)}{(1 - (V/C_{bt})^2)k^2 + l^2 + \alpha_{bt}^2}$$

and  $\hat{F}(k, l)$  is the two-dimensional Fourier transform of the curl of the wind stress  $\tau(x, y)$  in TC:

$$\begin{aligned} \hat{F}(k, l) &= \iint_{-\infty}^{+\infty} dx dy F(x, y) e^{i(kx+ly)}, \\ F(x, y) &= \frac{(\nabla \cdot \tau)_z}{\rho_0}. \end{aligned}$$

In the equations above,  $k, l$  – components of the wave vector;  $f$  – Coriolis parameter;  $C_{bt} = \sqrt{gH}$  – phase speed of long waves ( $g$  – acceleration due to gravity,  $H$  – ocean depth) and  $\alpha_{bt} = f/C_{bt}$  – reciprocal of the barotropic radius of deformation.

The vertical velocity at the surface, associated with the  $n$ -th baroclinic mode, is found using the dynamic boundary condition at the sea surface, according to which the velocity at the level  $z = 0$  is proportional to the vertical gradient of the vertical velocity at the surface:

$$w_{bc}^{(n)}(x, y, 0) = \left(\frac{C_n^2}{g}\right) \frac{\partial w_{bc}^{(n)}(x, y, 0)}{\partial z}, \quad (4)$$

where  $C_n$  – eigenvalue (long wave speed) for the  $n$ -th baroclinic mode (see Appendix for the calculation of eigenvalues). Three-dimensional field of vertical velocity of the  $n$ -th baroclinic mode is represented as the product of two functions:

$$w_{bc}^{(n)}(x, y, z) = W_z^{(n)}(z) W_{xy}^{(n)}(x, y).$$

The function  $W_z^{(n)}(z)$ , depending on the vertical coordinate, has the following piecewise-smooth form in the three-layer ocean approximation:

$$W_z^{(n)}(z) = \begin{cases} a_{1n} \sin(N_1 z/C_n), & z > -d_1, \\ a_{2n} \sin(N_2[z + d_2]/C_n + \phi_n), & -d_2 < z < -d_1, \\ a_{2n}(z + H)/(H - d_2) \sin \phi_n, & z < -d_2, \end{cases}$$

where  $d_1, d_2$  – depths of lower boundaries of seasonal and main pycnoclines, respectively,  $N_1, N_2$  – buoyancy frequencies corresponding to the two layers. Original equations for nondimensional coefficients  $a_{1n}$  и  $a_{2n}$  are given in [6, p. 3483]. In this study, we modified them to allow for a more accurate description of the finite-depth effects that can influence the shape of  $W_z^{(n)}(z)$ . The modified expressions for  $a_{1n}$  and  $a_{2n}$  as well as expressions for  $\phi_n$  are given in Appendix at the end the article.

Taking into account the above expressions for the baroclinic vertical velocity, the dynamic boundary condition (4) can be rewritten as

$$w_{bc}^{(n)}(x, y, 0) = g^{-1} a_{1n} N_1 C_n W_{xy}^{(n)}(x, y). \quad (5)$$

The function  $W_{xy}^{(n)}(x, y)$ , depending on the horizontal coordinates, is given by two different Fourier integrals. The choice of the integral depends on the ratio between the TC translation speed  $V$  and the long wave speed for the  $n$ -th baroclinic mode. At  $V > C_n$ , the function  $W_{xy}^{(n)}(x, y)$  is determined by one-dimensional integrals:

$$W_{xy}^{(n)}(x, y) = \frac{f}{(V^2 - C_n^2)} \frac{1}{2\pi} \int_{-\infty}^{\infty} dl k_n^{-1} Q_n(x, l) e^{-ily},$$

$$Q_n(x, l) = \int_{-\infty}^x dx' \hat{F}(x, l) \sin k_n(x - x'),$$

where

$$\hat{F}(x, l) = \int_{-\infty}^{\infty} dy F(x, y) e^{ily}$$

is the one-dimensional Fourier transform of the wind stress curl in the TC, and

$$k_n = \sqrt{\frac{l^2 + \alpha_n^2}{(V/C_n)^2 - 1}},$$

where  $\alpha_n = f/C_n$  – reciprocal of the  $n$ -th baroclinic radius of deformation.

At  $V < C_n$ , the baroclinic vertical velocity has a spatial shape similar to that of the barotropic velocity:

$$W_{xy}^{(n)}(x, y) = \frac{f}{C_n^2} \frac{1}{(2\pi)^2} \iint_{-\infty}^{+\infty} dk dl P_n(k, l) e^{-i(kx+ly)},$$

where

$$P_n(k, l) = \frac{\hat{F}(k, l)}{(1 - (V/C_n)^2)k^2 + l^2 + \alpha_n^2}.$$

Thus, by applying equation (2) to equations (3) and (5), one can obtain two-dimensional fields of the SSH anomaly associated with the barotropic and baroclinic modes excited by the moving TC.

As can be seen from equation (3) and the function  $W_{xy}^{(n)}(x, y)$  in equation (5), the forcing exciting the vertical motion in the ocean according to the model [6] is represented by the wind stress curl only. Terms associated with the wind stress divergence and atmospheric pressure perturbation, which could be, in general, included in equation (3) and the expression for  $W_{xy}^{(n)}(x, y)$  in equation (5), are not considered in [6]. This is due to the fact that it is the wind stress vorticity that determines the steady-state response of the ocean to the TC passage in the form of SSH anomaly measured by altimeters. As shown in [1, 7–9], significant disturbances of the SSH caused by atmospheric pressure anomaly in the TC and wind stress divergence are localized in the area under the TC eye and disappear in its wake, i.e., after the TC passage. Since the probability of an altimeter taking measurements in the vicinity of the TC eye is rather small (in [4, 5] the time delay between the TC passage and the altimeter measurement ranged from 0 to 7 days), the contribution of

atmospheric pressure anomalies and wind stress divergence in the TC to the SSH anomaly measured by satellite altimeters can be easily assumed to be virtually zero.

Further, we will show that the barotropic SSH anomaly obtained with equations (3) and (2) has a shape of a trough, extended along the TC trajectory and decaying in the cross-track direction, with the decay rate being the inverse of the barotropic radius of deformation [1]. The baroclinic SSH anomaly field obtained with equations (5) and (2) under the condition  $V < C_n$  has a shape of a trough as well, which, however, decays at the rate equal to the inverse of the baroclinic radius of deformation. If the TC translation velocity  $V > C_n$ , then the trough is superimposed by a wave wake resulting from the excitation of inertia-gravity waves. The kinematic properties of this wake were analyzed in detail in [1].

We expect that satellite altimetry data reflects SSH anomalies formed by the superposition of barotropic and baroclinic displacements of the ocean surface behind TCs, which are discussed in the next section.

### TC and stratification parameters

In this section, we apply the model described above to model SSH anomalies produced by real TCs. We consider TCs that existed in different regions of the World Ocean from 2010 to 2020. We selected those TCs whose category did not fall below category one on the Saffir-Simpson scale for at least one day. The total number of TCs satisfying this condition was 417. Data on the location of TCs, their maximum wind speed  $U_m$  and translation speed  $V$  were taken from the IBTrACS database [10] (variables with the *usa\_* prefix), in which the time series have 3-hour time resolution.

To construct a two-dimensional wind field, we use the model of tangential wind speed in the TC proposed in [11]. To apply this model, we used information on the radii of reference wind speeds (34, 50 and 60 kt) in different quadrants of TCs, which is available in the IBTrACS. The resulting profile of the tangential wind speed is set equal to the profile of the wind vector magnitude. To specify a two-dimensional wind vector field, we introduced an inflow angle of  $22.5^\circ$ , which is a measure of the deviation of the wind direction from purely cyclonic one. The radius of the maximum wind speed  $R_m$ , which is necessary for subsequent analysis, was determined as the radius at which the wind speed profile obtained with [11] attains its maximum. For the analysis, we retained TC positions at which the condition  $U_m/(fR_m) \geq 10$  was satisfied, because the model [11] reproduces the maximum wind speed in the TC only in the limit  $U_m/(fR_m) \ll 1$ . An example of the wind speed radial profile is shown in Fig. 1, *a*.

It follows from the previous section that one of the input parameters of the model is the wind stress curl at the surface of the ocean. The wind stress vector was calculated using the standard relationship:

$$\boldsymbol{\tau} = \rho_a C_d |\mathbf{U}| \mathbf{U},$$

where  $\rho_a = 1.15 \text{ kg}\cdot\text{m}^{-3}$  – air density;  $\mathbf{U}$  – wind vector, and  $C_d$  – sea surface drag coefficient calculated in the same way as in [12]. At  $U_m < 40 \text{ m}\cdot\text{s}^{-1}$   $C_d$  behaves like the drag coefficient in equation (18) [3], where we used  $C_d$  from COARE3.5 [13] as a reference. At  $U_m > 40 \text{ m}\cdot\text{s}^{-1}$   $C_d$  equals 0.0015. The wind-speed dependence of  $C_d$  is shown in Fig. 1, *b*. An example of wind stress curl radial profile is shown in Fig. 1, *c*.

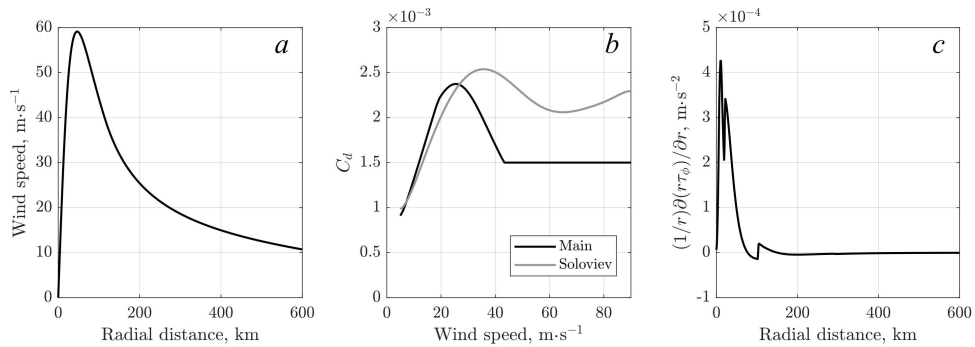


**Fig. 1.** Radial profile of wind speed obtained using the model [11] (a); dependence of the drag coefficient on the wind speed (the black line is  $C_d$  from [12] used throughout this study; the gray line is the drag coefficient from [14] (b); radial profile of wind stress curl (the variable on the vertical axis divided by sea water density) (c)

To define the ocean stratification, we use temperature and salinity profiles from the MAXSS Storm Atlas <sup>1</sup> (product – atlas of multi-source earth observations over tropical cyclones for the time period 2010–2020). The four-dimensional datasets (three spatial dimensions and one time dimension) are Argo float data interpolated onto a regular spatiotemporal grid (ISAS20 product <sup>2</sup>). The temperature and salinity data have monthly time resolution, a spatial resolution of  $0.5^\circ$  in longitude, and a variable resolution in latitude. The vertical grid with 187 grid points covers the water column from the surface to 5500 m depth. The temperature and salinity profiles at the TC positions were obtained using the linear interpolation in space and time. The potential density of seawater was calculated from these profiles using the TEOS10 thermodynamic equation of state <sup>3</sup>. Finally, the potential density profiles were converted to those of the buoyancy frequency (see Figs. 2, a, b). We note that the three-layer approximation of the water column in the model [6] performs poorly when the local ocean depth is low. Therefore, we excluded those TC positions which had local depths less than 200 m from consideration.

The model of the baroclinic and barotropic ocean response [6] was derived for idealized conditions in which the TC parameters are constant in time, the ocean stratification is horizontally uniform, and the changes in the Coriolis parameter with latitude are not taken into account. To apply this model to real conditions, we assume that the parameters  $U_m$ ,  $R_m$ , and  $V$  corresponding to a given TC at a given time are constant, and the buoyancy frequency profile obtained from the temperature and salinity profiles interpolated onto the TC location point is horizontally uniform.

<sup>1</sup> Piollé, J.-F., Reul, N. and De Boyer-Montégut, C., 2023. *Atlas of Multi-Source Earth Observations over Tropical Cyclone (2010-2020) for ESA MAXSS Project*. Ver. 1.0. Plouzane, France: Ifremer. [Accessed: 07.12.2022]. <https://doi.org/10.12770/6C56BCDE-050F-42EB-92B8-8E882E1F4DB9>

<sup>2</sup> Kolodziejczyk, N., Prigent-Mazella, A. and Gaillard, F., 2023. *ISAS Temperature, Salinity, Dissolved Oxygen Gridded Fields*. SEANOE. <https://doi.org/10.17882/52367>

<sup>3</sup> McDougall, T.J. and Barker, P.M., 2011. *Getting Started with TEOS-10 and the Gibbs Seawater (GSW) Oceanographic Toolbox: Version 3.0*. CSIRO Marine and Atmospheric Research, 28 p.

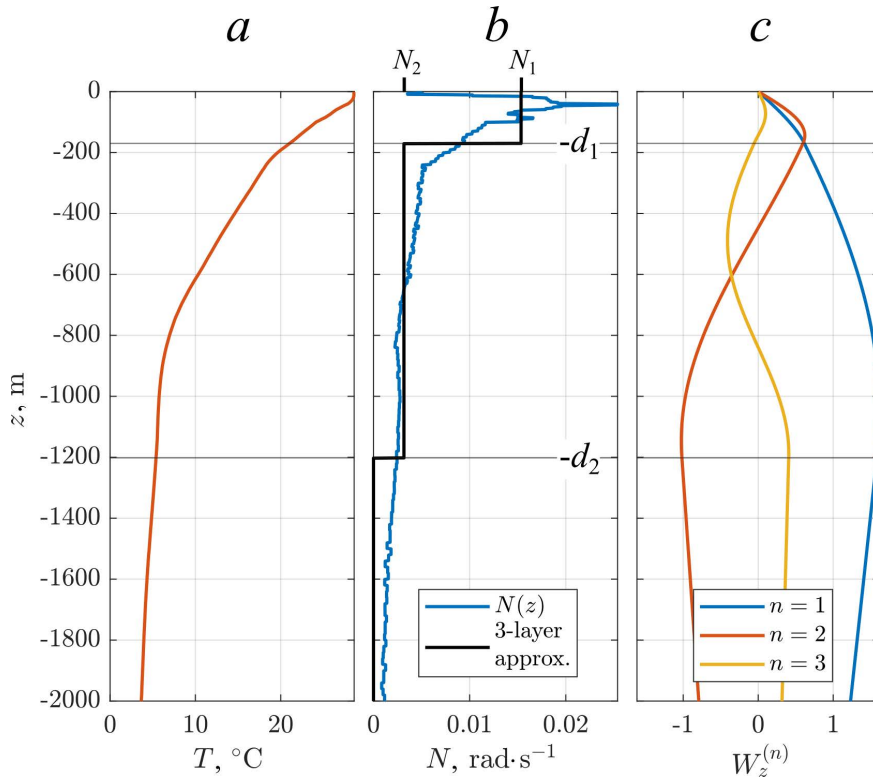


**Fig. 2.** Initial temperature profile (a), initial buoyancy frequency profile (b), and profiles of the first three baroclinic modes of vertical velocity (c). The result of breaking the water column into three layers based on the buoyancy frequency profile is shown in the center figure, where the horizontal lines denote the lower boundaries of the seasonal and main pycnocline, respectively, and the black line shows the piecewise constant buoyancy frequency profile used in the model. To display the details of the vertical distribution of the parameters near the ocean surface, the depth range is limited to 2 km. The ocean depth in this case is 4.8 km

Then, the model is run in the idealized computational domain, in which two-dimensional fields of the SSH anomaly associated with the baroclinic and barotropic modes and their superposition are calculated. The computational domain in the horizontal plane has the shape of a square with a side of  $2R_{bt}$ , where  $R_{bt}$  is the barotropic radius of deformation at the given TC position, and the spatial resolution is set to  $R_m/5$ .

The total number of TCs left in our database after the removal of TC positions based on local depth and values of  $U_m/(fR_m)$  parameter was 400.

## Results

### Examples of modelled baroclinic and barotropic TC-induced SSH anomalies

To illustrate the modelled SSH anomaly described in the previous section, we consider a specific example of TC Igor – category 4 TC that occurred in the North Atlantic in 2010. At 15:00 UTC on 15 September 2010, the TC had the following parameters: maximum wind speed  $U_m = 59.1 \text{ m}\cdot\text{s}^{-1}$ , translation speed  $V = 3.2 \text{ m}\cdot\text{s}^{-1}$ , coordinates of the TC eye  $19.6^\circ\text{N}$ ,  $55.0^\circ\text{W}$ . The radial profile of the wind speed in

the TC, constructed using the model [11], is shown in Fig. 1, *a*, and the corresponding profile of the wind stress curl is shown in Fig. 1, *c*. According to the wind model, the radius of the maximum wind speed  $R_m$  was 41.9 km. The temperature and salinity profiles obtained by spatiotemporal interpolation of ISAS20 data onto the given TC position are shown in Fig. 2. The same figure shows the buoyancy frequency profile and vertical velocity eigenfunctions for the first three baroclinic modes.

SSH anomalies of the first three baroclinic modes calculated using equations (2) and (5) are shown in Fig. 3, *a*, *b* and *c*. The baroclinic response possesses wave oscillations associated with inertia-gravity waves characteristic of these conditions, in which  $C_n$  do not exceed the TC translation speed. The wave-filled wake has features typical of a baroclinic response: higher-order modes have a longer wavelength and a smaller wedge angle. In addition to wave motions on the ocean surface, the baroclinic response also consists of a trough (see Fig. 5, *a*). The amplitude of wave oscillations and the magnitude of the surface trough weaken as the mode number increases. The shape of the sea surface corresponding to the barotropic mode calculated using equations (2) and (3), has no wave-filled wake, but a trough aligned with the TC track (Figs. 3, *d*, 4, *d* and 5, *a*).

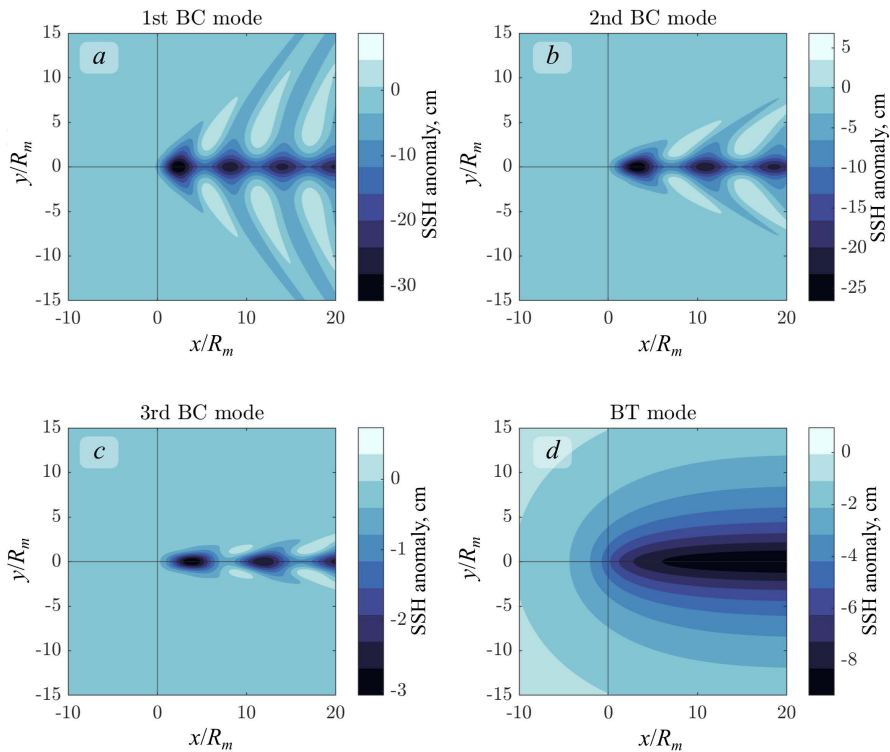


**Fig. 3.** SSH anomaly in the deep ocean (4.8 km depth), corresponding to the first baroclinic mode (*a*), second mode (*b*), third mode (*c*), and barotropic mode (*d*). Parameters  $x/R_m$  and  $y/R_m$  represent the distance from the TC eye normalized by the radius of maximum wind speed. TC parameters in this particular case are  $U_m = 59.1 \text{ m}\cdot\text{s}^{-1}$ ,  $R_m = 41.9 \text{ km}$ ,  $V = 3.2 \text{ m}\cdot\text{s}^{-1}$ , latitude =  $19.6^\circ$

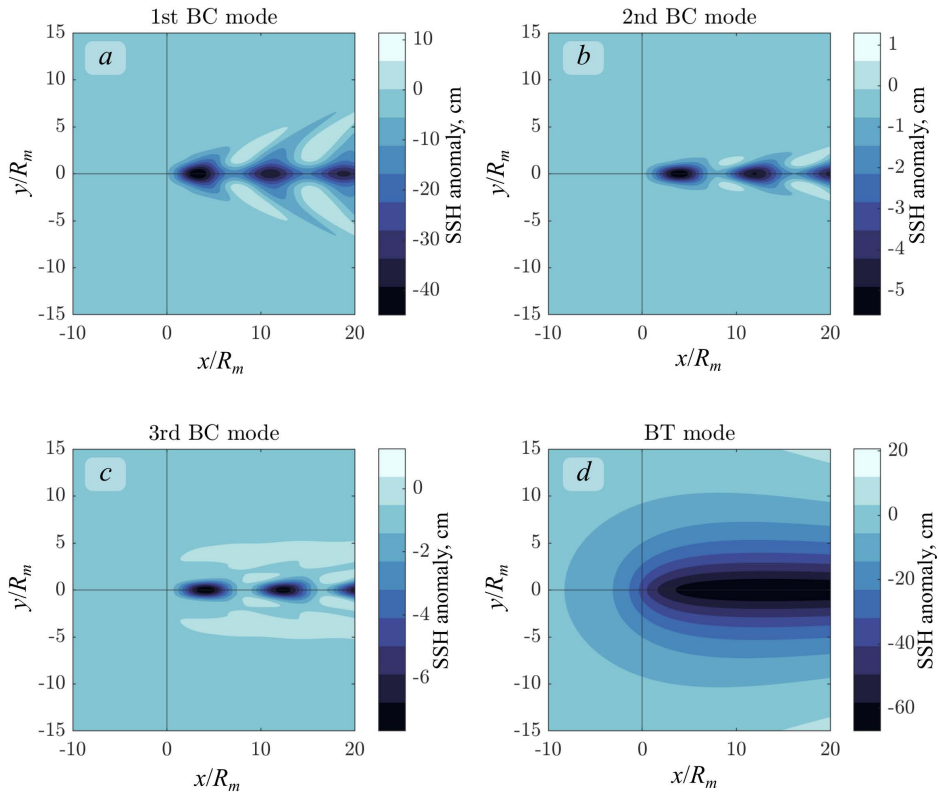


**Fig. 4.** The same as in Fig. 3 but in the shallow ocean (0.5 km depth)

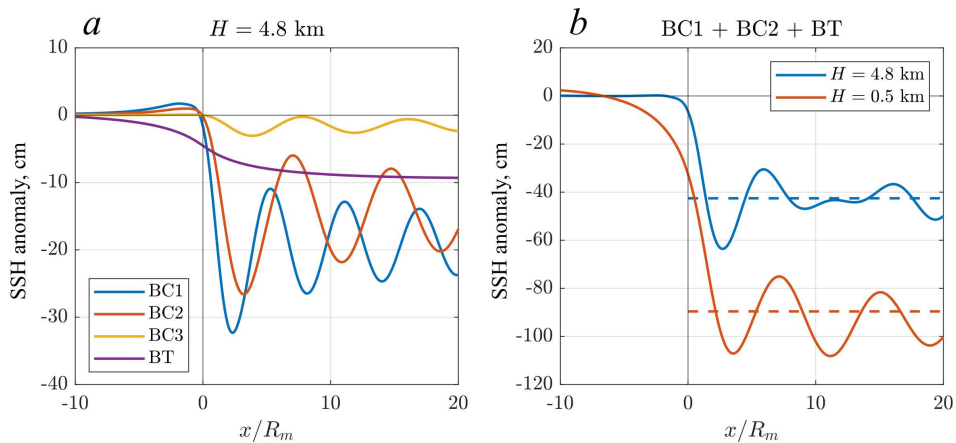


**Fig. 5.** Transections of the two-dimensional SSH anomaly fields along the line  $y/R_m = 0$ , corresponding to the first (BC1), second (BC2), third (BC3) baroclinic modes and the barotropic mode (BT) from Fig. 3 (a), corresponding to the superposition of the first two baroclinic modes and the barotropic mode in deep (blue line) and shallow (orange line) ocean conditions (b). The dashed horizontal lines show the average SSH anomaly, which is analyzed and used in comparison with SSH anomalies calculated from the parameterizations [3–5]

If we decrease the ocean depth, the long wave speeds  $C_n$  for the baroclinic modes decrease, which leads to changes in the shape of the wave-filled wake: the wavelength becomes greater and the wedge angle becomes smaller, as shown in Fig. 4 (cf. Fig. 3). At the same time, the decrease in the ocean depth leads to a significant increase in the barotropic displacement of the sea surface (cf. Fig. 4,  $d$  with Fig. 3,  $d$ ). We will address the dependence of the barotropic SSH anomaly on the local ocean depth in the next section.

To compare the modelled SSH anomalies with the observed ones described by the relation (1), we use the average SSH anomaly along the line  $y/R_m = 0$  at  $x/R_m > 0$ . The choice of the average anomaly is justified by the fact that the altimeter acquisition time has a random shift relative to the time of TC passage through a given point in the sea surface (in studies [4, 5] this shift reached 7 days). Therefore, when considering a large dataset of satellite altimeter measurements, SSH anomalies induced by inertia-gravity waves give a zero contribution, and it is the average TC-induced surface displacement (displacement left after the TC passage), associated with troughs of baroclinic and barotropic modes, that dominates the altimetry signal.

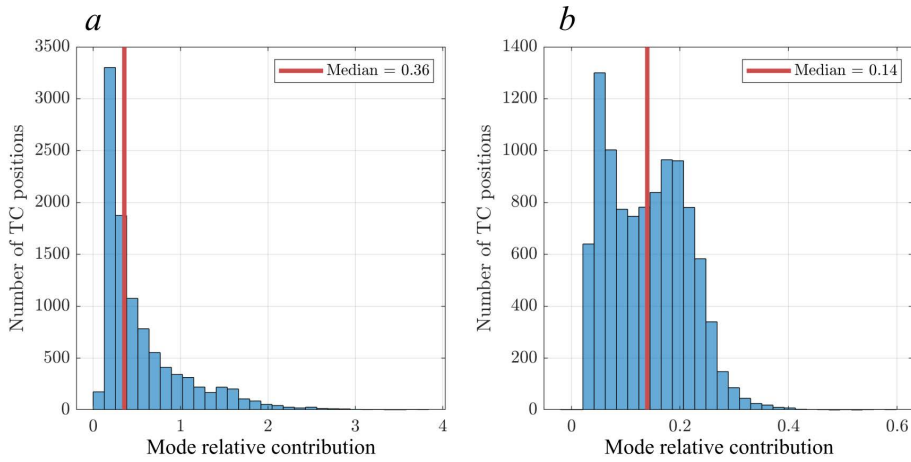
### **Modelling of TC-induced SSH anomalies in the World Ocean**

In the same way the model was applied to TC Igor in the previous section, we applied the model to simulate and then calculate SSH anomalies produced by all the TCs from the considered set at different points of the World Ocean at different times. At each TC position, we calculated the average SSH anomaly produced by different modes and their superposition (as in Fig. 5). These calculations are analyzed here.

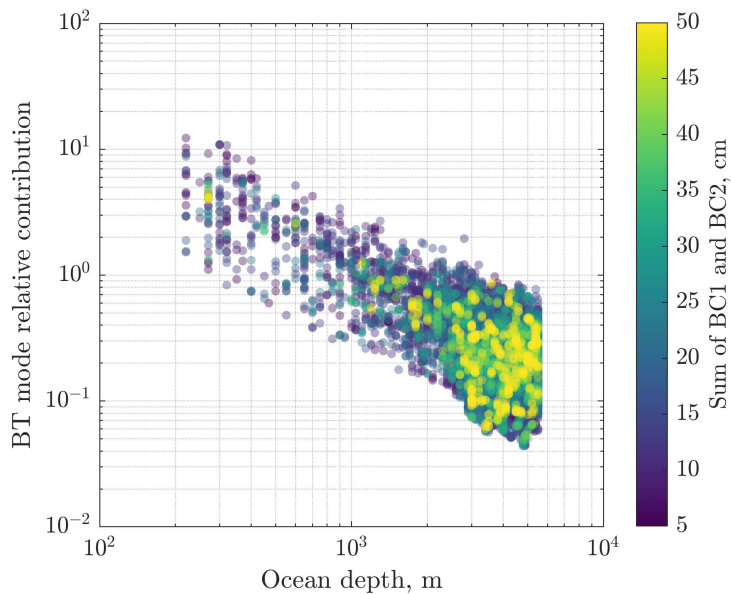
Fig. 6 shows the relative contribution of the second and third baroclinic modes to the SSH anomaly. The contribution of the second baroclinic mode to the modelled SSH is significant. In 50% of cases, the second baroclinic mode leads to an increase in the average SSH anomaly by more than 36%. Among these, we can also highlight cases in which taking into account the second mode leads to an increase in the average SSH anomaly by a factor 2 or greater. The contribution of the third mode to the baroclinic SSH anomalies leads to a less significant effect. In the overwhelming majority of cases, accounting for the third mode leads to SSH anomaly increase that does not exceed 30%, and in half of the cases the increase in the anomaly does not exceed 14% compared to the average SSH anomaly produced by the superposition of the first two baroclinic modes.

Fig. 7 shows the relative contribution of the barotropic mode to the average SSH anomaly produced by the superposition of first two baroclinic modes and the barotropic mode. It follows that even at the ocean depth of 5.5 km, barotropic mode accounts for 20% of the total SSH anomaly caused by the two baroclinic modes and the barotropic mode, which means that the barotropic mode cannot be considered negligible. At depths less than 2 km, barotropic SSH anomalies can be more significant, and at depths less than 500 m, taking into account the barotropic motions, can increase the total SSH anomaly by more than a factor of two. The color coding in Fig. 7 shows that the barotropic mode increases the SSH anomaly associated with the two baroclinic modes by more than 100% in situations when the total baroclinic SSH does not exceed 50 cm. Note that in Fig. 7 the maximum depth is 5.5 km, which is the maximum depth in the ISAS20 database. If, however,

we consider ocean depths taken, for example, from the ETOPO database, the results in cases where the ocean depth exceeds 5.5 km remain practically unchanged.



**Fig. 6.** Histogram showing the contribution of the second baroclinic mode to the average SSH anomaly calculated from the first baroclinic mode (*a*), the contribution of the baroclinic third mode to the average SSH anomaly calculated from the superposition of the first and second baroclinic modes (*b*). Red vertical lines show median values



**Fig. 7.** Contribution of the barotropic mode to the average SSH anomaly produced by the first two baroclinic modes as a function of the local ocean depth

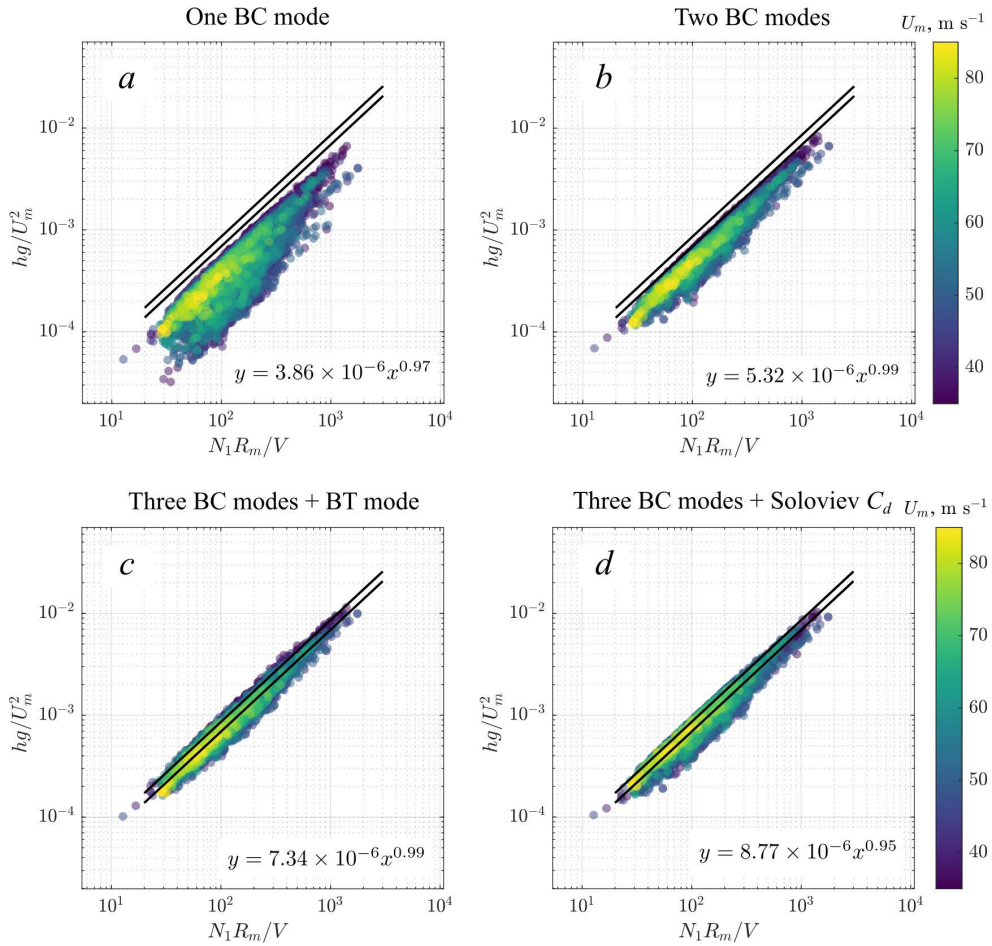


**Fig. 8.** Average SSH anomaly normalized by  $U_m^2/g$  as a function of the parameter  $N_1 R_m/V$ , calculated from the first baroclinic mode (*a*), the superposition of the first two baroclinic modes (*b*), and the superposition of the first three baroclinic modes and the barotropic mode (*c*), obtained from the superposition of the first three baroclinic modes modelled using the drag coefficient from [14] (*d*). Black lines show the parameterizations from [3, 4] (lower black line), and from [5] (upper black line). Only the cases in which the local ocean depth was greater than 2 km are shown

Fig. 8, *a* shows the modelling results in dimensionless variables dictated by equation (1). To be consistent with [4, 5], we excluded cases with the local depths less than 2 km from Fig. 8. It is evident that SSH anomalies calculated from only the first baroclinic mode follow the power-like law, but the ‘level’ of the modelled anomalies significantly underestimates that of the parameterizations obtained in [3–5]. Indeed, the proportionality coefficient of the power law fit to the modelled SSH anomaly in dimensionless variables is  $3.85 \times 10^{-6}$  as opposed to  $6.9 \cdot 10^{-6}$  from [3, 4]. If we add the second baroclinic mode to the first mode, the power-law dependence becomes more pronounced, and the level of the modelled SSH anomaly increases significantly (Fig. 8, *b*). Despite these improvements, the average SSH anomaly still does not reach the level of anomalies predicted by the parameterizations of [3–5]. Addition of the third baroclinic mode and

the barotropic mode separately to the superposition of the first two baroclinic modes does not significantly improve the results. If, however, we add both of these modes, the SSH anomalies represented by the superposition of three baroclinic modes and the barotropic mode are appreciably enhanced, leading to significant improvement in the agreement between the modelled and parameterized SSH anomalies (Fig. 8, *c*).

Approximation of the modelling results by the relation (1) shows that the exponent, equal to 0.99, practically coincides with unity, and the proportionality constant, equal to  $7.46 \cdot 10^{-6}$ , is between the values of the constants in the parameterizations [3, 4] ( $6.9 \cdot 10^{-6}$ ) and [5] ( $8.6 \cdot 10^{-6}$ ). This result indicates that TC-induced SSH anomalies measured by altimeters are composed of not only several baroclinic modes but apparently the barotropic mode even in deep ocean conditions with depths exceeding 2 km.

### Discussion

Fig. 8, *c* shows that the observed SSH anomalies produced by moving TCs, presented in the form (1), are reproduced by the superposition of the first three baroclinic modes and the barotropic mode. However, in the model [6], the changes in the Coriolis parameter with latitude were not taken into account. As noted in [1], the currents corresponding to the barotropic trough and the baroclinic ridge (lifted pycnocline) should respond to the changes in the Coriolis parameter with latitude. It means that the steady-state barotropic and baroclinic perturbations should be altered by breakdown into planetary waves. The time required for the breakdown is given in [15] and is estimated as one day for the barotropic trough and several weeks for the baroclinic ridge. We conclude that the barotropic component happens to be substantially dissolved by planetary wave radiation by the time the altimeter passes over the TC track, since the time lag between the altimeter acquisition time and TC passage time is likely to be greater than one day. Based on this, consideration of the barotropic component when interpreting satellite altimeter measurements seems unjustified.

In this context, we consider the modelled SSH anomalies in Fig. 8, *c* as unrealistic. Unfortunately, as we noted in the previous section, the superposition of three baroclinic modes, producing a more stable perturbation of SSH, underestimates observed SSH anomalies presented in the form of parameterizations [3–5] (Fig. 9). To improve the agreement between the model and parameterizations [3–5], we consider wind-dependence of the drag coefficient different from that used so far (Fig. 1, *c*).

Little is known about the behavior of the drag coefficient at wind speeds greater than  $40\text{--}50 \text{ m}\cdot\text{s}^{-1}$ . Experimental estimates differ from one another even in terms of tendencies. For example, the results of studies [16, 17] indicate an almost constant value of the drag coefficient at hurricane winds, which ranges from 0.002 to 0.0025. In turn, the results of recent studies [3, 18, 19, 5] suggest a decrease in the drag coefficient with increasing wind speed. The authors of [14] proposed a different parameterization of the resistance law based on the results of laboratory experiments and numerical modelling. In that study, there is no monotonic attenuation of the drag coefficient with increasing wind speed. At wind speeds greater than  $25 \text{ m}\cdot\text{s}^{-1}$ , this parameterization gives systematically larger values of  $C_d$  (around  $2.25 \cdot 10^{-3}$ ) compared to that used in our calculations so far (see Fig. 1, *b*).

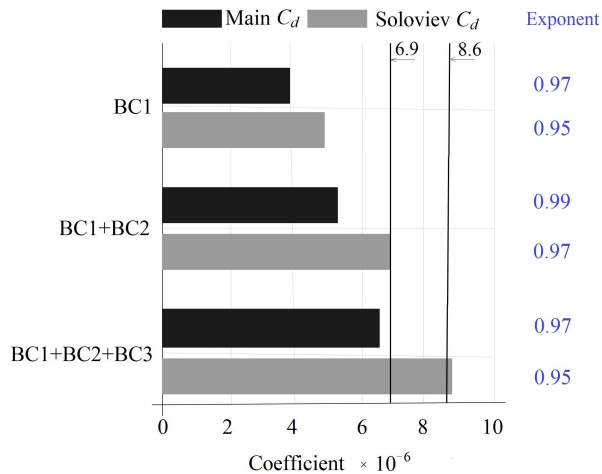


**Fig. 9.** Values of proportionality constants in the approximation of modelled SSH anomalies by a power function of the form (1) for different combinations of modes and using different drag coefficients. Black and gray bars correspond to calculations with the drag coefficients shown by black and gray lines in Fig. 1, *b* respectively. Numbers in blue show the exponents in the approximation of modelled SSH anomalies by a power function (1). Horizontal lines show the values of the proportionality coefficients in the parameterizations [3, 4] –  $6.9 \cdot 10^{-6}$  and [5] –  $8.6 \cdot 10^{-6}$

If we apply the parameterization [14] to estimate the wind stress and repeat the calculation SSH anomalies associated with the superposition of the first three baroclinic modes, the agreement between the modelled surface displacements and the displacements predicted by the parameterizations [3–5] is noticeably improved (Fig. 8, *d*). The approximation of the modelled SSH anomalies by the power function (1) has the proportionality constant  $8.77 \cdot 10^{-6}$  which is close to  $8.6 \cdot 10^{-6}$  – the proportionality constant in the parameterization [5]. Fig. 9 shows how the results change in terms of the proportionality constant and the exponent in the approximation of the modelled SSH anomalies by expression (1) when considering different combinations of baroclinic modes. It is evident that usage of  $C_d$  from [12], whatever the combination of baroclinic modes, cannot reproduce parameterizations [3–5]. On the other hand, usage of  $C_d$  from [14] results in better agreement with the mentioned parameterizations when two or three baroclinic modes are considered. If a more definite choice of the mode combination is needed then the superposition of three baroclinic modes is the optimal one. This is because low-wind-speed points cluster slightly below the power law approximation of the modelled SSH anomalies, and they are uniformly distributed between the parameterizations [3–5]. The better performance of the drag coefficient from [14] in modelling SSH anomalies is in some contradiction with the conclusions of work [3], in which it was shown that  $C_d$  for hurricane-force winds should decay with increasing wind speed, ensuring asymptotically constant wind stresses at extremely high wind speeds (see Fig. 15 in [3]).

## Conclusion

In this paper, we analyzed the formation of TC footprints in sea surface height (SSH) anomalies that are observed by satellite altimeters, and which have simple parameterization in the form of relation (1) [3–5]. For the analysis, a simplified model of the barotropic and baroclinic response of the ocean to moving TCs proposed in [6] was used. The model was applied to simulate SSH anomalies produced by TCs of the first category and higher, which propagated in different regions of the World Ocean in the time period from 2010 to 2020. SSH anomalies were simulated for 400 TCs using observed TC parameters and ocean stratification.

The main factor determining the steady-state SSH anomaly in the wake of the TC is the vorticity of the wind stress. The atmospheric pressure anomaly in the TC and the divergence of the wind stress generates significant disturbances of the sea surface directly under the TC, which, however, fade out in the wake and therefore do not significantly contribute to the steady-state SSH anomaly which dominates satellite altimeter signal.

Applying the model [6] to the global set of TCs, we showed that the relative contribution of the second baroclinic mode to the SSH anomaly compared to the first mode is significant and is more than 36% in half of the modelled cases. The contribution of the third baroclinic mode relative to the superposition of the first two is not as significant and does not exceed 30% with a median value of 14%.

Addition of the barotropic mode to the superposition of the first two baroclinic modes results in an increase in the ocean surface displacement. In the ocean with a local depth exceeding 2 km, the influence of the barotropic mode is appreciable so that this mode can increase SSH anomaly associated with the first two baroclinic modes by about 100%. With decreasing depth, addition of the barotropic mode can increase the total SSH anomaly (barotropic plus two baroclinic) by more than 100%. However, the geostrophic currents associated with the barotropic perturbation of the sea surface is less stable than the baroclinic one, so that the barotropic trough is altered by the radiation of planetary waves on time scales of the order of one day [1, 15]. Therefore, it can be expected that the barotropic surface displacements are absent in the altimetry data on the SSH anomalies parameterized in [3–5], because in these studies the time delay between local altimeter measurements and TC passage reached 7 days.

Analysis of modelled TC-induced SSH anomalies in dimensionless variables clearly indicated that the ocean surface displacements which were parameterized in [3–5] are multimodal. The average level of the observed SSH anomalies is well reproduced by the superposition of three baroclinic modes when the drag coefficient proposed in [14] is used to calculate the wind stress. This conclusion differs from the results of the study [3], from which it follows that in the range of hurricane-force winds the drag coefficient decreases monotonically with increasing wind speed.

## Appendix

Dimensionless coefficients in the equation for  $W_z^{(n)}(z)$  are given by the following expressions:

$$a_{1n} = -\left(\frac{2}{\Sigma_n}\right) \frac{\cos(\Sigma_n + \phi_n) - r \cos(\delta_n - \phi_n)}{\cos(\Sigma_n + \phi_n)(1 + \Phi_{\Sigma n}) - r(\delta_n/\Sigma_n)\cos(\delta_n - \phi_n)(1 - \Phi_{\delta n})}$$

$$a_{2n} = -\left(\frac{2}{\Sigma_n}\right) \frac{2N_1/(N_1 - N_2)}{\cos(\Sigma_n + \phi_n)(1 + \Phi_{\Sigma n}) - r(\delta_n/\Sigma_n)\cos(\delta_n - \phi_n)(1 - \Phi_{\delta n})},$$

where

$$\Phi_{\Sigma n} = \frac{\partial \phi_n}{\partial \Sigma_n} = \frac{C_n \sin^2(\phi_n)}{N_2(H - d_2)\Sigma_n}$$

$$\Phi_{\delta n} = \frac{\partial \phi_n}{\partial \delta_n} = \frac{C_n \sin^2(\phi_n)}{N_2(H - d_2)\delta_n}$$

and  $r = (N_1 - N_2)/(N_1 + N_2)$ . Variables  $\Sigma_n = \Sigma(C_n)$ ,  $\delta_n = \delta(C_n)$ ,  $\phi_n = \phi(C_n)$  are defined by the following functions evaluated at  $C = C_n$ :

$$\Sigma(C) = \frac{N_1 d_1}{c} + \frac{N_2(d_2 - d_1)}{c},$$

$$\delta(C) = \frac{N_1 d_1}{c} - \frac{N_2(d_2 - d_1)}{c},$$

$$\phi(C) = \arcsin \frac{N_2(H - d_2)/C}{\sqrt{1 + [N_2(H - d_2)/C]^2}}.$$

Separation constants  $C_n$  are calculated as roots of the transcendental equation (values of  $C_n$  decrease with the mode number  $n$ ):

$$\sin(\Sigma(C) + \phi(C)) - r \sin(\delta(C) - \phi(C)) = 0.$$

## REFERENCES

1. Geisler, J.E., 1970. Linear Theory of the Response of a Two Layer Ocean to a Moving Hurricane. *Geophysical Fluid Dynamics*, 1(1-2), pp. 249-272. <http://doi.org/10.1080/03091927009365774>
2. Ginis, I. and Sutyrin, G., 1995. Hurricane-Generated Depth-Averaged Currents and Sea Surface Elevation. *Journal of Physical Oceanography*, 25(6), pp. 1218-1242. [https://doi.org/10.1175/1520-0485\(1995\)025<1218:HGDACA>2.0.CO;2](https://doi.org/10.1175/1520-0485(1995)025<1218:HGDACA>2.0.CO;2)
3. Kudryavtsev, V., Monzikova, A., Combot, C., Chapron, B., Reul, N. and Quilfen, Y., 2019. A Simplified Model for the Baroclinic and Barotropic Ocean Response to Moving Tropical Cyclones: 1. Satellite Observations. *Journal of Geophysical Research: Oceans*, 124(5), pp. 3446-3461. <http://doi.org/10.1029/2018JC014746>
4. Combot, C., Mouche, A., De Boyer Montegut, C. and Chapron, B., 2024. Toward Comprehensive Understanding of Air-Sea Interactions under Tropical Cyclones: On the Importance of High Resolution and Multi-Modal Observations. *Geophysical Research Letters*, 51(19), e2024GL110637. <http://doi.org/10.1029/2024GL110637>
5. Zhang, B., Wen, L., Perrie, W. and Kudryavtsev, V., 2024. Sea Surface Height Response to Tropical Cyclone from Satellite Altimeter Observations and SAR Estimates. *IEEE Transactions on Geoscience and Remote Sensing*, 62, pp. 1-9. <http://doi.org/10.1109/tgrs.2024.3371168>

6. Kudryavtsev, V., Monzikova, A., Combot, C., Chapron, B. and Reul, N., 2019. A Simplified Model for the Baroclinic and Barotropic Ocean Response to Moving Tropical Cyclones: 2. Model and Simulations. *Journal of Geophysical Research: Oceans*, 124(5), pp. 3462-3485. <http://doi.org/10.1029/2018JC014747>
7. Orlanski, I. and Polinsky, L.J., 1983. Ocean Response to Mesoscale Atmospheric Forcing. *Tellus A: Dynamic Meteorology and Oceanography*, 35, pp. 296-323.
8. Price, J.F., 1983. Internal Wave Wake of a Moving Storm. Part I. Scales, Energy Budget and Observations. *Journal of Physical Oceanography*, 13(6), pp. 949-965. [http://doi.org/10.1175/1520-0485\(1983\)013<0949:IWVOAM>2.0.CO;2](http://doi.org/10.1175/1520-0485(1983)013<0949:IWVOAM>2.0.CO;2)
9. Khain, A. and Sutyurin, G., 1983. *Tropical Cyclones and Their Interaction with the Ocean*. Leningrad: Hydrometeoizdat, 272 p. (in Russian).
10. Knapp, K.R., Kruk, M.C., Levinson, D.H., Diamond, H.J. and Neumann, C.J., 2010. The International Best Track Archive for Climate Stewardship (IBTrACS): Unifying Tropical Cyclone Data. *Bulletin of the American Meteorological Society*, 91(3), pp. 363-376. <http://doi.org/10.1175/2009BAMS2755.1>
11. Chavas, D.R., Lin, N. and Emanuel, K.A., 2015. A Model for the Complete Radial Structure of the Tropical Cyclone Wind Field. Part I: Comparison with Observed Structure. *Journal of the Atmospheric Sciences*, 72(9), pp. 3647-3662.
12. Kudryavtsev, V.N. and Pivaev, P.D., 2025. Mixed Layer Depth Parameterization and Ocean Surface Cooling Induced by Tropical Cyclones. *Ocean Modelling*, 195, 102514. <http://doi.org/10.1016/j.ocemod.2025.102514>
13. Edson, J.B., Jampana, V., Weller, R.A., Bigorre, S.P., Plueddemann, A.J., Fairall, C.W., Miller, S.D., Mahrt, L., Vickers, D. [et al.], 2013. On the Exchange of Momentum over the Open Ocean. *Journal of Physical Oceanography*, 43(8), pp. 1589-1610. <http://doi.org/10.1175/JPO-D-12-0173.1>
14. Soloviev, A.V., Lukas, R., Donelan, M.A., Haus, B.K. and Ginis, I., 2014. The Air-Sea Interface and Surface Stress under Tropical Cyclones. *Scientific Reports*, 4(1), 5306. <http://doi.org/10.1038/srep05306>
15. Longuet-Higgins, M.S., 1965. The Response of a Stratified Ocean to Stationary or Moving Wind-Systems. *Deep Sea Research and Oceanographic Abstracts*, 12(6), pp. 923-973. [http://doi.org/10.1016/0011-7471\(65\)90814-4](http://doi.org/10.1016/0011-7471(65)90814-4)
16. Donelan, M.A., Haus, B.K., Reul, N., Plant, W.J., Stiassnie, M., Graber, H.C., Brown, O.B. and Saltzman, E.S., 2004. On the Limiting Aerodynamic Roughness of the Ocean in Very Strong Winds. *Geophysical Research Letters*, 31(18), 19460. <http://doi.org/10.1029/2004gl019460>
17. Takagaki, N., Komori, S., Suzuki, N., Iwano, K., Kuramoto, T., Shimada, S., Kurose, R. and Takahashi, K., 2012. Strong Correlation between the Drag Coefficient and the Shape of the Wind Sea Spectrum over a Broad Range of Wind Speeds. *Geophysical Research Letters*, 39(23), 53988. <http://doi.org/10.1029/2012GL053988>
18. Ye, L., Li, Y. and Gao, Z., 2022. Surface Layer Drag Coefficient at Different Radius Ranges in Tropical Cyclones. *Atmosphere*, 13(2), 280. <http://doi.org/10.3390/atmos13020280>
19. Ermakova, O., Rusakov, N., Poplavsky, E., Sergeev, D. and Troitskaya, Y., 2023. Friction Velocity and Aerodynamic Drag Coefficient Retrieval from Sentinel-1 IW Cross-Polarization C-SAR Images under Hurricane Conditions. *Remote Sensing*, 15(8), 1985. <http://doi.org/10.3390/rs15081985>

Submitted 20.12.2024; approved after review 08.02.2025;  
accepted for publication 13.03.2025.

*About the authors:*

**Pavel D. Pivaev**, Junior Researcher, Marine Hydrophysical Institute of RAS (2 Kapitanskaya Str., Sevastopol, 299011, Russian Federation), Engineer-researcher, Satellite Oceanography Laboratory, Russian State Hydrometeorological University (98 Malookhtinskiy Ave., Saint Petersburg, 195196, PHYSICAL OCEANOGRAPHY VOL. 32 ISS. 3 (2025) 425

Russian Federation), **SPIN-code: 4200-1129, ORCID ID: 0000-0003-2218-5774, ResearcherID: JBJ-6552-2023, Scopus Author ID: 57430050200**, pivaev.pavel@gmail.com

**Vladimir N. Kudryavtsev**, Head of the Satellite Oceanography Laboratory, Russian State Hydrometeorological University (98 Malookhtinskiy Ave., Saint Petersburg, 195196, Russian Federation), Leading Researcher, Marine Hydrophysical Institute of RAS (2 Kapitanskaya Str., Sevastopol, 299011, Russian Federation), DSc. (Phys.-Math.), **SPIN-code: 2717-5436, ORCID ID: 0000-0002-8545-1761, ResearcherID: G-1502-2014, Scopus Author ID: 7102703183**, kudr@rshu.ru

*Contribution of the co-authors:*

**Pavel D. Pivaev** – writing of the original draft of the manuscript, data curation, visualization and processing, discussion of the results

**Vladimir N. Kudryavtsev** – conceptualization, review and editing of the manuscript, discussion of the results

*The authors have read and approved the final manuscript.*

*The authors declare that they have no conflict of interest.*